The Fractal Nature of Cement-Based Systems Under Sustained Elevated Temperatures

by

Muhammad Mamun

A thesis submitted in partial fulfillment of the requirements for the degree of

Doctor of Philosophy

in

Structural Engineering

Department of Civil and Environmental Engineering
University of Alberta

ABSTRACT

Macro-mechanical behaviour of a material in response to applied loads is governed by its microstructural characteristics. The relative volume fraction of the constituent phases, their connectivity and interface are some of the microstructural features that have significant impact on the load carrying capacity of the material. During its service life, a structure may be exposed to extreme environmental actions, such as elevated temperatures, causing hygro-thermal degradations to the material. The severity of this deterioration depends largely on the nature of the source of exposure, the rate of temperature rise, the density of the material, and its moisture content. Cement-based materials are particularly susceptible to damage upon exposure to sustained elevated temperatures. The physical and chemical aspect of the properties of hydrated cement paste are the major sources of thermal damage. Furthermore, the thermally driven coupled heat and mass transport phenomena is controlled by the prevailing pore structure that is formed during cement hydration. In order to understand the behaviour of cement-based systems under sustained elevated temperatures, it is essential to examine the evolution of the microstructural parameters with an increase in the temperature and their impact on the thermal and mechanical response of the material. Notwithstanding the extensive literature on the behaviour of cement-based composites under elevated temperature, further investigations were deemed necessary to explain the mechanisms of the deterioration. Accordingly, this thesis examines the evolving microstructure and models the thermal properties using a fractal approach for sustained temperatures up to 600 °C at a heating rate of 5 °C/minute. In turn, the fracture mechanical behaviour and mechanical response are predicted. To this end, several state-of-the-art experimental methods were employed in this study. These include the Transient Plane Source method of thermal analyses per ISO, Backscattered Electron Imaging, Computed Micro-Tomography, and fracture mechanical tests. The experimental results were analyzed and discussed using appropriate modelling approaches. The findings show that the pore volume fraction increases with an increase in the temperature of exposure across all mortar mixtures. In addition, the fibre reinforced mortar shows a marginally lower porosity than the plain ones. However, it is essential to note that the lowering of porosity does not necessarily indicate a reduction in pore connectivity, which is the dominant factor in terms of the efficiency of polymeric fibres against spalling. The two-point correlation function, a morphological image processing technique, shows that the presence of monotonic nature of the asymptotic end of the function indicates a spatially uncorrelated nature of the pore structure beyond the distance associated with characteristic pore radius. Further, the thermal exposure results in a coarsening effect in capillary pores as well as in the meso pores. Additional image processing shows that the box-count based fractal dimension of the mortar increases with temperature, indicating an increasingly rougher pore perimeter. The three-dimensional pore fractal dimension, estimated through the computed microtomography, exhibits a space filling nature of the thermally degraded microstructure of the mortar. In addition, the change in fractal dimension with temperature implies an increase in compliance. Investigations regarding the fracture mechanical behaviour reveal that the crack growth resistance of the heated mortar drops with an increase in the temperature of exposure. In addition, according to the R-curve response of cement mortar—based on both the effective crack length and the crack tip opening displacement—the crack-growth resistance of the mortar approaches a constant value at elevated temperatures, which is characteristic of brittle materials. These findings are expected to broaden the knowledge base on the behaviour of

cement-based composites at elevated temperature. In other words, the information generated through this thesis will provide guidelines regarding the development of mixture proportioning process, where the selection of a composite reinforced with moderate dosage of polymeric microfibre will be capable of absorbing higher fracture energy and render a more durable structure. Further, the fractal-based model can be used to study the temperature distribution within any cement-based system, which will enable the prediction of fire resistance rating. It is also expected that the discussion presented in this thesis on the characteristics of cement mortar will facilitate the development of cement-based insulating materials for various components of a structure.

ACKNOWLEDGEMENTS

I would like to take this opportunity to express my sincere gratitude to my supervisor Dr. Vivek Bindiganavile for his encouragement, technical expertise, and unstinting financial support that brought this research towards a successful completion. I am particularly thankful for his invaluable guidance over the course of this research program. I would also like to acknowledge the generous financial support as well as the state-of-the-art research facilities provided by the Department of Civil and Environmental Engineering at the University of Alberta.

This research program would not have been completed without the assistance of the technical support staff from several different laboratories at this university. I am especially thankful to Mr. Greg Miller and Mr. Cameron West for their assistance with the instrumentation while conducting the experiments at the I. F. Morrison Structures Laboratory. I would like to express my gratitude to Mr. Rizaldy Mariano for his support during the specimen preparation stage. My sincere thanks are also due to Mr. Mark Labbe and Mr. Martin Von Dollen at the Thin Section Laboratory for preparing the specimens with painstaking attention to detail. I would also like to thank Mr. Nathan Gerein from the Scanning Electron Laboratory for his assistance with the image acquisition process.

I would also like to thank Dr. Murray Gingras for providing the access to his high resolution X-ray microtomography facility. This acknowledgement would be incomplete without expressing my gratitude to my friend and colleague Mr. Md Toihidul Islam and Mr. Rupak Mutsuddy for their continued support during this program.

I am greatly indebted to my elder sister, elder brother, and my sister-in-law for their emotional support and encouragement. Last but not the least, I am eternally grateful to my parents for encouraging me with their unwavering support throughout the course of this doctoral program.

TABLE OF CONTENTS

LIST OF TABLES

LIST OF FIGURES

LIST OF NOTATIONS

Chapter 2

a	radius of the inclusion (Section 2.4.3.1 only)
a	radius of the sensor
C_i	specific heat of i^{th} phase
D	dimensionless time function
$\dot{E}$	rate of evaporation of water
E_d	dynamic modulus of elasticity
h_c	convection heat transfer coefficient
I_0	modified Bessel function
K	thermal conductivity
k_c	thermal conductivity of the continuous phase
k_d	thermal conductivity of dispersed phase
k_e	effective thermal conductivity
k_p	thermal conductivity at percolation threshold
n	calibration factor
n	shape factor of the filler materials (Section 2.4.3.1 only)
P	pressure
P_0	input power to the sensor
q	heat flux
Q	heat input
Q_0	strength of the heat source
R	gas constant
r_k	Kelvin radius
r_p	pore radius
S	average of the slopes of temperature vs. time
T	boiling point of nitrogen (Section 2.7.3)
T	temperature

t	thickness of the adsorbed layer
T_0	initial temperature
t_r	thickness of the observed layer
V_i	velocity of i^{th} phase
V_L	velocity of primary wave
V_m	molar volume of liquid nitrogen
V_p	actual pore volume
γ_m	surface tension between mercury and pore surface
ε_i	volume fraction of i^{th} phase
θ	thickness of the sensor
θ	contact angle between mercury and the porous material (Section 2.7.2)
λ	latent heat of vaporization
v	dynamic Poisson's ratio
ρ_i	density of i^{th} phase
ϕ	volume fraction of dispersed phase
ϕ_p	percolation threshold
κ	thermal diffusivity

Chapter 3

A	input image
A_0	pre-exponential factor
B	structuring element
C	mass of surface-dry specimen
D	apparent mass of specimen in water
E_a	activation energy
g_1	bulk density
g_2	absolute density
M	molar ratio of the constituents to that of 1 cm^3 of water
m	quantity of water dehydrated in moles
N_A	number of areas

N_v	number of spherical pores
P_{hp}	volume fraction of the hydration products
P_{w}	volume fraction of water released
r	length of line segment, or distance
R	universal gas constant
r_c	characteristic pore radius
s	specific surface area
S_2	two-point correlation function
T	temperature
X	mass of oven-dried specimen in air
Δ	size interval
α	degree of hydration
β	degree of decomposition
ϕ	porosity
ρ_c	density of cement
ρ_w	density of water

Chapter 4

A	cross-sectional area
a	radius of the outermost ring of the sensor
C	cut-out size of Sierpinski carpet (Section 4.6.3.2 only)
C	specific heat
C_{bw}	specific heat of bound water
C_c	specific heat of cement
C_{fw}	specific heat of free water
C_s	specific heat of sand
D	dimensionless function of τ
D_f	fractal dimension
k	thermal conductivity
k_1	thermal conductivity of the continuous phase

k_2	thermal conductivity of the dispersed phase
k_a	thermal conductivities of air
k_e	effective thermal conductivity
k_{para}	equivalent thermal conductivities from parallel model
k_{per}	equivalent thermal conductivities from series model
k_s	thermal conductivities of solid
k_w	thermal conductivities of water
L	side length of Sierpinski carpet
m	volume fraction of water
M_{bw}	mass fraction of bound water
M_c	mass fraction of cement
M_{fw}	mass fraction of free water
M_s	mass fraction of sand
n	stage or number of iterations
P_0	output power from the sensor
R	resistance (subscript 1, 2, and 3 denote different region of Sierpinski carpet)
R_0	initial resistance of the TPS sensor
R_c	contact resistance
R_t	total resistance
T	temperature
t	time
t	thickness of contact resistance (Section 4.6.3.2 only)
t^*	dimensionless contact resistance parameter
V	moisture content by volume
α	temperature coefficient resistivity
β	ratio of t. conductivity of solid to that of air (subscripts denote different stage)
ϕ	volume fraction of pores
ϕ_1	volume fraction of the continuous phase
ϕ_2	volume fraction of the dispersed phase
κ	thermal diffusivity of the specimen
θ	volume fraction of the material oriented perpendicular to the heat flow
ρ	density of the specimen

ρ_{dry}	density of dry specimen
ρ_{wet}	density of wet specimen
τ	characteristic time

Chapter 5

a	half length of the crack
a_0	initial length of the notch
a_{eff}	effective crack length
b	width of the specimen
C	compliance
C_0	initial compliance
c	effective crack extension
c_f	limiting value of size independent crack extension
$CTOD_c$	critical crack tip opening displacement
d	depth of the specimen
d_f	fractal dimension
E	modulus of elasticity
f_{MOR}	modulus of rupture
f_t	tensile strength
G	energy release rate
g	geometry correction factor
G_f	limiting value of size independent fracture energy
G_F	fracture energy
K_I	stress intensity factor
K_{Ic}	fracture toughness
l_{ch}	characteristic length
P	applied load
R	crack growth resistance
u_b	deflection due to bending

u_c	deflection due to fracture
W_0	energy absorbed due to the applied load
W_1	work done due to the self-weight of the specimen
W_p	total energy released
σ	nominal stress
α	ratio of crack length to depth

Chapter 6

C	intercept of vertical axis
D	diffusion coefficient in porous space
D_0	diffusion coefficient in free space
D_f	fractal dimension
D_v	damage variable
E	dynamic modulus of damaged mortar
E_0	dynamic moduli of undamaged
E_d	dynamic modulus of elasticity
K	function of dynamic Poisson's ratio
L_0	length of the shortest path
L_e	length of tortuous path
N	number cubes
r	mean displacement in porous space
r_{free}	mean displacement in free space
V	ultrasonic pulse velocity
ε	size of cubes
ν	Poisson's ratio
ρ	density of the mortar
τ	geometric tortuosity
τ_d	diffusion tortuosity

LIST OF ABBREVIATIONS

AFt	Alumina, ferric oxide, tri-sulphate (Ettringite)
BJH	Barrett-Joyner-Halenda (nitrogen sorption)
BSE	Backscattered electrons
CS	Calcium sulphate
CH	Calcium hydroxide
CMOD	Crack mouth opening displacement
C-S-H	Calcium silicate hydrate
CTE	Coefficient of thermal expansion
CTOD	Crack tip opening displacement
FD	Fractal dimension
FPZ	Fracture process zone
GU	General use
HCP	Hydrated cement paste
HPC	High performance concrete
HRWRA	High range water reducing admixture
ITZ	Interfacial transition zone
LEFM	Linear elastic fracture mechanics
LVDT	Linear variable displacement transducer
mCT	Micro-computed tomography
MIP	Mercury intrusion porosimetry
MOR	Modulus of rupture
NSC	Normal strength concrete
PP	Polypropylene (fibre)
PT	Polyester (fibre)
SCC	Self-compacting concrete
SE	Secondary electron
SEM	Scanning electron microscopy
SSA	Specific surface area

TC	Thermal conductivity
TPC	Two-point correlation
TPS	Transient plane source
UPV	Ultrasonic pulse velocity
WRA	Water reducing admixture
XCM	X-ray computed micro tomography

CHAPTER 1. INTRODUCTION

1.1 Background

The behaviour of a structural element in resisting the imposed external actions is governed by the magnitude of loads, the structural configurations, and the response of the constituent materials to the applied loads. Design of these elements involves estimation of the loads, selection of appropriate materials, and proportioning them according to the established limit states criteria. Efficient structural performance requires the assessment of the material's behaviour, utilized to construct the elements, under the anticipated service conditions. When subjected to imposed loads and environmental actions, each material responds in a characteristic manner which depends on its atomic and molecular structure as well as its macroscopic properties such as internal flaws and interfaces between various constituent phases. However, a material's response cannot be determined from the behaviour at molecular level with acceptable degree of accuracy because of the presence of microstructural defects. The presence of these flaws reduces the number of available load paths that are involved in carrying the imposed loads. Stresses induced by these loads increase with the disappearance of available load paths caused by the propagation of internal defects in response to the applied loads. Furthermore, the physical dimension of the element itself may decrease due to the environmental actions, thereby compromising the integrity of the element. Thus, in order to ensure the most efficient transfer of loads from one element to another, structural integrity of the element is crucial throughout the expected service life of the structure. It can be achieved through an understanding of the characteristic behaviour of the material.

Cement-based materials are regarded as particulate composites that are quasi-homogeneous and quasi-brittle in nature. Generally, the properties of particulate composites are governed by those of the constituent components and, in case of cement-based systems, they are significantly influenced by the interface between the components—the hydrated cement paste and filler materials such as aggregates. The interaction between these components under the prevailing environmental condition is chiefly responsible for the quasi-brittle behaviour that is observed in response to the applied loads. It is essential to recognize that the structure of the interfacial zone is considerably different from that in the bulk of the matrix of hydrated cement paste. It is this structure that triggers the reduction in the amount of available load transfer paths in a structural member when subjected to mechanical and thermal actions. Depending on the orientation of the microstructural defects in the interfacial zone, stress concentration may occur upon the application of load causing the propagation of cracks, which reduces the load carrying capacity of the member. Furthermore, multi-phase systems such as cement-based materials are susceptible to dimensional changes as the ambient condition—a combination of humidity and temperature—changes during the service life of the structure. Their effects on the solid and fluid phases alter the mechanical properties of cement-based systems.

From an atomistic point of view, the distance between two atoms of a system is such that it possesses a minimum potential energy, in other words, the system is in equilibrium. The slope of the potential energy versus the interatomic distance curve is equal to the interatomic force. Any externally applied force causes a change in the interatomic distance resulting in a change in the potential energy of the system. This change in interatomic distance manifests as the deformation of the continuum body. Furthermore, the macro-mechanical properties such as modulus of elasticity is associated with the potential energy of the system where it is proportional to the second derivative of the potential energy with respect to the interatomic separation distance. If the system is subjected to elevated temperature, a portion of the potential energy of the system is converted into the kinetic energy of the atoms which results in an increase in the separation distance. The increase in the separation distance is proportional to the coefficient of thermal expansion of the system. Since the potential energy decreases in response to the exposure to elevated temperature, the modulus of elasticity of the material decreases owing to the fact that the slope of the force–separation curve decreases at high temperature. In addition, due to the availability of vibrational energy, the atoms begin to vibrate about their equilibrium position. If sufficient energy is supplied to the system, a phase transformation eventually follows.

Portland cement is the most commonly used binder to manufacture mortar and concrete. It holds the filler materials, the aggregates, together by forming a highly amorphous product upon mixing with water. While the presence of water is essential for the ordinary Portland cement to react and combine the ingredients, there are other types of binder—for instance, waterglass, aluminum phosphate, and magnesia—that do not require water to impart strength to the composite. As the cement particles hydrate, the volume of the hydrated cement paste increases to about two times the volume of the cement. The hydration products fill the space originally occupied by the cement particles and water. However, a portion of the space previously occupied by the water forms the capillary pore space in the composite, which plays an important role in the durability of the material. Furthermore, the chemically combined water in hydrated cement paste impacts the behaviour of the material at elevated temperatures, where the phase transformation of the water affects the thermal and mechanical properties.

Aggregates in cement-based composites, which occupy about 75% of the volume, act as fillers. A transition zone is formed between the aggregates and the surrounding cement paste matrix, having a distinctly different microstructure that is critical to the evaluation of the properties of the composite. By modifying the microstructure of this zone, the behaviour of the composite can be enhanced to a significant degree. Upon exposure to elevated temperature, both the matrix and the aggregates sustain thermal expansion. The differential expansion between these constituent phases is a source of thermal degradation in the composite.

As mentioned earlier, when cement-based materials are exposed to elevated temperatures, the microstructure undergoes a transformation and consequently affects the macro-mechanical properties. The damage sustained by the materials varies depending on the severity of the exposure and the microstructure of the material. The severity of the exposure may be described in terms of the length of the exposure or the rate at which the temperature in the structure increases. A relatively low rate of heating along with a long duration of exposure could cause severe degradation of the structure. On the other hand, short duration of exposure to fire especially those from burning of hydrocarbons—a very high rate of heating—is capable of causing considerable damage to the structure. The microstructural characteristics such as the composition of hydration products, moisture content, and the pore structure characteristics are some of the key aspects of cement-based materials that control its behaviour at sustained elevated temperatures.

Polymeric microfibres, having a low modulus of elasticity, are incorporated in cement-based composites primarily to improve its early age dimensional stability. At low dosages, these fibres help control the plastic shrinkage cracking in the composite. The presence of these fibres also alters the connectivity of the pore network in the composite, which influences the transport properties of the material. This modified nature of the pore structure is known to benefit the performance of cement-based composites at elevated temperatures, although a clear understanding of the underlying mechanism does not exist. It has been hypothesized that the fibre enables the creation of additional connected pore reservoir upon melting, which helps release the thermally induced pressure in the composite at elevated temperatures and thereby reduces the spalling of the composite. Further, on account of the hydrophobic nature of the fibre, the poor bond between the polymeric fibre with the cementitious matrix (undesirable from a mechanical standpoint) results in additional pore space between the fibre and the matrix that in turn is believed to be beneficial for the composite at elevate temperatures.

1.2 Motivation

Cement-based composites are being utilized—in addition to regular structural applications, where the likelihood of being exposed to elevated temperatures is high—for the construction of containment structures and as thermal insulators for metallic structural elements. The material must maintain its serviceability in the event of exposure to elevated temperature which would allow the safe evacuation of occupants or rehabilitation of the structure. Understanding the behaviour of cement-based composites at elevated temperature enables one to evaluate the performance of structural members, which would facilitate the optimization of mixture proportioning process of the composites.

Understanding how the microstructure evolves is fundamental to studying the characteristics of any material subjected to extreme environmental action. In cement-based materials, the physical and chemical transformations of the hydrated cement paste and aggregates take place with the increase in ambient temperature. Consequently, the pore structure of the material changes, which in turn influences the heat transfer process. Therefore, an extensive investigation of these changes and their consequences is instrumental in understanding the resulting macroscopic properties. Furthermore, polymeric microfibres appear to have beneficial effect on the overall performance at elevated temperature. However, the role of these fibres on the changes in microstructure is not apparent. Therefore, a study on the effect of these fibres on microstructure as well on the mechanical and thermal properties is deemed necessary.

Cement-based composites can be regarded as fractals allowing for observation of their microstructural details at various scales. They are however, self-similar only in the sense of statistical analysis, as opposed to the deterministic fractals. Furthermore, these composites show fractality only within a certain range of scales. In fractal analysis, the fractal dimension, which could be fractional, is used as a descriptor of the spatial complexity when observed at different scales. At elevated temperatures, the constituent phases of cement-based composites undergo thermal degradation, such as the loss of physically and chemically combined water from the hydrated cement paste. These dehydration processes are responsible for an increasingly complex pore structure with the rise in temperature. Consequently, the concept of fractal geometry can be employed to study the changes in pore structure at different elevated temperatures. The variation of the macro-mechanical properties of the material can also be correlated with the fractal dimension.

The thermal degradation of cement-based materials depends largely on the pore structure, moisture content, and more importantly on the thermal gradient. When the material is heated to elevated temperatures, the thermal gradient is dependent on thermal properties such as thermal conductivity and thermal diffusivity. Once these properties are evaluated, the heat flow phenomenon can be modelled to simulate the behaviour of the material at elevated temperatures. Sometimes, the experimental determination of material thermal properties is either cost prohibitive or impractical. Therefore, explanation of the experimental observations of thermal properties using prediction models would help understand the underlying physical phenomena.

Microcracks develop in cement-based materials when subjected to elevated temperature due to a thermal gradient and differential thermal expansion between the aggregates and the cement paste. As a consequence, the mechanical properties of the material degrade to varying degrees depending on the pore characteristics, moisture content, and the severity of the exposure. Moreover, the evaluation of mechanical properties helps determine the damage sustained by the material. An assessment of the damage may facilitate the optimization of the mixture design of cement-based composites that would be able to withstand different degrees of thermal degradation.

A number of factors may influence the behaviour of the cement-based materials at elevated temperatures. These include the density of the material, the type of aggregates, the type of binder, and the temperature profile. In order to limit the number of variables that describe the aggregate and so affect the outcome of this study, all investigations were conducted using a cement-based mortar prepared with a commercially manufactured silica sand.

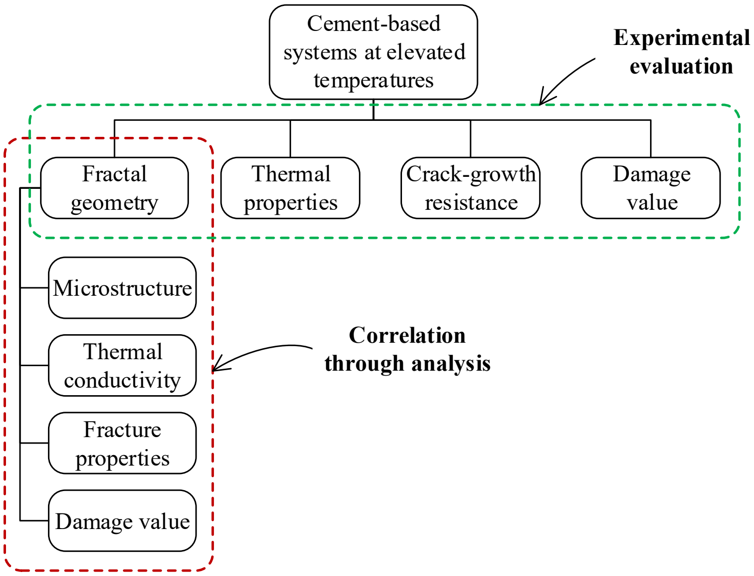

Figure 1.1 Flow chart outlining the contributions original to this thesis.

The contributions original to this thesis are expected to enrich the knowledge-base on the behaviour of cement-based systems at sustained elevated temperatures. These include: characterising the thermally decomposed microstructure with the aid of fractal geometry; predicting the thermal conductivity using a fractal dimension-based model; establishing the crack-growth resistance of cement-based systems at sustained elevated temperatures; quantifying the damage sustained in terms of pore connectivity and pore tortuosity; and correlating the porosity, thermal conductivity, fracture energy, fracture toughness and damage value with the fractal dimension. These contributions are outlined in the flowchart shown in Figure 1.1.

1.3 Objectives

The primary aim of this thesis is to characterize the microstructural parameters of cement mortar under sustained elevated temperatures and relate them to physical and macro-mechanical properties, using the state-of-the-art experimental techniques. Furthermore, the study is set out to investigate the thermal characterization of the Portland cement mortar at elevated temperatures both at the residual state and at the in situ (or 'hot') state. The outcome of this thesis is expected to assist in developing design guidelines that will mitigate damages sustained by cement-based composites when exposed to elevated temperatures.

The following aspects of the microstructure-property relationship were studied in this thesis through several experimental investigations:

- Characterization of mortar microstructure using the concept of fractal geometry, covariance method, and morphological opening method.
- Prediction of the changes in capillary porosity caused by elevated temperature using the stoichiometry and dehydration kinetics.
- Modelling of the thermal conductivity at different exposure temperature using a fractal geometry-based approach.
- Characterization of the fracture mechanical properties at elevated temperature.
- Prediction of the load-deflection response of the mortar subjected to four-point bending using fracture mechanical approach.
- Assessment of the damage sustained by the mortar using a suitable damage variable evaluated from the experimental results.

1.4 Scope

In order to limit the number of variables that affects the behaviour of cement-based systems at elevated temperatures, it was decided to conduct the present study using cement-based mortar.

A polyester fibre having an aspect ratio of 240 was incorporated to investigate the mechanism governing the role of such fibre in creating an interconnected pore network. Since 600 °C is regarded as the limiting temperature for the structural integrity of cement-based systems (Neville 2011), a temperature of 600 °C was chosen as the upper limit of the exposure temperature with a heating rate of 5 °C/minute.

In order to improve the performance of structural elements under sustained elevated temperatures, knowledge of the behaviour of the material—microstructural and macro-mechanical—is essential. It is also necessary to establish the relationship between these multi-level properties. Despite the availability of a number of studies addressing such relationships, several aspects of the behaviour of cement-based systems still require further investigations. Therefore, the outcome of this research is expected to help develop materials that would be capable of mitigating the deteriorations sustained when exposed to elevated temperatures. Such materials can be engineered through the modification of pore structure network. Furthermore, the knowledge generated in this thesis will aid in the development of rehabilitation schemes to restore the functionality of thermally damaged concrete structures.

1.5 Organization

The outcome of this research program is presented by categorizing the aforementioned objectives into key topics of characterization. These are (i) the microstructure, (ii) the thermal properties, (iii) the mechanical properties, and (iv) the damage assessment. Each topic is addressed in an individual chapter with adequate details relevant to the subject matter. Although the topics are presented individually, the author intends to illustrate a well-connected relationship between them to underpin objectives of this work.

The present chapter (Chapter 1) describes briefly the background on the behaviour of structural materials under loading and environment. As well, the motivation and objectives for this study are presented along with the organization of the thesis. A comprehensive discussion of the relevant literature is presented in Chapter 2. Along with a description of the relevant material properties, it presents a critical review of the experimental methods commonly employed to investigate the microstructure, heat flow mechanisms, and thermal spalling of cement-based materials. The procedure and findings from the microstructural investigation conducted here are discussed in the Chapter 3. Together with an evaluation of the air void network, the chapter presents a discussion—regarding the changes in capillary porosity caused by thermal degradations—of prediction models based on the stoichiometry and the dehydration kinetics of processes involved. Further discussion on the evolution of mortar microstructure, as determined through image processing method, is provided. This chapter presents the findings from a fractal geometry-based analysis. Chapter 4 illustrates the residual and in situ thermal constants at elevated temperature. The results are explained with the help of suitable models that incorporate the outcome of microstructural investigations from Chapter 3. In addition, a fractal model is employed to explain the variation in thermal conductivity of the mortar at elevated temperatures. The procedure and results for residual mechanical properties are presented in Chapter 5. These properties are examined against the findings on the microstructure from Chapter 3. Note that emphasis is laid on the fracture mechanical characterization of the material. This chapter concludes with a fracture energy-based model that is employed to predict the load-deflection behaviour of mortar under four-point bending load. Chapter 6 presents the damage sustained by the mortar at elevated temperatures. Experimental methods include the ultrasonic pulse velocity and computed microtomography. The results of this investigation is summarized in Chapter 7. Furthermore, a list of possible areas where these results may be applied, is provided. Lastly, multiple recommendations are made to inform ongoing and future studies on the behaviour of cement-based systems at elevated temperatures.

CHAPTER 2. LITERATURE REVIEW

2.1 Introduction

This chapter presents a brief review of various aspects of cement-based materials at elevated temperatures available from the published literatures. At the outset, the changes in the microstructure of cement-based systems when exposed to different temperatures is discussed. Knowledge of the heat and mass transfer phenomena in a multiphase material such as concrete is essential when studying the behaviour of concrete at high temperatures. Therefore, a brief discussion of heat conduction through cement-based composites is presented along with that of the parameters required to model the hygro-thermal behaviour of cement-based systems. Afterwards, a review of the thermal and mechanical properties of thermally decomposed cement-based composites is presented. Finally, the underlying damage mechanisms and the relevant experimental techniques are reviewed.

2.2 Microstructure

In a multi-phase system such as cement based composite, characterization of the microstructure assists in understanding and predicting the macro-mechanical properties. Due to its complex and dynamic nature, it is a difficult task to study the relationship between the phases—hydrated cement paste, interfacial transition zone, and aggregate—of cement-based materials. These phases are affected by the change in humidity, temperature and, interaction of external agents. At elevated temperatures, the cement paste and aggregates in concrete undergo physical alterations. It transforms the microstructure and in turn, characterizes the macro-mechanical behaviour of the material. A brief review of these microstructural aspects is presented below.

2.2.1 Cement Paste Hydration Products

Generally, hydrated cement paste is composed up to 50–65 percent of calcium silicate hydrate (C-S-H), 20–25 percent of calcium hydroxide (CH) crystal, and 15–20 percent of calcium sulphoaluminate hydrates (Mehta and Monteiro 2013). These components gradually decompose when exposed to elevated temperatures. Upon exposure, calcium tri-sulphate aluminate hydrate (AFt phases), also known as ettringite, decomposes first. AFt loses its water from the crystalline structure which is eventually released outside in the form of water vapour. It undergoes complete decomposition at a temperature between 80–150 °C (Hager 2013). At about 70 °C it loses about 20–24 molecules of water, out of 32 molecules, while the rest of the water releases at higher temperature (Shimada and Young 2001). The decomposition products include calcium aluminate sulphate ($C_4A_3\bar{S}$), calcium sulphate ($C\bar{S}$), and calcium oxide (C), (Zhou and Glasser 2001). C-S-H, on the other hand, starts to dehydrate at the beginning of the heating process. Interlayer water and some of the chemically combined water in C-S-H is lost when the temperature reaches about 300 °C. As the C-S-H continues to decompose, a volumetric reduction takes place causing an increase in the porosity of the cement paste. At about 900 °C, a complete decomposition of C-S-H results with the formation of β-C_2S, β-CS, and water vapour (Bažant and Kaplan 1996; Hager 2013; Mehta and Monteiro 2013).

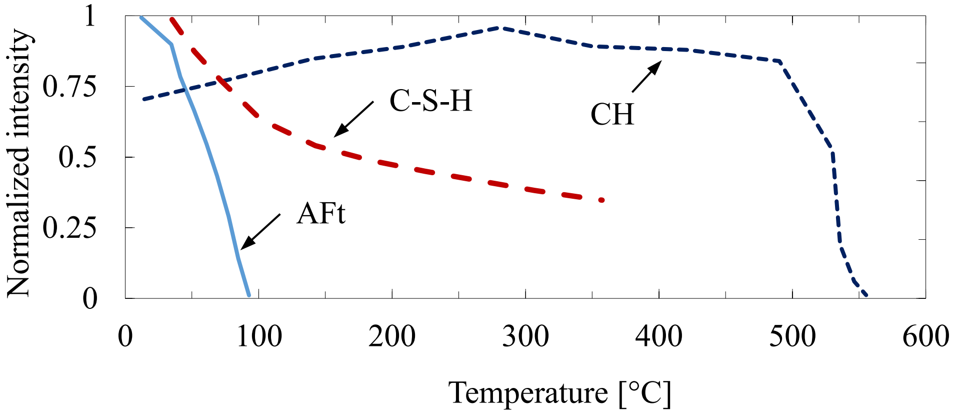

Figure 2.1 Evolution of intensities of cement paste hydration products with the increase in temperature (Castellote et al. 2004)

The calcium hydroxide (CH) crystals, otherwise known as Portlandite, decomposes into CaO and water vapour at 450–550 °C. Castellote et al. (2004) investigated the evolution of different phases in a cement paste at elevated temperatures. The normalized intensities of each phase, as shown in Figure 2.1, decrease with a rise in the temperature except for the CH phase. An increase in CH phase is generally observed up to about 300 °C. It was hypothesized (Saad et al. 1996) that recrystallization of the amorphous calcium hydroxide is responsible for this slight increase in CH phase. Exposure to high temperature also triggers the hydration of the unhydrated fraction of cement grains present in the matrix by providing the required activation energy (Lin et al. 1996). Saad et al. (1996) explains it by referring to a process known as internal autoclaving caused by steam generated pressure build-up at a temperature ranging between 100–300 °C.

2.2.2 Pore Characteristics

When hardened cement paste is exposed to elevated temperatures, the free water in the capillary pore evaporates first, followed by the loss of the water held by capillary tension. Further desiccation occurs with the loss of interlayer water and the chemically combined water. The latter is part of the crystalline structure of hydrated products and denotes the decomposition of the hydration products with an increase in temperature. As a consequence, a change to the pore volume and the pore size distribution occur. The extent of this transformation could be significant depending on the exposure temperature. It is, however, noted that the initial loss of free evaporable water does not affect the porosity (Harmathy 1970).

As the temperature increases, the progressive decomposition of crystalline structure causes an increase in porosity that approximately follows a parabolic pattern (Bažant and Kaplan 1996; Vydra et al. 2001). The temperature at which the porosity reaches its peak value was found to vary, depending on the proportion of mixture constituents, from 600 °C to 900 °C. According to Vydra et al. (2001), the rising trend of porosity can be attributed to the micro-cracks formed (Hossain 2006; Naus 2010; Pliya et al. 2011; Vodák et al. 2004) due to the thermal gradient, in addition to an increase in the pore space formed due to the loss of physically and chemically held water, in crystalline hydration products. The falling trend, on the other hand, is the outcome of several phenomena—chemical reaction, phase transformation, and sintering process— that are associated with the decomposition of C-S-H and CH crystals. Schneider and Herbst (1989) showed that the temperature dependence of the porosity of concrete may be approximated by a linear relationship. It is noted that such linear functions may be valid only up to the peak of the parabolic variation discussed above.

The loading condition on specimens during heat exposure is reported to influence the porosity of the composite (Bažant and Kaplan 1996). Concrete tested for changes in porosity with temperature while subjected to load showed a lower porosity than when heated without any load. Ye et al. (2007) investigated the microstructure variation along the depth of concrete from the heated surface. They observed an increase in total porosity by a factor of two at a distance of 10 mm from the heated surface. A study on the effect of fibre reinforced concrete suggested that an increase in porosity at a temperature associated with the melting point of fibre can be attributed to the additional pore channel created after melting of the fibres (Sideris and Manita 2013).

Pore size distribution of porous solids can be determined by mercury intrusion porosimetry (MIP), Wood's metal intrusion, Nitrogen adsorption method, and Image analysis techniques. Despite its limitation—underestimating the pore sizes visible to microscope—MIP method is extensively used to characterize the pore structure of cement-based materials (Chan et al. 2000b; Chatterji 2001; Diamond 1989; Poon et al. 2003; Ye et al. 2007). Diamond (2000) suggested that this method should be discarded as far as pore size estimation is concerned. However, the pore size distribution from MIP may be used for relative comparison as opposed to a measurement of actual pore structure parameters.

Several studies reported a coarsening effect of elevated temperature on the pore size distribution due to the desiccation and thermal decomposition of solid phases (Chan et al. 2000b; Harmathy 1970; Hossain 2006; Khoury 1992; Peng and Huang 2008; Poon et al. 2003). An increase in pore size indicates that the bulk density decreases with an increase in the temperature. Hossain (2006) reported a fourfold increase in mean pore size, as measured by MIP, when the concrete is exposed to a temperature of 800 °C. Ye et al. (2007) studied the behaviour of self-compacting concrete at elevated temperature and found that the threshold dimeter and critical diameter, calculated from MIP size distribution, increase in the direction towards the heated surface of the specimen. Investigation of normal and high strength concrete under elevated temperature showed an increase in both the threshold diameter and critical diameter (Figure 2.2), associated with the peak value of the differential volume of mercury intrusion (Chan et al. 2000b).

Connectivity of pore network is a critical aspect of fluid flow through porous media. As the size of the gel pores or capillary pores increases with an increase in exposure temperature, the pore system changes from an isolated, closed system to an interconnected an open one (Bažant and Kaplan 1996). Study (Tsimbrovska et al. 1997) on the permeability of cement-based mortar showed a 200% increase in permeability with the increase in temperature from 200 °C to 300 °C, while porosity remained approximately unchanged, indicating an increased level of pore connectivity.

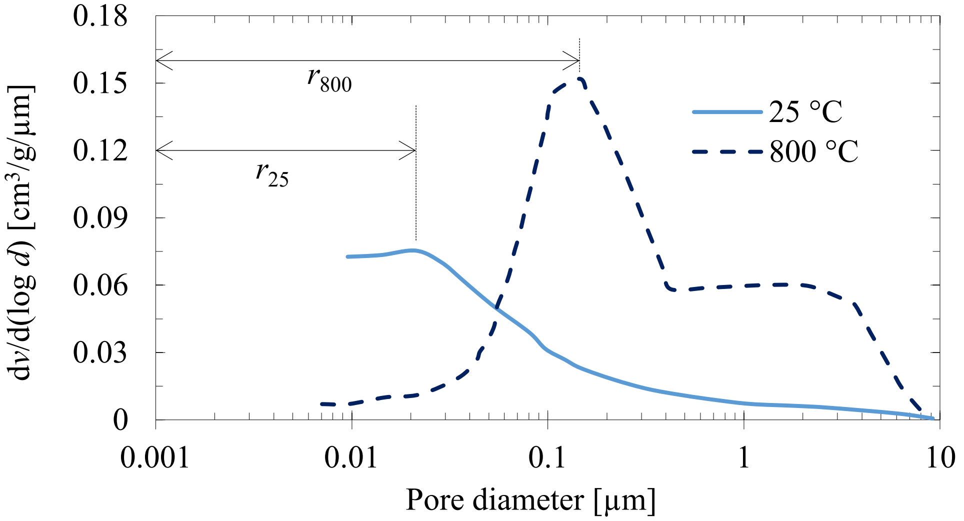

Figure 2.2 Critical pore diameter of normal strength concrete at high temperature observed using MIP (Chan et al. 2000b)

2.2.3 Interfacial Transition Zone

The region of concrete in the vicinity of solid inclusions such as aggregates, fibre, and reinforcing bar, known as interfacial transition zone (ITZ), is regarded as its weakest zone. Localized bleeding and inefficient packing of cement particles leads to higher water-to-cement (w/c) ratio around these inclusions making ITZ relatively more porous and percolated than the bulk of the cement paste in concrete. Due to its inability to efficiently transfer stress from the bulk cement paste to the aggregates, ITZ strongly influences the strength and durability characteristics of concrete. Higher w/c ratio causes increased amount of large CH and AFt crystals (Mehta and Monteiro 2013; Mindess et al. 2003). At elevated temperatures, the evaporation of free water and decomposition of hydrated cement paste (HCP)—especially AFt and CH phases—enhances the porosity and pore connectivity of ITZ. The thickness of ITZ is typically 30–40 μm around aggregates. Exposure to elevated temperature increases this thickness depending on the temperature and mixture proportions (Fares et al. 2009). Xu et al. (2001) studied the influence of elevated temperature on ITZ by conducting a micro-hardness test. They reported a 40% increase in ITZ range in ordinary Portland cement concrete at 250 °C. Hossain (2006) also observed similar increase in ITZ range, suggesting the formation of micro-crack along the paste-aggregate interface. Cracks in concrete—either thermally induced or in response to external load—propagate preferentially through the weakest zone, usually across ITZ. However, cracks may propagate through weak and porous aggregates present in the concrete. A study (Andiç-Çakır and Hızal 2012) on lightweight aggregate concrete reported that thermal expansion causes the cracks follow a path through pumice aggregate. In high performance concrete (HPC), ITZ plays an important role at elevated temperature. Percolated ITZ helps release vapour pressure, one of the mechanisms considered responsible for explosive spalling, which builds up with rising temperature by providing an escape route through connected pore network. In HPC, according to Bentz (2000), ITZ is relatively thinner and not percolated, which makes it prone to explosive spalling at high temperature. However, presence of synthetic micro-fibre was found to be (Bentz 2000; Kalifa et al. 2001) beneficial in preventing the spalling by creating a percolated pore structure upon thermal exposure.

2.2.4 Fractal Nature

The pore structure of cement-based systems reveals an increasing level of detail with the decrease in scale of observation, which can be characterized as statistically self-similar. Due to this self-similarity in structure, porous medium such as concrete can be described using fractal geometry. Unlike mathematical or deterministic fractals, natural objects—if they possess fractality—show self-similarity across a finite range of scale of measurement. Recently, researchers (Brandt 2009; Castaño et al. 1990; Chiaia et al. 1998; Diamond 1999; Hu 2004; Kaye 1989; Lange et al. 1994; Russ 1992; Wang 1995; Winslow 1985) have given considerable attention to the investigation of the fractal nature of concrete microstructure.

Fractal geometry deviates from its Euclidean counterpart by having non-integer (generally) dimensions. The larger the fractional part of this dimension, the higher the roughness of the boundaries of the feature being described using the fractal dimension (Diamond 1999; Winslow 1985). According to Diamond (1999), pore structure of cement-based system may exhibit two distinct fractal dimensions, termed as mixed fractal, depending on the length scale of the measurements.

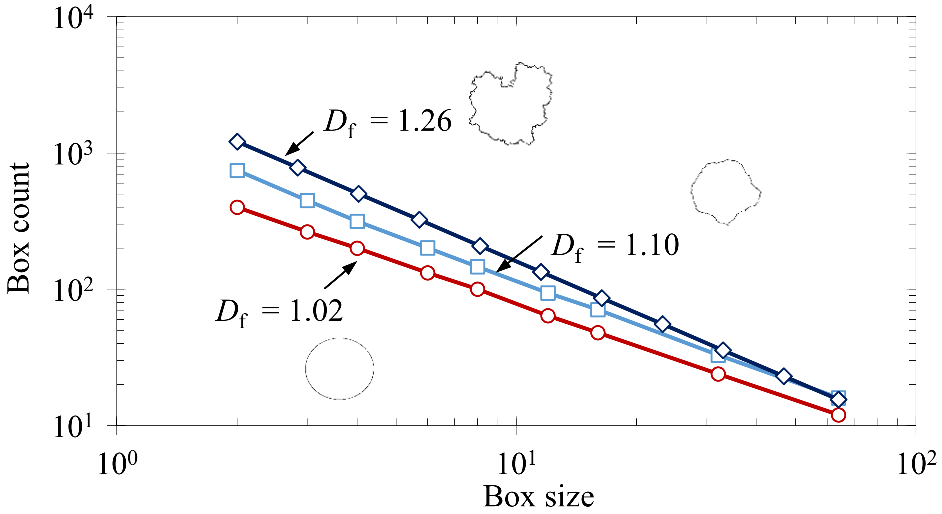

Figure 2.3 Fractal dimension of some arbitrary shapes using box-counting method.

Several techniques are available to determine fractal dimension of porous media. Winslow (1985) investigated the fractal nature of cement paste using small angle x-ray scattering, Castaño et al. (1990) utilized optical microscopy to determine the fractal dimension of cement paste with varied amount of polymer replacement, several studies (Diamond 1999; Lange et al. 1994; Wang 1995) employed backscatter scanning electron microscopy images to determine fractal dimension by using an image processing technique called dilation, Chiaia et al. (1998) estimated fractal dimension of crack pattern using box-counting method, Ji et al. (1997) discussed a method based on pore size distribution obtained from mercury intrusion porosimetry.

As shown in Figure 2.3, roughness of the shape boundary increases with the increase in fractal dimension. In other words, higher fractal dimension is associated with the larger perimeter of the shape boundary. Depending on the measurement technique and feature of interest, fractal dimension of cement-based materials vary widely. Winslow (1985) reported that fractal dimension vary from 2.95–3.09 for cement paste as the water-to-cement ratio decreased from 0.6 to 0.3, suggesting a space-filling nature of paste microstructure. Wang (1995) showed, using backscatter technique, that cement paste behaves like mixed fractals having two different regimes of fractality with fractal dimensions ranging from 1.1–1.3, where the larger dimension is associated with the low resolution of observation. Lange et al. (1994) investigated cement paste with varying w/c ratios using dilation method and concluded that fractal dimension cannot be used to differentiate pore structure even if the specimens have different porosity. This is in direct contrast with the results obtained by Castaño et al. (1990) who reported that the fractal dimensions decreased with an increase in the polymer content in cement paste. Their observation agrees with the theoretical relationship between the fractal dimension and porosity, which is applicable to porous media as suggested by Yu and Li (2001).

2.3 Heat and Mass Transfer

Concrete elements sustain microstructural damage due to microstructural changes when exposed to elevated temperature. Study of hygro-thermal behaviour of concrete enables the prediction of such material degradation. Knowledge of structural mechanics, continuum mechanics, and heat transfer is essential to develop mathematical models that describe thermal as well as mechanical characteristics at high temperature. Heat transfer mechanism may be categorized as (a) conduction and convection inside the porous structure and (b) convection and radiation at exterior surfaces (Çengel and Ghajar 2015; Khoury et al. 2002).

When developing simplified mathematical model, cement-based materials may be treated as a porous medium. In this medium, cement hydration products form the solid skeleton and the gel pores or capillary pores constitute the void space which may be regarded as partially filled with water or vapour. Heat energy from the external sources is transferred by these components in addition to that consumed during the transformation of cement hydration products, aggregates, and water. The temperature gradient as well as the gradient of moisture concentration is the driving force behind heat transfer. It is important to note that these two driving forces are also responsible for the transport the moisture in heated concrete. According to Bažant et al. (1996) it is essential to consider the coupling of these two phenomena while formulating the governing differential equations to predict the failure mechanism of concrete at elevated temperature. Once the appropriate mathematical models governing the coupled heat and mass transfer are set, numerical solution can be performed to predict the moisture content and pore pressure.

The mass of individual component changes with time and the rise in temperature, which must be included when formulating equation of conservation of mass (Khoury et al. 2002). Mass changes may occur either due to physical transformation of solids through dehydration or continued hydration or rehydration of solid phases in concrete. Furthermore, phase transformation affects the conservation of heat energy through endothermic or exothermic reactions. Latent heat due to vaporization or condensation of water vapour also needs to be considered as part of the heat conservation equation.

Dehydration of C-S-H phase takes place by first losing adsorbed water and later the chemically bonded interlayer water, which causes a change in both mass and thermal energy in the system. In addition, as the exposure temperature increases, the unhydrated cement particles reacts with water and increase the C-S-H content in the cement paste. Similarly, the thermal decomposition of AFt phase affects the heat and mass conservation in concrete at high temperature. The CH phase undergoes similar transformation with the increase in temperature. It disintegrates into CaO and water by transforming through an endothermic process. Furthermore, supplementary cementitious admixtures reacts, an exothermic chemical process, with CH and produce C-S-H provided that hygro-thermal condition is favourable. The CH phase also reacts with atmospheric CO_2 to produce $CaCO_3$ causing a change in mass and gain in heat energy. On the other hand, the decarbonation process converts CaCO3, present both in bulk cement paste and in aggregates, to CaO and CO2 resulting in a loss of heat energy during the process. Other type of aggregates, such as quartz, go through an endothermic α–β conversion and causes a loss in heat energy in addition to a volumetric expansion (Lamond and Pielert 2006).

According to Li et al. (2002), the heat transfer process in concrete can be modelled using the principle of energy conservation, as shown in the following equation:

$$\nabla \cdot \left(k \nabla T \right) - \sum \left(\varepsilon_i \rho_i V_i \right) \nabla T - \lambda \dot{E} = \sum \left(\varepsilon_i \rho_i C_i \right) \frac{\partial T}{\partial t} \tag{2.1}$$

where k is the thermal conductivity, T is the temperature, ε_i is the phase volume fraction (solid, liquid or gas), ρ_i is the corresponding density, V_i is the velocity, C_i is the specific heat, λ is the latent heat of vaporization, and $\dot{E}$ is the rate of evaporation of liquid water. Each term, from the left, in Equation 2.1 represents the following: rate of change of heat flux as described by Fourier's law heat conduction, the heat flow due to bulk fluid motion, the heat loss caused by evaporation, and the heat energy change in each phases in the control volume.

2.4 Thermal Characteristics

Thermal characterization is a crucial part of mathematical modelling of the behaviour of concrete at elevated temperature. Thermal conductivity and heat capacity, or specific heat, are the two essential parameters when developing models to predict temperature distribution in heated concrete. Prediction of pore pressure at elevated temperatures is critical in understanding the damage mechanisms (Bažant and Kaplan 1996). Knowledge of temperature profile can be used to quantify the pore pressure that builds up with the rise in exposure temperature. Thermal properties of cement paste and aggregate also influence the thermal incompatibilities caused by volumetric change (Lamond and Pielert 2006).

2.4.1 Measurement Methods

Heat transfer through concrete is a complex phenomenon especially when it occurs at elevated temperatures. The non-homogeneous and constantly evolving nature of the microstructure make it challenging to determine the thermal properties experimentally. Factors that influence the thermal properties include the ingredients, the heating rate and history, moisture content, density, continued hydration of cement particles, dehydration of hydrated products, and the experimental techniques (Bažant and Kaplan 1996; Harmathy and Allen 1973; Lamond and

Pielert 2006; Shin et al. 2002; Thompson 1968). As pointed out by several investigators (Harmathy 1964; Shin et al. 2002; Thompson 1968), physical and chemical changes render the steady-state test methods unsuitable for the determination of thermal properties of cement-based materials at elevated temperatures. A meaningful test data from steady-state method, such as Guarded Hot-Plate Apparatus (ASTM International 2011) and Hot Box Apparatus (ASTM International 2013a), can only be obtained after achieving the moisture equilibrium (Thompson 1968). The experimental techniques that use transient methods have been found to provide reliable thermal properties for concrete at elevated temperatures (Kodur and Khaliq 2011; Lamond and Pielert 2006; Neville 2011; Shin et al. 2002). Even some transient methods, such as hot wire method, provide erroneous results because of the non-homogeneous nature of the contact surface in the vicinity of the heat source (Lamond and Pielert 2006; Shin et al. 2002). Several transient methods—Harmathy's curve fitting method (Harmathy 1964; Harmathy and Allen 1973), transients plane source method (Log and Gustafsson 1995), and transient line source method (ASTM International 2014)— were found to be reliable for the measurement of the thermal properties.

2.4.1.1 Transient Plane Source Method

The hot-disk method, a transient plane source method, is being widely used (Bentz et al. 2011; Kodur 2014; Zhang et al. 2016) to characterize the thermal conductivity, thermal diffusivity, and specific heat of concrete at elevated temperature. A double spiral nickel sensor is used as the heat source, which also serves as the temperature probe. A constant amount of current is supplied to the heat source and the resulting increase in temperature is recorded as a function of time by observing the change in electrical resistance of the sensor. The change in temperature in the sensor is dependent on the thermal characteristics of the material. Therefore, the thermal properties can be determined by analyzing the temperature change over the heating duration (He and Ng 2002). A brief mathematical background of transient plane source is presented below.

In an isotropic solid, the governing differential equation for transient heat conduction is given by the following (Carslaw and Jaeger 1959; Çengel and Ghajar 2015):

$$\frac{\partial^2 T}{\partial x^2}+\frac{\partial^2 T}{\partial y^2}+\frac{\partial^2 T}{\partial z^2}=\frac{1}{\kappa}\frac{\partial T}{\partial t} \tag{2.2}$$

where $T(x,y,z,t)$ is the temperature at time t, κ is the thermal diffusivity expressed as $k/\rho C$, k is the thermal conductivity, ρ is the density, and C is the specific heat.

The solution of Equation 2.2 can be obtained by integrating the point source solution—for the ring source in hot-disk method, using the cylindrical coordinate system— as follows (Carslaw and Jaeger 1959; He and Ng 2002):

$$T(r,\theta,z,t)-T_0=\frac{2\pi\, a\, Q_0\cdot e^{-(r^2+a^2+z^2)/4\kappa t}}{8(\pi\kappa t)^{3/2}}\cdot I_0\left(\frac{ra}{2\kappa t}\right) \tag{2.3}$$

where a is the radius of the sensor, Q_0 is the strength of the heat source, T_0 is the initial temperature, I_0 is the modified Bessel function.

Since the temperature T does not vary with θ and thickness of the sensor can be ignored, it may be expressed as a function of r and t only, i.e., $T(r,t)$. The average temperature increase can be obtained by averaging the temperature change from Equation 2.3 as shown below:

$$\Delta\overline{T}(\tau)=\frac{P_0}{\pi^{3/2}ak}D(\tau) \tag{2.4}$$

where τ is expressed by $\sqrt{\kappa t}/a$, a dimensionless characteristic time ratio, P_0 is the input power to the sensor, $D(\tau)$ is the dimensionless time function.

In hot-disk test method, this temperature increase is measured by monitoring the resistance of the heating element. By evaluating the term $P_0/(\pi^{3/2}ak)$ in Equation 2.4, one can determine the thermal conductivity of the material. Since $D(\tau)$ is not known due to the fact that the thermal diffusivity is not determined yet, a special computational technique needs to be employed. Using a range of trial values of κ, a series of $\Delta\overline{T}$ versus $D(\tau)$ is plotted and the correct value of the κ is taken from the trial value that fits the measured data in a straight line.

2.4.1.2 Transient Line Source Method

Thermal needle method, a standardized transient line source method, is commonly used to measure the thermal properties of homogeneous materials over a temperature range of 0–100 °C (ASTM International 2014). The thermal needle consists of a heating element and temperature monitoring probe. The dimension of the needle is such that it is capable of simulating the infinitely long and thin heat source. The needle is inserted into the specimen and a known amount or current is supplied to the heating element for a period of time. The time and temperature history is recorded during the heating and cooling cycle. Thermal conductivity can then be determined from the time-temperature record. Use of the data set from both the heating and cooling cycle helps compensate for any temperature drift. A calibration factor may be used to approximate the theoretical behaviour of infinitely long heat source as that of the heat source having a finite dimension. By fitting the time temperature data from the heating and cooling cycle, the thermal conductivity can be determined using the following equation (Penner 1970):

$$k = \frac{nQ}{4\pi S} \tag{2.5}$$

where k is the thermal conductivity, n is the calibration factor, Q is the heat input, S is the average of the slopes of temperature vs. time plots fitted in straight line using natural logarithmic scale.

2.4.2 Thermal Strain

Concrete undergoes thermal deformation causing volumetric strain in the structure. Thermal stresses in concrete normally do not cause any shear deformation due to the fact that thermal strain is same in all direction (Bažant and Kaplan 1996). Several mechanisms—pure thermal dilatation, thermal shrinkage or swelling, and relative humidity change—are being used to describe the thermal strain that develops in concrete at elevated temperature (Sellevold and Bjøntegaard 2006). In addition to temperature gradient, thermal incompatibility between cement paste and aggregate in concrete is responsible for differential thermal strain, which may cause severe thermal stress leading to spalling. Note that the measured thermal strain is affected by time dependent volumetric changes caused by moisture diffusion and chemical reaction (Neville 2011).

When cement paste is exposed to elevated temperatures, thermal expansion occurs up to an exposure temperature of 150 °C to 300 °C depending on the mixture composition especially the water-to-cement ratio (Cruz and Gillen 1980; Harada et al. 1972). However, thermal contraction occurs with further increase in temperature. The initial thermal expansion—net effect of shrinkage and expansion, up to about 300 °C—may be attributed to the increased molecular movement and swelling pressure (Bažant and Kaplan 1996). On the other hand, the contraction results in due to the net effect of shrinkage—caused by the loss of evaporable water and chemically combined water—and expansion of the hydrated cement paste (Lankard 1970).

Aggregate phase occupies a considerable fraction of the total volume of concrete. It has dissimilar thermal expansion when compared to the hardened cement paste. This thermal incompatibility is responsible for differential thermal stress causing microstructural damage. Therefore, it is important to investigate the coefficient of thermal expansion of aggregate to be used in concrete. Browne (1968) investigated several types of commonly used aggregates for their coefficient of thermal expansion. It was found that mineralogical composition is the most important factor affecting their thermal characteristics (Hager 2013). For example, aggregates with high silica content, such as sandstone and quartz, have higher coefficient of thermal expansion than the ones with low silica content, such as limestone.

As mentioned above the thermal expansion of concrete is dependent on that of the cement paste and the aggregates. It was found (Mitchell 1953) that coefficient of thermal expansion of concrete can be estimated from the weighted average values of its constituents. Investigation (Schneider et al. 1982) of concrete with various types of conventional aggregates showed that the linear expansion of concrete increases with the increase in temperature. A study of fire exposed concrete reported (Hertz and Sørensen 2005) that restrained thermal expansion causes thermal stress which may lead to explosive spalling. Research on the effect of fibre addition on the thermal expansion of self-compacted concrete and high-strength concrete showed a marginal decrease in thermal expansion due to the presence of polypropylene fibre (Kodur and Khaliq 2011).

2.4.3 Thermal Conductivity

Thermal conductivity of a solid is its ability to conduct heat when subjected to a temperature gradient. It is a measure of the rate of heat flow through the materials. The following expression, also known as Fourier's law of heat conduction, mathematically defines thermal conductivity of a material:

$$q = -k \nabla T \tag{2.6}$$

where q is the heat flux, k is the thermal conductivity, T is the temperature at any point. Thermal conductivity of cement-based materials depends on its constituents especially the moisture content and the type of aggregate used to prepare it.

Harmathy (1970) investigated the thermal properties of oven-dried cement paste with varying water-to-cement (w/c) ratio ranging from 0.25 to 0.5 at elevate temperature up to 1000 °C. The paste with higher water w/c showed lower thermal conductivity. It was also reported that the thermal conductivity largely remained unchanged till 400 °C followed by a gradual reduction with the increase in temperature. This reduction was attributed to the microcracking, loss of moisture, and increased porosity (Bažant and Kaplan 1996).

Aggregates in cement-based materials have relatively higher thermal conductivity depending on their crystalline structures and porosity. Orientation of the crystalline structure to the direction of the heat flux also known to have influence on the measured value of thermal conductivity (Neville 2011). Quartz aggregates have high thermal conductivity due to their high crystalline structure (Bažant and Kaplan 1996; Clauser and Huenges 1995). When normal weight aggregates are exposed to increasing temperature, the thermal conductivity gradually decreases. It was reported that this reduction is correlated to the thermal expansion of the aggregates (Zoldners 1971). On the other hand, due to their porous nature, lightweight aggregates show relatively lower thermal conductivity which does not change significantly with the increase in the exposure temperature (Harmathy 1970).

Thermal conductivity of mortar and concrete depends on the type of aggregate, moisture content, and test methods (Blundell et al. 1976). At elevated temperature, oven-dry concrete shows a decrease in thermal conductivity as the temperature increases (Bažant and Kaplan 1996; Harmathy 1970; Kodur and Khaliq 2011; Naus 2010; Schneider 1988; Shin et al. 2002). On the other hand, the moist concrete shows an increase initially up to a temperature ranging 50–90 °C, depending on the type of aggregate used, followed by a reduction in thermal conductivity with increasing temperature. This increase-decrease trend is attributed to the thermal conductivity of water which initially increases up to a temperature of 130 °C and later compensated due to the loss of moisture from the heated concrete (Bažant and Kaplan 1996).

Kodur and Khaliq (2011) investigated the thermal conductivity of high strength concrete (HSC) and self-compacting concrete (SCC) at elevated temperature. They reported a value of 2.5 W/mK for HSC and 3.25 W/mK for SCC at room temperature which decreased to a value of 1 W/mK at 800 °C. Harmathy (1970) measured thermal conductivity of two light weight concrete, where they found the values predominantly remained unchanged for a temperature range of 25–900 °C. A study on the effect of fibre reinforcement by Kodur (2014) reported that polypropylene microfibre did not have any influence of the thermal conductivity of concrete heated from 20 °C to 800 °C. However, it was reported (Lie and Kodur 1996) that presence of steel fibre showed a slightly higher thermal conductivity value than the plain counterpart.

2.4.3.1 Thermal Conductivity Models

Prediction of thermal conductivity (TC) of various composite media has captured the interest of researchers since late 19th century. There are many factors that influence the choice of modelling technique employed to estimate the effective thermal conductivity of the material being studied. These includes heterogeneity of the material, shape and size of the particles, interaction between the filler particles, interfacial thermal resistance at the boundary between phases, and the heat conduction mode (Pietrak and Wisniewski 2015; Progelhof et al. 1976).

Modelling the thermal conductivity of porous materials is substantially different than that of the materials involving solid–solid heat transfer mechanism. Depending on the characteristic dimension of the pores, thermal radiation mode of heat transfer through these materials may not be negligible, especially at elevated temperatures. Furthermore, one may need to consider the shape and distribution of the phases involved to arrive at a model capable of predicting the thermal characteristics accurately.

Numerous thermal properties models have been developed over the years. Many of these models are based on theories, what is known as the effective medium theories, that use the volume fraction and properties of the individual phases to estimate the properties of the composites. A very common approach in these models is to idealize the composite structure using electrical circuit analogy due to the underlying mathematical similarity. Maxwell developed the first analytical expression of thermal conductivity for composite material through his publication on electricity and magnetism. However, this model does not include the interaction between the solid inclusions or the interfacial thermal resistance (Pietrak and Wisniewski 2015). The expression for Maxwell's model is given below:

$$\frac{k_e}{k_c} = 1 + \frac{3\varphi}{\left(\frac{k_d + 2k_c}{k_d - k_c}\right) - \varphi} \tag{2.7}$$

where k_e is the effective thermal conductivity, k_c is the thermal conductivity of the continuous phase, k_d is the thermal conductivity of dispersed phase, ϕ is the volume fraction of dispersed phase. There have been many modified versions of the Maxwell's original model to include multiple different phase, interaction between phases, shape of the phase, interfacial thermal resistance, and to extend the applicability to composites having higher fraction of inclusions (Agari and Uno 1985; Hamilton and Crosser 1962; Hasselman and Johnson 1987).

Hesselman-Johnson (1987) derived a model which incorporates the size of inclusions and boundary conductivity, to model the interfacial thermal resistance, as follows:

$$k_e = k_c \frac{2\left(\frac{k_d}{k_m} - \frac{k_d}{ah_c} - 1\right)\varphi + \frac{k_d}{k_m} + 2\frac{k_d}{ah_c} + 2}{\left(1 - \frac{k_d}{k_m} + \frac{k_d}{ah_c}\right)\varphi + \frac{k_d}{k_m} + 2\frac{k_d}{ah_c} + 2} \tag{2.8}$$

where a is the radius of the inclusion and h_c is the convection heat transfer coefficient.

Hamilton and Crosser (1962) developed a model from the work of Maxwell and Fricke (Progelhof et al. 1976) to include the phase distribution as an empirical factor. The model is shown in the following equation:

$$\frac{k_e}{k_c} = \frac{k_d + (n-1)k_c - (n-1)\varphi\left(k_c - k_d\right)}{k_d + (n-1)k_c + \varphi\left(k_c - k_d\right)} \tag{2.9}$$

where n is the empirical parameter defining the shape factor of the filler materials. Using extensive analysis of experimental data, Harmathy (1970) suggested that $n = 1.5$ is applicable to cement-base materials having a wide range of porosity.

Using the volumetric fraction and thermal conductivity of individual phases, one can only approximate the thermal properties of a composite because of the statistical nature of phase distribution. Hashin and Shtrikman (1962) showed that two bounds can be found based on volume fractions and thermal conductivities which would define the upper and lower limits of experimentally determined values. Their bounds are given in the following two equations:

$$k_{el} = k_1 + \frac{\varphi_2}{\dfrac{1}{k_2 - k_1} + \dfrac{\varphi_1}{3k_1}} \tag{2.10}$$

$$k_{eu} = k_2 + \frac{\varphi_1}{\dfrac{1}{k_1 - k_2} + \dfrac{\varphi_2}{3k_2}} \tag{2.11}$$

where k_1, k_2 are the thermal conductivities of the phases ($k_2 \geq k_1$), ϕ_1, ϕ_2 are the volume fractions of each phase.

Russell (1935) used a series-parallel electrical resistance network to calculate the thermal conductivity of cubic pore in a matrix. Bentz (2005) utilized this model by assigning thermal conductivity values to individual cubic voxels and analyzing the micro-tomography scan data using finite difference approach. The model is shown below:

$$k_e = k_c \frac{\varphi^{2/3} + \frac{k_c}{k_d}\left(1 - \varphi^{2/3}\right)}{\varphi^{2/3} - \varphi + \frac{k_c}{k_d}\left(1 + \varphi - \varphi^{2/3}\right)} \tag{2.12}$$

Effective medium theories do not always yield accurate results, especially when the volume fraction of the inclusions approaches the so called percolation threshold (Pietrak and Wisniewski 2015; Zhang et al. 2010). At percolation threshold, a continuously connected network of filler materials forms resulting a significantly high thermal conductivity, assuming the fillers' conductivity is greater than the matrix. Models derived based on percolation concept was found to be more accurate than the effective medium theories. Using the percolation theory Zhang et al. (2015) developed a model as follows:

$$k_e = k_d \left(\frac{k_p}{k_d}\right)^{\left(\frac{1-\varphi}{1-\varphi_p}\right)^n} \tag{2.13}$$

where k_p is the thermal conductivity at percolation threshold, ϕ_p is the percolation threshold, and n is the percolation exponent representing the filler type, shape and distribution. Using experimental data one may be able to estimate these parameters.

Several researchers (Feng et al. 2004; Ma et al. 2003; Yu and Cheng 2002) developed fractal geometry-based models to calculate the effective thermal conductivity from the properties of its constituents. Yu and Cheng (2002) investigated the thermal properties of bidispersed porous media by considering two types of pore cluster—those are in contact with neighbouring particles and the ones that do not touch each other. They developed the thermal conductivity model by using the fractal dimension of the pores and the tortuosity fractal dimension assuming one dimensional heat conduction. However, several parameters in this model cannot be determined analytically. Ma et al. (2003) developed a fractal model by simulating the pore structure using Sierpinski carpet of various stages to match the fractal dimension and the porosity of the composite being studied. This model is applicable to only to a porosity range of 0.3–0.5. Feng et al. (2004) generalized it to extend its applicability to a porosity range of 0.14–0.8.

2.4.4 Specific Heat

Specific heat is defined as the amount of heat required to increase the temperature of a material of unit mass by 1 degree. As mentioned before, concrete at elevated temperature undergoes physical and chemical transformation, which is associated with the latent heat of different phase present in hydrated cement paste. Therefore, the measured specific heat of cement-based materials at high temperature has two components; the sensible heat component and the latent heat due to the phase transformation (Bažant and Kaplan 1996). Studies (Harmathy 1970) on cement paste and concrete with various types of aggregate at elevated temperature reported that specific heat does not vary significantly with the type of aggregate or mix proportions. Harmathy (1970) also reported a significant rise in specific heat at about 500 °C due to the thermal decomposition of CH in hydrated cement paste.

2.4.5 Thermal Diffusivity

Thermal diffusivity is the rate at which temperature changes within a material due to an imposed thermal gradient. It is also defined as the ratio of the amount of heat conducted to the amount of heat absorbed per unit volume. As shown in Equation 2.2, it is used to determine the temperature distribution for transient heat conduction. When measured at normal temperature, thermal diffusivity is governed by the properties of aggregates (Naus 2010). At elevated temperature, it follows the same trend as the thermal conductivity (Bažant and Kaplan 1996).

2.5 Mechanical Properties

Concrete loses a fraction of its strength at elevated temperatures due to the physical and chemical transformations. There are a number of factors that must be considered when evaluating the mechanical properties at elevated temperatures. These includes whether the tests are conducted during heating or after cooling, heating rate, cooling rate, moisture condition, state of stress, type of aggregates, presence of supplementary cementitious admixtures, presence of fibres, and thermal cycling. A brief review of compressive strength, tensile strength, flexural strength, creep, and bond characteristics is presented below.

2.5.1 Compressive Strength

Compressive strength of cement-based materials depends on several key factors such as porosity, solid/space ratio, water/cement ratio, presence of microcracks, and the interface between the matrix and aggregates. At elevated temperatures, the microstructure is altered both physically and chemically, which has significant influence on the percentage of strength retained after an exposure to high temperatures.

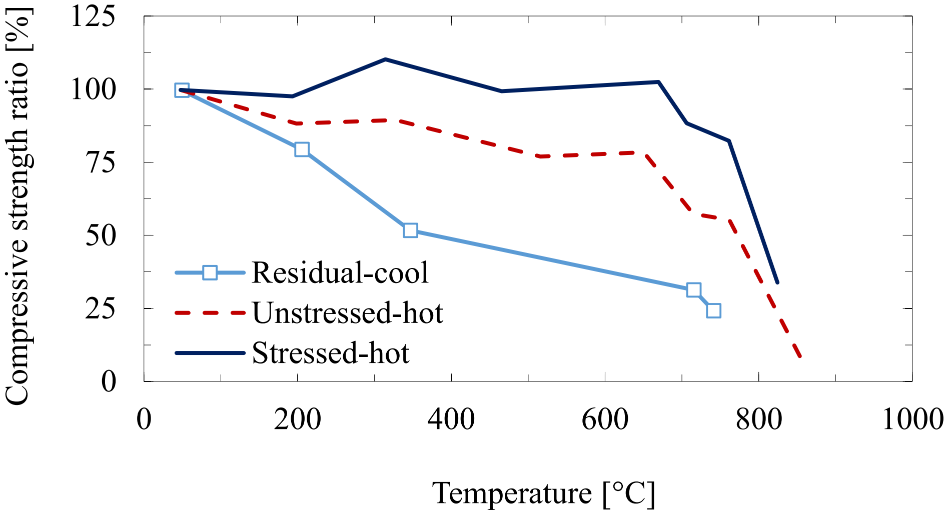

Figure 2.4 Compressive strength of concrete at elevated temperature, tested during heating and after heating with an applied stress of 40% of ultimate strength, also without any stress tested after cooling to ambient temperature (Abrams 1971).

It is well known that water/cement (w/c) ratio plays an important role in determining the compressive strength at ambient temperature. It controls the porosity, especially the capillary porosity, of concrete which can be correlated to the mechanical strength of cement paste, mortar, and concrete. A study (Malhotra 1956) on the effect of different w/c ratio—0.4, 0.45, and 0.50—showed no noticeable influence on residual strength after exposure to high temperature. Although, Sullivan (2004) mentioned that very low w/c ratio, such as 0.35, causes explosive spalling, thereby causing considerable damage in the microstructure which results in a lower post-exposure compressive strength. Furthermore, a very low w/c ratio, which is frequently employed to manufacture high strength concrete, renders very poor performance at elevated temperatures (Neville 2011).

Conducting compression tests during heating or after cooling also affects the compressive strength of concrete. Strength determined from the tests that were performed using cool specimens is called the residual strength. As shown in Figure 2.4, it was reported (Abrams 1971) that specimens tested while still hot retained a higher proportion of strength compared to residual tests. The reduction in strength in both cases may be attributed to the microstructural damages sustained by the specimens caused by the hygro-thermal transformation at high temperatures (Malhotra 1956). It was hypothesized (Khoury 1992) that, on cooling, thermal stress may cause microcracks due to temperature gradient, which renders the specimen weaker when tested after cooling. In addition, rehydration CaO to CH causes loss of strength due to the expansive nature of CH (Dias et al. 1990).

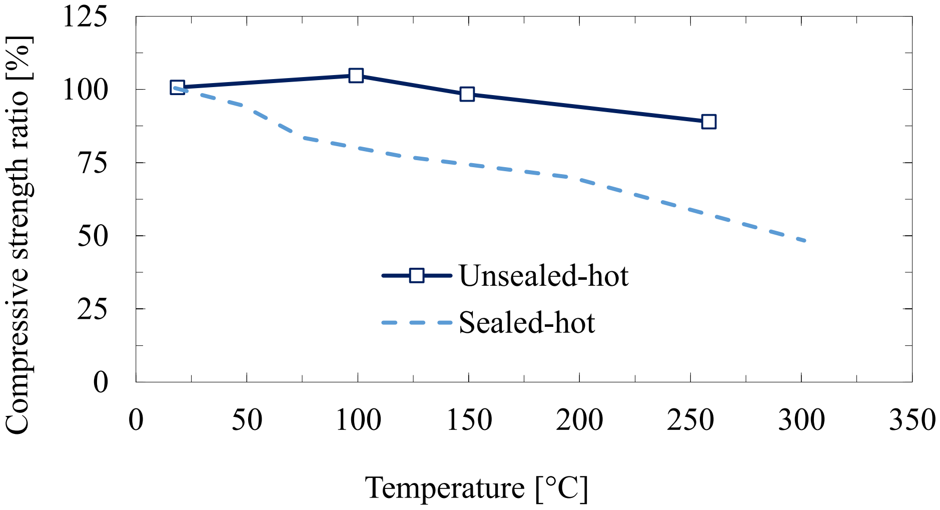

Figure 2.5 Compressive strength of concrete sealed and unsealed specimens at elevated temperature (Khoury 1992).

State of stress was also found to influence the compressive strength of concrete after heat exposure. It was reported that specimens tested while subjected to vertical compression, showed no significant loss of strength up to a temperature of 650 °C. However, an exposure beyond 650 °C resulted a gradual decrease in strength. On the other hand, the unstressed specimens showed a gradual reduction in strength at all temperatures (Abrams 1971; Bažant and Kaplan 1996; Malhotra 1956). This difference in mechanical behaviour may be attributed to the diminishing thermal expansion caused by the applied stress (Weigler and Fischer 1972), a reduction in porosity (Bažant and Kaplan 1996), prevention of crack development by load (Abrams 1971), and densification cement paste (Khoury 1992).

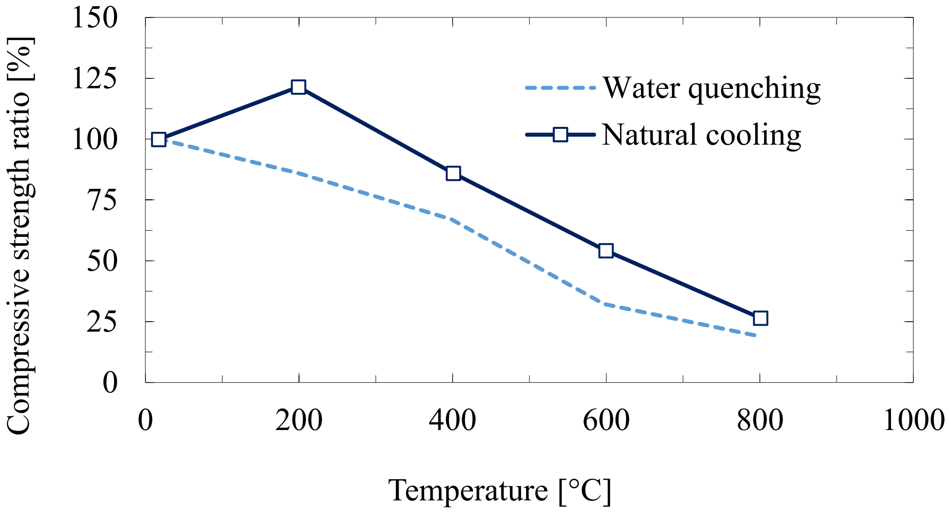

Figure 2.6 Effect of cooling rate on the compressive strength of concrete at elevated temperatures (Peng et al. 2008).

There are many structural application of concrete—for example, mass concrete, offshore vessel, and nuclear reactors—where the loss of moisture from the concrete is prevented. This restraint of moisture causes a considerable reduction of compressive strength. As shown in Figure 2.5, Compressive strength of sealed concrete was reduced gradually with the increase in exposure temperature. According to Khoury (1992), the hygro-thermal reaction that occurs under sealed condition alters the microstructure significantly. Depending on the C/S ratio in the cement paste, this transformation could either be beneficial or detrimental to concrete. At low C/S, C-S-H in hydrated cement paste transforms into tobermorite gel, which enhances the strength of concrete. On the other hand, at higher C/S ratio, a crystalline form of C-S-H is formed which reduces the cohesion by decreasing the van der Waals forces, resulting a reduction in strength.

Rate of heating can either be defined as the rate of temperature rise inside the furnace or at the core of the specimen. At higher heating rate, more microcracks develop due to the associated high thermal gradient (Phan 2008). Therefore, it is not unusual to observe a lower residual compressive strength in concrete when heated at relatively higher heating rate. It was reported that concreted exposed to elevated temperature showed lower strength when heated at a faster rate (Mohamedbhai 1986). However, Khoury (1992) found that concrete heated at a slower rate, 0.2 °C/min, showed lower strength than that at 1 °C/min, which was attributed it to the thermal degradation due to the longer time required to reach the target temperature. Similarly, the cooling rate also affects the observed mechanical properties. As shown in Figure 2.6,quenching by sudden immersion in water reduces strength compared to natural cooling due to the severe thermal gradient (Neville 2011).

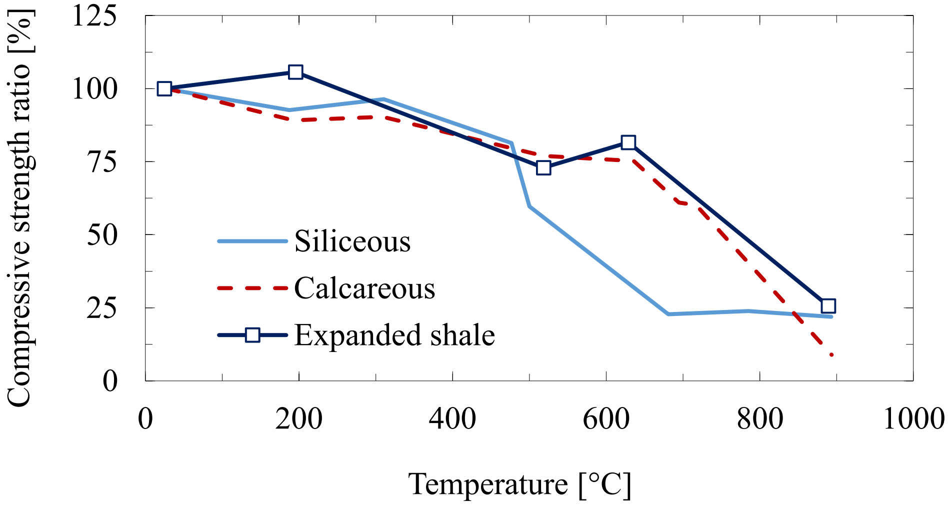

Figure 2.7 Effect of different types of aggregates on the compressive strength at elevated temperatures (Abrams 1971).

Thermal stability of aggregate and its interaction with paste are very important factor when selecting materials for better fire resistance. Dolomitic aggregate concrete, which contains calcium carbonate, were reported to possess better resistance at elevated temperatures due to the endothermic nature of the calcination that it goes through and to the lower density of the calcined materials (Neville 2011). Siliceous aggregates, on the other hand, were reported to perform poorly due to its high thermal expansion and volumetric change associated with the conversion of quartz from α to β form (Abrams 1971). As shown in Figure 2.7, siliceous aggregate concrete shows lower residual strength starting at a temperature of 450 °C.

Role of supplementary cementitious materials—such as fly ash, silica fume, and metakaolin—in concrete at high temperature were found to be beneficial when incorporated to reduce the CH content of hydrated cement paste. Inclusion of pozzolanic materials prevents microcracks in concrete by reducing expansive CH formed due to the rehydration CaO upon cooling (Neville 2011). Also, as mentioned earlier, supplementary cementitious materials may improve the mechanical properties when concrete is in sealed condition, where moisture movement is prevented, by reducing the C/S ratio. However, when pozzolanic materials are utilized in concrete with the intension of reducing the porosity, its performance at elevated temperature will be degraded due to the reduced permeability, hindering the release of pore pressure (Khoury 1992; Neville 2011).

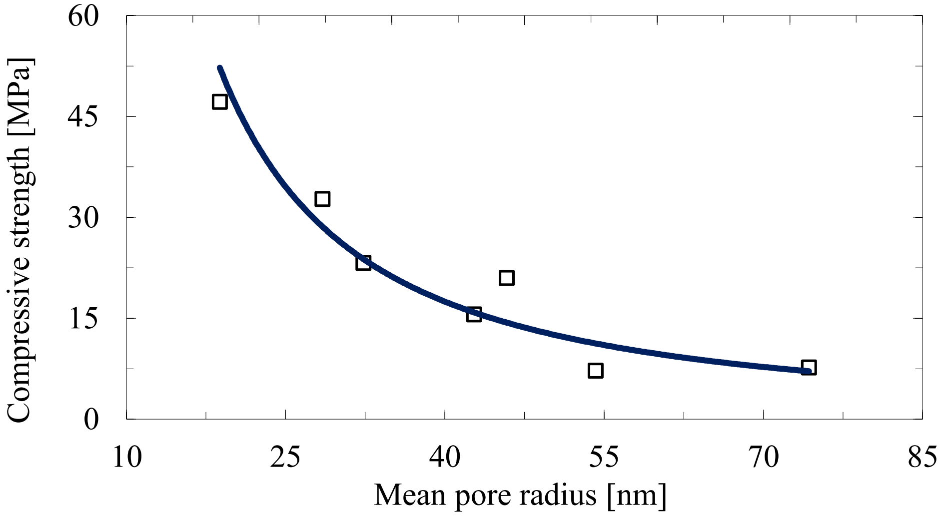

Figure 2.8 Correlation between compressive strength and mean pore radius (Jambor 1973).

In general, concrete loses a portion of its compressive strength with the increase in temperature. There are several reasons (Jambor 1973; Khoury 1992; Neville 2011) that may be associated with this reduction of compressive strength. These includes thermal expansion of aggregates, thermal incompatibility of aggregates and cement paste, increased porosity, pore coarsening, thermal decomposition of C-S-H, chemical transformation of hydrated cement paste under hygro-thermal condition, development of microcracks, and increased molecular movement causing a reduction in surface energy. As reported by Jambor (1973), shown in Figure 2.8, compressive strength of concrete reduces as the pores are coarsened due to the exposure to elevated temperatures.

Depending on the test condition, whether sealed or unsealed, concrete may show slightly higher compressive strength at intermediate temperature ranging from 100–200 °C (Fares et al. 2010). This phenomenon is associated with the reduction in disjoining pressure due to the dehydration of adsorbed water from C-S-H upon heating, causing an increase in van der Waals force of attraction. This beneficial effect counter balances the detrimental effect of thermal decomposition and thermal incompatibility between the aggregates and the cement paste (Dias et al. 1990; Mehta et al. 2006; Neville 2011).

2.5.2 Tensile Strength

The knowledge of tensile strength of concrete at elevated temperature is essential to evaluate the microstructural damaged caused by hygro-thermal processes. Increased tensile strength may help minimize the microcracks and spalling (Ali 2002). The residual and hot tensile strength was reported to follow the same trend as in the compressive strength (Thelandersson 1972). Investigation on the effect of polypropylene fibre showed that addition of fibre does not yield higher tensile strength upon exposure to high temperatures (Behnood and Ghandehari 2009).

2.5.3 Flexural Strength and Fracture Energy

Flexural strength of concrete at elevated temperature is more sensitive to microcracks that develop due to hygro-thermal transformations. Studies (Lamond and Pielert 2006; Zoldners 1971) showed that loss of flexural strength, at high temperature, is much higher than the compressive strength. Furthermore, investigation (Komonen and Penttala 2003) regarding the influence of polypropylene fibres reported that the addition of fibres, about 0.8% by volume, improved residual flexural strength up to an exposure temperature of 450 °C.

Fracture energy is an important parameter used to assess the crack growth resistance of a material. It can be determined from the load–deflection response recorded during flexure test. Generally, it is a size dependent quantity due to the energy absorption, normally unintended, outside the fracture zone in the specimen (Shah et al. 1995). Baker et al. (1996) investigated the fracture energy of plain concrete at elevated temperature and found that fracture energy reaches a peak at a temperature of 300 °C followed by a gradual reduction with the increase in temperature. This transition temperature happens to be the so called "activation temperature"—the energy level beyond which atomic bonds disrupt and an increase in the rate of crack growth occurs— calculated by Bažant and Prat (1988) for dry concrete. Yu et al. (2012)reported this temperature to be around 450 °C for normal strength concrete. Addition fibres also reported to have influence of the fracture energy at high temperatures. An improvement in residual fracture energy was observed when steel and polypropylene fibre were incorporated in the mixtures. It is attributed to the crack arresting and bridging mechanisms of microfibres (Suhaendi et al. 2007).

2.5.4 Creep

Creep, defined as time-dependent strain at sustained load, in cement-based material occurs due to the loss of physically adsorbed water from the hydrated cement paste. It is further amplified by the hygro-thermal process when concrete is subjected to sustained elevated temperature. According to Bažant and Kaplan (1996), accelerated breaking and reformation bond in C-S-H is the cause of increased creep strain in concrete at elevated temperature. A study (Marechal 1972) on the creep of concrete with a sustained stress of 10 MPa showed that at 400 °C creep measured at 50 days increased about three time that tested at 250 °C. It was also observed that pre-dried specimens sustained higher rate of creep than those tested at saturated and sealed condition. Wang (1971) also studied creep at temperature from 90 °C to 430 °C and reported an increase in creep rate with the increase in temperature. It seems creep rate in concrete is higher than mortar at temperature above 200 °C, which Sullivan and Poucher (1971) attributed to the microcracks developed in the interfacial transition zone. One of the most important factors that affects creep in concrete is the w/c—concrete with low w/c ratio exhibits less creep (Lamond and Pielert 2006).

2.5.5 Bond

It is crucial that structural elements, especially the steel reinforced member, remain functional in the event of fire. Therefore, evaluation of the bond strength of steel reinforcing bar at elevated temperature is important. Bond performance of rebar in concrete at high temperature depends on the type of bar, properties of concrete, depth of concrete cover, and the level of temperature exposure. The experimental techniques—heating rate, cooling regime, loading condition— are also known to have influence on the observed bond behaviour.

The coefficient of thermal expansion (CTE) of reinforcing steel and concrete are very close to each other at ambient temperature. But at high temperature the value for steel changes in a dissimilar manner to that of concrete (Lamond and Pielert 2006). This discrepancy in CTE values has significant impact on the bond strength of concrete at high temperature. Generally, the bond strength of steel embedded in concrete decreases with exposure temperature. Hertz (1982) investigated the anchorage of steel reinforcement at a temperature up to 800 °C and attributed the failure to either splitting of concrete or failure of the bond. It was also reported that the bond strength could be estimated from the compressive strength of concrete at the same temperature. A study (Bažant and Kaplan 1996) on the effect of the type of aggregate showed that limestone aggregate concrete retains twice the bond strength compared to the concrete made with quartzite aggregates. Investigations (Diederichs and Schneider 1981) on the effect of bar type—plan and deformed bar—showed that bond strength of deformed bar is slightly higher than that of plain bar. This increased bond strength may be attributed to the bearing of concrete against the ribs on deformed bars (Morley and Royles 1980). The depth of concrete that covers the rebar also influences the bond characteristics at high temperature. It was reported that pull-through type failure is associated with bars having larger concrete cover whereas, splitting type bond failure occurs with smaller concrete covers (Morley and Royles 1983). Study on the effect of supplementary admixtures and fibre reinforcement, such as natural pozzolans, concluded that the presence of pozzolans further reduces the bond strength while steel fibre reinforcement enhanced the bond strength at elevated temperature (Haddad and Shannis 2004; Haddad et al. 2008).

2.6 Spalling at Elevated Temperature

Depending on the heating rate and the nature of microstructure, violent explosion may occur on the heated surface of concrete. This violent disintegration of concrete fragments from the heated surface is called spalling. It is more likely to occur in high strength concrete due to its dense microstructure. However, normal strength concrete could also explode if it is subjected to a very high rate of heating (Hertz 1992). The factors influencing the explosive behaviour of heated concrete includes moisture content, density, permeability, and heating rate. Any favourable combination of these factors could trigger spalling in concrete causing a reduction in member dimension which could compromise the integrity of the structure.

As mentioned earlier, heating rate influences the spalling phenomenon. In a fire scenario, heating rate could be as high as 80 °C per minute. In terms of rate of heating, hydrocarbon fire is more damaging than building fire incidents. Faster rate of heating results in a more severe spalling (Kodur 2000). However, regardless of heating rate, once it is triggered, spalling occurs within a consistent range of temperatures (Majorana et al. 2010). For materials having a very dense microstructure, spalling could occur at a low level of heating rate. Spalling was reported to occur in concrete with 14% micro silica at a heating rate of 1 °C per minute (Hertz and Sørensen 2005). Furthermore, the severity of spalling is also associated with the exposed surface area structural elements—beam elements, having three sides exposed, sustained more damage than slabs (Majorana et al. 2010).

The moisture content of concrete plays a dominant role on the spalling behaviour. At elevated temperature, evaporable moisture causes a build-up of pore pressure. Once it exceeds the tensile strength of concrete, it may trigger unstable crack growth, resulting in an explosive spalling. Higher moisture content could lead to a higher degree of spalling—ratio of mass lost to the original mass of specimen (Kodur 2000; Majorana et al. 2010). It is more pronounced when the compressive strength of concrete exceeds certain threshold. Cha et al. (1999) studied the behaviour of high-performance concrete exposed to fire and concluded that concrete having a compressive strength higher than 60 MPa is more likely to sustain explosive spalling. Normal strength concrete having a moisture content of 2% by mass is not likely to exhibit spalling despite unfavourable exposure conditions (Copier 1983). Once again, it is important to note that even at a moisture content of 2% by mass, spalling could occur in concrete having a very high density. High strength concrete and high performance concrete are produced by reducing the w/c ratio, which renders these concrete low fire resistant due to their very low permeability. Despite having low moisture content, the release of the physically and chemically combined water contributes to the pore pressure build-up with the increase in temperature. In addition, the type aggregate also influences the spalling behaviour of high strength concrete. It was found that high strength concrete with lightweight aggregates are more susceptible to spalling when exposed to hydrocarbon fire due to the higher amount absorbed water by these aggregates (Bilodeau et al. 2004). The mineralogical composition of the aggregates also important when studying the spalling susceptibility of concrete. Siliceous aggregate, having high thermal expansion and relatively low heat capacity, was reported to cause more spalling than carbonate aggregates—owing to its endothermic transformation at high temperatures.

2.6.1 Mechanisms

Spalling occurs only when a favourable combination of the controlling parameters such as moisture content, permeability, heating rate, and temperatures exists. The interdependency of these parameters gives an inconsistent picture, as discussed above, of spalling phenomenon. In order to explain spalling, three of theories can be found in the literature—the pore pressure spalling (Harmathy 1965), the thermal stress spalling (Saito 1966), and the combination of pore pressure and thermal stress spalling (Zhukov 1975).

According to pressure spalling theory, as the temperature rises, the vapor from heated surface migrates inward. Due to the temperature gradient, the vapour condenses as it enters a relative cooler interior zone. As this process continues, pore water content increases and a completely saturated zone is developed. It prevents inward movement of vapour generated near the heated surface. The redirected vapour must migrate outward to the dry surface. Depending on the moisture content, rate of heating, and permeability of concrete, vapour may not be able to escape fast enough to prevent the build-up of pore pressure as the temperature continues to rise, shown in Figure 2.9. Spalling occurs once the pore pressure exceeds the tensile strength of the concrete. Indeed, experimental and theoretical evidence show an increase in pore pressure, with the increase in temperature, in concrete having a dense microstructure and low permeability (Kalifa et al. 2000). In high strength concrete, pore pressure may reach as high as 8 MPa which could potentially exceed the tensile strength of the matrix (Kodur 2000).

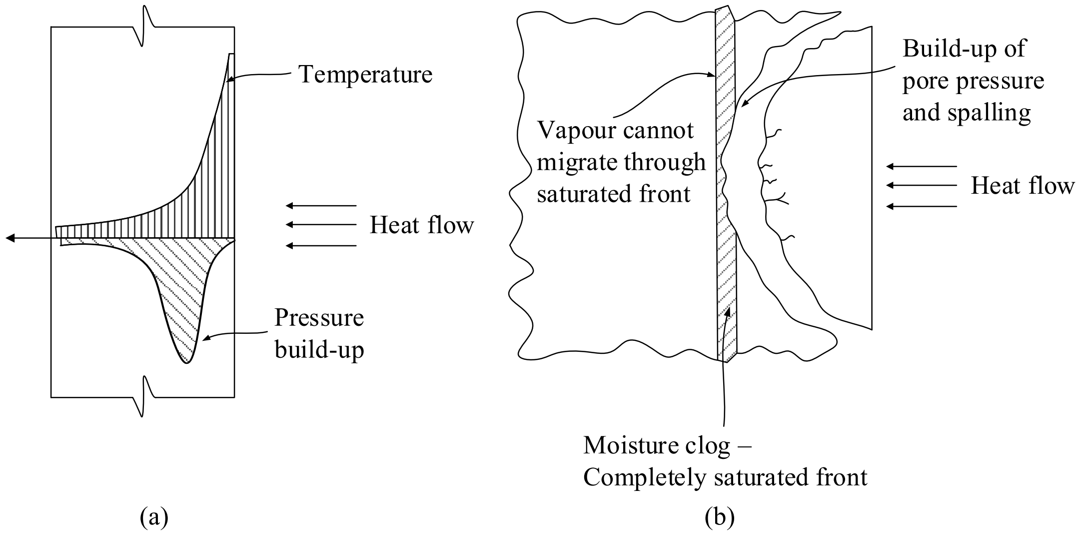

Figure 2.9 Spalling mechanism - "Moisture clog" (a) temperature and pressure profile, and (b) Saturated front (Consolazio et al. 1998)

Thermal stress spalling was first proposed by Saito (1966) to explain the spalling phenomenon is dry concrete. At high rate of heating, excessive thermal stresses are developed and spalling occurs without the presence of pore pressure. As shown in Figure 2.10, temperature gradient in concrete causes bi-axial compressive stress in a zone near the heated surface due to the restrained thermal expansion. The cooler interior zone, however, experiences a tensile stress. Sometimes, the compressive stress is further amplified the by existing state of stress in the structure. Nevertheless, this mechanism was found to be very rare (Majorana et al. 2010).

The combination of thermal stress and pore pressure is more likely to cause spalling of concrete. Hygro-thermal transformation in concrete causes numerous microcrack. An unstable growth of these cracks may be triggered by the pore pressure acting perpendicular to the heated surface. Spalling could occur due to the brittle fracture of concrete under the combined action of bi-axial stresses acting parallel to the heated surface and outward forces exerted by pore pressure.

It has been argued that the pore pressure build-up cannot be the only reason behind spalling (Bazant 1997; Hager 2013). Because as the microcracks in heated concrete start to grow, they act a reservoir and the pore pressure begins to drop. Therefore, after triggering the crack propagation, the subsequent explosive spalling is dependent on the thermal stresses.

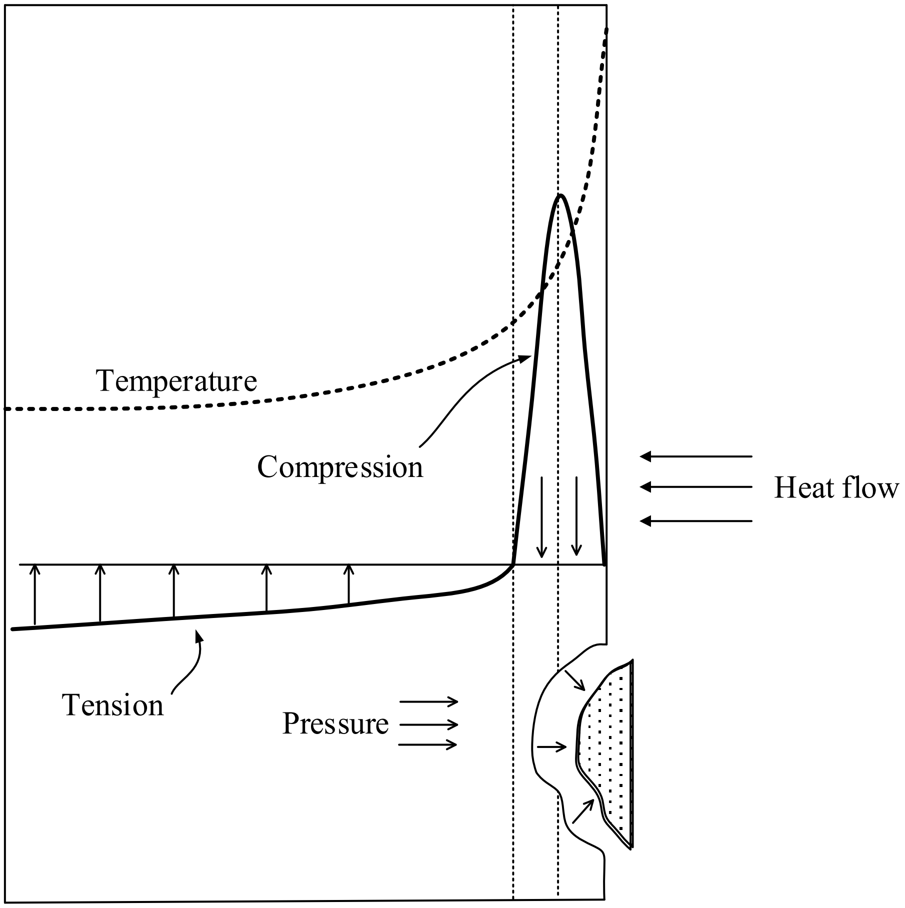

Figure 2.10 Spalling mechanism - “Restrained thermal dilation” (Majorana et al. 2010)

2.6.2 Mitigation of Spalling

Spalling of structural elements may potentially compromise the integrity and serviceability of the entire structure. It could expose the reinforcing bar which may cause sudden increase in temperature surrounding the concrete resulting a loss of anchorage and bond between steel and concrete. The reduced cross-section of beams and columns could pose a serious danger to the post-fire rescue operation. In addition, if fibre reinforced polymers are used as reinforcement, spalling could expose them to melting temperature. In order to avoid these risks associated with spalling, several aspects of concrete microstructures require considerations. These are the porosity, pore connectivity, permeability, strength of concrete, type of aggregate, the addition of fibres, and the moisture content.

Addition of polypropylene (PP) fibre is reported to be very effective in preventing spalling of high strength concrete (Khoury et al. 2008; Lee et al. 2012; Phan 2008; Zeiml et al. 2006). The efficiency of pp fibres depends on the heating rate, strength, and porosity of the concrete. The dosage of fibre required to prevent spalling of the concrete depends on the state of stress and strength of concrete (Khoury and Anderberg 2000). It is suggested that fibre dosage of 0.1% by volume be used to eliminate spalling in high strength concrete. Due to the denser microstructure of high performance concrete, slightly higher dosage of 0.2–0.3% by volume was suggested (Bilodeau et al. 2004; Khoury 2008). Khoury (2008) suggested that the selection fibre geometry and dosage should be such that it maximizes the total amount surface area created around the fibre-matrix interface. In addition, the length of the fibre is important, where longer fibre is capable of creating more interconnectivity of pore network than the shorter ones (Bangi and Horiguchi 2012). Simulation study by Garboczi et al. (1995) showed that certain combinations of fibre aspect ratio and dosage is required to achieve a percolated pore network.

Physical properties of fibre also affects its performance in mitigating spalling in concrete. Monofilament type fibre is expected to perform better than the fibrillated ones because of their poor bonding characteristics with the cement matrix (Johnston 2010). Further discussion regarding its poor adhesion is presented below. The melting of the fibre material is found to be associated with the temperature at which the relief of internal pore pressure occurs in heated concrete. Therefore, PP fibre, having a lower melting point, performs better than polyvinyl alcohol fibre (Bangi and Horiguchi 2012). However, with a slightly higher melting point than pp fibre, nylon fibre outperforms pp fibre in terms of pore pressure reduction due to the higher aspect ratio (Heo et al. 2010).

There are many hypotheses available in the literature which attempt to explain the spalling prevention mechanism of micro-fibres. First of all, addition of fibre creates extra air-voids which act as reservoirs and thus help reduce the internal pore pressure caused by the vapour generated during elevated temperature exposure. Secondly, micro-fibres create internal cracks due to volumetric expansion of fibres and differential thermal expansion between hydrated cement paste and fibres. Thereby creating additional reservoirs for vapours to escape. Thirdly, certain type of fibres, such as pp fibres, do not bond well with the concrete matrix due to the polarity mismatch (Khoury and Willoughby 2008). The interface between these fibres and the matrix provides an escape route for the vapour even before the melting point is reached. This mechanism is called the “pressure-induced tangential space” (Hager 2013; Khoury 2008). In addition, a well dispersed network of fibres is capable of intercepting the interfacial transition zones, which is inherently more porous than the bulk matrix. Thus creating a continuously connected pore network and providing a mechanism of reducing pore pressure (Bentz 2000; Kalifa et al. 2001). Fourthly, a more commonly mentioned mechanism is that the melting of fibres creates a network of channels providing a vacated network of pathways which would allow the transportation of expanding vapour to escape (Kodur 2000). It was, however, criticized based on the fact that due to high viscosity and larger molecular size, melted fibre would not vacate the fibre bed at a temperature close to the melting point of the fibre. The creation of vacated channel is possible only after the vaporization of the fibres (Khoury 2008; Majorana et al. 2013).

Besides adding micro-fibres, there are other preventive measures available against spalling (Khoury and Anderberg 2000). For example, use of aggregates that has low coefficient of thermal expansion and low moisture absorption, could help reduce the probability of spalling. Since presence of moisture is essential for spalling to occur, reduction of moisture would minimize the risk of spalling. By incorporating air-void through air-entraining agent, additional reservoirs can be added which would reduce the pore pressure that develops with the increase in concrete temperature.

2.7 Methods of Microstructure Characterization

Quantifying the various features of concrete microstructure is essential to understand its mechanical behaviour as well as durability characteristics. A number of techniques were developed over the years to study the microstructures of cement-based systems. Some of these techniques which are relevant to examine the internal structures of concrete exposed to elevated temperatures are reviewed in this section.

2.7.1 Ultrasonic Pulse Velocity

The velocity of wave propagation, which depends on the elasticity and inertial properties, through a solid can reveal insightful information regarding its microstructure. Depending on the motion of particles, there are two independent types of wave propagation through a solid mass—primary wave, also known as pressure wave or longitudinal wave and secondary wave, also known as shear wave or transverse wave. A combination of longitudinal and transverse wave called surface wave also exists.

When longitudinal wave travels through a solid the displacement of the particles occurs along the direction of the wave propagation causing a change in volume of the medium. It is the fastest of the three types of wave mentioned above. Therefore, it is used widely as a non-destructive technique to assess the properties of concrete. Elastic properties of the medium can be determined by knowing the mas velocity and density of the material. The velocity of longitudinal wave in homogeneous, isotropic, and elastic medium can be expressed as follows (Mehta et al. 2006):

$$V_L = \sqrt{\frac{E_d}{\rho}\frac{(1-\nu)}{(1+\nu)(1-2\nu)}} \tag{2.14}$$

where V_L is the velocity of primary wave in km/s, E_d is the dynamic modulus of elasticity in MPa, ρ is the density in kg/m^3, ν is the dynamic Poisson's ratio.

In transverse wave, the particles move in the direction perpendicular to the direction of wave propagation. There is no volumetric change associated with the propagation of transverse wave. It is relatively slower than longitudinal wave. The velocity of transverse wave can be expressed as follows:

$$V_T = \sqrt{\frac{E_d}{\rho}\frac{1}{2(1+\nu)}} \tag{2.15}$$

The Rayleigh surface wave in a solid causes the particles to displace in elliptical paths. As the distance from the surface increases, the amplitude of the wave and the width of the elliptical path decreases. These waves are useful in detecting flaws in concrete near the surface of structural elements (Mehta et al. 2006). The following expression relates the elastic properties of solids to the velocity of Rayleigh surface waves (Maierhofer et al. 2010):

$$V_R = \frac{0.87+1.12\nu}{1+\nu}V_T \tag{2.16}$$

As mentioned earlier, the longitudinal wave is used to perform several non-destructive assessment of cement-based materials. Since the wave velocity decreases with the increase in porosity, the hydration process of concrete can be studied by monitoring ultrasonic pulse velocity (UPV) through the concrete. Similarly, the moisture condition, type and amount of aggregate, presence of microcracking, and other heterogeneity of cement-based systems can be evaluated using UPV.

Due to the non-homogeneous nature of concrete microstructure, the expression shown in Equation 2.14 is not strictly applicable to concrete. The variation of Poisson's ratio also influences the measured value of elastic properties. Although it was found that the values of modulus of elasticity do not vary significantly for the usual range of Poisson's ratios (Neville 2011). Despite these limitations, UPV technique has been found to be useful in assessing the modulus of elasticity of concrete. Furthermore, the modulus of elasticity of concrete, consequently the pulse velocity, depends on the amount and elastic properties of its constituents especially that of aggregates. However, the strength is not affected significantly by the properties of aggregates. Therefore, no unique relationship between strength and UPV can be expected (Bungey et al. 2006).

A study on the fire performance of concrete with recycled inclusions showed that dynamic elastic modulus of concrete reduces with the increase in the amount of recycled inclusions (Hernández-Olivares and Barluenga 2004). Another investigation with fire damage in concrete reported that reduction in the UPV, up to 30%, was not associated with significant reduction in compressive strength (Hung-Wan and Kwok 1985). It was attributed to the loss the capillary and adsorbed moisture due to high temperature. Yang et al. (2009) reported that the change in mixture proportion did not have significant effect on the relationship between residual compressive strength and ratio of UPV between before and after thermal exposure.

2.7.2 Mercury Intrusion Porosimetry

Mercury intrusion porosimetry (MIP) is a very common technique used to determine the pore size distribution of porous materials. It is a relatively easy and quick method to determine the pore size distribution of cement-based systems. Besides, it is considered (Scrivener et al. 2015) the only method that covers the range of pore sizes relevant for studying the behaviour related to pore structures such as fluid permeability, modelling mechanical properties, and investigating thermal properties.

Mercury is a non-wetting liquid, having a contact angle greater than 90°, when it comes in contact with many material such as concrete. External pressure must be applied to overcome the surface tension that prevents the intrusion of liquid mercury into the pore system. The following equation, known as Washburn Equation, can be used to calculate the pore radius based on the cylindrical pore model:

$$r_p = -\frac{2\gamma_m \cos\theta}{P} \tag{2.17}$$

where r_p is the pore radius, γ_m is the surface tension between mercury and pore surface, θ is the contact angle between mercury and the porous material, and P is the pressure required for the intrusion of a measured volume of mercury.

Using the volume of intruded mercury and associated pressure, a cumulative pore size distribution can be generated. Specific surface area can also be calculated from the mercury intrusion data by assuming a simplified shape of pore structure (Aligizaki 2005).

MIP technique has several disadvantages that one needs to be aware of when interpreting and comparing results from different sources. These includes, retention of mercury, assumption of cylindrical pore shape, degradation caused by mercury under high pressure, and most importantly the so-called ″ink-bottle effect″—the presence of narrow entrance into large pore volumes. Due to the "ink-bottle" effect MIP is known to misrepresent the actual pore size distribution of cement-based materials (Aligizaki 2005; Allen 1990; Diamond 2000; Scrivener et al. 2015). It has been suggested that MIP results may be used to only compare microstructure and not to be used as an absolute method(Allen 1990).

2.7.3 Nitrogen Sorption

Gas sorption method is a convenient way of measuring surface area and pore size distribution, ranging from 0.3 nm to 300 nm, of porous material. Nitrogen is one of the most commonly used adsorbate to assess the meso-level structure of porous materials in gas sorption methods. When a porous solid is exposed to a gas, the gas molecules adsorb onto the surface of the solid. The amount of the gas adsorbed depends on the nature of the surface, the gas being adsorbed, the temperature, and the pressure. The amount of the gas adsorbed or desorbed can be determined by monitoring the volume removed from or returned to the system. The volume of gas is plotted against the relative pressure at a constant temperature is called isotherm. Finally, surface area and pore size distribution can be determined by analyzing the isotherms using an appropriate method.

The radius of the pore corresponding to a relative pressure can be determined from the following expression (Allen 1990):

$$r_p = r_k + t \tag{2.18}$$

where r_p is the actual pore radius, r_k is Kelvin radius, the radius of the pore in which condensation occurs, t is the thickness of the adsorbed layer. The r_k and t values may be calculated using the following equations:

$$r_k = \frac{-2\gamma V_m}{RT\ln\left(P/P_0\right)} \tag{2.19}$$

where γ is the surface tension of adsorbate, nitrogen, V_m is the molar volume of liquid nitrogen, R is the gas constant, T is the boiling point of nitrogen, P/P_0 is the relative pressure.

$$t = 3.7403/[\log\left(P/P_0\right)+0.034]^{0.5} \tag{2.20}$$

The volume of each pore can be calculated from the following equation using BJH (Barrett et al. 1951) method:

$$V_{pn} = \left(\frac{r_{pn}}{r_{Kn}+\Delta t_n}\right)^2\left(\Delta V_n - \Delta t_n \sum c_j A_{pj}\right) \tag{2.21}$$

where n represents n^{th} pore, V_p is the actual pore volume, Δt is the change thickness of the adsorbed layer, ΔV is the observed volume of gas desorbed, $c = (r_p - t_r)/r_p$, $A_p = 2V_p/r_p$, and t_r is the thickness of the observed layer at the corresponding relative pressure.

This method is only capable of determining meso-level pore sizes (Westermarck 2000). For macro-level pore sizes, other complementary methods are required. It is to be noted that only the open pores can be measured with nitrogen sorption method. In addition, the pores are assumed to be cylindrical when calculations are performed based on the recorded isotherms. Due to the presence narrower channels in the pore network, the shape of the pore size distribution could be different for the desorption isotherm compared to the adsorption counterpart (Allen 1990).

2.7.4 Scanning Electron Microscopy

Scanning electron microscopy (SEM) is a powerful technique to examine the structure of cement-based materials. It can be used to study either the topographical details or to identify different phases in concrete. The type of microstructural information that can be captured depends on the scanning and detection technique.

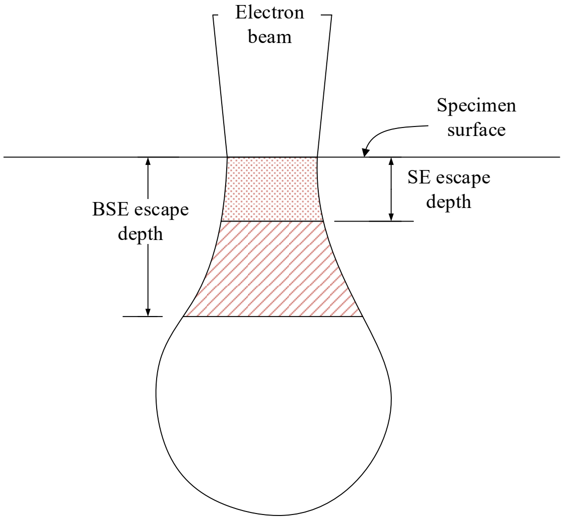

Figure 2.11 Schematics of scanning electron microscopy showing the escape depth of SE and BSE, adopted from (Hafner 2007).

In SEM, details about the specimen is acquired by detecting signals from the interaction of a beam of electrons and the specimen being studied. Incident electron beam causes elastic and inelastic events when interacting with the atoms in the specimen. Expulsion of secondary electrons (SE) is the outcome of low energy inelastic interaction whereas the elastic interaction produces the backscattered electrons (BSE). These are the two types of imaging that can be performed using SEM technique. Due to their lower energy, secondary electrons are unable to reach detectors from the deeper layer of specimen, as shown in Figure 2.11. Therefore, they can only be detected when scattered from a layer very close the surface of the specimen. In addition, due to smaller sampling depth, SE scanning cannot be used to identify different phases in the specimen (Zhao and Darwin 1990). Since the intensity of SE depends on the inclination of the surface being scanned, a fractured specimen surface is used to produce better quality image (Scrivener 1989). On the other hand, backscattered electrons are the results of elastic events caused by the interaction of nuclei of atoms in the specimen and the incident beam of electrons. BSEs have high energy which enables them re-emerge from relatively deeper layers of the specimen. Consequently, BSE images have slightly lower resolution than SE images. The backscattering coefficient, which is the ratio of the number electrons in the incident beam to that of backscattered signal, is a function of the atomic number or mean atomic number for heterogeneous specimen (Zhao and Darwin 1990). The higher the mean atomic number the brighter the image formed. Therefore, BSE can be used to identify various phases in the specimen.

When examining the structure of cement-based materials using BSE scanning, one must prepare the specimen by polishing its surface. In order to prevent damage while preparing the specimens, epoxy resin impregnation technique is usually employed. When the pores are filled with epoxy resin they produce a very low backscattering coefficient resulting in a dark pixel values in the captured image (Diamond 2000).

As mentioned earlier that the intensities of BSE images are functions of the mean atomic numbers of scanning area of the specimen. Using these intensity variations, various features of the specimen surface can be quantified with the help of morphological image processing techniques. Furthermore, the phases in hydrated cement paste—unhydrated cement particles, CH, C-S-H, AFm, AFt—can be identified from the backscattering coefficient, in other words from image intensities. In order of decreasing intensities, phases in hydrated cement paste may be organized as unhydrated cement particles, CH, C-S-H, and voids (Zhao and Darwin 1992).

BSE can be used to quantify the pore fraction in cement paste. It was reported that image-based quantifications were in agreement for lower levels of porosity while at higher levels it underestimated the pore fraction (Scrivener 2004). Using BSE images, Lange et al. (1994) performed pore size distribution, two-point correlation function, and fractal analysis on cement paste and mortars. Zhao and Darwin (1992) quantified the area fraction of unhydrated cement particles, CH, C-S-H, voids in cement paste using images from two different magnifications, 500x and 1000x.

2.7.5 X-ray Micro-Computed Tomography

X-ray micro-computed tomography (mCT) is a non-destructive technique that is being used to investigate the microstructure of cement-based materials. This technique allows the study of microstructural features both in two and three dimension. It enables quantitative investigation of concrete microstructure through various image processing algorithms.

When an X-ray beam from a high-flux source pass through a material, a portion of it is either scattered or absorbed. This attenuation of X-ray depends on X-ray energy, absorptivity of the material, and the travel distance. The absorptivity of the material again depends on its molecular structure i.e., type and number of atoms (Landis and Keane 2010). By capturing a series of X-ray attenuation maps at different angular orientation of the specimen, a three dimensional model of the specimen can be generated.

The specimen is placed on a rotating stage in between the X-ray source and a scintillator. The scintillator converts the projected X-ray to visible light which is recorded as digital image using a photodetector. The images containing the projected absorption profiles are then used to mathematically calculate the spatial X-ray absorption profiles. The complex nature of this reconstruction process requires specialized computational algorithm.

Landis et al. (2007) studied the microstructure evolution of concrete, using mCT, subjected to different levels of in situ compressive load. They were able to quantify the changes in void objects with the increase in applied loading. Promentilla and Sugiyama (2007) investigated the diffusion tortuosity of cement-based materials by performing a random-walk simulation using mCT images. Poinard et al. (2012) studied concrete under mCT and evaluated the damage at different levels of applied loading. Another study utilized mCT to characterize the transport properties of concrete by assessing three dimensional pore structure parameters (Lu et al. 2006). Helfen et al. (2005) investigated the evolution of pore structure of cement paste at different stages of cement hydration using micro-tomography technique.

2.8 Conclusions

Based on the review of the relevant literatures on the behaviour of cement-based materials at elevated temperature, it was found that several aspects of the microstructural and macro-mechanical characterization were scarcely investigated. For instance, the influence of fibre reinforcement on the pore size distribution, pore connectivity, and pore tortuosity has not been investigated. These pore structure parameters help understand the role of microfibre in improving the performance of cement-based systems under elevated temperatures. Damage evolution and fracture mechanical parameters have not received adequate attention. Furthermore, the experimental methods in some the studies were found to be inappropriate. For example, the use of MIP technique to assess the pore structure does not reveal the true nature of pore characteristics.

CHAPTER 3. MICROSTRUCTURES OF CEMENT MORTAR AT ELEVATED TEMPERATURES

3.1 Introduction

Cement-based materials are heterogeneous systems composed mainly of hydrated cement paste, aggregates, water, and voids. Hydrated cement paste consists of both crystalline and non-crystalline products in its microstructure, formed from the reaction between the constituents of cement particles and water. The non-crystalline C-S-H phase occupies 50–60% of the total volume of solid constituents of cement paste. Its structure is idealized as irregular arrays of layers with a very high specific surface area which impart binding properties to the cement paste by means of van der Waals forces. On the other hand, crystalline hydration products such as CH, AFt, and AFm constitute about 35–40% of the solid volume and do not have any significant contribution to the strength of the material due to their lower specific surface areas. And, it is the aggregate phase that is mainly responsible for the bulk unit weight and modulus of elasticity of concrete. It is seen that the mineral composition of aggregate per se usually does not affect the properties of the overall composite. However, the interfacial transition zone (ITZ) between the aggregate and cement paste plays a very critical role in determining the strength and performance of concrete. Hence, a proper control of the thickness of ITZ becomes important. Besides the solid constituents, there are pores present in the hydrated cement paste. These pore space may be divided into three categories—interlayers pore space, capillary pores, and air-voids—depending on the equivalent pore diameter. The interlayer space between C-S-H is considered too small to have any significant influence on the macro-level properties. However, the capillary pore space, ranging from 10 nm to 5 µm, is considered to have significant impact on both the mechanical properties and the transport phenomena through the material. The size distribution of these pores can be used to develop models that allow the prediction of the strength and other physical properties such as permeability and thermal conductivity.

The structure—distribution, type, and quantity of above mentioned phases—of cement-based materials is multiscale in nature, which is ranging from a scale observable to the unaided human eye to nanoscale, requiring sophisticated atomic force microscope to examine various features. Further, the micro-scale structure, also called microstructure, of cement-based materials determines its response to the applied load as well as to the action of aggressive chemical agents. Therefore, a good understanding of the microstructure of cement based materials becomes important for assessing the mechanical properties, durability characteristics, and performance under exposure to elevated temperatures.

3.2 Objectives

The microstructure of cement-based materials changes physically and – more significantly-chemically, with the exposure to elevated temperature. As mentioned earlier, the structure of hydrated cement paste alters due to the loss of both the physically and chemically bound water. As the exposure temperature increases, breaking of chemical bonds causes decomposition of C-S-H. Furthermore, the thermal incompatibility between cement paste and aggregate phase causes microcracks. These degradations influence the properties of concrete that are necessary to serve its intended function in structural members.

This Chapter, therefore focuses on the experimental evaluation of the effect of sustained exposure to elevated temperatures on the microstructure of cement-based mortars. First, the changes in porosity with the increase in exposure temperatures are discussed. The experimentally measured porosity values are then compared with those calculated from the stoichiometry-based porosity model. Second, the variation in pore size distribution at different temperatures determined from image analysis is presented. Third, the results from a two-point correlation function along with specific surface area and characteristic pore size are discussed. Finally, the changes in pore structure, at a much finer scale than SEM, as evaluated using the Nitrogen Sorption Method is presented.

3.3 Microstructure at Elevated Temperatures

Changes in the cement paste microstructure occur as the heating temperature increases. It is a consequence of heat and mass transfer through the heterogeneous microstructure within cement mortar. The temperature, heating rate, duration of exposure, original porosity, moisture content, and the degree of hydration, all influence these changes within the microstructure. The rate at which thermal decomposition of various phases—AFt, CH, and C-S-H—occurs is revealed by thermo-gravimetric analysis (TGA) and differential scanning calorimetry (DSC). As the temperature increases, AFt phases gradually decomposes due to the dehydration process, which starts at 70–80 °C (Hager 2013). At around 230 °C it completely decomposes into metaettringite. Pourchez et al. (2006) studied the decomposition kinetics of ettringite and provided an expression to calculate the degree of conversion at different temperatures. Further, it has been shown that at 430 °C the decomposition of CH phase begins and it transforms into CaO and water vapour (Bažant and Kaplan 1996; Hager 2013; Zhao 2012). A complete transformation of CH occurs at 540–560 °C. Using differential scanning calorimetry, Zelić et al. (2002) studied the degree of conversion of CH at different temperature with a heating rate of 20 K/min. They provided a rate equation which enables the estimation of degree of CH decomposition at various heating rates. The dehydration of C-S-H begins when cement-paste reaches a temperature of 105 °C (Bažant and Kaplan 1996) and it continues to do so up to a temperature of 800 °C. Based on the investigation of idealized cement paste, Harmathy (1970) calculated the degree of conversion of C-S-H at different temperatures. However, in a study on the changes in hardened cement paste at elevated temperature, Peng and Huang (2008) observed that C-S-H does not show any measurable decomposition up to a temperature of 560 °C. It is attributed by them to the continued hydration of unhydrated cement particles due to the favourable hygro-thermal condition. All of these phase transformations in cement paste contribute to the overall change in porosity. Since the hydration products usually occupies a larger volume than that of the original compounds in Portland cement (Bentz and Garboczi 1991; Mehta et al. 2006), the changes in capillary porosity of cement paste can be predicted at different temperatures by using appropriate thermal decomposition kinetic reactions (Zhang and Ye 2012; Zhao 2012).

Studies have established that the porosity of heated concrete follows a parabolic trend with an increase in the temperature. While the initial increase up to 550 °C is attributed to the inherent microcracks and the loss of physically and chemically bound water, the falling trend later, which occurs in the temperature range of 550–800 °C, is caused by the reaction of CaO with the silicates (Vydra et al. 2001). Luo et al. (2000) measured changes in porosity of concrete using mercury intrusion porosimetry (MIP) and concluded that porosity alone is not sufficient to explain the degradation in mechanical properties of heated concrete. In addition, Luo et al. (2000a) demonstrated that a greater ratio of changes in porosity occurs in high performance concrete (HPC) than in normal strength concrete (NSC).

High temperature exposure not only changes the total pore volume in cement microstructure, but also alters the pore size distribution. Chat et al. (2000a) studied the pore size distribution of NSC and HSC using mercury intrusion porosimetry (MIP) at different temperatures. They concluded that both the threshold diameter and critical diameter increase due to thermal degradation of pore structures. Others report a coarsening of pore sizes in cement paste as a result of high temperature exposure (Komonen and Penttala 2003; Rostásy et al. 1980a; Vodák et al. 2004). A study (Komonen and Penttala 2003) on the effect of polypropylene fibre on the microstructure of cement paste at high temperatures reported that the changes in pore size distribution were predominantly seen for pore sizes ranging below 100 nm. They also observed that the coarsening of pore size was significant at temperatures above 600 °C. They attributed the pore size coarsening to the dehydration of ettringite crystals. In addition, slightly finer pore structure was observed in the fibre reinforced paste compared to the plain counterpart.

However, it should be mentioned here that the aforementioned studies on pore size distribution were conducted using mercury intrusion porosimetry (MIP). It is important to note that the MIP method suffers from certain notable limitations which need to be considered when interpreting the results. The two most important limitations are i) the assumption of a cylindrical pore model and ii) a misrepresentation of larger pore fraction due to the so called "ink-bottle" effect (Aligizaki 2005; Diamond 2000; Scrivener et al. 2015). According to Diamond (2000), pore sizes reported from MIP method are several orders smaller than the actual sizes. Therefore, an image-based analysis, is a promising alternative technique to characterize the pore size distribution. But here, the pore size that can be resolved is limited by the magnification of the captured image.

3.4 Experimental Details

In order to study the changes in the microstructure of cement mortars, experiments may be setup with the specimen left either in the 'hot' state, or in the 'cold' state. Due to the difficulty in assessing the pore structure while the specimens remain in hot state, it was decided in this study to perform the experiments after the cooling of mortar specimens. This means that the experiments showed the residual characteristics of the microstructure. A brief description of the experimental procedures is presented in the following sections.

3.4.1 Materials

Cement-based mortar was used to characterize the microstructure at elevated temperature. In this research program, Type GU cement, a general purpose cement complying with CSA A3001 (2013), was used to prepare the mixtures. The oxide composition and the associated compounds, estimated based on Bogue Equation, of this cement is presented in the Appendix A. Note that Type GU cement is the most commonly used binder in concrete construction projects in Canada. Since the use of pozzolanic admixtures, such as fly ash and silica fume, is reported to have considerable influence on the microstructure of cement paste at post-cooling stage (Khoury 1992), it was decided to exclude any such admixtures.

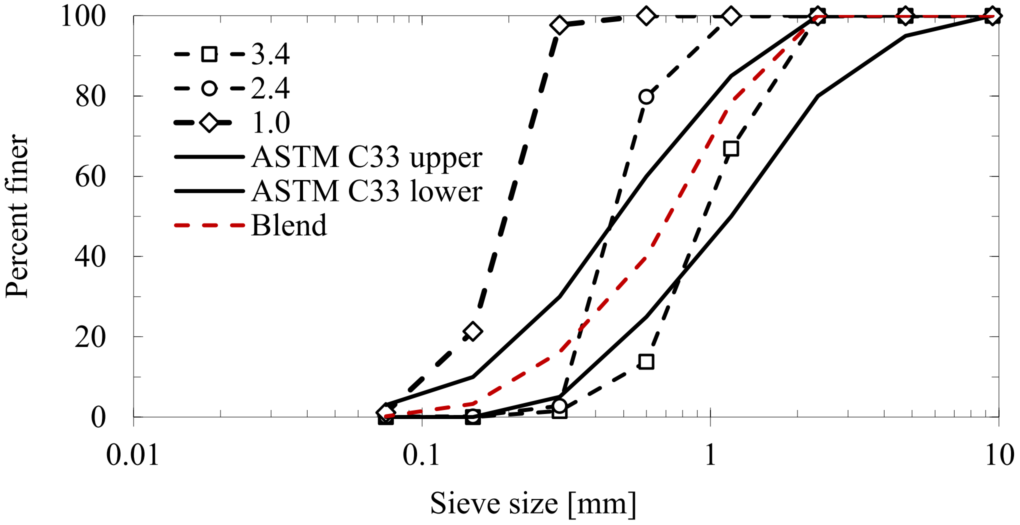

Figure 3.1 Grain size distribution of the fine aggregates.

Aggregates' mineralogical compositions are important when investigating the behaviour of cement-based materials at elevated temperature. Different minerals present in aggregates show different thermal response and thus have significant impact on the differential thermal expansion between aggregates and cement paste (Lamond and Pielert 2006). Therefore, in order to maintain the consistency in the mineralogical composition of fine aggregates, a commercially manufactured silica sand was used from a single source throughout this study. It contains 94% crystalline silica, 5% aluminum oxide, and 1% iron oxide, by mass. Similarly, the particle size distribution of the fine aggregate is crucial to the mixture composition as it determines the amount of cement paste required to fill space between aggregate particles. Therefore, a gradation of fine aggregate was chosen by blending three types of silica sand gradations, conforming to the guidelines provided by ASTM C33 (2003). The particle size distribution of the blended sand is shown above, in Figure 3.1.

It is well known that polymeric microfibre, besides reducing the early-age shrinkage cracks (Bentur and Mindess 2006), improves the performance of concrete during exposure to elevated temperature (Hager 2013). This influence is more noticeable in high performance concrete. Therefore, polyester fibres were added to the reference mixture at various volume fractions. This fibre melts at a temperature of 260 °C, and possesses a specific gravity of 1.35, a tensile strength of 970 MPa, and an elastic modulus of 15 GPa. The fibre was 50 µm in diameter with an aspect ratio of 240. The high aspect ratio of this fibre makes it potentially suitable for improving the spalling resistance by creating a connected network of reservoir to help release the vapour pressure build-up when concrete is exposed to elevated temperature (Hager 2013)

Fibres in cement-based systems tend to hinder the workability of the fresh concrete (Bentur and Mindess 2006). There are two ways to maintain the workability—either by adding more water or by adding suitable water reducing admixtures. However, the use of additional water in mixtures containing high dosage of fibres results in an inconsistent mixture proportioning. Thus, in this research program, an adequate amount of high range water reducing admixture was added to the mixture, so as to maintain the workability as measured by standard flow table test (ASTM C1437). After preliminary examination, a water-to-cement ratio (w/c) of 0.5 was chosen in order to achieve sufficiently strong cylinders that allowed for measurable residual mechanical properties after sustained exposure to the elevated temperatures. The cement to fine aggregate ratio was chosen at 1:3. The details of mixture proportions for the mortar specimens is shown in Table 3.1.

Table 3.1 Mixture proportions of the cement mortar

Materials	PT-0	PT-1	PT-2	PT-3
Type GU Cement [kg/m^3]	400	400	400	400
Fine aggregate [kg/m^3]	1200	1200	1200	1200
Water [kg/m^3]	200	200	200	200
WRA* [kg/m^3]	4	6	7	7
Fibre Type**	-	PT	PT	PT
Fibre volume fraction [%]	0	0.1	0.2	0.3

* WRA = Water reducing admixture
** PT = Polyester fibre

3.4.2 Specimen Preparation

Mortar mixtures were prepared using a rotary type mixing machine. The mixer has three components—a rotating mixing pan, a mixing blade, and a scrapping tool. The mixing blade is placed eccentrically which ensures adequate agitation of the ingredients. In addition, the mixer is equipped with controls allowing for variation of rotational speed.

First, the ingredients—blended sand and cement—were batched, measured, and pre-mixed using a hand trowel before transferring them to the mixing pan. Second, after agitating the sand and cement mixtures in the pan for 15 minutes in dry condition, approximately three-quarter of the total design requirement of amount of water was added and mixed for additional 20 minutes. Since the fibres have a tendency to clump together, the measured amount of fibres was gradually added while the mixing blade kept rotating. At the end of fibre addition, the remaining quantity of water was poured to the mixing pan and the mixing process was continued for another 15 minutes to allow for the optimal dispersion of the fibres.

The consistency of the mortar was measured using the flow table test conforming to ASTM C1437 (2013b). It was observed that the use of high range water reducing admixtures was able to compensate for the stiffening effect of the polyester fibres. The measured flow value for the plain mortar was 150–170 mm, while that for various fibre reinforced mortars were between 135–145 mm. This showed that the use of water reducing admixtures offset, to a good measure, the stiffening effects of polyester fibres.

Prismatic specimens (of size 50 × 50 × 200 mm) were cast with freshly prepared mortar. Before casting, the molds were sprayed with lubricating oil for easy demolding at a later stage. Casting was carried out in multiple layers, while the desired compaction of mortar was achieved through vibration. After casting, the molds were sealed to prevent the loss of moisture. At 24-hours after casting, the hardened mortar prisms were demolded and placed in a storage room, for curing, with a relative humidity of 95% and at an ambient temperature of 21 °C. After a 60-day curing period, the mortar prisms were sawn into 25 mm thick sections which were later exposed to different elevated temperatures.

3.4.3 Exposure to Elevated Temperature

It is seen that the rate of increase in the temperature inside the furnace has a considerable influence on the hygro-thermal response of the specimens. Depending upon the pore structure and internal moisture content, explosive spalling can occur at high heating rates. This is because the temperature, the vapour pressure and the thermal stress inside the specimen, all increase at a pace in excess of the specimen’s capacity to relieve these stresses. In other words, the thermal stress build-up will be far above the tensile strength of the material, thus resulting in a violent spalling of the specimen.

In an attempt to cause as much microstructural change as possible by increasing the heating rate, the temperature profile of the furnace has been programmed to achieve a heating rate of 20 °C/min. But, it was observed that the mortar specimens exploded violently at this rate of heating. Even reducing the internal moisture content by oven drying the specimens prior to sustained exposure to elevated temperatures did not prevent explosion. Thus, preliminary examination found a heating rate of 5 °C/min to be satisfactory for the mortar specimens used in this research. It is worthwhile to mention here that even at slower rates of heating, explosions are known to occur if the duration of exposure is long enough (Khoury 1992).

The dehydration of capillary and bound water in cement paste is a time dependent phenomenon. Thus, the duration of thermal exposure, also called soaking period, is important from the thermal equilibrium standpoint. Several factors influence the duration of exposure required for the specimen to reach equilibrium. These include rate of heating, moisture content, thermal properties of the material, porosity, and pore connectivity. Therefore, a sufficiently long exposure duration is necessary for adequate microstructural changes to occur that can be detected through the adopted experimental techniques. Consequently, for the purpose of studying the microstructure, a two-hour exposure duration was deemed sufficient.

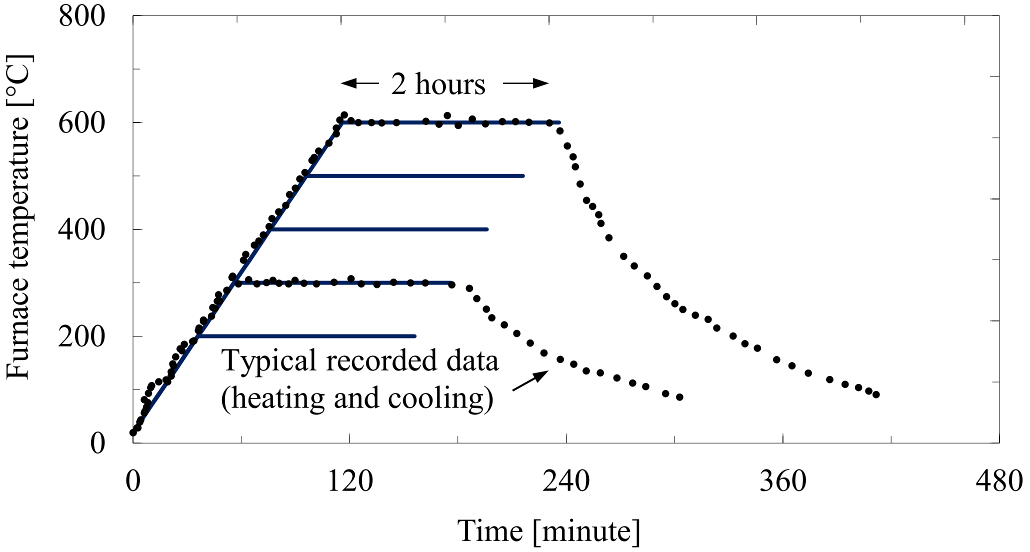

Figure 3.2 Temperature profile of the furnace as programmed and recorded.

After the soaking for the specified period, the specimens were allowed to cool down to examine their residual properties. The rate of cooling affects the porous structure of the heated specimen due to the fact that upon cooling the thermally decomposed compounds hydrates by reacting with the available atmospheric moisture. Cooling regime such as water cooling, immediately after thermal soaking, leads to a severe thermal shock causing considerable microstructural deteriorations. In this study, a natural ambient cooling was adopted so as to minimize the thermal shock and maintain a consistent rate of cooling of the specimens.

A furnace with a capacity of reaching a temperature as high as 1100 °C was used to heat the mortar specimens. It is equipped with a programmable micro-controller which allows the control of heating rate with a high degree of tolerance. Figure 3.2 shows the temperature profile, as programmed for different exposure temperature, of the furnace used to heat the mortar specimens. From the recorded data, it can be seen that the typical ramp and soaking stage fairly match the pre-programmed temperature profile. Also, to be noted is that the natural cooling regime takes about two to four hours, depending on the target exposure temperature (see Figure 3.2), for the specimens to cool down to the ambient temperature.

3.4.4 Porosity Measurement Using Displacement Method

Water displacement method is a convenient way of measuring the porosity of cement-based materials. In this method, the specimens were first oven dried at a temperature of 110 °C for 24 hours. The mass of the dry specimens was recorded at a temperature of 21 °C. Afterwards the specimens were immersed in water at 21 °C for 48 hours to allow saturation of pores. Subsequently, the water bath with the specimens was heated to 98 – 100 °C for 5 hours to help remove the entrapped air from the pore space and thus promoting water absorption. In order to determine the volume of the solids, the apparent mass and saturated surface-dry mass of the specimens were taken after cooling it down to a temperature of 21°C. By following the methods described in ASTM C642, the porosity of the mortar specimens were calculated using the following equations:

$$\varphi = \frac{g_2 - g_1}{g_2} \tag{3.1}$$

$$g_1 = \frac{X \cdot \rho_w}{C - D} \tag{3.2}$$

where ϕ is the porosity, g_1 is the bulk density, g_2 is the absolute density, X is the mass of oven-dried specimen in air, C is the mass of surface-dry specimen in air after immersion and boiling,

D is the apparent mass of specimen in water after immersion and boiling, ρ_w is the density of water.

3.4.5 Pore Size Distribution Using Nitrogen Sorption Method

Gas sorption method was used to determine the pore size distribution of micropores and mesopores. The rationale for using this method is that it enables examination of the influence of polyester fibre on the micropores of cement mortar. Adsorption of nitrogen onto the surface in the porous material occurs due to the van der Waals forces between nitrogen gas molecules and the surface of the solid.

When preparing specimens for nitrogen sorption, very specific requirements must be met in order to generate reproducible test results. Before starting nitrogen sorption, the specimen needs to be degassed to remove previously adsorbed gas molecules or any other surface contaminants. Degassing helps avoid the interference of these surface contaminants. In addition, the surface moisture has to be removed in order to accurately measure the pore volume of the specimen. This is usually achieved by using high temperature. However, use of high temperature, above 25 °C, is associated with decomposition of ettringite crystal which will alter the pore structure. In order to prevent this, an alternative degassing procedure that involves a vacuum source and an extended degassing period was used.

There are four steps in the nitrogen sorption method to determine pore size distribution. First, a small chunk of the fractured mortar specimen notably free from loose particles was weighed. Then, the specimen was placed into a degassing tube which was then transferred to the degassing station. The degassing was conducted at a temperature of 24 °C under vacuum for 12 hours. The specimen was weighed again after degassing which was used to calculate the normalized volume of the adsorbed nitrogen. Afterwards, the specimen was attached to the gas sorption station. Since low temperature promotes the adsorption process, the specimen tube was placed in a bath at a temperature of 77 K. An automated nitrogen sorption equipment was used which recorded the isotherm, the volume of nitrogen adsorbed along with the relative pressure at which the adsorption took place. The complete adsorption and desorption process took about 6 hours to complete. Using the methods described in Section 2.7.3, the isotherms were analyzed to obtain the cumulative and differential pore size distribution of the mortar at different elevated temperatures.

3.4.6 Setup for the Scanning Electron Microscopy

Image-based analyses are frequently used to quantify parameters of pore structure of cement-based materials. Scanning electron microscopy (SEM) is an ideal technique of capturing high resolution image for such analysis. Backscattered electron (BSE) detectors are used to take images because of BSEs ability to scatter from the deeper layers of the specimen. The details of the specimen preparation and image acquisition process are described below.

Cubic specimens having a dimension of 10×10×10 mm were cut from the corner of prismatic mortar bars to be used for SEM with BSE detectors. First, a low viscosity epoxy resin was impregnated into the specimen under vacuum and cured at a temperature of 21 °C for 24 hours. The purpose of epoxy impregnation is to support the microstructure against damage during polishing as well as shrinkage cracking that may occur afterwards. Second step is to expose the surface to be examined by grinding using mono-ethylene glycol. The exposed surface was then polished using successively finer polishers having diameters of 3, 1, and 0.25 μm.

The BSE images were obtained at an accelerating voltage of 25 kV. For each specimen 8–10 high resolution, 1024×768 pixel, images were captured by setting a working distance of 6 mm. The selected magnifications of each image set resulted a spatial resolution ranging from 0.1358 μm/pixel to 2.1354 μm/pixel.

3.4.7 Image Analysis

The intensity or gray value of SEM images depends on the molecular weights of compounds present in the specimens. Compounds with higher molecular weight, the solid components, produce brighter pixels and vice versa. The pore space, which is filled with epoxy resin, appear as relatively darker pixels compared to the solid portion of the specimen. By taking advantage of this difference in intensity, the porosity, pore size distribution, specific surface area, and especially, the fractality of concrete microstructure were determined from the analysis of SEM images.

It is essential that the captured SEM images are properly focused and the brightness values are consistent in each image. Therefore, images were obtained with the same level of brightness throughout the entire scanning session. In order to analyze the area fraction of each phase from SEM images, it was necessary to determine an appropriate threshold value of intensity that distinguishes the pores from solids. There are several methods to find the appropriate threshold for cement-based materials. It can be as simple as selecting a trial gray value while visually comparing the segmented pore regions with the original image. If the porosity of the specimen is known from any standard laboratory technique, then it can be used as a criterion for selecting the threshold. In this study, a method suggested by Wong et al. (2006) was adopted, where the threshold can be determined by finding the critical overflow point. In this method, as shown in Figure 3.3, a plot of the area of segmented pores against a set of trial gray values is created. The critical overflow point is the intensity value corresponding to the inflection point which is determined by calculating the intersection of the tangents on the two straight portions of the curve. It provided a more reliable way of selecting threshold pixel intensity and thus helps generate consistent binary images for the later stages image processing.

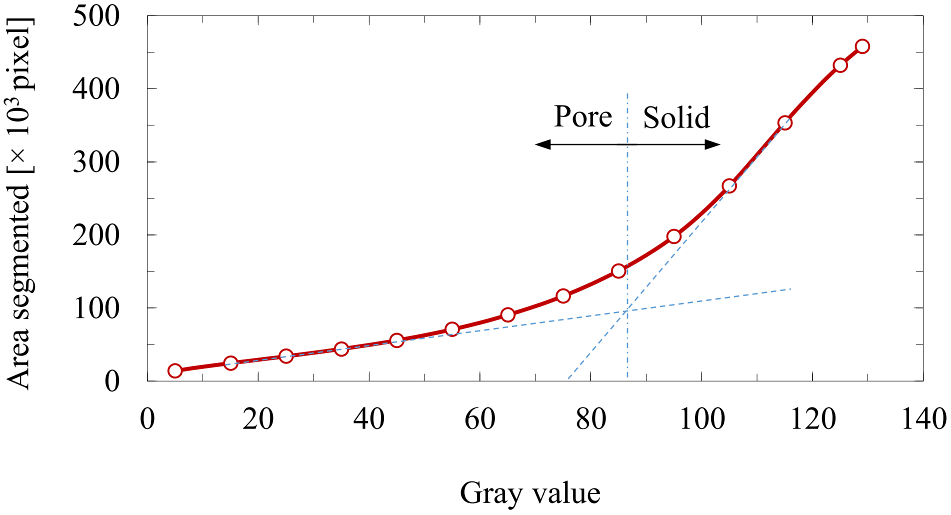

Figure 3.3 Threshold selection method for SEM images by finding the critical oveflow point.

3.4.7.1 Porosity Investigations

In order to compute the porosity of cement mortar, SEM images were first cropped to remove the extraneous regions of the images. Each image has a dimension of 1024×768 pixels. It is worth mentioning that the type of cropped images is 8-bit grayscale having an intensity value ranging from 0–255 where low intensity pixels represent the porous region of the specimen. Next, a threshold intensity value was determined for each image, using the procedure described in the preceding section, to convert the 8-bit gray images into binary images having intensity scale ranging from 0–1. In order to facilitate the pixel counting process, the binary images were inverted so that the pore pixels are represented by an intensity value of 1.A noise filtration process was then applied to remove the isolated single pixels from the images. Finally, using the intensity histogram the total count of the pore pixels was recorded. The porosity was determined by taking the ratio of the total number of pore pixels to area of the entire image.

It is to be mentioned here that a reliable porosity computation based on image analysis requires combining the results from several different images taken at different magnifications to encompass the contribution of a wide range of pore sizes. Accordingly, in this research work, porosities were determined by combining the pore fractions from three different magnifications namely—50×, 400×, and 800×. These chosen magnifications enabled this author to resolve a pore size as low as 0.1358 μm. And this was found to be sufficient to cover the range of pore sizes that are necessary to examine the thermally damaged mortar microstructure.

3.4.7.2 Pore Size Distribution Using Opening Method

It has been criticized that area histogram-based pore size distribution does not represent the pore structure of cement-based materials (Hu 2004; Scrivener 1989). Because of the interconnected nature of concrete microstructure, it is inappropriate to treat a two-dimensional pore feature as an individual object. Scrivener (1989) suggested that the pore size distribution based on Morphological Opening Operation could be a better alternative to the area histogram-based distribution approach.

Morphological opening is a combination of an erosion followed by a dilation operation. In this processing, a structuring element—a set of pixels of specified configuration—is used to inspect the input image. In erosion process, a pixel in the input image will be retained if, upon translation, the structuring element is completely contained within the input image. On the other hand, in the dilation process, a pixel will be in the output image if at least one pixel of the structuring element overlaps the input image. Mathematically, the opening operation is expressed as follows (Gonzalez 2009):

$$A \circ B = (A \ominus B) \oplus B \tag{3.3}$$

or

$$A \circ B = \bigcup \left\{ (B)_z \mid (B)_z \subseteq A \right\} \tag{3.4}$$

where $\ominus$ operator indicates erosion, $\oplus$ operator indicates dilation, A denotes the input image, B is the structuring element, $(B)_z$ denotes the translation of B. For complex interconnected structures such as long cracks and connected pores, features with smallest dimension less than the size of the structuring element is eliminated during the erosion step of the opening process. Similarly, the isolated features having overall size smaller than the structuring element is removed. Thus, the size of the structuring element provides a measure of pore size.

In this method, a disk shaped structuring element with increasing dimension was used to perform the opening operation on already binarized image. At the end of each operation, the size of the structuring element along with the pixel count of the pore features—normalized with respect to the total image area—is recorded. A plot of the size of structuring element against normalized pore area provides a type of size distribution of mortar at different exposure temperature. It is sometimes referred to as opening distribution. Scrivener (1989) reported that opening distribution provides analogous results as those from gas adsorption or calorimetric methods which are known to provide a realistic size distribution.

3.4.7.3 Number-Based Pore Size Distribution

From the measurement of pore areas, size distribution can be represented by plotting the number of pores against the size class. Now, the pore sizes can be estimated from the measured pore area by calculating the radii of equivalent circles. And a plot of the number of pores against pore size would give representative idea of the pore size distribution. But this is not a straightforward process for all the pore features especially for complex interconnected regions.

Therefore, the interconnected regions are first required to be separated by using morphological watershed operation. Two types of size distribution may be derived from plots of pore area versus size class—number of circular particles and number of spherical particles in each size class. The former is the outcome of sorting and grouping the pore areas according to their size class. The latter, on the other hand, requires estimation of number of spheres based on the probability of a plane intersecting a sphere of specified size class to produce areas of another size class (Underwood 1968).

Several methods are available to estimate the probable number of spherical pores from the two-dimensional area measurements. In this study, Saltykov's method (Russ and Dehoff 2012; Underwood 1968) was used to convert the number of area-based pores into the number of spheres per unit volume. The conversion was carried out using the following expression:

$$N_A(i,j) = N_v(j)\Delta\left[\sqrt{j^2-(i-1)^2}-\sqrt{j^2-i^2}\right] \tag{3.5}$$

where N_A is the number of areas of size class i from spheres of size class j, N_v is the number of spherical pores of size class j, Δ is the size interval.

3.4.7.4 Image Processing by the Two-Point Correlation Function

Another morphological image processing called the two-point correlation (TPC) function, otherwise known as autocorrelation function, can be used to characterize the mortar microstructure. It is defined by the probability of finding the end points of a randomly oriented line segment of known length on the phase of interest when translated on a two-phase system. In this case, the phase of interest is pore space. It starts with its maximum value at the origin and ends asymptotically, for overlapping pore space, with a value equal to the square of the pore fraction of the material. However, for the non-overlapping pore space, the end region of TPC function oscillates with a periodicity approximately equal to the pore diameter (Torquato 2002). Several useful parameters of mortar pore structure can be measured using TPC function—porosity, specific surface area, and characteristic pore size. The following equations describe how these parameters can be evaluated (Berryman and Blair 1986):

$$S_2(0) = \varphi \tag{3.6}$$

$$\lim_{r \to 0} \frac{dS_2(r)}{dr} = -\frac{s}{4} \tag{3.7}$$

$$\lim_{r \to \infty} \frac{dS_2(r)}{dr} = \varphi^2 \tag{3.8}$$

where $S_2(r)$ is the two-point correlation function, s is the specific surface area, r is the length of line segment or lag distance, ϕ is the pore area fraction.

At its simplest level, TPC can be evaluated by shifting a binary image with respect to its original image and counting the pixels in the intersected portion of the images followed by a normalization using the net image area. In this research, TPC function was evaluated using the procedure described by Berryman (1985).

3.4.7.5 Fractal Dimension

Fractal dimension describes the level of details that can be viewed with the change in scale of observation (Castaño et al. 1990). Image-based determination of fractal dimension of cement-based materials can be achieved either by using the *dilation method* or the *box-counting method*. In the dilation method, first, each pore feature in the binarized image is converted to single pixel outline. Then each contour is dilated gradually by a specified number of pixels. The perimeter of each dilated outline is then calculated. Dilation process is equivalent to the reduction in resolution (Lange et al. 1994). Finally, the slope of a plot of perimeter against the thickness of the contour is used to estimate the fractal dimension. However, this method is prone to incorrect determination of fractal dimension owing to the fact that open ended features introduces a sources of error due to the so called "cap effect" in which open ended lines are dilated incorrectly (Eins 1995). Therefore, in this study, box-counting method was chosen to determine the fractal dimension of pore space. The details of this method is discussed below.

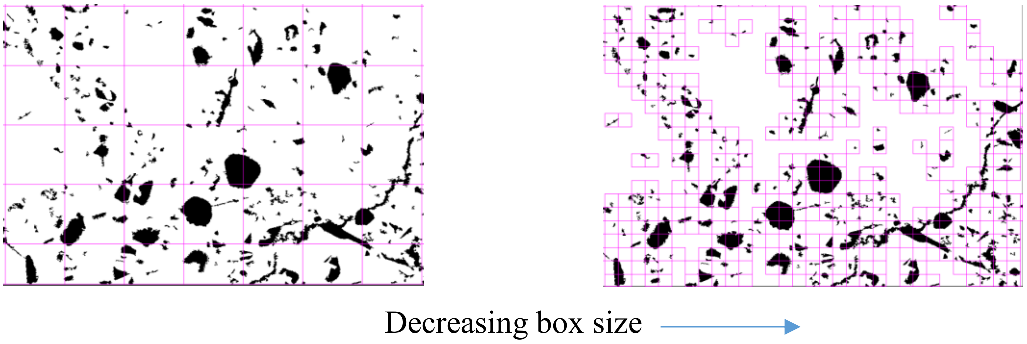

Figure 3.4 Box-counting method of estimating fractal dimension (only two example stages are shown).

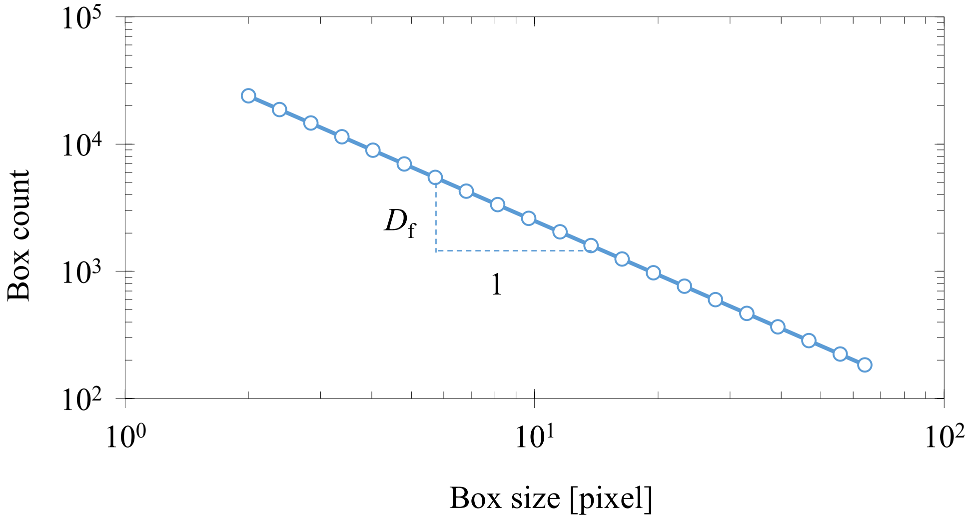

Figure 3.5 Determination of fractal dimension (D_f) using box-counting method.

The estimation of fractal dimension process starts with a binary image. First, a filter was applied to remove the isolated single pixels. The image was then covered with evenly spaced boxes of known side length, as shown in Figure 3.4 (left). Next, the number of boxes that covered the pore pixels was counted. Afterwards, the size of the boxes were then gradually reduced (Figure 3.4, right) and the corresponding number of boxes were counted. Notice that a decrease in the size of boxes results a gradual exclusion of the solid pixels. It is worth mentioning that the change in box sizes simulates a change in the scale of observation. Finally, as shown in Figure 3.5, the fractal dimension was determined by plotting the box count against the size of the boxes. The absolute value of the slope of this plot represents the fractal dimension of the pore space. In order to account for the effect of the orientation, the image was rotated incrementally by an angle of 15 ° and an average value of the slopes from all the scans was taken as the fractal dimension.

3.5 Results and Discussions

3.5.1 Porosity

Porosity of the mortar specimen exposed to different temperatures is shown in Figure 3.6. As described in Section 3.4.4 and Section 3.4.7.1, it was determined by following the procedure according to ASTM C642, herein referred to as the Displacement Method, as well as through processing of SEM images. It can be observed that the porosities increased from a value of 16% at 20 °C to 28% at 600 °C when determined using the water displacement method. It is noticeable that the ASTM procedure measured a significant change in porosity as the temperature increased beyond 300 °C. At its extreme, that is, at 600 °C the porosity increased by more than 75% compared to that at room temperature. On the other hand, SEM measurements showed a rather monotonic increase in porosity with the increase in temperature.

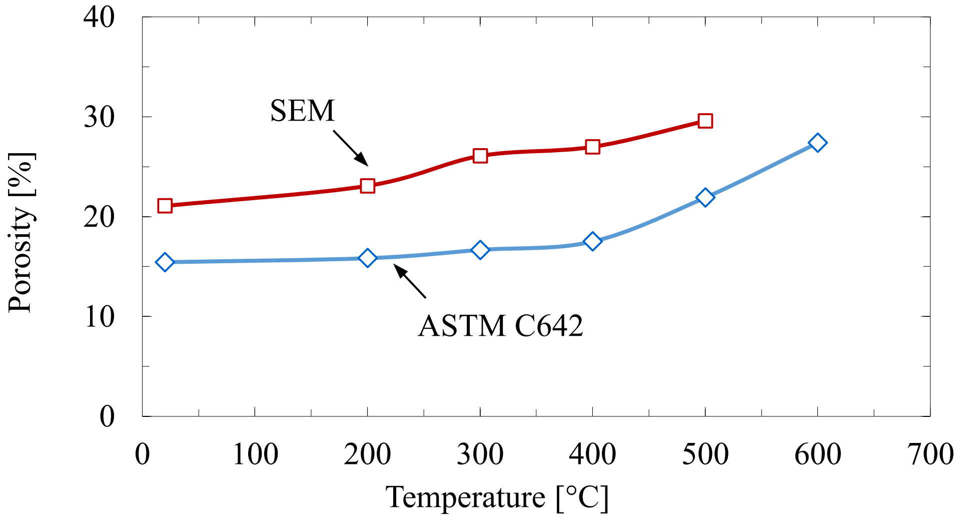

Figure 3.6 Porosity of cement mortar at different exposure temperatures as determined using SEM images and ASTM C642.

While the SEM image analysis limits the minimum pore size that can be detected with the available resolution, it is nevertheless capable of capturing the large cracks and air voids when results from several images having appropriate level of magnifications are combined. In contrast, porosity measurement using the displacement method includes capillary pores, pore size ranging from 10 nm to 10 μm depending on the degree of pore saturation that can be achieved under boiling condition. But this method is unable to include that fraction of the entrained air-voids in the cement-based materials (Bu et al. 2014). This explains why the SEM technique gives an apparently larger porosity than that from the displacement method (ASTM C642).

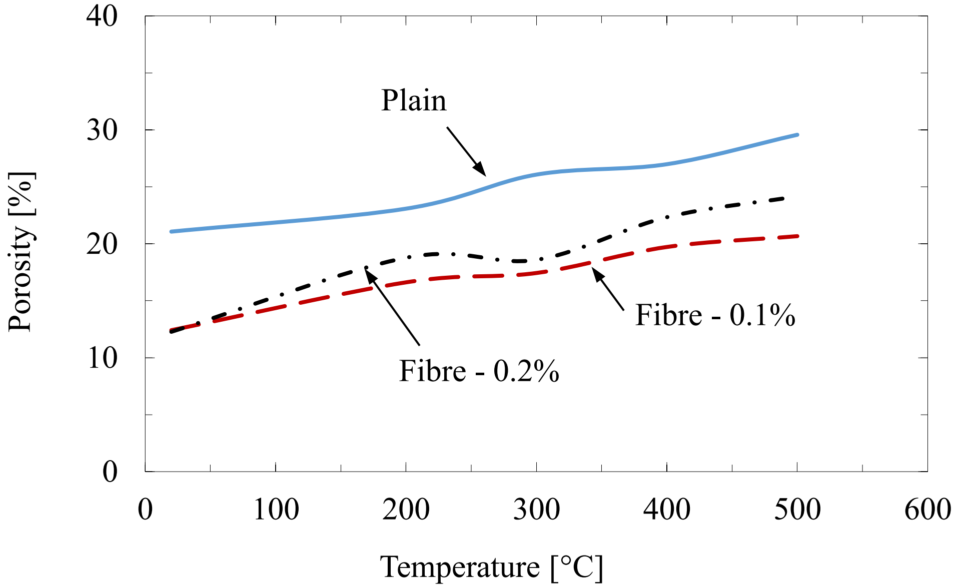

Figure 3.7 Effect of fibre content on the porosity of cement mortar at different exposure temperatures—based on SEM.

Elevated temperatures can increase the porosity either by increasing the pore volume (dehydration of capillary pore water) or by evaporation of the bound water in the crystalline and quasi-crystalline phases including the AFt, CH, and C-S-H fractions. With an increase in the loss of water giving way to steam pressure build up in its place, this pressure upon exceeding the tensile strength of the mortar, gives rise to microcracks surrounding the hitherto water containing pores. It registers as an increase in the pore volume. In addition, due to the incompatible thermal properties for the aggregate and the surrounding cement paste, thermal expansion of quartz particles being significantly in excess of the shrinkage of the surrounding bulk cement paste, microcracks develop at the aggregate-paste interface. But it is noteworthy that experimental observations have shown that this increasing trend of porosity does not hold true for a temperature beyond 900 °C (Vodák et al. 2004) at which point, the porosity decreases due to the phase transformation and sintering process, where a solidification of the dehydrated paste products occurs.

The effect of polyester fibre on the porosity of heated cement mortar is shown in Figure 3.7 along with that of plain mortar. The porosity of fibre reinforced, volume fraction of 0.1–0.2%, mortar was found to vary from 13% at 20 °C to 24% at 500 °C, with a slightly smaller value for mortars having low fibre dosage, as determined through image processing technique. It can be noticed that the porosities of the fibre reinforced mortar are considerably lower across all regime of thermal exposure when compared to the plain mortar. Despite an increase in capillary porosity, caused by dehydration, the reduced porosity for fibre reinforced mortar may be attributed to the lower amount of entrapped air content due to the presence of fibre and the reduction of capillary pores in the vicinity of fibre-matrix interface (Balaguru and Ramakrishnan 1988; Bentur and Mindess 2006; Pereira de Oliveira and Castro-Gomes 2011). Further discussion on the role of fibre reinforcement on the microstructure is presented in Section 3.5.5.

Although porosity is a rudimentary microstructural descriptor of cement-based materials, it is nevertheless useful in understanding the macro-level characteristics of the materials subjected to external loads. It plays an important role during the development of models to predict the physical properties. For instance, in conjunction with pore connectivity and tortuosity, porosity can be used to predict the fluid transport phenomena, thermal properties, and mechanical properties of cement mortar. Thus, it assumes an important role in the design of mortar and concrete.

3.5.2 Modelling of the Changes in Capillary Porosity

Changes in the microstructure of cement mortar occur when subjected to sustained elevated temperature due to the thermal decomposition of crystalline hydration products. Thus, by estimating the degree of decomposition of these crystalline products, the loss of water can easily be determined from the appropriate stoichiometric relationship. The changes in capillary porosity—pores having a diameter of 10 nm to 10 μm—can be estimated by accumulating the contribution of newly transformed pore space from different constituents of cement paste (Zhang and Ye 2012; Zhao 2012).

The estimation of the changes in capillary porosity is described below in several steps—determination of initial volume fractions of hydrations products, calculation of degree of hydration before thermal exposure, quantification of thermal decomposition of the hydration products, and estimation of the residual capillary porosity.

As mentioned earlier, a CSA Type GU cement was used in this study. The oxide composition of the cement was used to calculate the mass composition of the compounds—C_3S, C_2S, C_3A, and C_4AF—by using the Bogue calculation procedure; a set of equations that provides a simplified way of calculating the compound composition of the cement. From the experimental data it is established that at 100% degree of hydration 1 g of cement produces 0.68 cm^3 of hydration products (Hansen 1986; Mindess et al. 2003). In other words, for a known degree of cement hydration, the total volume fraction of hydration products can be determined using the water/cement ratio of the mixture, which is shown in the following equation:

$$P_{hp} = \frac{0.68\alpha}{\frac{w}{c} + \frac{1}{\rho_c}} \tag{3.9}$$

where P_{hp} is the volume fraction of the hydration products, α is the degree of hydration, ρ_c is the density of cement in g/cm^3.

At this point, the volume fractions of the individual hydration products can be calculated using appropriate stoichiometric relationship. From the hydration reactions, it has been shown that each gram of C_3S produces 0.95 g of C-S-H and 0.42 g of CH, each gram of C_2S produces 1.26 g of C-S-H and 0.13 g of CH, and each gram of C_3A produces 4.64 g of AFt (Mindess et al. 2003). In order to convert these mass fractions into volume fractions, the specific gravity of C_3S, C_2S, C_3A, AFt, CH, and C-S-H were taken as 3.15, 3.28, 3.03, 1.78, 2.24, and 2.0 respectively. The initial capillary pore volume fraction can then be expressed in terms of the volume fraction of solid reaction products as well as unhydrated cement fractions. The degree of cement hydration was determined by substituting the measured capillary porosity into Equation 3.9.

During the exposure to elevated temperatures AFt, CH, and C-S-H undergo decomposition and release water molecules—adsorbed physically or bonded chemically to the aforementioned products—in the form of vapour. This dehydration of water from the crystalline structures results an increase in the capillary pore volume of the paste. Furthermore, the decomposition of C-S-H transforms the small mesopores and interlayer micropores, 0.5–10 nm in diameter, into capillary pores (Mindess et al. 2003; Zhao 2012). The kinetics of thermal decomposition—which relates the degrees of decomposition, temperature, and heating rate—can be expressed using Arrhenius equation as follows (Zhao 2012):

$$\frac{d\beta}{dt} = A_0 \exp\left(-\frac{E_a}{RT}\right) f\left(\beta\right) \tag{3.10}$$

where β is the degree of decomposition, A_0 is the pre-exponential factor, E_a is the activation energy, R is the universal gas constant, and T is the temperature.

For AFt and CH dehydration kinetics, appropriate numerical values of the relevant parameters defining the kinetics can be found in the literatures (Pourchez et al. 2006; Zelić et al. 2002). The degree of decomposition, β, can be determined for a given rate of heating and exposure temperature by numerically solving the abovementioned differential equation. It was evaluated for each phases by using appropriate values of pre-exponential factor and activation energy. However, for C-S-H, the experimentally determined residual amount was used to estimate the rate of decomposition from the work of Peng and Huang (2008).

The temperature at which the decomposition begins depends on the molecular structure of the constituents. For instance, AFt starts to lose water when it reaches a temperature of 70 °C and the conversion of CH does not occur before 430 °C. Even though C-S-H dehydration triggers at about 110 °C, the measurable decomposition can be observed only when the temperature reaches about 560 °C (Peng and Huang 2008). It implies that the fraction of the decomposed C-S-H that occurs prior to reaching the aforementioned temperature cannot be captured from experimental data.

Once the degree of conversion is determined, the volume fraction of water released at a given temperature can be calculated using the following equation:

$$P_w = M\beta m \tag{3.11}$$

where P_w is the volume fraction of water released, M is the molar ratio of the constituents to that of 1 cm^3 of water, m is the quantity of water dehydrated in moles from each mole of the constituents. Upon adding the contribution of the capillary pore fraction from the constituents, the changes in mortar porosity due to elevated temperature can be determined.

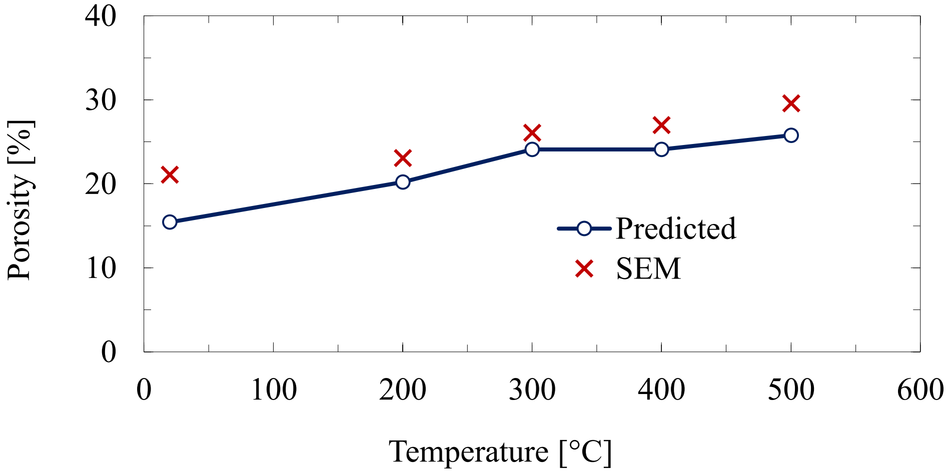

Figure 3.8 Mortar porosity from the stoichiometric prediction of residual capillary porosity at different temperatures.

The predicted porosity calculated based on the aforementioned procedure is shown in Figure 3.8. Note that the porosity from the SEM analysis generally agrees with that from the prediction. The apparent discrepancy, which is small, is due to the fact that image analysis considers microcracks and voids larger than capillary pores. Since this model only captures capillary pores, its application is limited to mortar exposed to a temperature not exceeding 600–700 °C, owing to the fact that at higher temperatures significant amount of microcracks usually develops in the mortar.

3.5.3 Number-based Pore Size Distribution

Frequency distribution of particulate matters is conventionally utilized to describe their pore structures. The same concept can be applied to the pore structure of the mortar. In the two-dimensional (2D) distribution, it is simply the number of pores that fall within certain size interval. On the other hand, the three-dimensional distribution (3D) is a probabilistic measure of the number of equivalent spheres within the size interval. It can be estimated based on the probability of producing a circular area of given radius by a two-dimensional section-cut through a polydispersed system of spheres. Both of these distributions rely on the assumption that the microstructure of the mortar comprised of spherical pores.

The frequency distribution of the mortar pore system is shown in Figure 3.9. Since a continuous size distribution would be rather impractical and too difficult to interpret, a discrete distribution is preferred, where the equivalent radii were calculated by grouping the histogram area distribution into 15 different of size classes. From a comparison of the 2D and 3D distribution, it can be stated that the 2D distribution underestimates the number of pores having a diameter below 2.7 μm. In addition, based on the 2D data, the calculated mean diameter of the non-symmetrical histogram is 3.53 μm; indicating a right-skewed distribution. Thus, as with any particulate system having a significant number of small pore features, one may use log-normal distribution to describe the pore structure of the mortar. It can be noticed that only one typical number-based distribution from plain mortar at 20 °C is shown. Note that a simple frequency distribution does not reflect the true nature of the microstructure of cement-based materials (Hu 2004; Scrivener 1989). A more appropriate approach, therefore, is to investigate the pore structure based on morphological image processing such as opening method of pore size distribution. This approach is adopted in this study and presented in the following section.

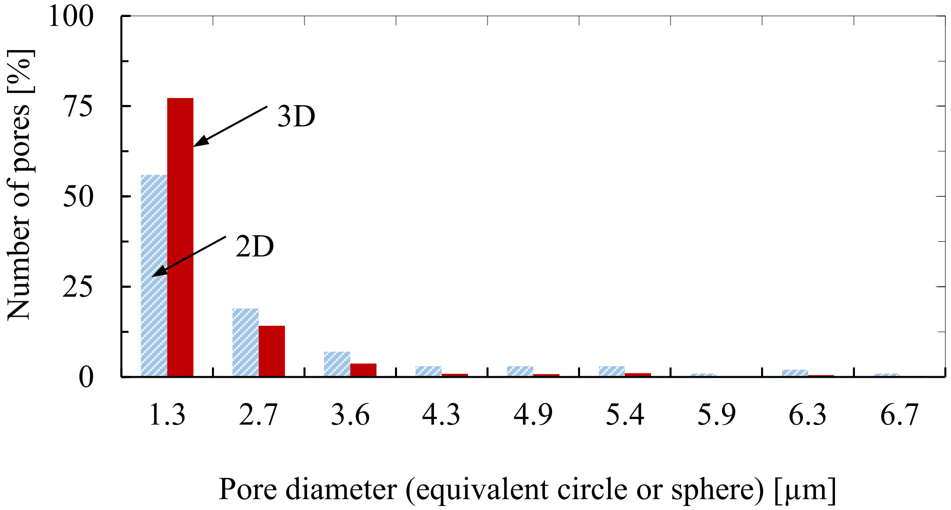

Figure 3.9 Number-based pore size distribution of plain mortar at 20 °C from image analysis.

3.5.4 Pore Size Distribution Using Morphological Opening Method

Morphological image processing is a powerful tool to investigate the microstructure of the mortar subjected to sustained elevated temperature. The morphological opening operation is a combination of the erosion and the dilation process on a binary image comprising only pore phase. As mentioned in the Section 3.4.7.2, in each step of opening operation, pores smaller than the size of the structuring element are removed from the image and thus providing a cumulative area fraction of pores having a size smaller than the size of the structuring element, also known as the kernel.

Given the complex and interconnected nature of the pore system of cement-based materials, area histogram-based size distribution is unable to reveal the true nature of the microstructure. The morphological opening method has the potential to provide a more realistic pore structure as opposed to simple area-based and hence number-based pore size distribution. In fact, a comparison between the aforementioned two methods showed that area histogram-based method over estimates the larger pores (Hu 2004). It has also been reported that the Opening Method provides results which are in better agreement with Wood’s metal intrusion porosimetry—a method capable of producing a more reliable size distribution, albeit requiring a complex experimental protocol (Abell et al. 1999; Hu 2004; Scrivener and Nemati 1996; Willis et al. 1998).

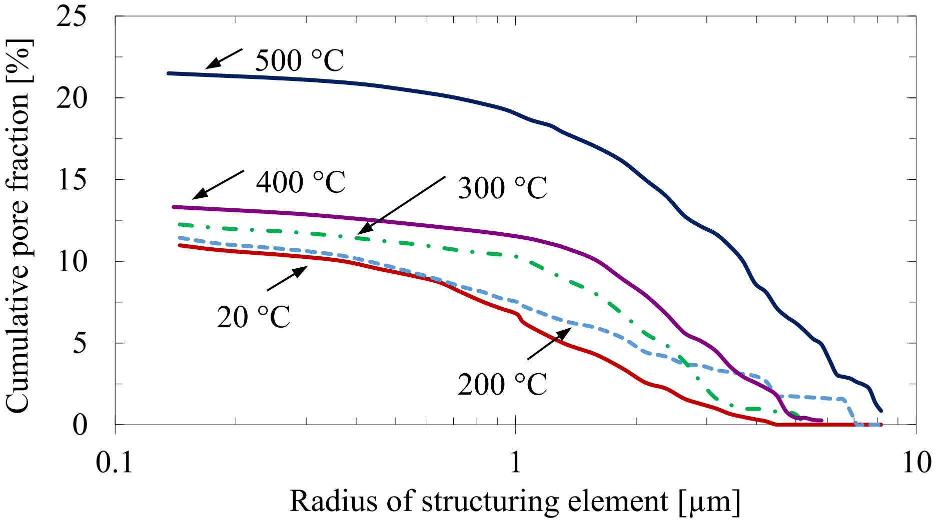

Figure 3.10 Pore size distribution of plain mortar using the opening method.

Despite severe limitations as reported by Diamond, (2000), mercury intrusion porosimetry (MIP) is a widely used technique to study the pore structure of cement-based systems. Note that MIP underestimates the larger pores due to the well-known 'ink-bottle' effect. Although MIP is capable of capturing the size distribution for a wide spectrum of pore sizes, in this research it was decided to employ an image-based method in an attempt to avoid those shortcomings associated with MIP. Image-based analysis is, however, limited in terms of the size of detectable smallest pores due to the limitations on the resolution of the captured images through SEM. However, since the exposure to elevated temperature generally alters the capillary pores size between 50 nm to 10 μm in diameter, image analysis method is still a viable approach to investigate the mortar pore structure at elevated temperatures.

Figure 3.10 shows the pore size distribution, based on the opening method, of plain mortar exposed to different temperatures. Results were combined from the analysis of SEM images having two different magnifications which allowed resolving pores as small as 0.14 μm in diameter. It can be noticed that the total detectable porosity of the mortar increased from 11% at 20 °C to 21% at 500 °C; an almost 100% increase in porosity. This increased porosity can be attributed to the dehydration of paste components and microcracks that developed due to the hygro-thermal process. While a relatively smaller increment in the porosity was observed at an exposure temperature up to 400 °C, a significant rise in porosity was observed by an exposure temperature beyond 400 °C. Upon a closer examination at those plots, one may notice that the median pore radius has increased from about 1 μm at 20 °C to about 4 μm at 500 °C, implying a coarsening of the overall pore system. The coarsening effect is further discussed using the differential pore area fraction toward the end of this section.

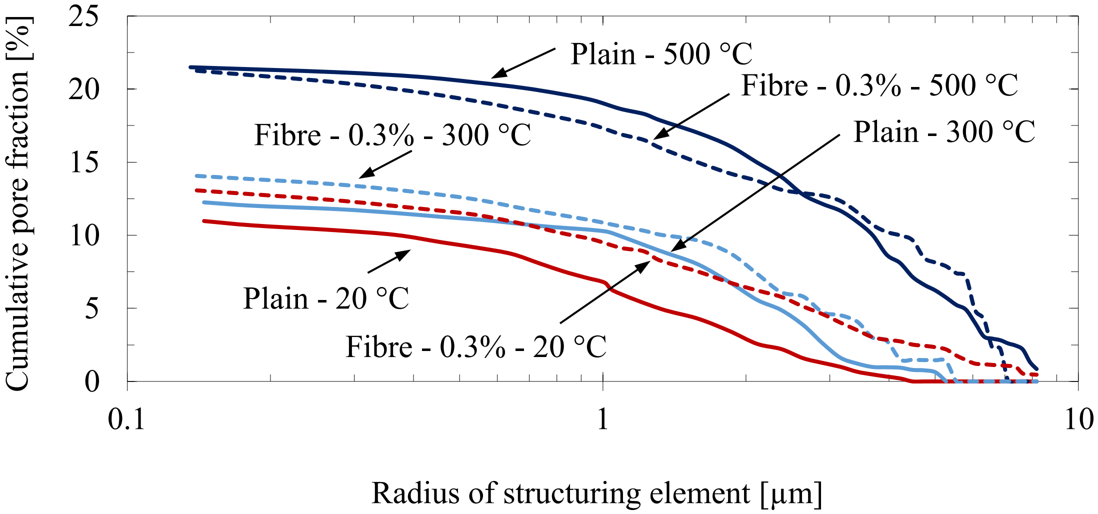

Figure 3.11 Comparison of the pore size distribution of plain and fibre reinforced mortar using the opening method.

The effect of fibre reinforcement on the pore size distribution is shown in Figure 3.11. Notice that the porosity, as indicated by the peak value of the plots, of fibre reinforced mixtures is slightly higher than the plain ones particularly at lower temperatures. This is in direct contrast with the results presented in Figure 3.7. This apparent mismatch can be explained by noting that Figure 3.7 reported the total porosity, only a fraction of which consists of slightly larger air-voids. The volume fraction of these air voids tend to diminish with the inclusion of microfibres (Bentur and Mindess 2006). As is to be expected since the very object of introducing fibres is to arrest void formation. Accordingly, it could be seen that at elevated temperature, the observed trend of pore size distribution is otherwise similar to that for plain mortars.

The differential pore size distribution for the mortar exposed to different temperature is shown in Figure 3.12. The pore radius associated with the peak differential pore fraction, of each plot, is the inflection point of the distribution. It may also be referred to as the critical radius of the pore system. For cement-based system, the critical radius, mean radius and median pore radius are in close proximity (Aligizaki 2005; Mindess et al. 2003). From percolation point of view, this critical pore radius may also be interpreted as the maximum radius of pores that are continuously connected.

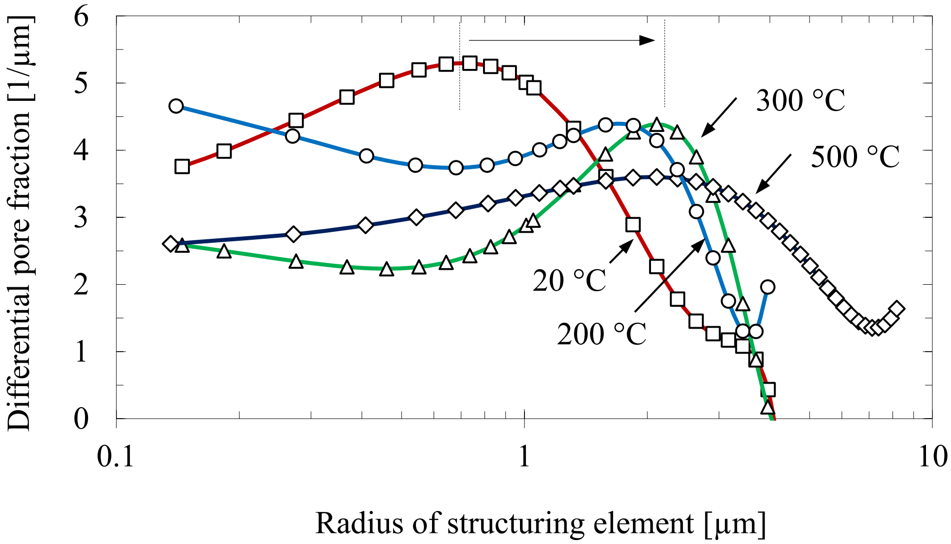

Figure 3.12 Differential pore size distribution of the plain mortar at elevated temperatures using the opening method.

In this study, the critical pore radius was found to vary from 0.74 µm at 20 °C to 2.1 µm at 500 °C of exposure temperatures. This coarsening effect—shifting of critical pore sizes towards the larger sizes—can be attributed to the thermal decomposition of CH and C-S-H present in the hydrated cement paste. Since all the specimens were oven-dried at 105 °C, the effect of

AFt conversion would have already transformed the microstructure of the paste. Furthermore, this study revealed that increasing the exposure temperature from 300 °C to 500 °C did not result in any significant coarsening of the pore size. This agrees with the results reported by Khoury (1992). As the coarsening of pores occurs through the conversion of C-S-H, the gel-to-space ratio decreases (Mitchell 1953). It must be emphasised that the implication of this modification in the pore structure is a definite reduction in the compressive strength of the mortar.

3.5.5 Two-Point Correlation Function

Spatial correlation is an elegant method for characterizing the evolution of the microstructure of cement mortar subjected to sustained elevated temperature. The two-point correlation (TPC) function for pore space is defined as the probability of two points, at a specified distance, lying within the pores. TPC function can be intuitively described as the degree to which features of a binary image overlap when a copy of it is shifted relative to the original. It is particularly beneficial for images where individual measurement of the said features is not feasible (Russ and Neal 2016), as in the case of cement-based system. As shown in Figure 3.13, several pore structure parameters—porosity, specific surface area, and mean pore size—can be directly determined from simple image processing. The maximum value of TPC at a distance, $r = 0$ measures the porosity of the mortar, while the slope of the plot at that distance provides a measure of surface area of pore-solid interface per unit volume. The details of the mathematical derivations related to TPC can be found in the literatures (Berryman 1985; Berryman and Blair 1986; Blair et al. 1996; Torquato 2002).

The TPC functions for the plain mortars heated to different temperatures in this study are shown in Figure 3.14. The plots were prepared by processing SEM images having a resolution of 0.2636 μm/pixel. Since the microstructural transformation of the mortar specimens predominantly takes place within the capillary pores, the aforementioned resolution will suffice for the purpose of this study. From the TPC plots, it can be observed that the peak values increase with an increase in temperature, reflecting an increased level of porosity caused by the increased amount capillary voids and other microstructural damage sustained by the mortar. One other interesting feature of these TPC functions is the monotonic nature of the asymptotic region, associated with larger value of *r*, indicating the interconnected nature of the pores in the mortar. According to Berryman and Blair (1986), the value of the distance, *r*, at which the correlation function, $S_2(r)$ approaches its asymptotic value (square of the pore area fraction, ϕ^2), indicates the mean size of the solid particles.

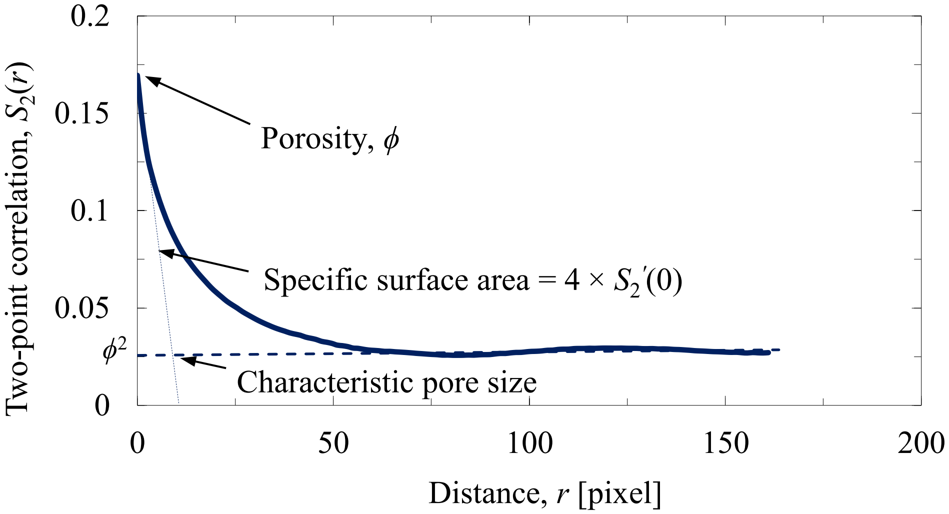

Figure 3.13 Pore structure parameters from the two-point correlation function.

As illustrated in Figure 3.15, the specific surface areas (SSA) extracted from TPC functions are plotted against the exposure temperatures for the plain and fibre reinforced mortar. For the plain mortar, SSA increase up to a temperature of 300 °C followed by a slight reduction at 400 °C. This phenomenon may be attributed to the additional surface area contributed by the conversion of gel pores into capillary pores, which decline due to the coalescence of pores when exposed at temperatures higher than 300 °C. This is most likely due to the coarsening effect. On the other hand, the SSA in fibre reinforced mortar remains largely unaltered throughout all thermal exposure. The most probable explanation regarding this behaviour would be the counteracting effect of the presence of fibre by minimizing thermal damage. It is to be noted however, that these estimations are based on 2D images. As discussed in a later chapter, while the general trends remain identical, one should expect a somewhat skewed outcome with a 3D estimation.

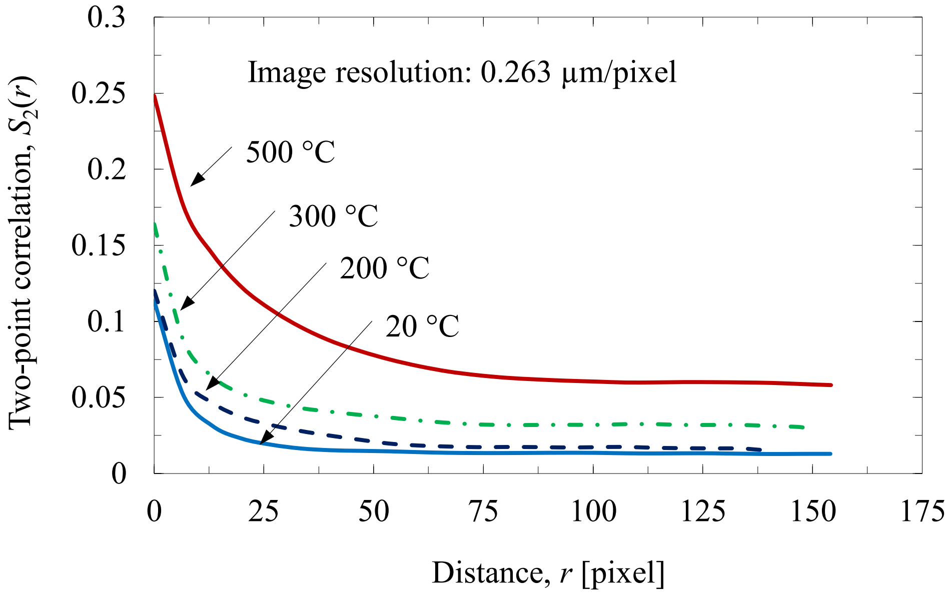

Figure 3.14 Two-point correlation function of the plain mortar at different exposure temperatures.

Unlike MIP or nitrogen sorption method, SSA estimation from TPC function does not require any assumption regarding the pore geometry, which makes it a more reliable alternative technique to characterize the pore structure of cement mortar. The estimated SSA can be interpreted as a measure of the roughness of pore-solid interface which has implications on the transport properties of the material. Furthermore, it has been shown that SSA can be correlated with the fracture mechanical properties such as critical crack length of concrete (Lange et al. 1994). A discussion on this aspect of the microstructure is presented in a later chapter of this thesis.

As mentioned earlier, the tangent of TPC plot at the origin, at zero separating distance, intersects with $S_2(r) = \phi^2$ line and thus provides the characteristic pore radius, r_c, of the mortar microstructure; a morphological estimate of the effective pore size. It is worth noticing that, with the increase in temperature, these slopes are gradually shifting towards the right hand side where the separating distance, r, is increasing. The calculated values of characteristic pore radii were plotted against temperatures, as shown in Figure 3.16. The radius is increasing from 2.3 µm at 20 °C to 3.3 µm at 500 °C for the plain mortar. Also notice that only a marginally higher value in the characteristic radius resulted for an exposure temperature beyond 200 °C, in the case of mortar with fibre incorporation.

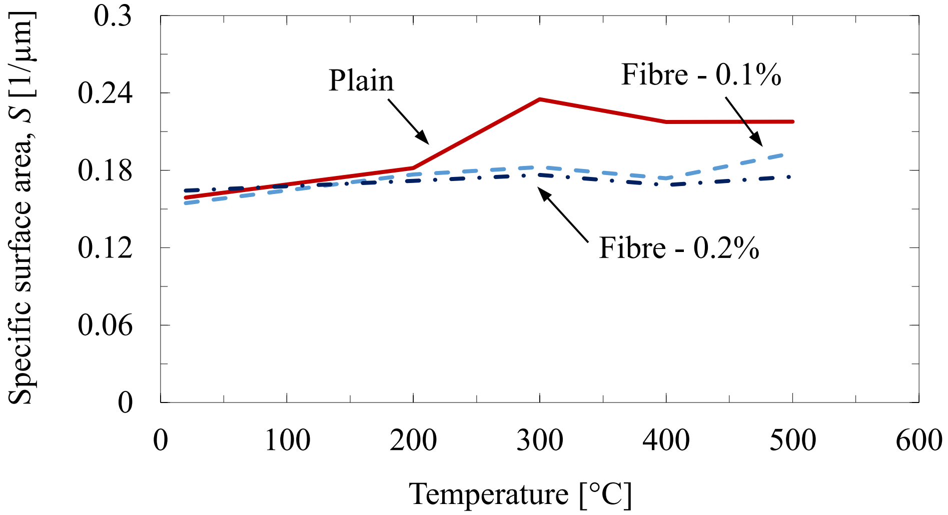

Figure 3.15 Specific surface area of the plain and fibre reinforced mortar determined using two-point correlation functions.

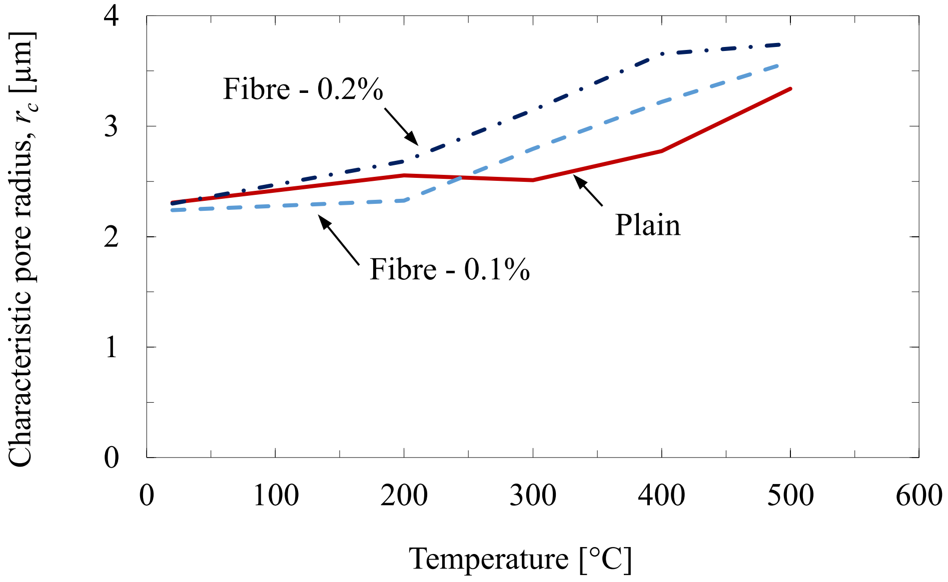

Figure 3.16 Characteristic pore radius determined using two-point correlation functions.

From the morphological point of view, the characteristic pore radius, r_c, indicates that the probability of finding a line segment lying on the pore space, having a length smaller than r_c, is positively correlated. This is particularly true for a system such as cement-based mortar having overlapping regions of solid hydration products. As described in a later chapter of this thesis, this transformation of pore structure has a bearing on the residual mechanical properties of the mortar. Furthermore, the value of r_c can be regarded as the mean pore radius of the mortar. These radii were found to be similar to the median pore radii that were estimated from the pore size distributions presented Section 3.5.4.

3.5.6 Pore Size Distribution from Nitrogen Sorption

The size distribution of mesopores and micropores provides us information that helps understand the structure of hydrated products of cement paste at elevated temperatures. Nitrogen sorption technique is a convenient way to examine the pore size distribution at such fine microscopic levels. To this end, after acquiring nitrogen sorption isotherms at 77 K, they were analyzed using BJH method (Barrett et al. 1951) to determine the cumulative pore size distribution. The analysis can be performed using both adsorption and desorption isotherms. However, due to the lower free energy state caused by lower relative pressure, determination of pore volume using the desorption isotherm is generally preferred.

The cumulative pore size distribution from BJH calculation is shown in Figure 3.17. The use of nitrogen as the adsorbent allowed the analysis of pores from a radius of 0.3 nm to 300 nm. Porosity of the cement mortar within the stated size range was found to vary from 1.5% to 2%. It can be noticed that the elevated temperature resulted an increase in the porosity through the decomposition of CH and C-S-H. Also notice that slightly higher pore volume was measured at 300 °C when compared to that at 500 °C. This apparent anomaly may be attributed to the difference in the prevalent hygro-thermal state of the specimen which may have caused favourable temperature distribution towards increased dehydration. Also, note that these results are based on single measurement from each exposure.

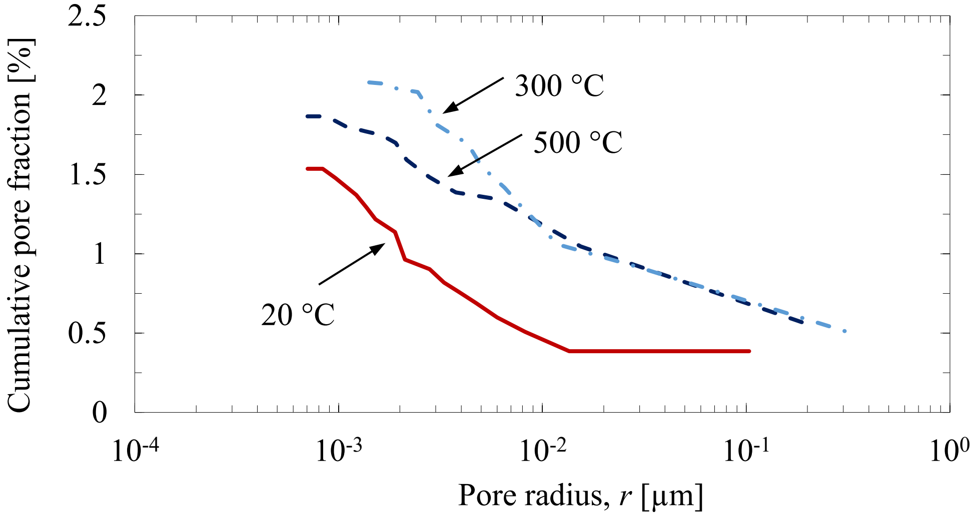

Figure 3.17 Pore size distribution of the plain mortar using the nitrogen sorption method.

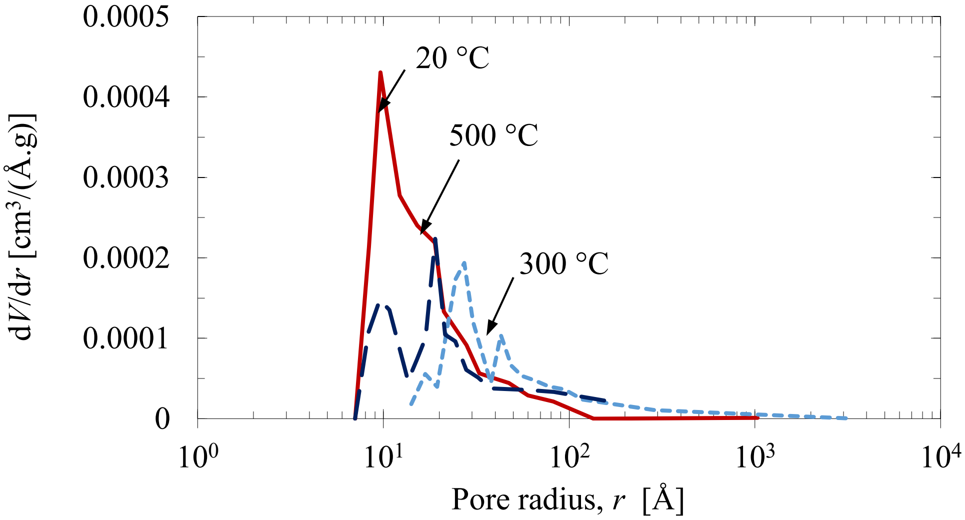

Figure 3.18 Differential pore size distribution of the plain mortar from the nitrogen sorption method at different temperatures.

In order to describe the changes in the critical pore size, the differential size distribution is shown in Figure 3.18. The critical pore radii for the heated mortar containing no fibre reinforcement were found to be 0.96, 2.72, and 1.9 nm for an exposure temperature of 20 °C, 300 °C, and 500 °C respectively. Once again, a shifting of the critical pore radius towards the right hand side, i.e., an increasing pore size, indicates a coarsening of the overall pore structure. This implies a lower macro-mechanical performance such as a reduction in load carrying capacity of the material owing to the well-established correlation between the strength and mean pore radius (Jambor 1973).

Microfibre reinforcement is known to alter the pore structure of concrete considerably. The characteristics of the fibre determines the nature of the transformation. Some fibre type improve the durability properties while others make concrete withstand high temperature by enhancing the spalling resistance of concrete. In order to investigate the influence of fibre reinforcement, the cumulative and differential pore size distribution are shown in Figure 3.19 and 3.20, respectively. It can be observed that at a given pore radius, especially at coarser level, cumulative pore volume in the fibre reinforced mortar is higher than the plain mortar.

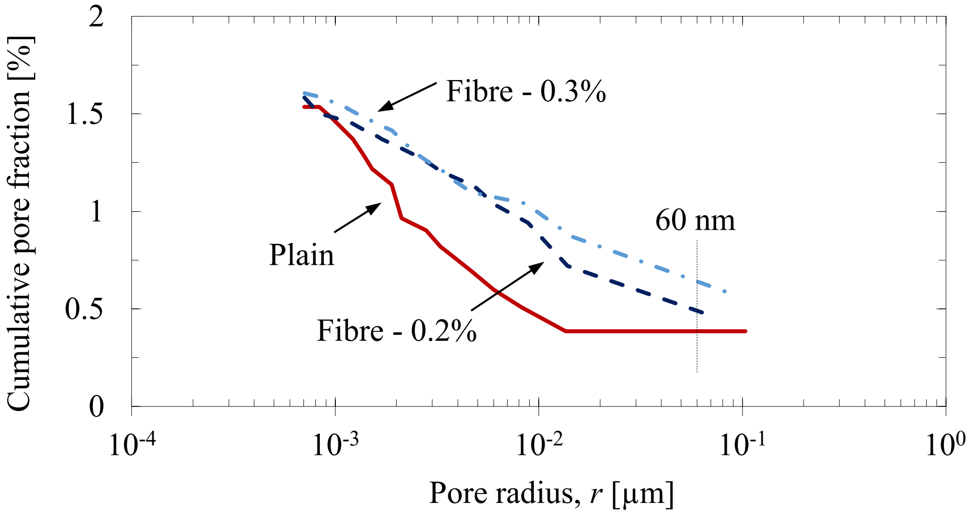

Figure 3.19 Effect of fibre on the pore size distribution using the nitrogen sorption method at 20 °C.

Fibre reinforced cement-based materials are known to improve the resistance to spalling at elevated temperature. There have been many theories surrounding the mechanism of this increased resistance due to the addition of fibre. Some researchers speculate it to be the increased *reservoir space* created after melting of fibres. However, it has been theorized that it is the space at the interface between the fibre and the matrix that causes the improvement as a result of the lack of affinity between the two (Khoury et al. 2008). Therefore, the increased pore volume of fibre reinforced mortar can be of a useful finding towards explaining the mechanism of fibre. However, it is to be noted that, in addition to pore connectivity, only pores having a radius of 60 nm or larger are of interest as far as the fluid transport phenomenon is concerned (Neville 2011).

The addition of polyester fibre was found to increase the critical pore radius, as shown in Figure 3.20, indicating a coarsening effect similar to that described in Section 3.5.4. The critical pore radius increased from about 1 nm to 2nm. Although the transformation of pore structure at this level does not influence the properties associated with moisture transport, it is useful when interpreting the mechanical properties.

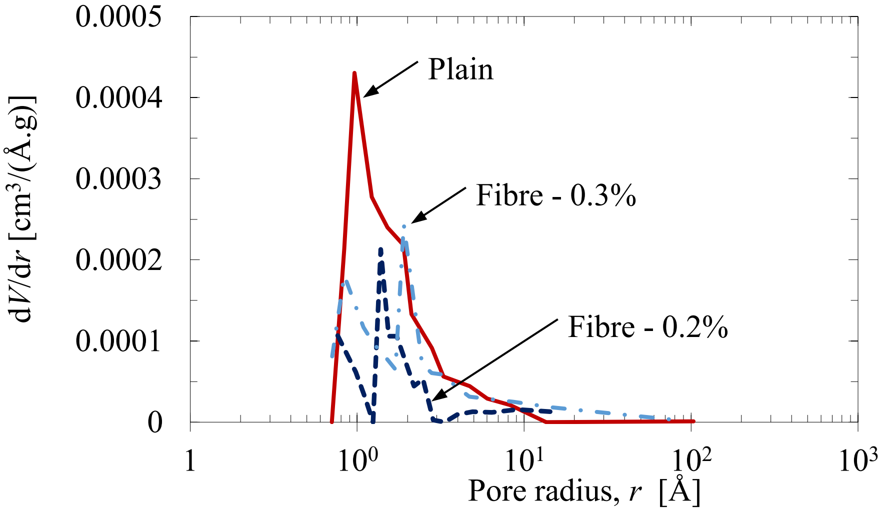

Figure 3.20 Effect of fibre on the differential pore size distribution of mortar evaluated using the nitrogen sorption method at 20 °C.

A study on the effect of cellulose microfibre on the pore structure parameters by Banthia et al. (2012) demonstrated a contrasting behaviour in terms of critical pore radius, where a pore refinement was occurred. In order to explain this phenomenon, the authors hypothesized that the moisture absorbed by the cellulose fibre during the mixing—due to its hydrophilic characteristics—made available at a later stage for a continued hydration and thus refining the pore radius. The same hypothesis is not applicable to the current study on account of the fact that hydrophobic type fibres, such as polyester, have a very poor water absorbency. Therefore, to explain the pore coarsening, one needs to consider the presence of interfacial zone in the mortar. As with any other inclusions to cement paste, monofilament type fibre introduces a relatively coarser porous zone in the vicinity of the inclusion. It is likely that this zone may have contributed to the observed coarsening effect.

3.5.7 Fractal Dimension

Fractal dimension (FD) of cement mortar exposed to different temperatures, as determined using box-counting method, is shown in Figure 3.21. The FD value increases monotonically with an increase in the temperature across all mixture compositions. For the plain mortar, it varies from 1.5 to 1.7 as the exposure temperature increases from 20 °C to 500 °C. As indicated by the error bars, the degree of reproducibility of the estimated values is reasonable. It is worth noting that a certain level of scattering vis-a-vis the estimated values is seen, which is due to the nature of the sampling process. For example, only a small portion of the polished specimen can be observed during the SEM. The polished specimens in turn represent a small region of the mortar prism. These sampling steps are responsible for the observed variability of the estimated FD. Nevertheless, by randomizing the field of observations together with statistically sufficient number of observations, the reproducibility of the average estimated values can be improved.

As discussed in Section 3.5.1, porosity of the mortar increases with the increase in exposure temperatures. And this research has shown that FD increases with an increase in the porosity of the mortar. In order to offer comparison, a study with polymer-modified cement paste by Castaño et al. (1990) may be cited. Using optical microscopy, they found that the FD of cement paste decreases with an increase in the polymer content. The reported FD values ranged from 1.12 to 1.4. Note that in polymer-modified cement paste, the porosity decreases with the increase in the polymer content (Ohama 1995). Thus, the findings of these two studies are in agreement with that from the present research. Further, Yu and Li (2001) developed an expression describing the relationship between FD of a material and its porosity—thus reinforcing the observation that fractal dimension of cement-based systems is related to its porosity. However, there are a few studies that are in direct contrast with this work. For instance, Lange et al. (1994) estimated, using dilation technique, the FD of cement paste with varying amount of silica fume, thereby having slightly different porosities, using the dilation technique. They concluded that FD essentially remains the same even with the change in porosity of the paste. This discrepancy may be attributed to the likely difference between the thermally dehydrated microstructure and the one that was produced by merely changing the water/cement ratio of the mixture, despite having the same porosity.

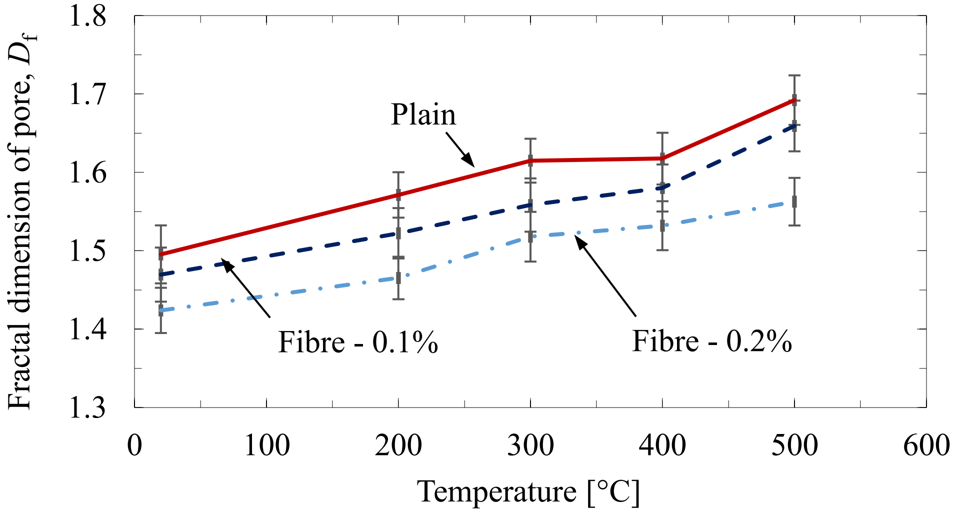

Figure 3.21 Fractal dimension of mortar exposed to different elevated temperatures (error bars showing ±1 standard deviation).

The addition of polyester fibre to the cement mortar was found to have marginally lowered the fractal dimension compared to its plain counterpart. For a fibre volume fraction of 0.1%, the FD values varied from 1.45 to 1.65 while the 0.2% volume fraction of fibre resulted in a change in fractal dimension from 1.4 to 1.55 with an increase in the temperature. This reduction in FD is in agreement with the lowering of porosity as evidenced from Section 3.5.1.

In case of deterministic fractals, FD refers to the self-similar characteristics of the geometry while for the natural fractals it describes the inherent statistical nature of self-similarity.

Another way of interpreting the measured FD values which varies from 1.4 to 1.7—a deviation from a Euclidean dimension of 1 and approaching a Euclidian dimension of 2—is that the FD values exhibit an area filling nature of the pore structures. Furthermore, the increasing value of FD reveals the increased level of complexities or details, for instance the roughness of pore space, as the scale of observation reduces. In other words, higher value of FD may be considered as an overall measure encompassing many complexities like an increasingly rougher or irregular pore perimeter, among others.

When cement mortar is exposed to sustained elevated temperatures, gradual dehydration of moisture from hydrated cement paste occurs. Furthermore, as described in Section 3.5.4, an increase in the temperature of exposure results in dehydration and in turn, a coarsening effect on the pores. All of which makes in the pore geometry significantly more complex and thereby contributes to the higher values of FD.

Fractal dimension is a descriptor of the shape irregularity. But, knowing the FD alone is not sufficient to reconstruct the geometry. There are mathematical expressions available that can be used to model an "*equivalent*" pore geometry using the FD, by incorporating additional pore structure parameters such as porosity, maximum pore size, and minimum pore size. Such an idealized pore geometry will still be helpful when modeling physical properties of the material. It is to be conceded however that such modelling effort is only as reliable as any two-dimensional approximations can achieve from three-dimensional objects (Russ and Neal 2016). Still, FD stands out as a useful parameter to describe the transformations in pore structure of cement mortar when subjected to elevated temperatures.

3.6 Conclusions

The structure of pore system of cement-based composites controls their transport properties as well as their mechanical properties. This part of the thesis is the result of research work undertaken to enrich the still developing knowledge base on the changes to the pore network within cement-based materials that are subjected to extreme condition of exposure. The key findings from this work through the experimental investigation, regarding the evolution of microstructure of cement mortar at sustained elevated temperatures, are summarized as follows:

- Pore volume fraction increases with the increase in exposure temperature across all mortar mixture. In addition, the fibre reinforced mortar was found to have marginally lower porosity than the plain ones. It appears to be in direct contrast with one school of thought where it was hypothesized that fibre incorporation causes additional reservoir space and thereby providing a mechanism to relief moisture clogging. However, one should note that lowering of porosity does not necessarily indicate a reduction in pore connectivity, which is the dominant factor in terms of the efficiency of polymeric fibre against spalling resistance.
- Distribution of number of probabilistic spherical pores shows a higher number of 3D pores, in the finer region of pore size spectrum, compared to the number 2D pore features
- From the two-point correlation function, the presence of monotonic nature of the asymptotic end of the function indicate a spatially uncorrelated nature of the pore structure beyond the distance associated with characteristic pore radius.
- While the specific surface area—defined as the area of pore-solid interface per unit volume—for the plain mortar is increasing with the increase in temperature, the fibre reinforced mixtures shows no significant variation.
- Thermal exposure results in a coarsening of effect in capillary pores as well as in meso pores.
- A slight increase in meso pore volume can be observed for fibre reinforced mortar at pore radii larger than about 2 nm.
- Box-counting fractal dimension of the mortar increases with temperatures indicating increasingly rougher pore perimeters.
- The image magnification employed here was found to capture capillary pores where a significant degree of transformation typically occurs due to thermal exposure.

This study reveals that a combination of experimental study offers interesting insight regarding the mortar microstructure. Furthermore, pore volume fraction is an essential parameter when modelling the thermal properties. In addition, innovative prediction model based on fractal nature of the pore geometry can also be developed to study the physical properties by employing the fractal dimension to simulate the pore geometry of the material. The knowledge gathered in this study would be useful to design mixture proportion targeting applications where the material is subject to elevated temperature.

CHAPTER 4. THERMAL CHARACTERISTICS

4.1 Introduction

Characterization of physical properties of engineering materials under different loading and environmental condition as encountered in the field is an essential requirement towards its application. These requirements often place conflicting demand on the macroscopic properties, especially in regard to thermal insulation. Consequently, this has led to the development of engineered materials. And, as with any multiphase material, the bulk properties of such engineered systems depend on the properties of its constituents under various conditions of exposure.

Determination of the physical properties—electrical conductivity, thermal conductivity, fluid permeability, and elastic modulus—is achieved experimentally for heterogeneous materials with relative ease when compared to the task of modelling these effective properties. Note that it is generally assumed that the material is microscopically homogeneous without compromising the accuracy of the experimental results. However, experimental evaluations must also incorporate the statistical variation of the measured properties.

Experimental evaluation of macroscopic properties may occasionally be time consuming or cost prohibitive for a range of parameters defining the properties and the distribution of the constituents. In such case the development of prediction model from microstructural parameters would be beneficial. There are several parameters that need to be considered when modelling properties of heterogeneous materials. These include volume fraction of each phase, topological characteristics, phase contrast, distribution, and shape. It is worth emphasizing that the interface between the adjacent phases has significant impact on the predicted properties (Wang and Pan 2008).

Prediction of physical properties from that of the constituents and volume fraction may either be based on accurate geometrical modelling of the heterogeneous system or an average representation of the system (Skorokhod 1995). Both approaches have inherent limitations in terms of applicability. For instance, the former case would rely on a set of simplified assumptions that may limit the application of the model to specific type microstructural geometry, whereas the later approach may only be valid for systems having the ratio of the properties of the component phases below certain threshold.

It has been demonstrated (Torquato 2000) that the simple rule of mixture fails to predict the physical properties accurately because of the spatial variation of the dispersed phase within the continuous phase. Further, the relevant microstructural parameters may not be accurately determined when the complexity of the microstructures of the materials increases. Therefore, one may attempt calculating the upper and lower bounds for the effective properties using the available microstructural information.

Evaluation of thermal properties of cement-based systems helps understand the heat flow through the materials. It also enables optimization of mixture proportions of concrete that can withstand exposure to elevated temperatures. In order to describe the temperature distribution in a body, three thermal properties—thermal conductivity, thermal diffusivity, and specific heat—are required. Thermal conductivity is the rate at which heat energy flows through a material when subjected to a thermal gradient, while thermal diffusivity measures the rate at which temperature changes within the material. On the other hand, specific heat is defined as the amount of heat energy required to increase the temperature of a body of unit mass by 1 degree. Both the theoretical prediction and the experimental evaluation of these properties would help one understand the microstructure-properties relationship of cement-based materials.

4.2 Objectives

As mentioned earlier, the aim of this study is to evaluate and also reliably predict the thermal properties of the mortar subjected to elevated temperatures. In this chapter, first, the influence of moisture content on the thermal characteristics is assessed using the computed values from several prediction models. Second, an experimental study of residual and in situ measurement of thermal conductivity, diffusivity, and specific heat is made. Third, the effect of polymeric fibre on the thermal properties are presented. Fourth, thermal conductivity of cement mortar at different exposure temperatures is modelled using empirical and fractal geometry-based approach.

4.3 Background

Thermal properties of cement-based materials determine its performance during an event of elevated temperature exposure. For instance, thermal conductivity together with specific heat capacity controls how the temperature within a structural member changes with the time of exposure. As the temperature rise progresses inward, the member experiences hygro-thermal damage due to the dimensional change induced by shrinkage, creep, and not the least, due to the thermal incompatibility between the paste and the aggregates. In order to ascertain the damage resulting from this exposure to elevated temperatures, it is essential to conduct a thermal analysis. This can be done by solving the governing differential equations. Inputs to solving these equations are the thermal properties of individual components, which may be measured through suitable experimental methods.

Thermal properties of cement-based materials are usually averaged over a region as opposed to the properties measured at a single point. This is because of the non-homogeneous distribution of different phases that makes the results based on single point measurement unreliable. Besides non-homogeneity, there are other factors that affect the measured thermal properties of cement-based materials. For instance, at elevated temperature the physico-chemical changes are known to affect the heat flow path to a considerable degree. Therefore, it is essential that one considers the impact of these changes before adopting an experimental technique. The change in moisture content due to its dehydration and diffusion is especially important because of the major effect it has on the specific heat capacity of the material by contributing both through the latent heat of vaporization and through mass transfer.

The steady-state method, a commonly used test method, under normal temperature conditions, is particularly unsuitable to measure the thermal properties of cement-based materials at elevated temperatures due to the longer time requirement to achieve the a steady-state condition (Thompson 1968). In addition, the presence of moisture makes the test duration even longer due to the fact that, under a thermal gradient, achieving a moisture equilibrium is a slow process. In order to avoid the aforementioned limitations associated with the steady-state method, a transient test method such as hot-wire method can be used since it allows a much shorter test duration compared to the steady-state methods. However, in this case too, it was reported that due to the absence of constant flux heated surface, results may be affected by the variation in the temperature rise in the vicinity of the line source surrounded by the non-uniformly distributed components having high thermal conductivity ratios (Lamond and Pielert 2006).

Thermal conductivity values of cement paste, conventional concrete, and high-performance concrete were measured by Jansson (2004) using a transient plane source (TPS) method. The cement paste were prepared with a w/c of 0.405. The thermal conductivity was found to have reduced from 0.7 W/mK at 100 °C to 0.5 W/mK at 600 °C. For conventional concrete with a w/c of 0.7 and having a compressive strength of 38.5 MPa, the thermal conductivity varied from 2.5 W/mK to 1.25 W/mK when tested at the aforementioned temperature range. On the other hand, the high-performance concrete, having a w/c of 0.28 and compressive strength of 114 MPa, showed slightly higher thermal conductivity at high temperatures, owing to its relatively denser microstructure. It is worth mentioning that the aggregate phase—occupying the largest volume fraction and having the highest thermal conductivity—has significant contribution to the overall thermal conductivity of the composite mix.

The addition of supplementary cementitious admixtures does not appear to have any effect on the thermal conductivity of normal concrete at elevated temperatures (Kodur and Khaliq 2011). However, some researchers reported a considerable drop in thermal conductivity of light weight aggregate concrete prepared with fly ash or silica fume (Demirboğa and Gül 2003; Kim et al. 2003). The reduction in thermal conductivity has been attributed to the relatively more amorphous structure and to the lower density of the concrete because of the higher void fraction due to the substitution of cement with the pozzolans. Kodur and Khaliq (2011) have indicated that the specific heat of concrete containing fly ash increases with temperatures. They attributed the increased specific heat to the additional amount of heat due to the latent heat of vaporization in relatively less permeable concrete containing fly ash.

A great number of researchers have worked on developing prediction models. These models can be categorized into three types—rule of mixtures, empirical method, and theoretical method. The rule of mixtures uses properties and volume fractions of the various components in the heterogeneous materials, whereas the empirical method relies on the regression analysis of the experimental data. Both of these methods have very limited applicability in terms of the range of porosities and the type of components in the material. On the other hand, the theoretical models are capable to simulating a wide range of parameters governing the heat transfer phenomenon through the material. Depending on the rigor of the modelling approach, theoretical models are capable of incorporating the influence of the shape of inclusions, its spatial distribution, interfacial resistance, and interaction with the surrounding phases.

Historically, James Clerk Maxwell employed an analytical technique to develop the first model which predicts the conductivities of composite media from the properties of the dispersed and continuous phases. In this model, the dispersed phase is idealized as non-interacting spheres. It does not consider the interfacial thermal resistance between the continuous matrix and the dispersed inclusions (Pietrak and Wisniewski 2015). As a result, this model is only applicable to composites where the fraction of dispersed inclusions does not exceed 0.25. Several modified versions of this model were proposed to extend its applicability to a wide range of materials. Eucken modified Maxwell's model to include multiple different phases in one continuous phase, while Hamilton and Crosser (1962) modified it to include the effect of particle shapes. Hasselman and Johnson (1987) further improved it by modelling the interfacial thermal resistance, whereas the interaction between spherical particles arranged in cubic array was implemented by Raleigh. However, the model is still not capable of predicting effective thermal conductivity for higher filler fractions. Bruggeman (1935) formulated a model, which was later modified by Landauer, using a differential effective medium theory (Pietrak and Wisniewski 2015). It can predict the thermal conductivities for composites having higher fraction of inclusions. In addition, their model can be used to calculate the thermal conductivities of multicomponent materials.

Fractal geometry-based modelling approach is relatively new to study the macroscopic behaviour of porous materials. In this approach, natural fractals, which are statistically self-similar over a limited range of scale, are simulated using the deterministic fractals such as Sierpinski carpet. Ma et al. (2003) developed a Sierpinski carpet-based model to investigate the thermal conductivity of porous composites. However, its applicability was limited to materials having a porosity ranging from 0.3–0.5. Feng et al. (2004) extended this model and were able to predict the thermal conductivities of composites with a wider range of porosity.

4.4 Materials and Specimen Preparation

In this study, thermal properties were measured using mortar specimen prepared with CSA A3000 (2013) Type GU cement. The fine aggregates used in this study was blended from commercially manufactured silica sand, which conforms to the limits specified in ASTM C33 (2003). The mixture was proportioned with a cement-to-fine aggregate ratio of 1:3 and a w/c ratio of 0.5. In order to investigate the effect of microfibre reinforcement of the thermal properties of the mortar, polyester fibre was added at a volume fraction of 0.1–0.3%. The fibre has a length of 12 mm and a diameter of 50 µm. An appropriate amount of high range water reducing admixture was incorporated in order to compensate for the loss of workability due to the addition of microfibres. The consistency of the fresh mortar was ensured by conducting a flow table test in accordance with ASTM C 1437 (2013b). The measured flow value for the plain mortar was 150–170 mm, while that for various fibre reinforced mortars were between 135–145 mm.

The ingredients were mixed using a rotary type high-shear mixer. Before adding into the mixer, the fine aggregates and the cement were mixed manually using a hand trowel. After transferring them to the mixing pan, the mixture was agitated for 15 minutes. About three-quarters of the total water was then added to the mixture and mixed at high speed, 30 cycle/s, for additional 20 minutes. Afterwards, the polyester fibres were added gradually to avoid clumping. At the end of fibre addition, the remaining water was added and the mixture was agitated for further 15 minutes allowing for proper dispersion of the fibres.

Prismatic specimens with a dimension of 50 × 50 × 200 mm were cast in multiple layers while using vibration to achieve proper compaction. After casting, the sealed specimens were kept at ambient temperature for 24 hours. Later the demolded prisms were cured in a humidity room with a relative humidity of 95% and a temperature of 21 °C for a period of 60 days. At the end of the curing period the mortar bars were sawn into 25 mm thick sections. The sawn sections were kept in the humidity chamber before conducting the experiments for thermal properties.

4.5 Experimental Details

In order to determine the effect of moisture content on the thermal properties, the specimens were pre-dried under ambient conditions, for a variable length of time so as to achieve different degrees of saturation. On the other hand, specimens intended for residual and in situ thermal tests were oven dried at a temperature of 105 °C until constant weight was reached, thus indicating a complete drying.

As discussed earlier the transient methods are the most suitable technique, compared to the steady-state methods, to determine thermal properties of cement-based materials especially at elevated temperatures. It is quite difficult to achieve an equilibrium condition, when using stead-state methods, due to the constantly evolving microstructure of cement-based materials during high exposure temperature. Therefore, the transient plane source (TPS) method developed by Gustafsson (1991) was employed in this study. It is worth noting that the TPS method is capable of measuring the thermal properties of wide range of materials including the ones having a very low thermal conductivity such as concrete.

In the TPS technique—also called the hot disk method—a disk shaped sensor composed of double spiral nickel wire arranged in concentric rings, wrapped on either sides by electrically insulating material, is used both as a temperature sensor and as a heating element. This insulating material could either be Kapton or mica depending on the exposure temperature of the specimen (Gustafsson 1991). The mica-based sensor is normally used for experiments where the specimen is exposed to temperatures up to 500 °C only. During the test, the sensor is placed in between two halves of a specimen while a known amount of current is supplied to it for a short period of time. The current causes an increase in sensor temperature by about 1–3 K (Log and Gustafsson 1995). As the temperature of the heating element increases, its resistance also changes according to the temperature coefficient resistivity of the material. As a result the voltage across the sensor also changes which can be measured using a high precision voltmeter. By monitoring the changes in voltage and current for a specified period of time, the heat transfer characteristics of the specimen can be obtained. Note that the chosen duration of heating should be sufficiently short, 40–160 s, to justify a semi-infinite state of the sensor in contact with the specimen. Thus, the influence of the boundaries of the specimen is minimized to an acceptable degree (Gustafsson 1991). In addition, at the initial stage of heating, there is usually a small drop in temperature due to the electrical insulation covering the sensor, which approaches a constant value after a small period of time. This influence, called the contact resistance, can however, be corrected when processing the average temperature increase as a function of time (He 2005).

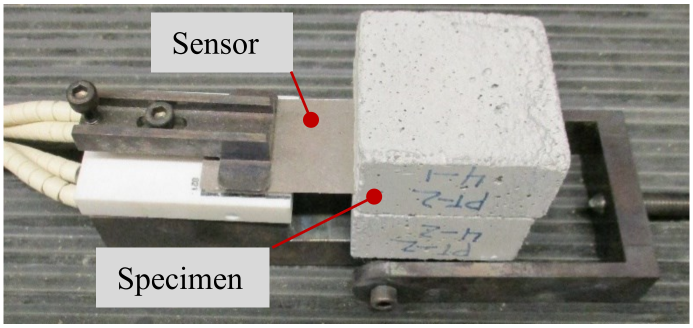

Figure 4.1 TPS sensor, with mica insulation, sandwiched between two sections of a mortar specimen.

In this research work, the whole sensor-specimen assembly, as shown in Figure 4.1, was placed in a furnace in order to measure the thermal properties at different elevated temperatures. The furnace is equipped with microcontrollers which allows for the control of heating profile including the heating and soaking duration. The sensor has a mica insulation which is suitable for conducting measurements at high temperature. The furnace was programmed to increase the temperature at a rate of 5 °C/min. This rate of heating was selected to avoid the possibility of explosion occurring due to surge in vapour pressure as already discussed in the previous chapter. Incidentally, this rate of heating is the same as was chosen for other companion tests where the specimen thickness was larger and thereby prone to explosion. Furthermore, a soaking period of two hours was deemed sufficient to achieve thermal equilibrium given the fact that the specimen had been pre-dried at 105 °C (Campbell-Allen and Thorne 1963; Thompson 1968).

During the experiment using TPS technique, the average rise in the temperature across the sensor is measured by monitoring the changes in electrical resistance of the sensor. The resistance can be expressed in terms of the temperature coefficient of the resistivity, α and average rise in temperature, $\Delta\overline{T}$ as follows:

$$R = R_0\left(1+\alpha\cdot\Delta\overline{T}(\tau)\right) \tag{4.1}$$

where R_0 is the initial resistance of the TPS sensor, τ is the characteristic time.

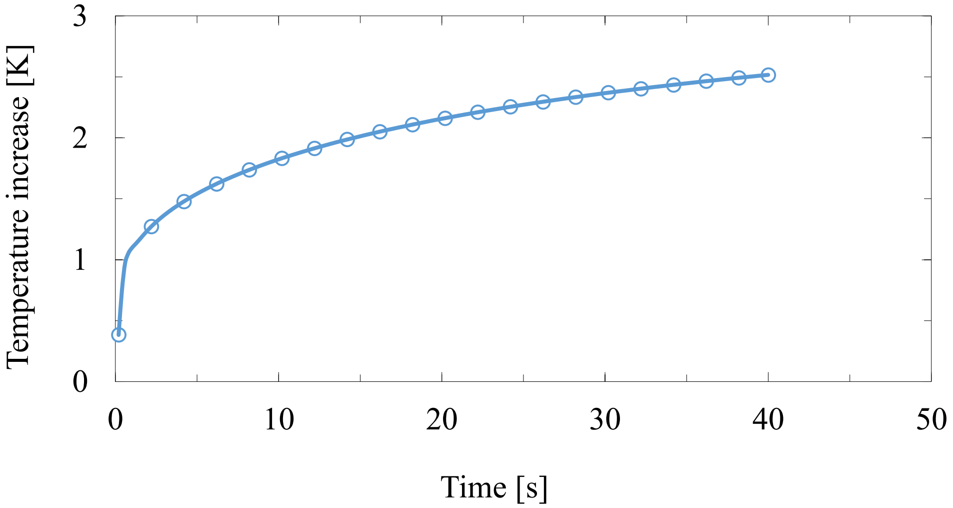

Figure 4.2 Typical temperature history recorded using TPS instrument.

The theoretically established expression for the average time-dependent temperature rise in the sensor, composed of double spiral concentric rings, is expressed as:

$$\Delta\overline{T}\left(\tau\right) = \frac{P_0}{\pi^{3/2}ak}D(\tau) \tag{4.2}$$

where P_0 is the output power from the sensor, a is the radius of the outermost ring of the sensor, k is the thermal conductivity of the specimen, and $D(\tau)$ is a dimensionless function of τ, expressed by $\sqrt{\kappa t}/a$, where κ is the thermal diffusivity of the specimen and t is the time. Analytical expression for $D(\tau)$ can be found in literature (Gustafsson 1991; He 2005; Log and Gustafsson 1995).

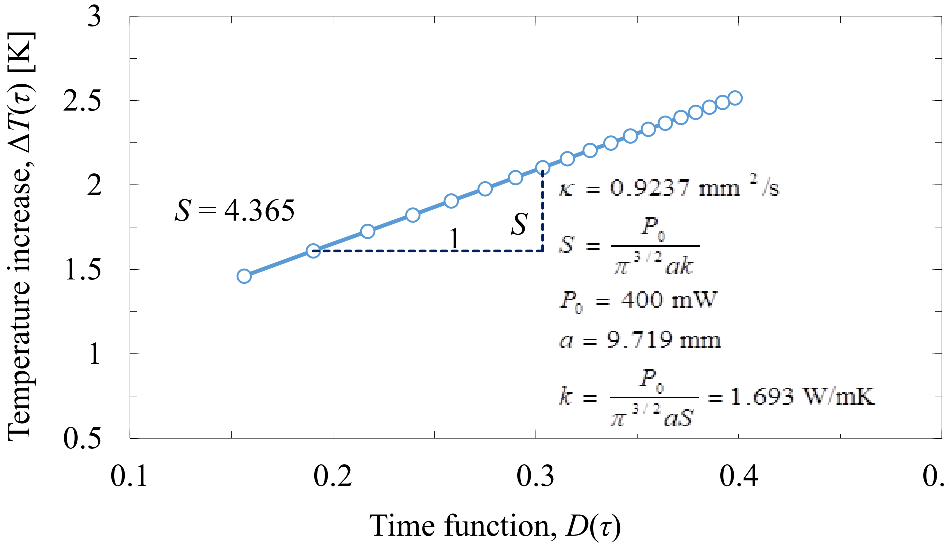

Figure 4.3 Calculation of thermal properties using transient plane source method.

When processing the temperature history as recorded during the transient heating, it is essential to bear in mind that besides the contact resistance, several other parameters affect the measurements. For instance, the temperature response of the sensor is not instantaneous due to the heat capacity of the sensor and there is a delay associated with the instrument's response. Consequently, a time correction is applied by using a computational technique. Furthermore, sometimes temperature drift around the sensor makes it difficult to maintain a homogeneous temperature distribution. Therefore, a temperature drift correction need to be determined for a more accurate measurement of the thermal properties (He and Ng 2002). A typical temperature history measured using a mica sensor is shown in Figure 4.2. It is noticeable that there is a large fluctuation in the initial part of graph resulting from the interference of sensor or the electrical insulation, but it is normally discarded as inconsequential when performing the calculation of thermal properties. Once the average temperature rise and the $D(\tau)$ are determined, one can calculate thermal conductivity by plotting $\Delta\overline{T}$ against $D(\tau)$. Since calculation of $D(\tau)$ involves thermal diffusivity of the material, a numerical technique is usually employed. By assuming a series of thermal diffusivity values and generating $\Delta\overline{T}$ versus $D(\tau)$ plots, the correct thermal properties can be calculated from the plot that yields a linear relationship as indicated by Equation 4.2. A sample plot of such relationship along with a typical computation of thermal conductivity is shown in Figure 4.3.

4.6 Results and Discussions

The experimentally evaluated thermal properties were compared with those predicted by suitable models from prior literature. Note that the thermal properties were determined using the transient plane source technique both at ambient conditions (after exposure to elevated temperatures) and at elevated temperatures (at the end of two hours of thermal soaking). In order to avoid the risk of explosive spalling, the specimens were oven dried prior to the tests.

4.6.1 Effect of Moisture Content on Thermal Properties at 20 °C

The efficiency of any insulating material depends on its thermal properties, volume fraction, distribution, shape and size of the constituent phases. One such constituent is the moisture, which is known to strongly influence the thermal conductivity of porous materials (Bouguerra 1999). Therefore, it is essential that one understands the crucial role of moisture when designing building envelope systems.

Moisture affects the thermal properties of a material in several ways. First, it enhances the thermal contact between the solid and the gas phases by modifying the interface between them. Second, due to the thermal gradient, also the resulting pressure gradient, moisture migration causes a change in the heat flux within the material. Third, the evaporation and the condensation of the solid and gas phases of water contributes to the heat conduction in the material. Therefore, any study on the thermal properties of moist materials must consider both the heat and the mass transfer coupled together (Bomberg and Shirtliffe 1978).

Moisture content in a material changes during its service life due to exterior or interior moisture diffusion and capillary suction from building foundation. Therefore, it is essential to assess the thermal performance of the material at various level of moisture content. Building codes frequently require the evaluation of thermal conductivity of cement-base envelope systems at a specified moisture content (Stuckes and Simpson 1985). It is fairly difficult to attain a certain level of moisture content in the specimen accurately. In such a situation, experimental determination of the thermal conductivity at a specified moisture content is not always convenient. On the other hand, simplified models offer a much easier route to predict the thermal properties of moist building materials.

4.6.1.1 Thermal Conductivity

In this study, the thermal conductivity, specific heat, and thermal diffusivity were evaluated at 20 °C for the cement mortar across a varying amount of moisture. Figure 4.4 shows the influence of moisture on the thermal conductivity, determined experimentally, of the plain and fibre reinforced mortar having a moisture content from 0–8.5% by mass of oven-dry mortar. Generally, the thermal conductivity increased by about 25% due to an increase in moisture content by 8.5%. It can be noticed that the fibre reinforced specimens showed a slightly lower thermal conductivity compared to the plain ones. A possible explanation for this marginally lower value lies with the inherent hydrophobic (Bentur and Mindess 2006; Zheng and Feldman 1995) nature of the polyester fibres, where the contact between the fibre and the water molecules slightly differs from that between cement-paste and water. Furthermore, the additional tangential pore space (Khoury and Willoughby 2008) that is formed between the cement paste and the fibre presents greater thermal resistance causing a reduction in heat transfer within the solid cement paste. It is easy to understand why the conductivity increases with moisture if one remember that free water occupies the air voids and the thermal conductivity of air is a good 20 times less than that of water.

A model developed by Kricher and Kroll (1956), originally published in German, cited by Taoukil et al. (2013), is employed in this study to predict the thermal conductivities at different moisture contents with the properties and volume fraction of different phases as input variables. This model uses a harmonic mean of thermal conductivities calculated using parallel and series model as shown below:

$$k_e = \frac{1}{(1-\theta)/k_{para} + \theta/k_{per}} \tag{4.3}$$

where k_e is the effective thermal conductivity, k_{para} and k_{per} are the equivalent thermal conductivities from the parallel and series model respectively, which were calculated using Equation 4.4 and 4.5, θ represents the volume fraction of the material oriented perpendicular to the predominant heat flow direction.

$$k_{para} = (1-\varphi)k_s + (\varphi - m)k_a + mk_w \tag{4.4}$$

$$k_{per} = \left[(1-\varphi)/k_s + (\varphi - m)/k_a + m/k_w\right]^{-1} \tag{4.5}$$

where k_s, k_a, and k_w are the thermal conductivities of solid, air, and water respectively; ϕ is the volume fraction of pores and m is the volume fraction of water.

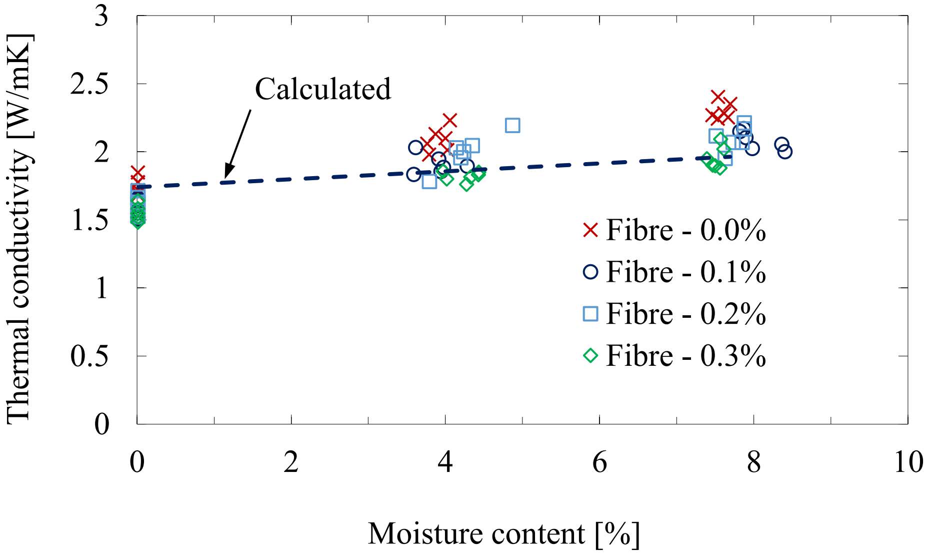

Figure 4.4 Effect of moisture conetnt on the thermal conductivity at 20 °C.

The value of θ and k_s were solved from the measured thermal conductivity values of oven-dry and fully saturated mortar specimens. The calculated values for the plain cement mortar are shown in Figure 4.4 which are largely in agreement with the experimental results.

4.6.1.2 Specific Heat

Specific heat capacity is defined as the amount of heat energy required to increase the temperature of a material of unit mass by one degree. It is an essential parameter required when computing heat transfer from one system to another. It is particularly worth noting that the determination of specific heat is sensitive to the presence of moisture in a material, where the phase transformation of water from one form to another—through evaporation and condensation—causes an increase in the required energy in addition to that from solid and air-void in the mortar. Figure 4.5 presents the measured specific heat, at different moisture contents, as volumetric heat capacity which is equal to the density of the material multiplied by the specific heat. As one would expect, there was an increase in the measured values with an increase in the moisture content. There was no noticeable influence due to the presence of the polyester fibre. At 8.5% moisture, where the mortar is nearly saturated, the specific heat increased by about 50% compared to the oven-dried mortar.

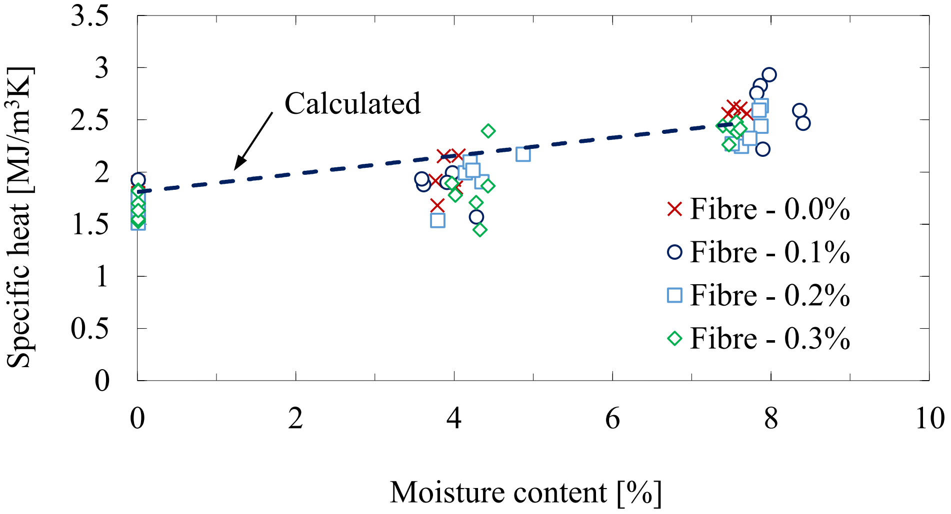

Figure 4.5 Effect of moisture conetnt on the specific heat at 20 °C.

Specific heat of the dry cement mortar can be computed using a simple rule of mixture from the mass fractions and the specific heat of the constituents (Bentz et al. 2011; Choktaweekarn et al. 2009). When using such a simplified model, it is necessary to distinguish between free water and bound water—physically adsorbed and chemically combined with the components of hydrated cement paste—because of their different specific heat characteristics. However, since the experiment in this study was conducted at 60 days after casting the specimens, almost all the added water may be taken as bound water. The following equation was employed to calculate the specific heat of dry mortar:

$$C_{dry} = C_{fw} M_{fw} + C_{bw} M_{bw} + C_c M_c + C_s M_s \tag{4.6}$$

where *C* and *M* denote specific heat and mass fraction respectively, the subscript *fw*, *bw*, *c*, and *s* denote free water, bound water, cement, and sand respectively.

The specific heat of cement, sand, free water, and bound water were taken as 740, 710, 4180, and 2200 J/(kg·K) respectively. Finally, the specific heat of moist mortar was calculated using Equation 4.12 as follows:

$$C_{wet} \rho_{wet} = C_{dry} \rho_{dry} + C_{water} V_{water} \tag{4.7}$$

where ρ is the density and *V* is the moisture content by volume.

As shown in Figure 4.5, the model predicted values of the specific heat fairly agrees with the measured values for data points near the saturated moisture content, whereas it overestimates the specific heat for partially saturated mixtures as well as for the oven-dried ones.

4.6.1.3 Thermal Diffusivity

Thermal diffusivity measures the rate of change of temperature within a material. It is defined as the ratio of the amount of heat conducted to the amount of heat stored in the material. The effect of moisture on the thermal diffusivity of mortar is shown in Figure 4.6. One again, fibre reinforcement does not influence the measured values significantly. While the intermediate moisture content causes a slight increase in thermal diffusivity, a 10% reduction can be observed when the mortar is fully saturated. This reduction indicates a lower heat propagation through the mortar caused by increased amount heat being stored by the moisture.

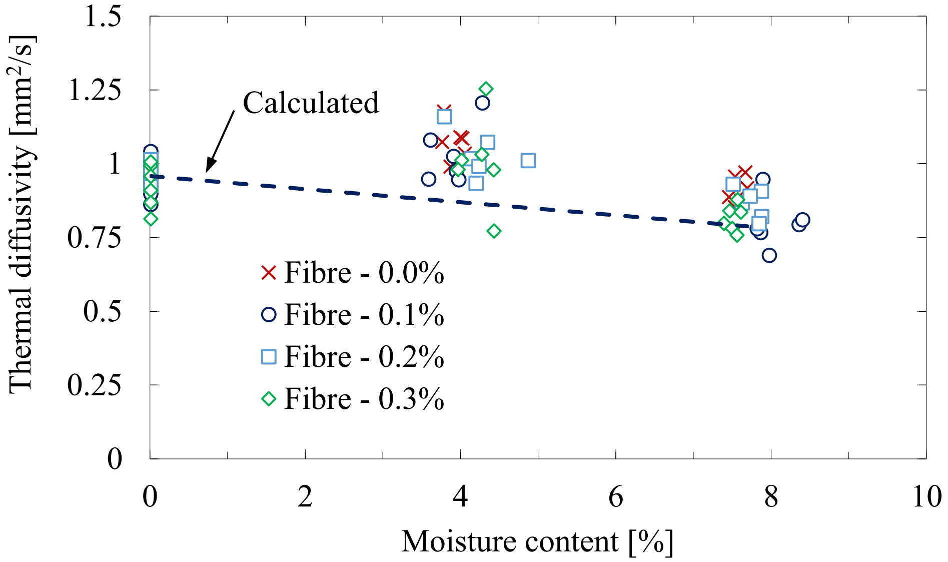

Figure 4.6 Effect of moisture conetnt on the thermal diffusivity at 20 °C.

Thermal diffusivity values was calculated by using Equation 4.3 and 4.7 based on the relationship $\kappa = k/(\rho \cdot C)$, where κ is the thermal diffusivity, k is the thermal conductivity, ρ is the density of the material, and C is the specific heat. As shown in Figure 4.6, the calculated values are largely in agreement with the measured ones, except for the values at intermediate moisture content, 3–5%.

4.6.2 Thermal Properties at Elevated Temperatures

In this work, thermal properties of mortar at different elevated temperatures were determined in two ways—residual and in situ. In residual measurements, the specimens were first heated to the target temperature and then after two hours of exposure, the measurements were carried out on specimens once they were cooled down to room temperature. On the other hand, the in situ measurements were conducted on specimens during the sustained period of thermal exposure. Note that the microstructure of the mortar transforms differently in these two test protocols. First of all, at high temperature some of the physically and chemically bound water evaporates, which later condenses upon cooling if it is unable to migrate outside the system through the pore network. Second, thermally decomposed hydration products recombine with the absorbed atmospheric moisture when cools down to room temperature and thus causes a difference in volumetric composition between residual and in situ specimen. For instance, the decomposed paste product, CaO reacts with the absorbed moisture and form a relatively expansive calcium hydroxide (Dias et al. 1990). Third, microcracks developed in mortar during cooling stage are most likely to influence the measured thermal properties. Generally, for investigations aimed at real-time behaviour in situ thermal properties would be preferred.

4.6.2.1 Thermal conductivity

Thermal conductivity results of the mortar from the in situ experiments are illustrated in Figure 4.7 and that from the residual tests are presented in Figure 4.8. In both cases thermal conductivity is reduced by about 35% at an exposure temperature of 500 °C. It can be seen that the in situ values are gradually reducing from their room temperature values, whereas the residual thermal conductivities remain largely constant up to 200 °C. And then, it decreases monotonically with an increase in temperature. Note that heat flow during the in situ measurement is influenced by the radiation mode of heat transfer which is negligible in residual tests. Further, as the thermal and pressure gradient cause additional heat conduction through moisture migration, a mathematical model to predict thermal constants including conductivity requires coupled heat and mass transfer equations.

It can be noticed that at relatively lower exposure temperature the fibre reinforced mortar shows slightly lower thermal conductivity than the plain counterpart. However, this too gradually diminishes with a rise in the temperature. Nevertheless, there is no clear trend across different dosage of fibre reinforcement. As demonstrated in the previous chapter, the porosity in fibre reinforced mortar is slightly lower when compared with that in the plain ones. Consequently, one would expect a slightly higher thermal conductivity due to the presence of fibres, based on the intuition that arises from simple rule of mixtures, where thermal conductivity of the composite is predicted from that of constituents and their volume fractions. However, this apparent anomaly may be attributed to the fibre-matrix interface in the mortar. Presence of fibres creates a porous zone around itself and thus forms a thermal contact resistance, which reduces heat conduction through the composite. Furthermore, melting of fibres in heated mortar creates a percolated pore network after vaporization and absorption of fibre residue into the surrounding paste. This pore network created by the melting of the fibres provides a continuous pathway for the water vapour to migrate outwards. In other words, the influence of moisture on the conductivity is lessened through vapour migration. This fact accounts for the reduction in heat conduction in fibre reinforced mortar. The findings here are corroborated by Khaliq and Kodur (2011) who too reported a slightly lower thermal conductivity in self-consolidated concrete when reinforced with fibres.

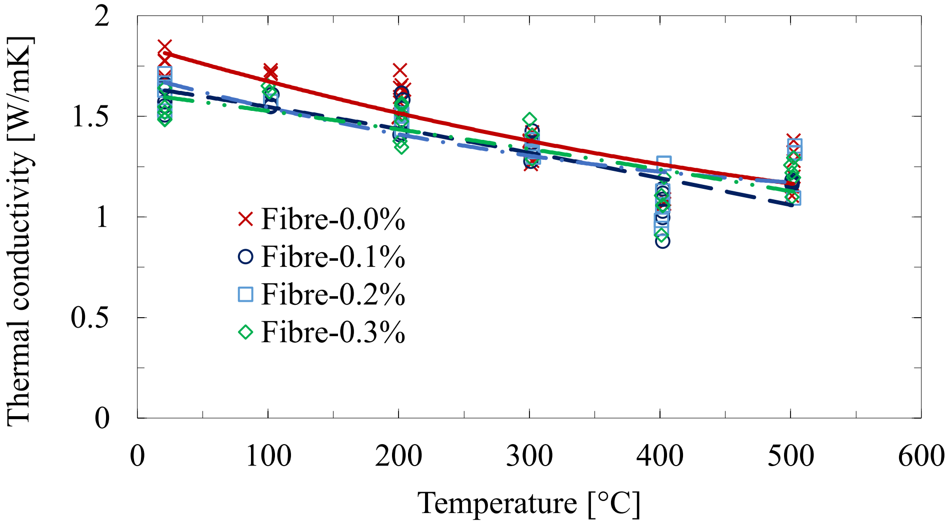

Figure 4.7 In situ thermal conductivity of the mortar at different temperatures.

As the exposure temperature increases, the porosity of the mortar increases— demonstrated in previous chapter. In addition, the dehydration of bound water from cement paste causes pore coarsening, which is likely to create a more interconnected pore network and thus promoting increased amount moisture loss from the mortar. The outcome is a gradual reduction in the thermal conductivity as witnessed above. A drop in the thermal conductivity of cement-based material at elevated temperature indicates a lower amount heat flow towards the interior of a structural member and thus increasing its endurance during extreme conditions such as exposure to fire.

A pronounced decrease in the thermal conductivity at 400 °C may be explained due to the onset of the thermal decomposition of calcium hydroxide into calcium oxide and water (Castellote et al. 2004; Khaliq and Kodur 2011). The resulting increase in water vapour is responsible for the slight increase in thermal conductivity at 500 °C for the in situ measurements.

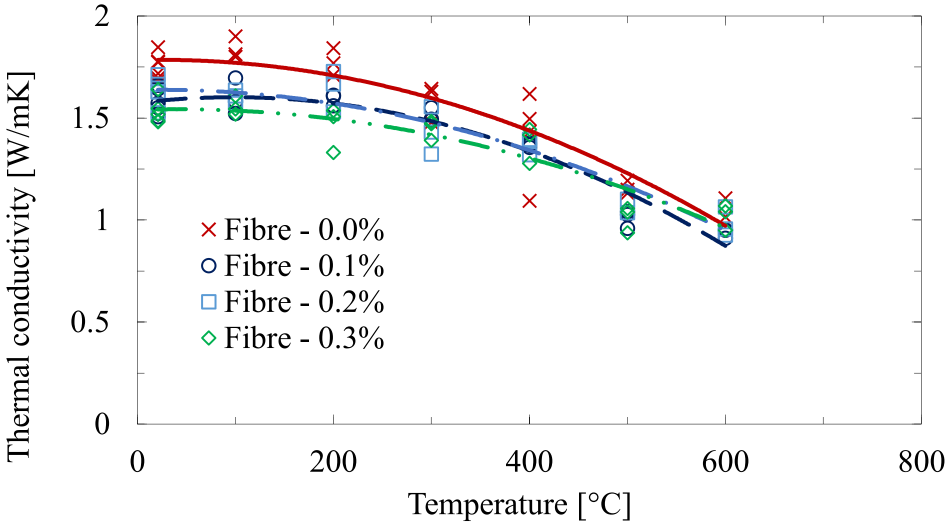

Figure 4.8 Residual thermal conductivity of the mortar at different temperatures.

4.6.2.2 Specific Heat

The in situ and residual specific heat determined using a transient plane source method are presented in Figure 4.9 and 4.10 respectively, for the plain and fibre reinforced mortar respectively. The fibre dosage ranged from a volume fraction of 0.1–0.3%. It can be observed from the in situ results that the specific heat increases with exposure temperature up to about 300 °C. On the other hand, the residual specific heat shows a monotonically decreasing trend. It may be attributed to the inherently different heat storage capacity of mortar during in situ and residual measurements.

The increasing trend, as seen up to 300 °C, was due to the release of bound water. This transformation of bound water into free water influences the specific heat of mortar in two ways. First, the higher specific heat of free water, 4180 J/(kg·K) compared to 2200 J/(kg·K) for bound water (Bentz et al. 2011), contributes to the increased amount of heat stored into the system. Second, heat energy is consumed in the form of latent heat during evaporation of free water as the heat continues to flow inward. On the other hand, in residual tests—after several hours of cooling in ambient condition—most of the free water would have already released into the atmosphere causing a continual decrease in measured specific heat with the increase in exposure temperature. Note that the reabsorbed atmospheric moisture during ambient cooling is recombined with the dehydrated constituents which has lower specific heat.

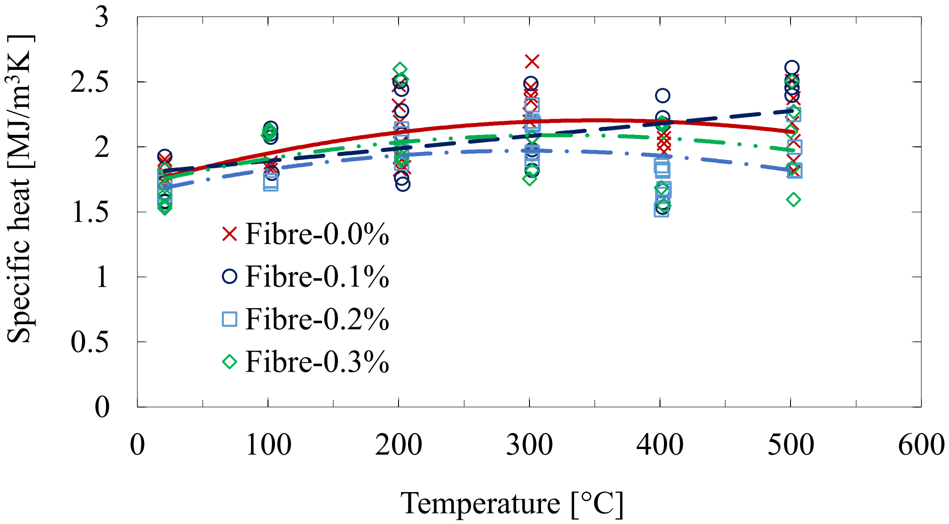

Figure 4.9 In situ specific heat of the mortar at different temperatures.

There is no apparent effect of the fibre on the residual specific heat of mortar, whereas a marginal decrease can be observed from in situ experiments. However, no perceptible difference can be noticed across different fibre dosage. In order to explain this behaviour, one needs to understand the migration of water vapour in the fibre reinforced mortar. Specific heat decreases when water vapour escapes through continuous pathways to the exterior face of the specimen. Note that the fibre enables connectivity of pore system after melting and hence reduces the specific heat (Kalifa et al. 2001). The gradual increase in specific heat, from the in situ experiments, indicates a relatively larger amount of heat storage within the mortar. It reduces the rate at which temperature within the specimen rises, causing a delay in the microstructural changes as well as reduction in mechanical properties.

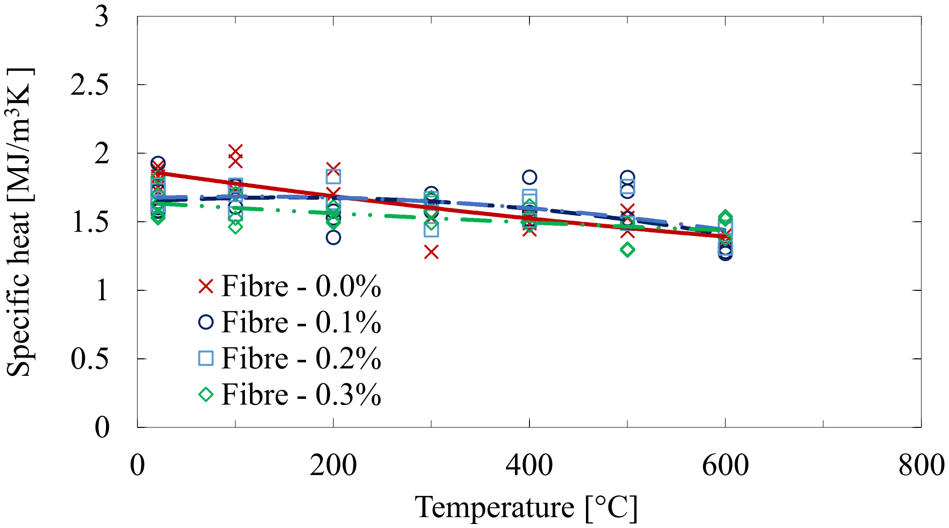

Figure 4.10 Residual specific heat of the mortar at different temperatures.

4.6.2.3 Thermal Diffusivity

Thermal diffusivity is an essential parameter when modeling the transient heat conduction. It can be calculated from thermal conductivity and specific heat capacity, also known as volumetric heat capacity, $\rho \cdot C$. Figure 4.11 and 4.12 show thermal diffusivity obtained by conducting experiments using transient plane source technique for in situ and residual test protocol respectively. It can be seen that, from the in situ test, thermal diffusivity is reducing monotonically with about 50% reduction upon exposure to a temperature of 500 °C. The fibre reinforced mixtures also show same decreasing trend. However, a shifting can be seen at exposure temperature between 200 to 300 °C, where the presence of fibres increases the thermal diffusivity slightly when compared with the plain mortar. The transition temperature appears to be associated with the melting temperature of polyester fibre which is 260 °C (Johnston 2010). As explained earlier, it indicates that fibre melting is accompanied by relatively lower specific heat which in turns results an increase in thermal diffusivity. On the other hand, for similar temperature regime, the residual tests show largely constant thermal diffusivity up to about 300 °C followed by a gradual reduction. Overall, it is seen that the residual values are slightly higher than those obtained from the in situ experiments.

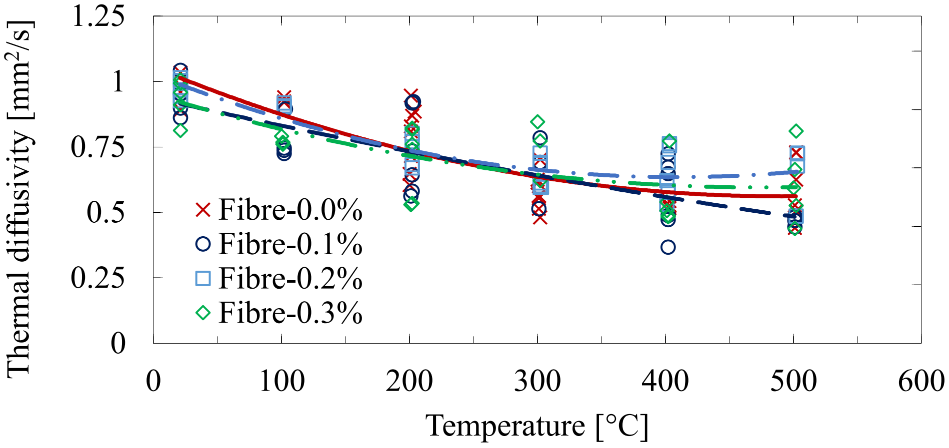

Figure 4.11 In situ thermal diffusivity of the mortar at different temperatures.

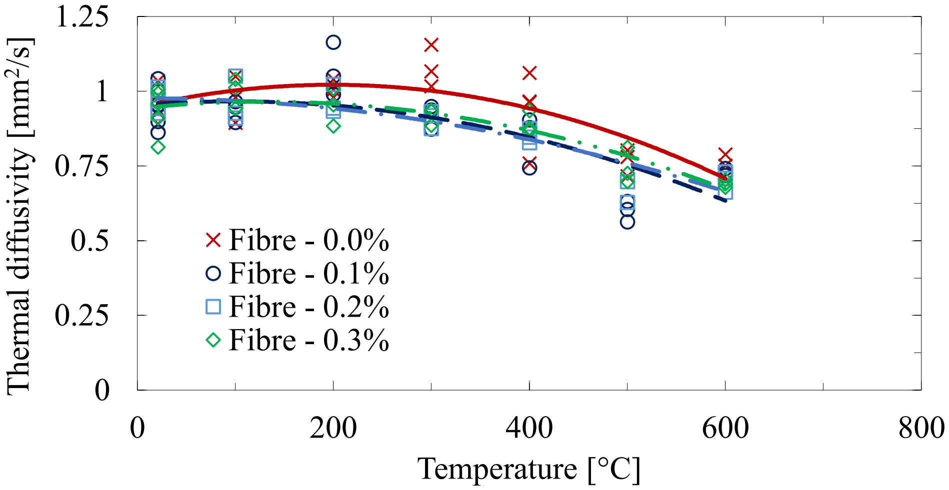

Figure 4.12 Residual thermal diffusivity of the moratr at different temperatures.

4.6.3 Modelling of Thermal Conductivity

It is often time consuming, and prohibitively costly, if not altogether impractical to experimentally determine the thermal conductivity of cement-based materials made from different types of aggregates or having different volume fractions of the constituents. Furthermore, the development of new materials for efficient building envelope benefits from the microstructure-property models by aiding with the selection of optimum mixture proportion. There are several modelling approaches from rules of mixture (ROM) to rigorous ones (Bentz et al. 2005; Pietrak and Wisniewski 2015), capable of simulating the microstructure and heat flow phenomenon to a more realistic level. It is worth noting that simple modelling approach, such as rules of mixture, frequently fails to predict the thermal conductivity with desired degree of accuracy. Therefore, it is essential to consider the spatial distribution of different phases and also the interface between them while investigating through modelling to get more reliable values.

In this study two modelling approaches are presented to predict the thermal conductivities of cement mortar at different elevated temperatures. In the first approach, an effective medium approximation model for two-phase materials developed by Hamilton and Crosser is used. It can be extended to three-phase materials such as cement mortar by successive application. One advantage of this model over Maxwell-type model is its applicability to heterogeneous materials with non-spherical inclusions. In the second approach, a fractal geometry-based concept is used to simulate the porous microstructure of the mortar. Using the electrical-thermal circuit analogy along with the assumption of one dimensional heat flow, the thermal conductivity of the simulated geometry can be computed at different temperatures.

4.6.3.1 Hamilton and Crosser's Model

Hamilton and Crosser (1962) proposed a thermal conductivity model for two-phase porous materials based on an average temperature gradient in each phase. The determination of the ratio of thermal gradients (in different phases) by solving the governing heat conduction equation for irregular geometry is a difficult task. In addition, the shape of the dispersed particles has significant influence on the effective thermal conductivity of a composite. Fricke (1924) derived a simplified relationship using the thermal properties and shape factor of the dispersed phase. Using Maxwell's theoretical work of electrical conduction and Fricke's expression, Hamilton and Crosser's model may be expressed as follows:

$$k_e = \frac{\left(\frac{dT}{dx}\right)_1 k_1\varphi_1 + \left(\frac{dT}{dx}\right)_2 k_2\varphi_2}{\left(\frac{dT}{dx}\right)_1 \varphi_1 + \left(\frac{dT}{dx}\right)_2 \varphi_2} \tag{4.8}$$

$$\left(\frac{dT}{dx}\right)_2 = \left(\frac{dT}{dx}\right)_1 \frac{n k_1}{k_2 + (n-1)k_1} \tag{4.9}$$

where k_e is the effective thermal conductivity, k_1 is the thermal conductivity of the continuous phase, k_2 is the thermal conductivity of the dispersed phase, ϕ_1 is the volume fraction of the continuous phase, ϕ_2 is the volume fraction of the dispersed phase, n is a function of phase geometry, which needs to be determined experimentally (Harmathy 1970), and $(dT/dx)_i$ is the average temperature gradient in i^{th} phase. Equation 4.9 can be derived by solving the governing differential equation of heat conduction for spherical particles and then extending it for arbitrary shape of dispersed phase.

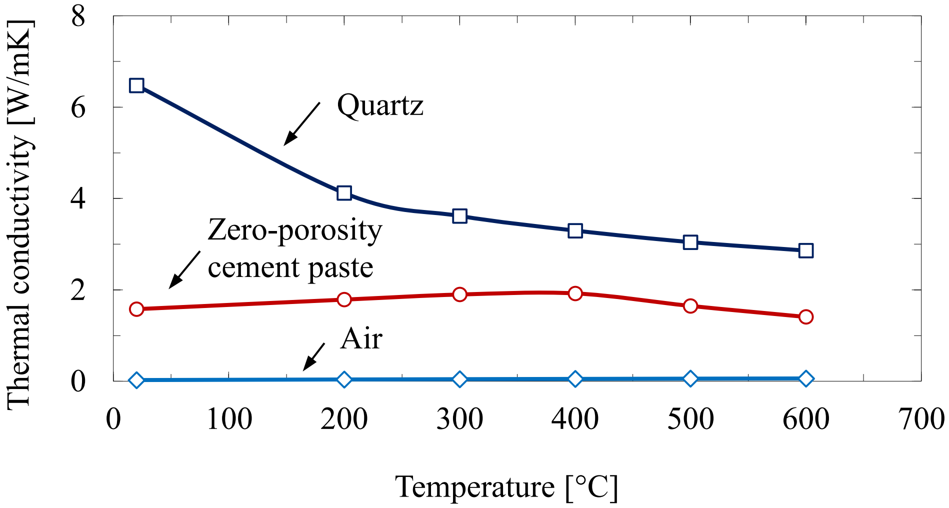

Figure 4.13 Thermal conductivity of different phases of cement mortar. Quartz conductivity data was taken from (Harmathy 1970); air conductivity data was extracted from (Kadoya et al. 1985)

When applying this model to mortar, pore space and fine aggregate phase were regarded as dispersed inclusion while the hydrated cement paste was treated as the continuous phase.

Consequently, a two-step calculation is necessary to determine the thermal conductivity of the mortar. First, the thermal conductivity of combined pores and cement paste was determined from the known thermal conductivities of air and zero-porosity cement paste at different temperatures. It is worth noting that the heat transfer phenomenon through the pore space is usually modelled as a combined effect of heat flow due to conduction, radiation, and the moisture transport. According to Harmathy (1970), the radiative heat flow may be ignored due to its negligible effect on the overall thermal properties. In addition, the effect of moisture transport was also excluded in this study on account of the fact that the experimental measurements were conducted on pre-dried mortar specimens. Second, the calculated thermal conductivity of the porous cement paste was combined with that of the fine aggregate by regarding it as the dispersed phase. The properties of the three phases are shown in Figure 4.13.

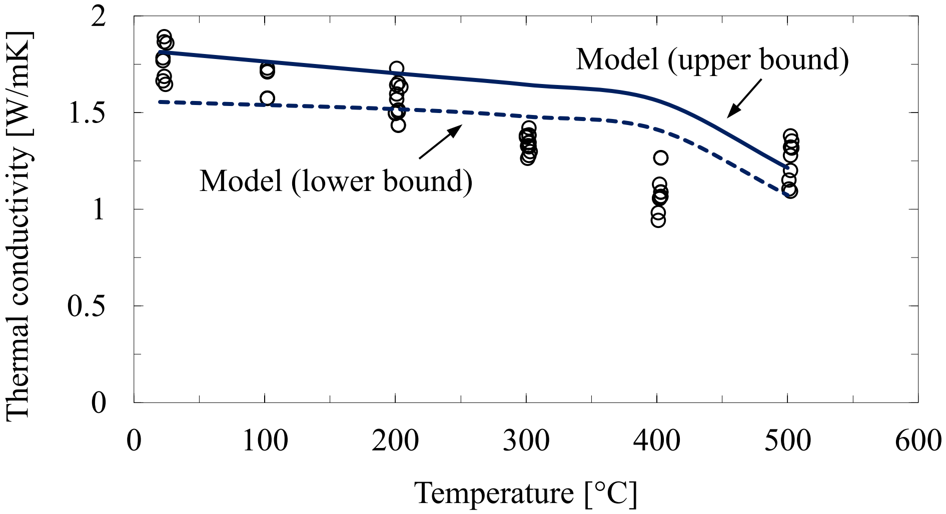

Figure 4.14 Prediction of thermal conductivity of the plain mortar using Hamilton and Crosser’s model.

The volume fraction of different phases—pore space, paste, and fine aggregates—were determined by capturing microstructural image using scanning electron microscopy. A simple image analysis routine was then used to estimate the fractions of each phase.

As mentioned earlier that the parameter *n*, which depends on the geometry of dispersed phases, can be determined from experimental data. Harmathy (1970) conducted an extensive survey of experimental data and suggested a value 1.5 for cement paste and 3.0 for concrete. Due to the difficulty associated with the estimation of the *n* values, an upper bound and a lower bound could be extracted from the experimental results. The two bounds of the thermal conductivity model are plotted in Figure 4.14. Note that the model is not capable of simulating the microstructural variation associated with the CH decomposition causing the dramatic drop in thermal conductivity at 400 °C. In order to predict the thermal conductivity with better reliability, a different modelling approach using the concept of fractal geometry is presented in the following section.

4.6.3.2 Fractal Model

The concept of self-similar geometry is useful in describing the complex microstructure of multiphase materials. Self-similarity implies that the object is composed of many smaller blocks, at different scale of observation, in which no matter the scale, the part exactly resembles the whole. The geometrical measures—length of a curve, area of surface, and volume—of these self-similar fractals are related to their length scale and fractal dimension. In case of deterministic fractals, one may notice the self-similar structure over an infinite range of scales of observation, which are also referred to as exactly self-similar fractals. However, due to the stochastic nature of the microstructure, natural fractal objects obey the aforementioned scaling law only over a certain range of scales. Naturally, cement-based materials fall into the latter category of fractals, which exhibit statistical fractality.

The essence of modeling a stochastic porous medium, such as cement mortar, to predict thermal properties lies on the appropriate idealization of the geometry, interface between different phase, and the underlying response of the medium to external stimulation, which in this case is thermal gradient. The microstructural geometry is usually simulated through a periodic arrangement of a representative unit or cell that allows solution of the governing differential equations or enables computation of the thermal properties through appropriate analogy. As heat flows from one phase to another phase, thermal gradient changes due to the interfacial thermal resistance. Therefore, it is essential to account for the thermal interface between the solid and fluid phase. Furthermore, simplified modelling techniques frequently employ one dimensional heat flow, which can be justified by ensuring insulation or infinite thermal resistance in the lateral direction. If the heating surface of the specimen is significantly larger than its thickness, then the heat flow in through-thickness direction can also be assumed as one-dimensional.

Sierpinski carpet, a deterministic fractal, is created by recursively subdividing a square into nine smaller blocks and then removing the central square. Standard Sierpinski carpet, which is generated by subdividing the initial square into nine congruent squares, has a fractal dimension of 1.893. By altering the initial size of the square and the size of the central cut-out, a Sierpinski carpet having a different fractal dimension can be generated (Gefen et al. 1980, 1984; Yu and Yao 1988). It is worth noting that, for deterministic fractal, after each iteration the porosity of the carpet changes, although the fractal dimension remains the same. However, for stochastic fractals found in nature, fractal dimensions of pore space was found to be increasing with the increase in porosity. For instance, Katz and Thompson (1985) studied pore fractal dimension of sandstones using scanning electron microscopy. Their results showed an increased pore space fractal dimension with porosity. Furthermore, Yu et al.'s work (2001) on fractal characteristics of textile fabrics also reported the same trend. As discussed in an earlier section of this research, mortar specimen studied using box-counting method also follow the aforementioned trend. In addition, the pore space fractal dimension of cement mortar approaches a Euclidian dimension of 2, indicating an area-filling nature of pore fractality.

In this work, a modified version of the fractal geometry-based model developed by Ma et al. (2003) was used to predict the thermal conductivities of the cement mortar exposed to different elevated temperatures. In order to model the heat conduction, the mortar microstructure is simulated using a Sierpinski carpet having the same porosity and fractal dimension as the mortar at different temperatures. The thermal conductivity is then computed from a thermal-electrical circuit analogy which requires the assumption of one-dimensional heat flow. Note that a two-dimensional temperature distribution is expected to output a more accurate results (Yu and Cheng 2002). However, simplified one-dimensional assumption is also reported to be reliable so long as the ratio of the thermal conductivity of continuous phase to that of the dispersed phase is about 100 (Ochiai 1993), which true for the cement-based mortar especially upon exposure to elevated temperature.

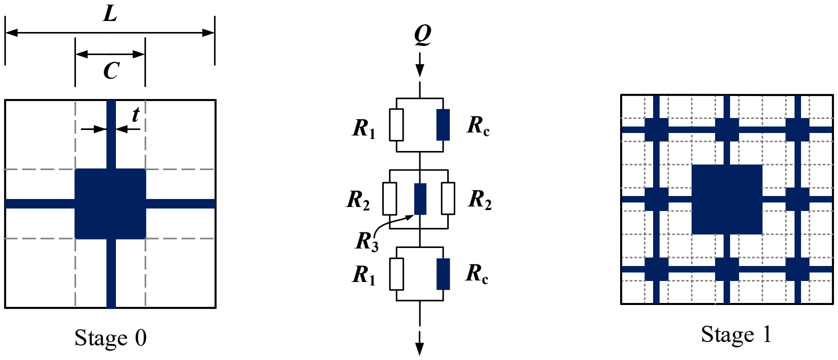

Figure 4.15 Thermal-electrical analogy based on Sierpinski carpet; only two stages are shown.

Pore structure of the mortar is simulated through an appropriate selection of the geometry of Sierpinski carpet where the length of the side and the cut-out are adjusted using an iterative approach. Figure 4.15 shows the modified Sierpinski carpet and the corresponding electrical circuit analogy employed in this model. The dark regions in the figure are the solid particles, whereas the white regions represent the pore space. As illustrated in the schematics, the fractal dimension and the porosity of the simulated geometry vary depending on the side length, *L* and cut-out size, *C*. Although the fractal dimension does not change for a given set of *L* and *C* values, the porosity decreases as the iteration proceeds to the next stage when generating the carpet. The fractal dimension and the porosity can be computed using Equation 4.10 and 4.11 as follows:

$$L^{D_f} = L^2 - C^2 \tag{4.10}$$

$$\varphi = \left(\frac{L^2 - C^2}{L^2} \right)^{n+1} \tag{4.11}$$

where D_f is the fractal dimension, ϕ is the porosity, and n is the stage or number of iterations. For instance, with $L = 7$ and $C = 3$, the stage-zero Sierpinski carpet's fractal dimension is 1.896 and porosity is 0.816, at stage-one the fractal dimension remains the same but the porosity reduces to 0.667. Note that the standard configuration of Sierpinski carpet does not provide any connectivity among the dark regions. Therefore, a modified form of Sierpinski carpet was employed to simulate the connectivity between solid particles. The connecting elements, in the form of contact thermal resistance between solid particles, was modelled using bars having a width of *t*. However, the lateral contact resistances were taken as zero indicating an infinite lateral thermal resistance which is characteristic of one-dimensional heat flow phenomenon.

In order to evaluate the thermal conductivity using an electrical circuit analogy, the resistances of each element of the circuit needs to be determined. It is well known that thermal resistance of a material is dependent on its geometry and thermal properties. Therefore, an expression for thermal resistance can be derived from Fourier's Law of heat conduction as $R = L/(kA)$, where L is the length of resistive element, k is the thermal conductivity, and A is the cross-sectional area. Figure 4.15 depicts the arrangements of resistance corresponding to pore space, solid, and thermal contact between the solid particles. Each resistance value is calculated as follows:

$$R_c = \frac{(L-C)/2}{k_s t} \tag{4.12}$$

$$R_1 = \frac{(L-C)/2}{k_a (L-t)} \tag{4.13}$$

$$R_2 = \frac{C}{k_a (L-C)/2} \tag{4.14}$$

$$R_3 = \frac{1}{k_s} \tag{4.15}$$

where R_c is the contact resistance, R_1 is the resistance of pore space layer across the heat flow direction located before or after the solid central region, R_2 is the resistance of pore space positioned parallel to the central solid region, R_3 is the resistance of solid central region, k_s is the thermal conductivity of the solid, and k_a is the thermal conductivity of air.

It can be seen from Equation 4.14 that the contact resistance was not considered as part of the circuit due to its negligible effect on the overall resistance (Ma et al. 2003). It has been found that ignoring the lateral contact resistance produces an error only in the range of 0.006–0.05% for the usual range of k_s/k_a values, which is negligible. By excluding this lateral contact resistance from the heat flow calculation, the computational procedure can be significantly simplified.

The total resistance, R_t, of the circuit for the stage-zero Sierpinski carpet is:

$$R_t = \frac{2R_1R_c}{R_1 + R_c} + \frac{{R_2}^2R_3}{2R_2R_3 + R_2^2} \tag{4.16}$$

The effective thermal conductivity of the stage-zero carpet can be expressed as follows:

$$k_{e(0)} = k_a\left[\frac{1 - C/L}{t^*(\beta_0 - 1) + 1} + \frac{C}{C(\beta_0 - 1) + L}\right]^{-1} \tag{4.17}$$

where $t^* = t/L$ and $\beta_0 = k_s/k_a$.

Similarly, the effective thermal conductivity of stage-one Sierpinski carpet can be derived by regarding the regions, except the central region, as having an effective thermal conductivity of $k_{e(0)}$, and replacing β_0 with β_1 as follows:

$$\beta_1 = \beta_0\frac{k_a}{k_{e(0)}} \tag{4.18}$$

A generalized form of the thermal conductivity after n^{th} iteration can be expressed as shown in Equation 4.19 (Ma et al. 2003):

$$k_{e(n)} = k_{e(n-1)}\left[\frac{1 - C/L}{t^*(\beta_{n-1} - 1) + 1} + \frac{C}{C(\beta_{n-1} - 1) + L}\right]^{-1} \tag{4.19}$$

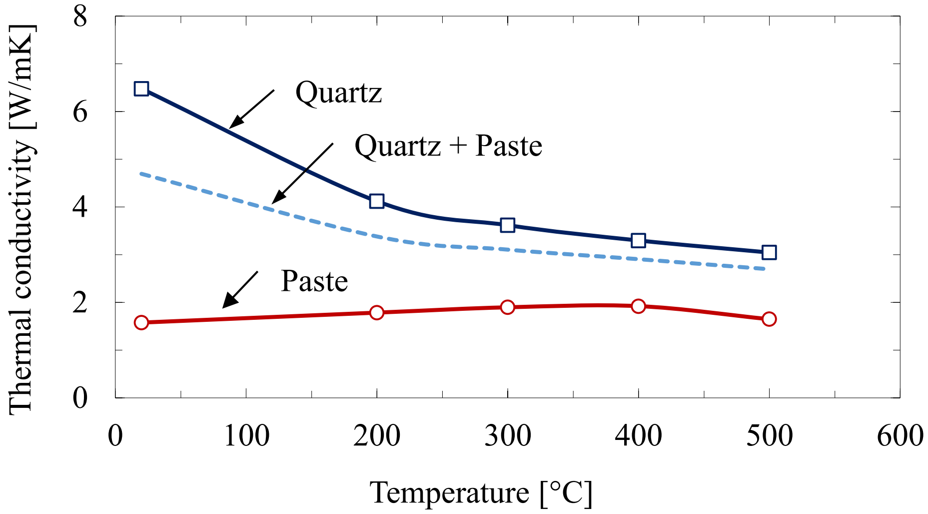

Figure 4.16 Combined thermal conductivity of quartz and cement paste. Note that the experimental data for quartz and paste were adopted from Harmathy (1970).

In order to compute the effective thermal conductivity using this model, first a Sierpinski carpet having specific values of L and C that reflect the desired fractal dimension of the mortar must be selected. This is accomplished by a trial-and-error procedure. The required number of iteration stage is then determined based on Equation 4.11 matching the porosity of the mortar. It is worth mentioning that the parameter t^*, defining the contact resistance must be determined experimentally in order to use Equation 4.19. Feng et al. (2004) suggested that for porous materials a value of t^* in the vicinity of 0.009 yields a reasonably accurate results.

Since the solid component of the mortar is composed of hydrated cement paste and fine aggregates, the thermal conductivity of solid phase, k_s, is determined, using a suitable model, by regarding it as a two-phase solid mixture with quartz as the dispersed phase and cement paste as the continuous phase. Cheng and Vachon (1969) proposed one such model applicable to solid mixture having a thermal conductivity ratio between the dispersed and the continuous phase less than 100. The thermal conductivity of the combined solid mixture calculated using this model is presented in Figure 4.16.

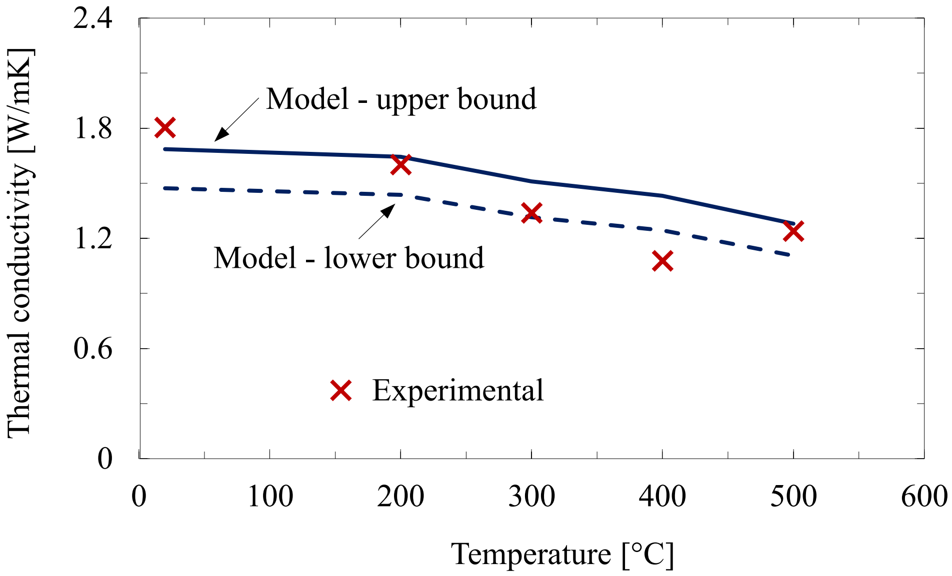

Figure 4.17 Prediction of thermal conductivity of the plain mortar using fractal approach.

The effective thermal conductivities of the mortar as predicted by the fractal model is shown in Figure 4.17. Notice that two bounds of the model predicted values are plotted along with the experimentally evaluated results. The upper bound corresponds to the t^* value of 0.015, whereas the lower bound was calculated with a value of 0.012. While a theoretical expression regarding t^* has not been established, the aforementioned values were estimated based on regression analysis of the experimental data. It is worth noting that once an appropriate value of t^* is estimated based on several experimental data, this fractal model can be expected to yield fairly accurate results for partially water saturated mortar or concrete. Some of the limitations of the model include rectangular shape pores and solids associated with the adopted Sierpinski carpet. Although it is possible to simulate the pore geometry using circular or elliptical cut-outs while generating the Sierpinski carpet, the solution for the effective thermal conductivity would be computationally intensive.

4.7 Conclusions

In this work, the effect of the moisture content on the thermal conductivity was not studied at elevated temperature due to time limitations. A further look at the influence of moisture may reveal more interesting aspect of microstructure-property relationship. Modelling using fractal approach may be improved by developing a method to theoretically relate the thermal contact resistance with microstructural parameters. Nevertheless, one may find the results of this study useful while investigating the performance of cement-based materials at extreme events such as exposure to fire. Based on the study conducted in this investigation, the following concluding remarks can be made:

- Presence of moisture increases thermal conductivity and specific heat due to the partial or full replacement of pore space with water, which is highly conductive and can store considerably higher amount heat.
- Thermal diffusivity of mortar at 20 °C decreases with the increase in moisture content.
- At elevated temperature, the thermal conductivity reduces on account of the thermal decomposition of the hydrated cement paste.
- Release of the physically and chemically bound water increases the volumetric heat capacity of the mortar as the exposure temperature rises.
- The effect of polyester fibre on the thermal properties is marginal. Its ability to control the internal water vapour manifests through the reduction in specific heat of the mortar.
- The fractal geometry-based model has shown to be able to predict thermal conductivity fairly accurately.

CHAPTER 5. MECHANICAL BEHAVIOUR

5.1 Introduction

The mechanical properties of cement-based materials, are largely influenced by those of each constituent component and of the interface between them. Macroscopically, concrete is composed of the mortar matrix with a dispersed coarse aggregate phase which may be composed of one or more minerals. The mortar in turn consists of hydrated cement paste and fine aggregates. It is essential to realize that the strength of these cement-based composites differs substantially from the strength of the components especially due to the interface between the matrix and the aggregates.

The interfacial transition zone (ITZ) is the region that forms in the immediate vicinity of the solid inclusions embedded in hydrated cement paste. In concrete or mortar, the ITZ forms around aggregates, reinforcing bars, and fibres. The extent of the ITZ depends upon the water-to-cementitious materials ratio (w/c), the presence of chemical and mineral admixtures, and the mixing technique (Mindess et al. 2003). The ITZ is characterized by a significantly higher porosity than that of the bulk cement paste, making it one of the most critical phases within the microstructure when controlling the strength as well as durability related aspects of cement-based materials. It is predominantly composed of ettringite and relatively larger sized CH crystals forming oriented layers around the embedment (Mehta et al. 2006). There are several reasons that are frequently cited as the cause of such porous regions. First, the increased accumulation of water on the surface of larger embedded particles causes a localized rise in w/c ratio. Second, bleeding in freshly placed concrete further increases this w/c ratio. Third, inefficient packing of the cement particles around the aggregates, which results in an increase in porosity. Fourth, in the ITZ, the w/c ratio is relatively higher than elsewhere, and this promotes the formation of larger CH crystals, which in turn renders a weaker paste-aggregate bond. The thickness of the ITZ around aggregates is largely dependent on the size and gradation of aggregates. It has been suggested that poorly graded aggregates tend to attract a larger amount of water and thereby are responsible for a larger thickness of the ITZ (Ollivier et al. 1995). It is generally accepted that the presence of numerous microcracks in the ITZ before application of loading is the primary reason for it to be a strength-limiting factor for concrete and mortar. These cracks may develop due to the differential displacement of the aggregates and the surrounding paste (Woodson 2009). It may also form because of the thermally induced tensile strain in hydrated cement paste and aggregates having different stiffness. When concrete is subjected to external load, fracture usually originates in the ITZ owing to the fact that relative lower amount of energy is required to initiate the unstable crack growth in the ITZ due to its lower tensile strength (Neville 2011; Shah and Winter 1968). Therefore, improving the microstructure of ITZ is the key to enhance the overall performance of cement-based materials. There are several well established steps that result in a substantial densification of the ITZ and resultant reduction in it thickness. These include: lower w/c ratio, incorporating silica fume, use of properly graded aggregates and, incorporating other specialized chemical admixture (Diamond and Huang 2001; Goldman and Bentur 1992).

Compressive strength is the most commonly evaluated property of cement based composites in routine engineering practice because it is a dominating design parameter that in turn informs other mechanical and durability related properties. Under uniaxial compressive load, the observed stress-strain response is linear until the loading reaches a point where microcracks in ITZ grow in numbers and even coalesce to wider cracks, and thus the concrete gradually exhibits a non-linear behaviour (Mehta et al. 2006; Mindess et al. 2003). After reaching the ultimate strength, due to the growth of unstable cracks, the descending branch of the stress-strain response leads to the failure stage—under the combined action of primary compressive load and secondary tensile stresses induced by imposed compressive load—in a generally quasi-brittle manner. While concrete is significantly strong in compression, it is relatively weak in tension due to the relative ease of crack propagation under tensile loading. It is worth noting here that under bending, the failure triggers due to the combined action of shear, compression, and tensile stresses developed due to imposed loads.

Exposure to elevated temperature causes physical and chemical transformation of hydrated cement paste. The physical structure and the chemical composition of the hydrated products undergo changes when losing water and so, understandably the HCP undergoes changes under elevated temperatures (Khoury 1992). As the exposure temperature increases, the response of the heated concrete or mortar to external load also evolves. As mentioned earlier in Section 2.2.3, the ITZ is mainly composed of AFt and CH which after sustained exposure to elevated temperatures, undergo thermal decomposition causing the loss of water through dehydration. Furthermore, the loss of water from poorly crystalline C-S-H, the most important strength contributing hydration product, is associated with reduction in disjoining pressure which affects the van der Waals forces of attraction in C-S-H (Mehta et al. 2006; Mindess et al. 2003; Neville 2011). In addition, there is a coarsening of capillary pores (Rostásy et al. 1980b) when exposed to elevated temperatures, which can be expected to have influence on the surface area of C-S-H. A reduction in the surface area of C-S-H results a decrease in the overall residual or in situ mechanical properties (Mehta et al. 2006).

The loss of water from the HCP not only increases ITZ porosity but also results in additional microcracks due to the pore pressure build-up. Numerous thermally induced cracks also develop in the ITZ due to the differential thermal expansion between cement paste and aggregates, which may extend into the bulk cement paste depending on the exposure temperature and soaking duration. Consequently, the residual mechanical response of the heated concrete under compressive load may reduce in a non-linear manner even at a relatively lower level of applied load.

5.2 Objectives

It is essential to assess the structural performance of a cement based composite after exposure to elevated temperature. Knowledge of the residual strength may help fix the load carrying capacity in the post-exposure scenario. Therefore, the objectives of this chapter are to evaluate the residual mechanical properties namely, compressive strength, the modulus of elasticity and Poisson's ratio. In order to correlate the residual mechanical performance with the microstructural parameters, the fracture energy and fracture toughness of prismatic mortar specimens were assessed and described using fractal geometry developed under sustained elevated temperatures.

5.3 Background

The mechanical properties of concrete and mortar generally degrade due to the thermal decomposition of hydration products. The transformation of microstructure especially the formation of microcracks has considerable influence on the load carrying capacity. However, in the initial stages of heat, between 100–300 °C, one may observe an increase in strength. This is due to the hydration of unreacted cement particles or the rehydration of already decomposed products (Fares et al. 2009). In addition, once the moisture between layers of C-S-H releases to the atmosphere, the resulting reduction in disjoining pressure enhances the strength. It has also been shown that the compressive and flexural strength of these materials at elevated temperature vary depending on whether the tests are performed 'hot', that is while the specimen is being heated or after cooling down to ambient temperature. In situ tests retain relative higher proportion of initial strength compared to residual tests. If the released moisture is confined within the capillary pore space, the strength could increase or decrease depending on the C/S ratio in C-S-H. At low C/S ratio, the formation of tobermorite gel causes an increase in strength (Khoury 1992). On the other hand, high C/S ratio renders the material weaker because of the presence of a crystalline form of C-S-H. There are several reasons that are cited for the higher reduction of strength in residual tests. First of all, at cooling stage specimen reabsorbs atmospheric moisture. This absorbed moisture reacts with CaO and forms CH which is expansive and responsible for additional microcracks (Dias et al. 1990). Secondly, heated specimen experience higher thermal gradient upon cooling and thereby causing increased amount interfacial as well as matrix microcracks. However, it has also been reported that storing heated concrete at high relative humidity environment for long time may help recover a fraction of the strength (Weigler and Fischer 1972).

The mineralogical composition of aggregates used in concrete and mortar plays important role on the strength at elevated temperatures. Concrete prepared with calcareous aggregates are known to retain higher fraction of strength at ambient temperature due to the endothermic calcination process (Neville 2011). On the other hand, siliceous aggregate concrete loses relatively higher fraction of original strength because of large amount of microcracks caused by differential thermal expansion between the cement paste and the aggregates.

As mentioned earlier, cement-based materials contain microcracks even before the application of load. The mechanism of fracture in such materials, having pre-existing cracks, can be described using energy principles. The development of modern fracture mechanics was based on the work of Griffith, who proposed an energy balance between the decrease in potential energy and the associated increase in surface energy required to create a new crack surface. However, this classical approach is applicable to perfectly brittle material only. Based on the principle of linear elastic fracture mechanics (LEFM), for perfectly brittle material, Mode I stress intensity factor due to a centre crack in a plate subjected to uniaxial tensile load is expressed as $K_I = \sigma\sqrt{\pi a}g(a/b)$, where σ is the nominal stress, a is the half of the crack length, $g(a/b)$ is a correction factor that depends on the geometry of the specimen and the loading configuration, b is the width of the plate. An unstable fracture occurs when this stress intensity factor reaches a critical value, also called fracture toughness factor.

According to LEFM, the stress that develop at the crack tip reaches singularity, which is not true for real materials. Therefore, for materials that can undergo yielding, a zone ahead of crack tip must exist where plastic deformation occurs. It is necessary to apply appropriate corrections to account for the crack tip plasticity. If the size of this inelastic zone is small compared to the original crack length, a simple modification would suffice, otherwise alternative parameters, considering nonlinear behaviour, must be introduced to describe crack propagation. When the size of the crack tip plastic zone is small, compared to initial crack length, two approaches are commonly employed—Irwin's (1958) effective crack length approach and Dugdale's (1960) plastic strip model. In Irwin's approach, the effective fracture toughness is evaluated by calculating the effective crack length as the sum of original crack length and a fraction of plastic zone such that the force carried by it is equivalent to the stress, in excess of yield stress of the material, that is developed in the plastic zone. On the other hand, Dugdale's model considers a fictitious crack extension at the tip of original crack which is still capable of sustaining the yield stress that tends to bring the cracked surfaces together. The size of this fictitious zone is determined in such a way that the sum of the stress intensity factors, at the tip of fictitious crack, due to applied load and crack closing pressure equals to zero. But, the fracture phenomenon in cement-based materials, as in other quasi-brittle materials, exhibits strain softening behaviour rather than yielding. It cannot be adequately described using the aforementioned plastic zone corrections since the size of the inelastic zone is considerably larger than initial crack length.

In quasi-brittle and heterogeneous materials such as concrete, the inelastic zone is called the fracture process zone (FPZ) where several mechanisms, that are responsible for toughening during crack propagation, are found. These include microcrack shielding, crack deflection due to weaker interface or intercepting pre-existing flaws, aggregate interlocking, crack tip blunting when a propagating crack intercepts air-voids, and crack branching. All of these mechanisms cause dissipation of additional energy enabling the crack to advance (Bindiganavile and Banthia 2005; Shah et al. 1995). It is the presence of this fracture process zone that hinders the direct application of LEFM to analyze and establish acceptable fracture mechanical failure criteria. In order to model the effect of fracture process zone, two most commonly used methods are available—the cohesive crack model (Hillerborg et al. 1976) and the effective crack model (Jenq and Shah 1985). In the former one, the toughening mechanism is modelled by applying a closing pressure at the crack tip, whereas in the latter, an equivalent traction-free crack is assumed for which LEFM criterion is applicable.

There are very few studies concerning the fracture mechanical behaviour of cement-based materials exposed to elevated temperatures. In this study, fracture toughness, critical crack tip opening displacement, and *R*-curve behaviour were evaluated using compliance calibration method. In addition, a response prediction model based on fracture mechanical parameters is also discussed.

5.4 Materials

The materials used for specimen preparation consisted of general purpose Type GU cement conforming to CSA A3000 (2013), a fine aggregate prepared by blending three different grades of commercially manufactured silica sand containing about 94% crystalline silica, 4% aluminum oxide, and trace amount of iron oxide and titanium oxide. This grain size distribution, as shown in Section 3.4.1, of the blend falls within the specified limits of ASTM C33 (2003) and thus yields a mortar with adequate cohesiveness and plasticity. The mortar mixture was designed to have a fine aggregate-to-cement ratio of 3 with a w/c ratio of 0.5. In addition to the plain mortar mixture, a series of fibre reinforced mortar specimens was also prepared using polyester fibre having a diameter of 50 μm and a length of 12 mm with a volume fraction of 0.1–0.3%. Since the incorporation of microfibre is accompanied by a loss of workability, especially at higher volume fraction, an adequate amount of high range water reducing admixture (HRWRA) was added to restore the workability of the fresh mortar. The dosage of HRWRA was adjusted by monitoring the consistency of fresh mortar using flow table tests in accordance with ASTM C1437 (2013b). The measured flow value for the plain mortar was 150–170 mm and that for the fibre reinforced mortar was 135–145 mm.

The mortar mixture was prepared using a high-shear and rotary type mixing machine. The machine has two main rotating components—the rotor and the pan, along with a regulator which can be used to set desired rotational speed for either rotating component independently and thus allows optimal mixing of the ingredients. In order to achieve a uniform mixture, the fine aggregates and cement were first mixed in a mixing bowl manually using a hand trowel in dry condition. After transferring them to the pan, both the rotor and the mixing pan were set to agitate the mixture at a high rotational speed for 15 minutes. About three-quarter of the total water, properly mixed with HRWRA, was then added to the mixture and agitated at high speed for additional 20 minutes. Afterwards, the polyester fibre was added into the pan gradually, while the machine kept agitating at a medium speed, to ensure that fibres do not clumped together. Once all the fibres were added, the machine was switched off and rotor blades were scrapped off. The remaining water was then transferred and the mortar was mixed for additional 15 minutes allowing optimal dispersion of the fibres in the mortar matrix. Before casting the mortar into the specimen molds, a flow table test was conducted to measure the consistency of the mortar. It is worth mentioning that the dosage of HRWRA was determined using a trial batch to maintain a consistent level of workability of the mortar.

For compression tests, cylindrical specimens, having a dimeter of 75 mm and a height of 150 mm, were cast in three layers using vibration to achieve adequate compaction. Prismatic specimens of 50 × 50 × 200 mm were also cast for fracture tests. After casting, the specimens were kept sealed in air-tight plastic bags for 24 hours to prevent the loss of moisture. After 24 hours of sealed curing, the specimen were demolded and transferred to a controlled curing chamber where a relative humidity of 95% at a temperature of 21 °C was maintained. The specimens were cured in this chamber for 60 days prior to conducting experiments.

5.5 Experimental Details

Mechanical properties of cement-based materials may be evaluated either at residual state or in situ state. In this research, the compression and fracture experiments of the mortar were conducted at residual state, where the specimens were first heated to the desired temperatures for a specified soaking period and then cooled down to ambient temperature before applying load.

5.5.1 Exposure to Elevated Temperature

In order to determine the effect of elevated temperature, the mortar specimens were exposed to sustained high temperature by placing them into an electric furnace. The furnace is equipped with a programmable microcontroller which is capable of applying heat by following a specified heating profile in terms of heating ramp, sustained soaking period, and ambient cooling temperature. For the purpose of this study, a heating rate of 5 °C/minute was specified to avoid an explosion that might occur through rapid build-up of vapour pressure. The heating profile used in this study is discussed previously and shown in Section 3.4.3. It is to be noted that the specimens were over-dried at a temperature of 105 °C for a period of 24 hours. The purpose of this pre-drying is twofold. First, it reduces the likelihood of explosive event during thermal exposure. Second, it provides a fairly consistent level capillary pore condition by removing the evaporable water. These pre-dried specimens were exposed to a sustained temperature ranging from 200–600 °C. Once the temperature reaches the target set-point, the microcontroller switches to the soaking segment of the heating profile where the heating element is switched off and on at an appropriate cycle to maintain the desired temperature, with a tolerance of ±1°C, for a 2-hour soaking period. This 2-hour soaking period was deemed to be satisfactory since most microstructural changes and resultant damage to the system occur by then and an equilibrium is established in the first 2 hours of the exposure. At the end of this soaking period, the specimens were allowed to cool down to ambient temperature, through natural cooling, over a period of 2–4 hours depending on the heating temperature.

5.5.2 Uniaxial Compression Tests

The effect of sustained elevated temperature on the compressive strength of mortar was evaluated by conducting uniaxial compression tests on specimens after a 2-hour of exposure to different levels of sustained elevated temperatures. Cylindrical specimens having a diameter of 75 mm and a height of 150 mm were first examined for planeness requirements as specified in ASTM C469 (2010). Where required after preliminary inspection, the specimen ends were ground for 40 s on each side, before placing them into the furnace. In order to measure the longitudinal and transverse displacements, a compressometer was used. It was equipped with two linear variable displacement transducers (LVDT), one for each of the aforementioned displacement measurements. Both LVDTs were placed in such a way that they pivot around a point located diametrically opposite side on the supporting yoke. The compressometer was attached to the specimen at mid-height by setting a gauge length of 100 mm between the support points. Compressive load was then applied using a servohydraulic loading frame having a capacity of 1000 kN. The test was performed using a displacement controlled mode with a displacement rate of 1 mm/minute. The load and displacement histories from the loading frame and compressometer were recorded using a data acquisition device at rate of 5 Hz. Since the LVDTs were placed at diametrically opposite point with respect to a pivotal axis on the circumference, the measured displacement was twice the actual deformation of the specimen caused by the applied load. This has been taken into account while performing the calculation of stress-strain response.

5.5.3 Fracture Tests

In order to determine the fracture properties of cement mortar after an exposure to elevated temperature, a series of four-point bending tests were conducted. The size of the prismatic specimen was 50 × 50 × 200 with a span length of 150 mm. In order to aid in the analysis of the fracture mechanical parameters, a notch having a length of 20% of the specimen depth (50 mm) and a width of 1.5 mm. The midpsan deflection of the specimen was measured by mounting a yoke system, equipped with two LVDTs, around the specimen which enabled the recording of true deflection of the specimen by avoiding any extraneous displacements such as settlement of either supports or displacement that may result from the undesirable twist of the specimen during the test. Fig 5.1 shows the schematic representation of the experimental setup.

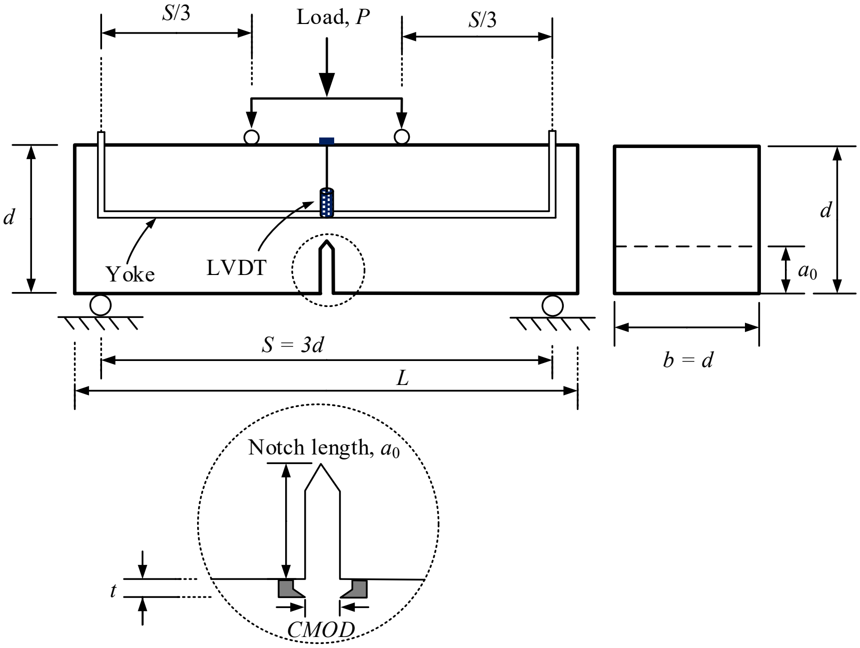

Figure 5.1 Fracture test setup using four-point bending.

Experimental determination of mode I fracture toughness requires the displacement data in the direction of crack opening, which can be found from the measured value of crack mouth opening displacement (CMOD). In this work, as shown in Figure 5.1, the CMOD was measured by placing an extensometer across the notch using a set knife edge grips attached on the either side of the notch. It is worth mentioning that the measured value of the CMOD requires an adjustment due to the thickness of the attached grips. The tests were conducted using a displacement controlled mode with a rate of 0.1 mm/minute. Since peak load under flexure was relatively low, a load cell with a capacity 25 kN was used in order to avoid noise in the recorded load history. Data from the load cell, displacement transducers, and extensometer were recorded at a frequency of 5 Hz with a data acquisition device.

5.5.4 Microstructural Properties

Pore structure characteristics of heated mortar specimens were evaluated using image processing techniques. For this purpose, the mortar specimens were subjected to 20, 200, 300, 400, and 500 °C. Thin pieces of cooled specimens were then extracted and polished for back scattered electron (BSE) imaging. High resolution images were captured at suitable magnification using scanning electron microscopy equipped with BSE and analyzed to determine several microstructural parameters. The details of this procedure is presented in Section 3.4.6.

5.6 Results and Discussions

5.6.1 Response to Uniaxial Compression

Compressive strength of cement-based composites is one of the most widely evaluated mechanical properties because of its relative ease to perform the tests and more importantly, it provides valuable insight to the other mechanical properties. In this work, the residual method of evaluation was adopted so that the compressive strength of the mortar specimen subjected to elevated temperature can be determined after cooling. This provides information regarding the residual behaviour of thermally deteriorated mortar, as shown in Figure 5.2. Note that the data shown in the Figure was averaged from three replicates.

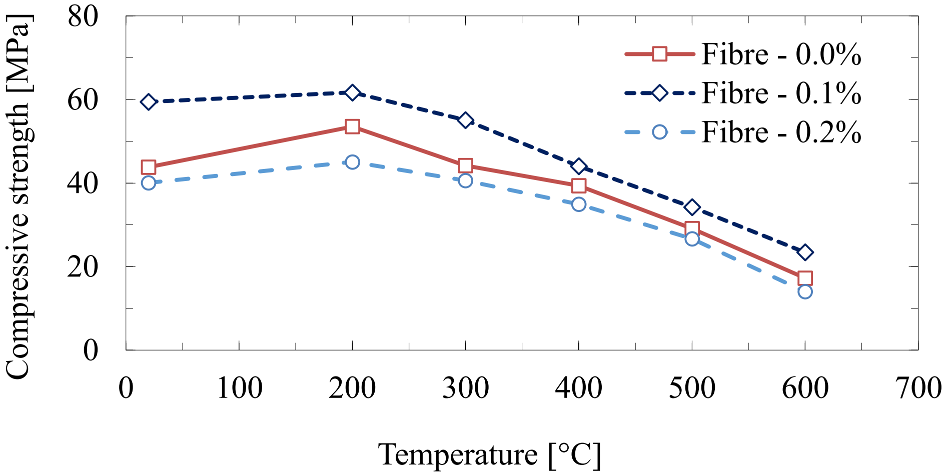

Figure 5.2 Compressive strength of the mortar at different exposure temperature.

Several aspects of the effect of elevated temperature on the compressive strength can be noticed. First, the compressive strength increases, or at worst, remains the same as the initial strength, up to 200 °C. This is due to the increased hydration of the remaining unhydrated cement particles under steam pressure resulted due to the partial release of physically or chemically combined moisture under the influence of the heat supplied (Saad et al. 1996). Although a certain fraction of strength loss is expected due to the aforementioned thermal decomposition of hydrated cement paste, it is more than compensated by the gain in strength due to the action of steam pressure in hydrating the previously unhydrated cement particles. Another probable explanation would be the reduction of disjoining pressure within the layers of C-S-H due to the dehydration which increases the van der Waals forces of attraction and thus enhances the load carrying capacity (Mehta et al. 2006; Neville 2011). There is a monotonic reduction in strength beyond an exposure temperature of 200 °C. For instance, the plain mortar loses as high as 67% of its strength at ambient temperature when heated to 600 °C. There is no noticeable influence of fibre reinforcement in arresting this drop in the compressive strength. It is to be noted that the residual strength was slightly lower than the strength measured in situ (hot test), because of the additional microstructural damage caused by the reabsorption of atmospheric moisture upon cooling (Dias et al. 1990).

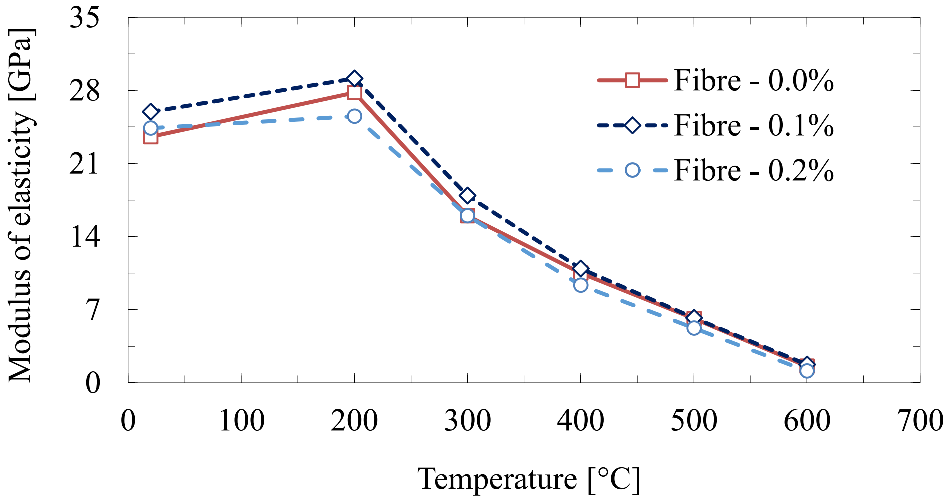

Figure 5.3 Modulus of elasticity of the mortar at different temperature.

The chord modulus of elasticity, referred to as modulus in subsequent text for simplicity, as defined by ASTM C469 (2010), is usually the preferred type of stiffness evaluation of cement-based materials that is widely used to compute serviceability requirement such as deflection. It is also an important parameter that is required when one develops model to predict structural response. Since some error in the measurement during the very initial stages of loading is a possibility, the chord modulus (as opposed to initial tangent modulus) is more representative of the material's stiffness.

The modulus of elasticity determined, as described above, from the stress-strain response is presented in Figure 5.3. Once again, an increase in the modulus was observed at 200 °C followed by a gradual drop in value with an increase in the temperature of exposure. It has been showed that the elastic modulus of concrete or mortar is considerably affected by the properties of ITZ (Mehta et al. 2006). Elevated temperatures cause hygro-thermal damage, that amplifies the already flawed microstructure of the ITZ, which in turn reduces the modulus of elasticity beyond 200 °C of exposure, making the composite more compliant than the original one.

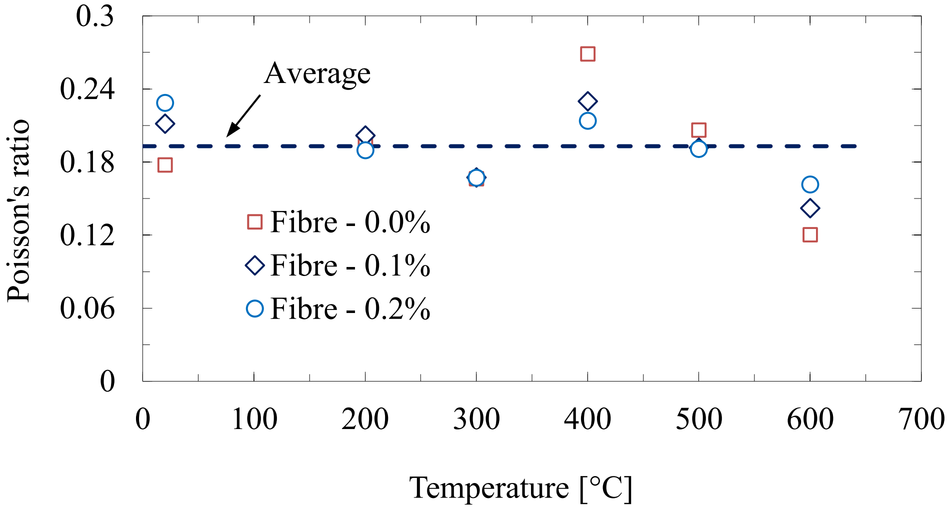

Figure 5.4 Poisson's ratio of the mortar at different temperature.

The Poisson's ratio was determined by measuring the axial and the transverse strain during a uniaxial compression test. The results for the plain and the fibre reinforced mortar are shown in Figure 5.4. The values remain largely unchanged over the course of the heating regime. However, at 600 °C, the Poisson's ratio drops noticeably across both the plain and fibre reinforced systems. It implies that the mortar has sustained a considerable degree of structural damage, resulting in a sudden loss in strength. Thus, the longitudinal deformation was decidedly high.

The axial stress-strain response of the mortar under compression is shown in Figure 5.5 and 5.6, for the plain and fibre reinforced mortar mixtures, respectively. It can be noticed that slope of the pre-peak response of the mortar does not change considerably up to a temperature of 300 °C. This indicates that the microcracking was not extensive in the paste-aggregate interface at this stage. Beyond 300 °C, the slope, and hence the elastic modulus, decreases drastically. It also indicates that the mortar developed severe microstructural damage. Further, there was a pronounced increase in the axial strain at peak stress with an increase in the temperature at 600 °C. It may be attributed to the increase in the number of cracks having a favourable orientation with respect to the direction of the applied load. One may describe the overall response of the mortar as a progressively compliant composite with an increase in the temperature of exposure.

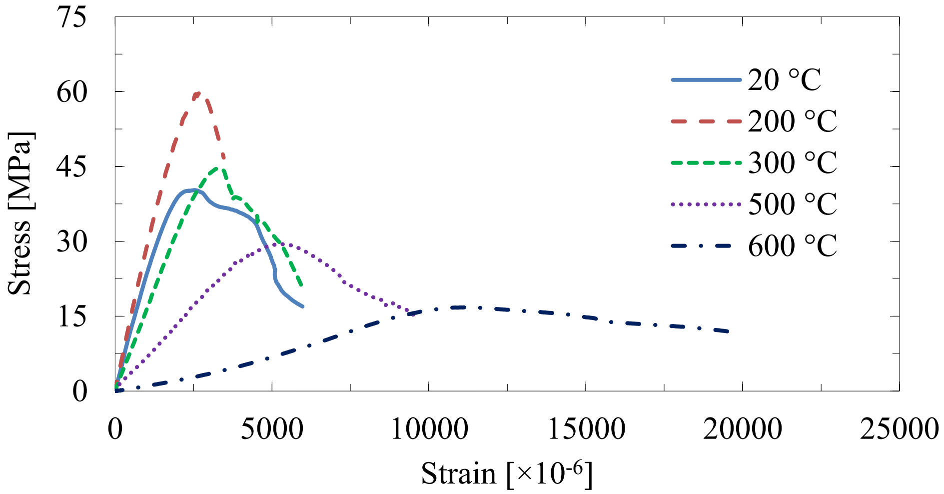

Figure 5.5 Stress-strain response of of plain mortar.

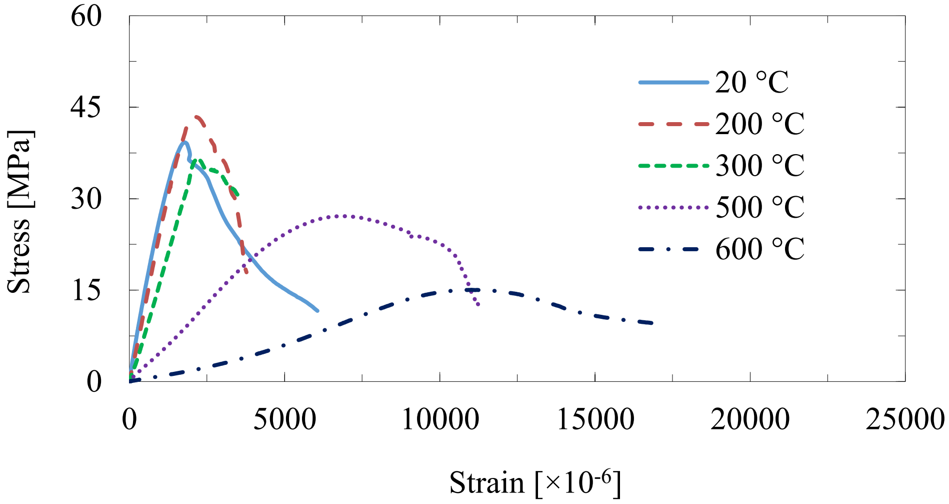

Figure 5.6 Stress-strain response of mortar with 0.2% fibre.

5.6.1.1 Analysis of Uniaxial Compression Response

The mechanical properties of a material can be modelled if the microstructural parameters are known. For instance, the strength-microstructure relationship of the heated mortar may be described by determining its porosity. It should be emphasized that a single parameter model such as strength-porosity correlation does not always predict accurate results. Two materials having the same porosity but different pore size distribution as well as connectivity could yield a dramatically different properties. Furthermore, in case of concrete or mortar, ITZ is found to be the most critical phase of the microstructure controlling the response to applied stresses.

Two simple regression models, as illustrated in Figure 5.7 and 5.8, are attempted in this study to correlate the compressive strength of the mortar with their porosities and mean pore radii, determined by processing images captured using scanning electron microscopy. It is well established (Mindess et al. 2003) that the strength of cement-based composite varies with the third power of gel to space ratio, which implies an inverse relationship between the strength and the porosity. The porosity of the mortar appears to correlate well with the compressive strength measured in this study, especially for the mixtures with fibre volume fraction of 0.0–

0.1%. Note that the moisture in the microstructure makes it difficult for single parameter models to predict reliable strength. Consequently, the above mentioned correlations are presented by including only the data points beyond an exposure temperature of 200 °C in order to exclude the influence of moisture related to reduction in the disjoining pressure in C-S-H layer.

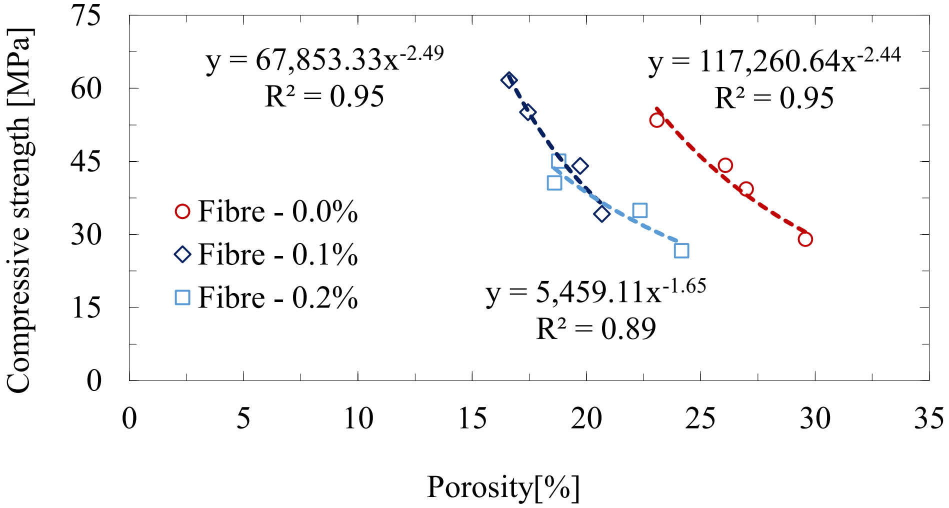

Figure 5.7 Effect of porosity on the compressive strength of mortar at elevated temperatures.

Another single parameter regression model, correlating the mean pore radius with the compressive strength, is shown in Figure 5.8. Note that the mean pore radii were determined from two dimensional images. As explained earlier that the mortar pore space is gradually coarsened due to the coalescence and conversion of gel pores into capillary pores. It indicates that the coarsening of pore space tends to increase the connectivity of pore network causing a reduction in available load paths, and thereby a reduction in compressive strength is observed. Jambor (1973) also reported that for a given porosity the strength vary inversely with the mean pore size.

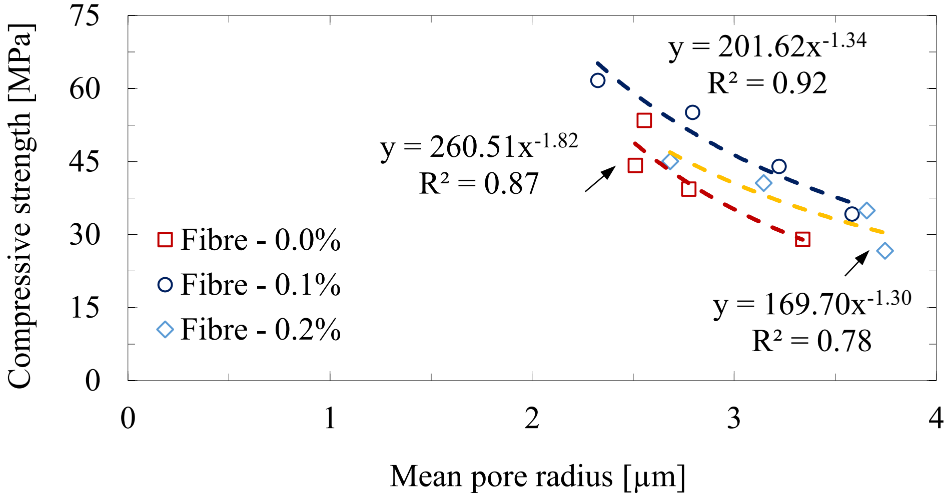

Figure 5.8 Relationship between the compressive strength and mean pore radius at elevated temperatures.

5.6.2 Flexural Response

As mentioned earlier, flexural tests were conducted using a four-point loading configuration to evaluate the properties related to fracture mechanical behaviour of the mortar after exposure to different levels of elevated temperature. The four-point loading configuration enables the analysis of experimental results and subsequent response prediction under pure bending and thus simplifies the required computations by excluding the effect of shear force that would otherwise have some influence on the experimentally determined load-deflection response.

The modulus of rupture (MOR) is often used to characterize the tensile strength of cement-based composites. However, it was found that the modulus of rupture tends to overestimate the tensile strength because of the assumed linear stress distribution across the depth of the specimen (Mehta et al. 2006). MOR of the heated mortar, measured on the cooled specimens, from four-point bending tests are shown in Figure 5.9. The trend is similar to that observed for the uniaxial compressive strength, with a generally marginal increase at 200 °C followed by a drop in MOR as the temperature continued to rise. There is no noticeable influence of the fibres on MOR at ambient temperature, although the mixtures with 0.2% fibre dosage showed about 15% reduction in MOR at 200 °C when compared to its plain counterpart. It may be attributed to the formation of additional interfacial transition zone arising from the higher fibre content resulting in a weaker fracture resistance.

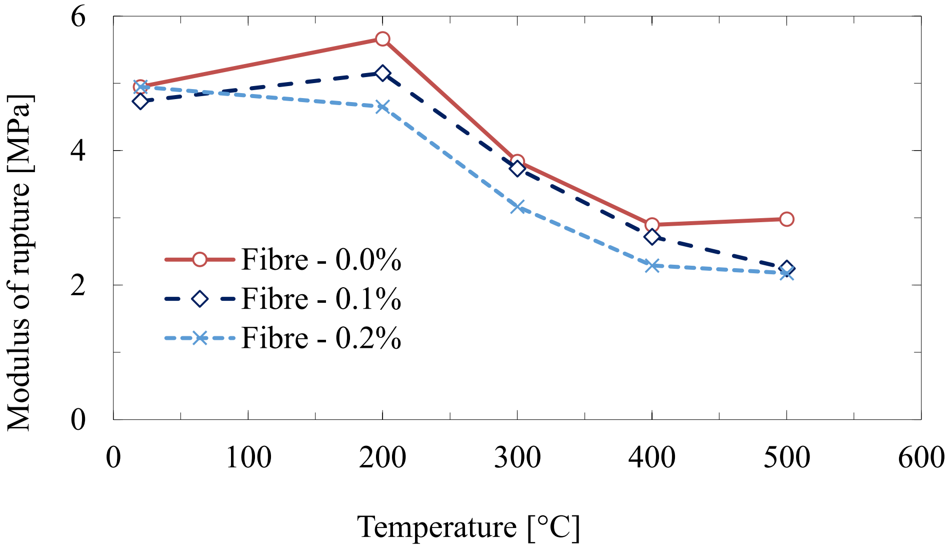

Figure 5.9 Modulus of rupture of the mortar under four-point bending.

5.6.3 Fracture Energy and Characteristic Length

The amount of energy that is dissipated during the four-point flexure can be used to calculate the fracture energy of the mortar. Figure 5.10 illustrates the calculation procedure adopted in this study. The area marked as W_0 denotes the energy absorbed due to the applied load only, whereas the area W_1 marks the work done due to the self-weight of the specimen. It has been shown that the area associated with the right tailing portion of the load-displacement curve is approximately equal to W_1 (Shah et al. 1995). Therefore, by assuming that the energy is only absorbed in the fracture process zone, one may compute the fracture energy from the total work done by the applied load and the self-weight of the specimen per unit area of the ligament as follows:

$$G_F = \frac{W_0 + 2W_1}{(b - a_0)d} \tag{5.1}$$

where G_F is the fracture energy, b and d are the width and depth of the specimen respectively, a_0 is the initial length of the notch.

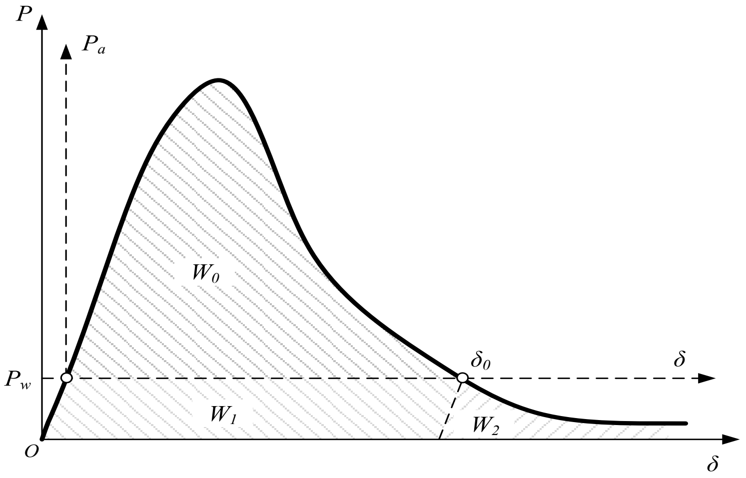

Figure 5.10 Determination of fracture energy, G_F.

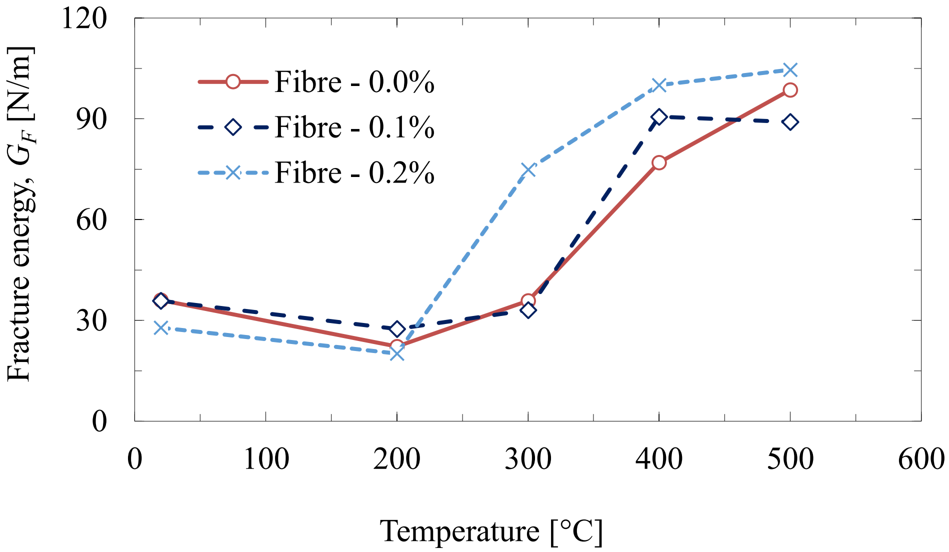

Figure 5.11 Fracture energy absorpbed during the four-point bending tests.

Fracture energies (G_F) of the mortar for different heating temperatures are shown in Figure 5.11. It can be noticed that a reduction of G_F drops initially to around 200 °C. As Bažant and Prat (1988) describes fracture as a thermally activated process, where the likelihood of fracture energy exceeding the activation energy barrier increases with the rise in temperature. They also estimated an activation temperature of 308 °C for normal strength concrete. However, in this case, the phenomenon occurs at around 200 °C. Therefore, the above mentioned drop in G_F may be attributed this activation temperature. Beyond 200 °C, an increasing trend of G_F can be observed which is characterized by a relatively ductile response as evident from the descending or softening branch of the load-CMOD response, shown in Figure 5.12. The increasing trend of G_F may be explained with the brittleness number—otherwise known as characteristic length which is discussed later in this section—of the mortar with temperature. As noticed earlier that the mortar exhibits an increasingly higher compressive and tensile strains at peak load due to thermal exposure and thereby shows relatively more ductile response. It can be observed that the low fibre dosage does not have any effect on the G_F whereas higher dosage shows a substantial increase beyond 200 °C.

It is worth stating that the values of G_F measured, using the approach described in this section, are dependent on the specimen size. It was reported that G_F increases with the increase in beam depth. This size dependence may be attributed to the undesirable energy dissipation in the area other than the fracture process zone (Shah et al. 1995). It has also been reported that the size dependency of G_F may be attributed to the reduction of so called "local fracture energy" with increased specimen dimension (Shah et al. 1995). It is, however, possible to derive a set of expressions to compute size independent fracture energy (Bazant and Pfeiffer 1987), which can then be used as a material property. There are several procedures to estimate the size independent fracture energy through flexure tests. For instance, Bažant's size effect law can be utilized to perform the computation of fracture energy from the experimental results of several geometrically scaled specimens (Bažant and Planas 1997). Another, rather convenient method of computing the size independent fracture parameters would be conducting the flexural tests using specimens having a single size but different initial notch depth. This later method is used, in this study, by adopting a computational approach proposed by Ouyang et al. (1996). According to this approach, the critical stress intensity factor and the critical crack tip opening displacement can be computed from the peak bending load using simple numerical procedure. These parameters will be utilized later in this chapter to predict the structural response of the mortar under four-point bending.

The characteristic length, also called the brittleness number, is a material property and it can be determined using the following expression (Hillerborg et al. 1976):

$$l_{ch} = \frac{EG_F}{f_t^2} \tag{5.2}$$

where l_{ch} is the characteristic length, E is the modulus of elasticity, G_F is the fracture energy, f_t is the tensile strength. Note that in the absence of experimental data, the value of f_t was estimated using the recommended expression from CEB-FIP Model Code (1993):

$$f_t = f_{MOR} \frac{2\left(d/d_0\right)^{0.7}}{1+2\left(d/d_0\right)^{0.7}} \tag{5.3}$$

where f_{MOR} is the modulus of rupture, d is the depth of the beam, and d_0 = 100 mm.

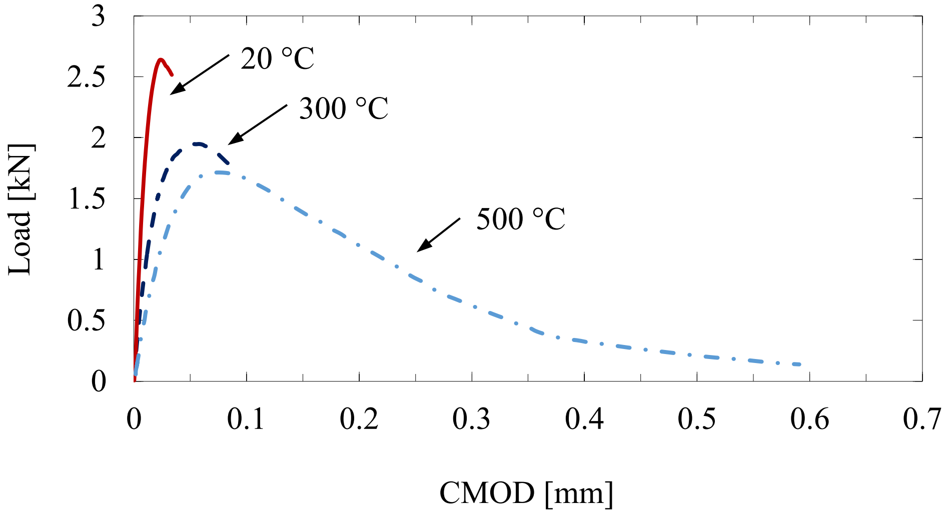

Figure 5.12 Crack mouth opening displacement of the plain mortar under four-point bending.

The estimated values of l_{ch} is plotted against the heating temperatures and is shown in Figure 5.13. Brittleness number or characteristic length is directly proportional to the length of fracture process zone of the mortar. Therefore, a larger l_{ch} value would indicate a relatively ductile behaviour characterized by an increased amount of energy dissipation. A comparison between Figure 5.11 and 5.13, reveals that even though the fracture energy remains more or less the same value for 400 °C, there is a steep drop in the characteristic length, l_{ch}, from 400 to 500 °C. This is due to the significant reduction in the elastic modulus in this range of exposure temperature.

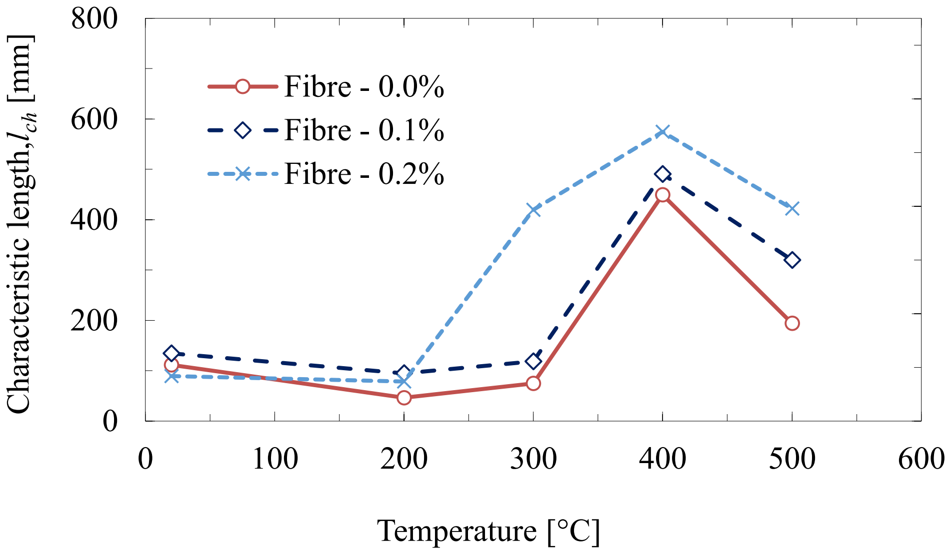

Figure 5.13 Estimated characteristic length from the fracture test.

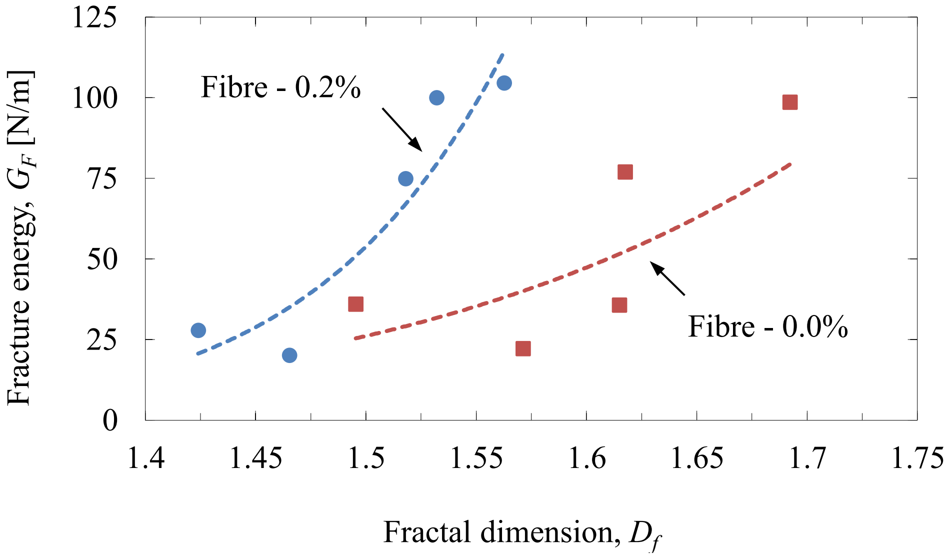

Figure 5.14 Correlation between the fracture energy and the fractal dimension of pore area.

As explained earlier in this work, the fractal concept can be used to describe the changes in the microstructural characteristics of thermally damaged mortar under sustained exposure to high temperatures. Hygro-thermal deterioration in the mortar manifests as an increase in the fractal dimension. Further, in cement-based composites, the fractal dimension may be regarded as a measure of the complexity or irregularity of the internal structure. Therefore, a higher value of fractal dimension indicates an increased roughness of the pore perimeter or increased interconnectivity of pore space or microcracks which is likely to cause increased deformation in response to applied stress, implying a more ductile response. Accordingly, a correlation between the fracture energy and the fractal dimension may be established to describe the trend in the amount of energy dissipated with the increased temperature. Figure 5.14 attempts such correlation for the plain and fibre reinforced mortar. It can be noticed that the fibre reinforced mixtures show better correlation than their plain counterpart.

5.6.4 Fracture Toughness

In cement-based composites, the length of fracture process zone ahead of the crack tip is significant which does not allow the direct application of LEFM to analyze the fracture mechanical parameters. As described earlier, this fracture process zone consumes considerable amount of energy that must be taken into account while performing the fracture analysis. In this study, the fracture toughness of the mortar subjected to sustained elevated temperatures was determined using the effective crack length, also called, the equivalent crack length method. In this method, the effective crack length is taken as the initial notch length plus the length of fracture process zone. Thus, only the remaining portion of the ligament is subjected to elastic stress, while the effective crack is assumed to be entirely traction free.

In order to determine the effective crack length, a compliance calibration-based method was adopted (Banthia and Sheng 1996). The details of the computation procedure is presented in Appendix B. Briefly, the procedure can be described as follows:

First, the bend over point—a point on the ascending portion of the load-CMOD curve which marks the end of linear behaviour of the composite—is located. Using a theoretical relationship, the elastic modulus is then computed as a function of the initial notch length, the compliance at bend over point, the nominal stress, and the geometry of the specimen. Since, the elastic modulus is a material parameter, the same value must hold true for any other point further along the load-CMOD curve for which the effective crack length is sought. Thus, by setting the expression for the elastic modulus at bend over point equal to that for any other point, one can evaluate the effective crack length using an iterative approach to solve the resulting non-linear equation having the effective crack length as the only unknown variable. The required equations to perform such computations are shown in Appendix B.

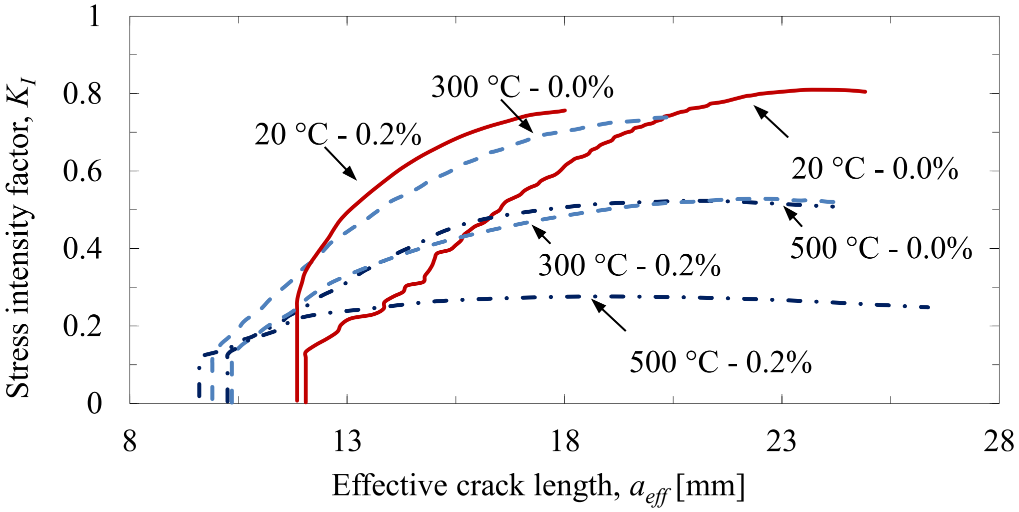

Figure 5.15 Crack growth resistance curve for the mortar at different temperatures. Note that the fibre dosages are shown in percentage.

Once the effective crack length is known, the LEFM formulations for the stress intensity factor can be used with appropriate modification factor that accounts for the loading configuration and the specimen geometry. A plot of such stress intensity factor against the effective crack length can be generated, which is known as the *R*-curve of the material. These curves describe the resistance of the material to the crack growth.

Figure 5.15 illustrates the crack growth resistance curves of the thermally damaged plain and polyester reinforced mortar. It can be noticed that the crack growth resistance of the mortar decreases with the increase in heating temperature. It is well known that a quasi-brittle material such as cement-based composites show a monotonically rising crack resistance followed by a horizontal plateau or a descending curve with the increase in crack extension. It can be observed that the thermal damage causes a drop in the rate of crack resistance indicating a gradual disappearance of the toughening mechanisms in the fracture process zone. This diminishing toughening behaviour may be the outcome of several microstructural damage. These include ineffective aggregate interlock due to severely damaged paste-aggregate interface, reduction of pore space tortuosity, and inability of the cracked voids to consume extra energy through crack-tip blunting. Notice that, at 500 °C, the crack growth resistance curve approaches the horizontal asymptote rapidly, resembling the behaviour of perfectly brittle materials having a constant crack growth resistance.

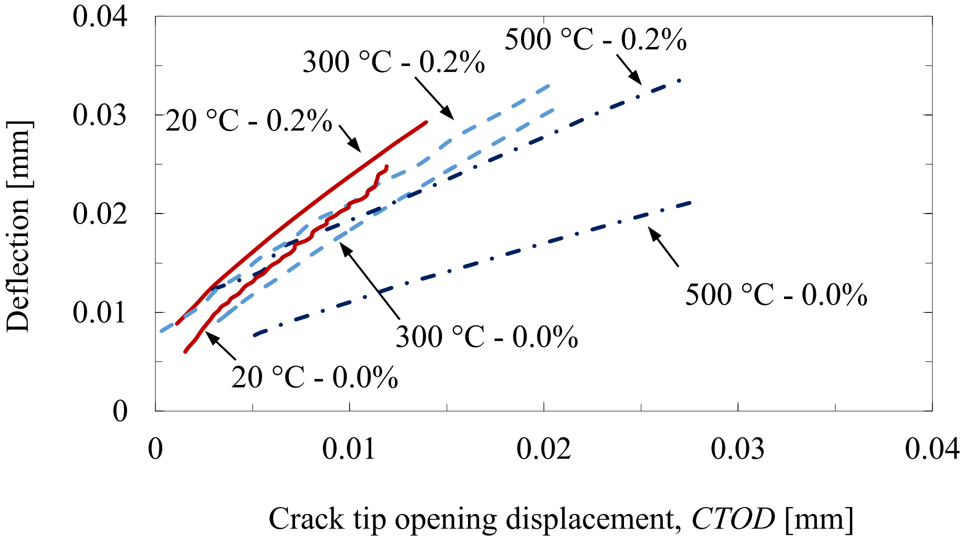

Figure 5.16 Deflection at midspan as a function of *CTOD* for the plain and fibre reinforced mortar. Note that the fibre dosages are shown in percentage.

On the other hand, the effect of fibre reinforcement on the crack growth resistance can also be noticed. At ambient temperature, the enhanced performance of the fibre reinforced mortar may be attributed to the fibre bridging action which contributes to the additional consumption of energy. However, this increased crack resistance disappears rapidly with the increase in heating temperature. Notice the considerably lower crack resistance, shown in Figure 5.15, of the fibre reinforced mortar when compared to their plain counterpart. This is because—in addition to introducing additional interfacial zones and the absence of the crack arresting mechanism due to elevated temperature—after melting the fibre bed acts as a continuously interconnected pore network which compromises the toughening mechanism.

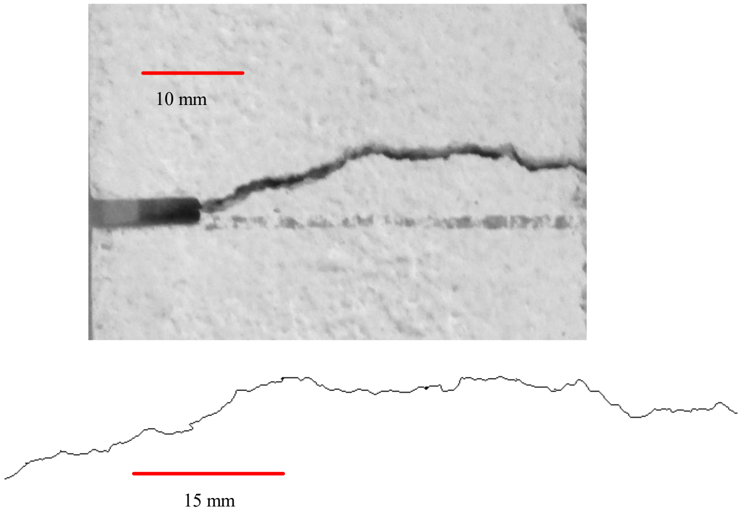

Figure 5.17 Crack surface tortuousness—an enlarged and enhanced view of the crack contour is shown at the bottom for clarity.

In Figure 5.16, the midpsan deflections are plotted against the crack tip opening displacement at different temperatures for both the plain and fibre reinforced mortar. It can be noticed that for a given deflection the crack tip opening displacement (*CTOD*) increases across all heating temperature indicating an increased compliance due to the damage sustained by the mortar. Once again the toughening of the fibre reinforcement is manifested through a reduction in *CTOD* values at ambient temperature. Although, no conclusion can be drawn from the reduction in *CTOD* for fibre reinforced mortar at elevated temperature, except it emphasizes the statement that a single parameter fracture criteria, such as the one based on K_{Ic}, cannot predict the unstable crack propagation accurately.

A typical crack profile from the four-point bending test is shown in Figure 5.17, which exhibits the tortuous nature of surface crack. Due to this tortuosity, the application of the crack growth resistance curve, in the form of K_{IC} versus a_{eff}, to describe the fracture behaviour of the mortar may not be a valid approach. According to Banthia and Sheng (1996), a *CTOD* based crack resistance curve may provide a more accurate description because the *CTOD* values approach failure condition in a stable manner when compared to the effective crack extension. Figure 5.18 and 5.19 show such crack resistance curves as a function of *CTOD*.

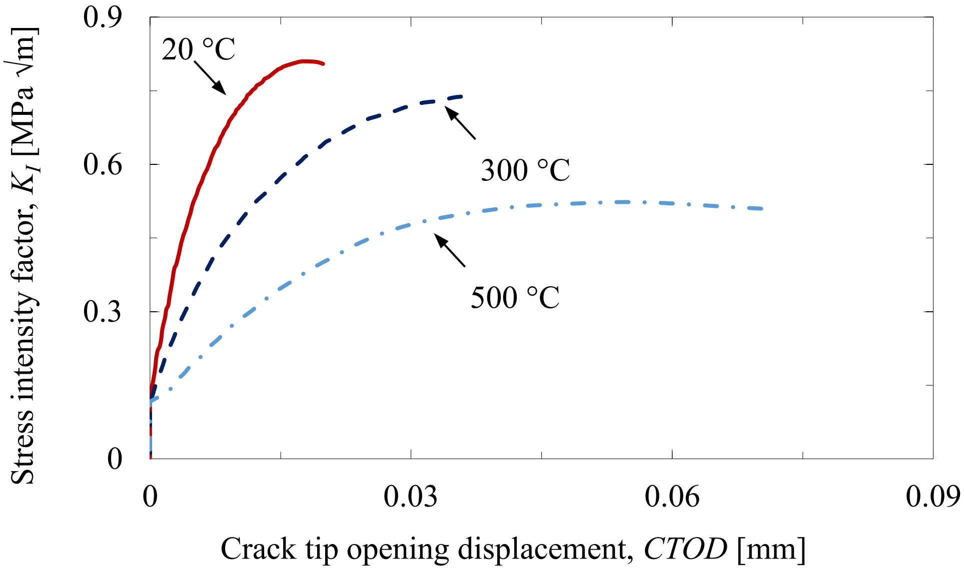

Figure 5.18 Crack opening resistance curves for mixtures with a fibre volume frcation of 0.0%.

The peak value of stress intensity factor is termed as the fracture toughness factor, K_{Ic}, as shown in Figure 5.21 . It is worth mentioning that the K_{Ic} value does not coincide with the peak flexural load. Notice that at 200 °C, the fracture toughness of plain mortar increases by about 25% due to the hydration of the unhydrated cement particles under steam pressure resulted from partial dehydration of AFt and CH. As the temperature increases from 200 °C to 500 °C, the K_{Ic} drops by about 50% of its value at 200 °C. The fibre reinforced mortar shows about 15–30% drop in the fracture toughness at elevated temperatures when compared to the plain mortar. This reduction may be attributed to the interconnected pore network formed after the melting of fibres which can be expected to degrade the crack arresting mechanism and thereby compromising the toughening mechanism.

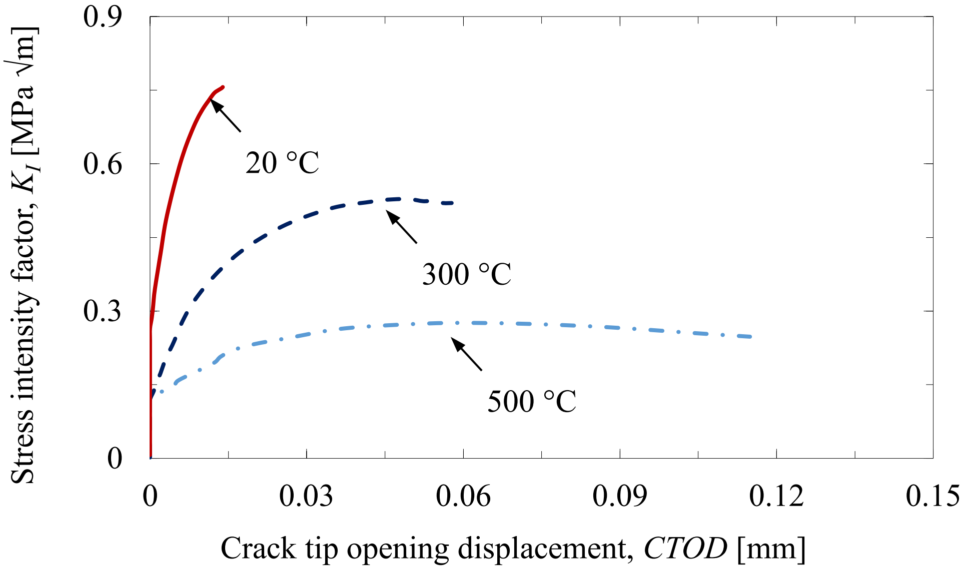

Figure 5.19 Crack opening resistance curves for mixtures with a fibre volume fraction of 0.2%.

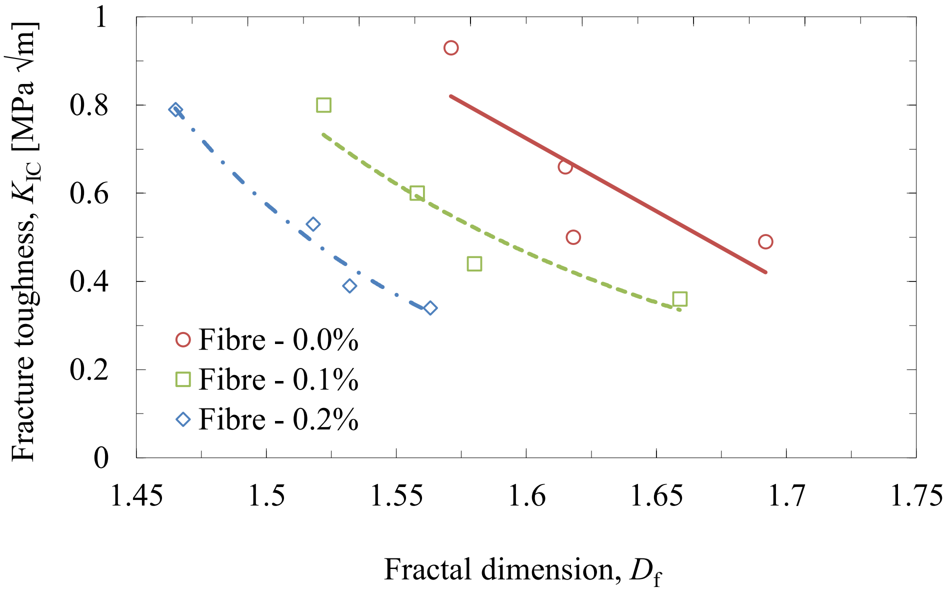

Figure 5.20 Correlation between the fracture toughness and the fractal dimension.

A correlation between the fracture toughness and the fractal dimension is presented in Figure 5.20. Note that the fracture toughness and the fractal dimension values for an exposure temperatures beyond 200 °C are shown due to the fact that an increased level of crack growth resistance occurs at 200 °C (as explained earlier in this section). The drop in the fracture toughness is due to the increased interconnectivity of the pore system resulted from the thermal degradation which is captured by the higher value of fractal dimension.

Table 5.1 Critical Mode I fracture toughness and *CTOD*

	Fibre – 0.0%		Fibre – 0.2%	
Temperature [°C]	K_{Ic} [MPa·√m]	$CTOD_c$ [mm]	K_{Ic} [MPa·√m]	$CTOD_c$ [mm]
20	0.779	0.018	0.731	0.017
200	0.932	0.023	0.788	0.026
300	0.657	0.039	0.531	0.046
400	0.498	0.059	0.386	0.058
500	0.494	0.060	0.343	0.069

It has been reported (Shah et al. 1995) that a single parameter based fracture criterion is inadequate to predict the unstable crack propagation in cement-based composites. It has generally been suggested that *R*-curve can be used as a material property to study the fracture phenomena of cement-based materials. Although *R*-curve is believed to be a material property, according to Bažant and Planas (1997), it depends on the size, the geometry, and the experimental technique that is used to generate it. A two parameter fracture criteria proposed by Jenq and Shah (1985) based on K_{Ic} and $CTOD_c$, was found to be reliable where both criteria must be satisfied in order for an unstable crack growth to occur. The K_{Ic} and $CTOD_c$ values determined using the compliance calibration for the thermally damaged mortars are shown in Table 5.1.

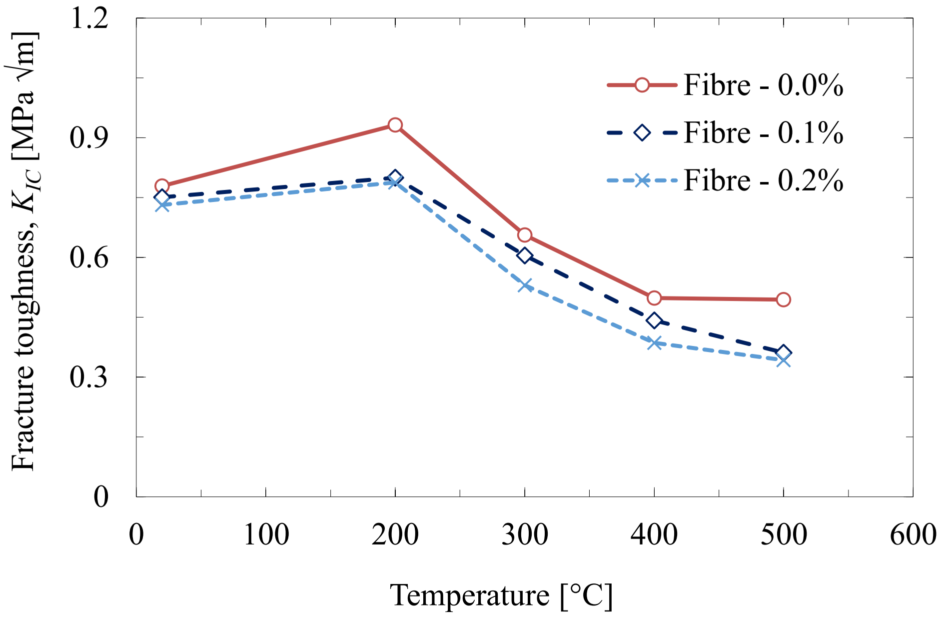

Figure 5.21 Fracture toughness of the cement mortar in Mode I.

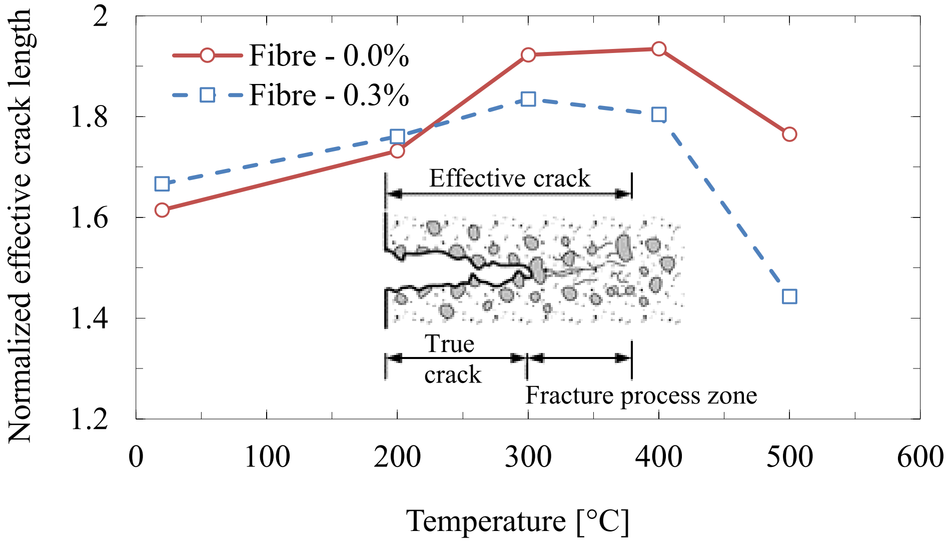

Figure 5.22 Normalized effective crack length, at peak bending load, as a function of temperature.

As mentioned earlier in this section, by considering the effective crack as a traction free zone, the principles of LEFM can be used to investigate the stress field in the ligament (region ahead of the crack tip) of the beam subjected to four-point bending. In other words, at peak load the stress distribution across the ligament may be assumed to be linear. The location of the neutral axis at peak load, for a given temperature of exposure, can be established from the engineering beam theory by regarding the section at midpsan akin to an un-cracked and un-reinforced flexural member. In order to analyze such a beam, one may estimate the depth of the section by subtracting the effective crack length from the overall depth of the beam. Thus, the depth of the neutral axis would be located at the mid-height of the now calculated section depth. Figure 5.22 shows the variation of the effective crack length at peak load, with an increase in the exposure temperature. Based on this observed trend for the effective crack length, it may be stated that the depth of the neutral axis is a function of the exposure temperature and it decreases with temperature up to 300 °C. As a result, a significant post-crack resistance is introduced in the flexural load-deflection response at elevated temperatures in comparison with the lack thereof at room temperature. This is illustrated further in the following section.

5.6.5 Predicting the Load-Deflection Response

Using the fracture mechanical analysis along with Euler-Bernoulli beam theory and Castigliano's theorem, one may predict the response of a mortar beam subjected to pure bending. In this study, an analytical prediction model developed by Bažant et al. (1991) was adopted to perform the prediction of flexural response of the plain mortar exposed to a temperature of 500 °C. The method employs the size independent fracture energy, G_f, and the limiting value of the effective crack extension, c_f —both of which are associated with very large specimen size and are regarded as material parameters—to determine the resistance to crack growth, R.

The parameters G_f and c_f can be determined using Bažant's size effect method (Bažant and Kazemi 1990a; b; Bazant and Pfeiffer 1987) if the peak flexural load, the tensile strength, and the modulus of elasticity of the mortar are known. However, this method requires the determination aforementioned parameters using experimental data from a set of specimens having geometrically scaled dimensions. An alternative method to estimate those parameters, without using size effect models, was proposed by Ouyang et al. (1996), which allows the use of experimental data from fixed sized specimens having different initial notch length. The proposed method utilizes LEFM formulations to calculate the fracture toughness, K_{Ic} and the critical crack tip opening displacement, $CTOD_c$, using the effective crack length approach.

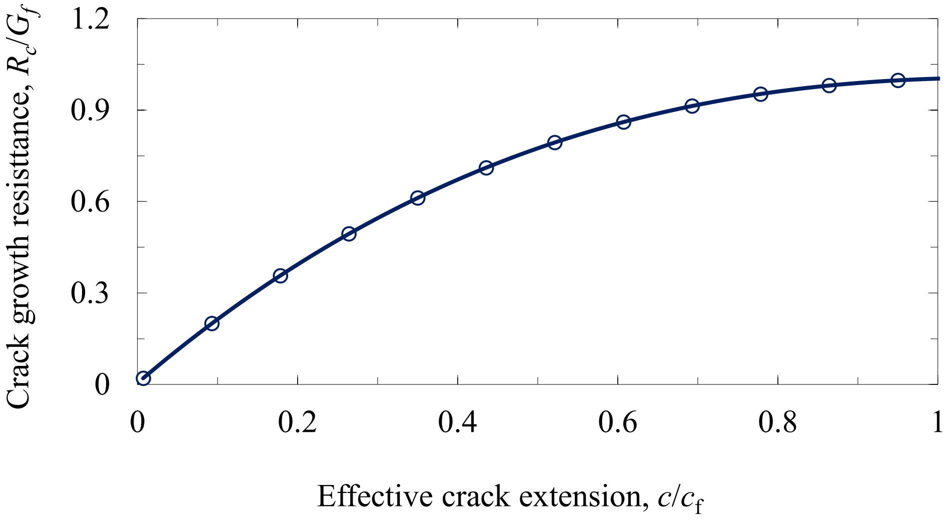

Figure 5.23 Normalized crack growth resistance, R, used to predict the load-deflection response.

Once K_{Ic} and $CTOD_c$ are determined using the above mentioned procedure G_f and c_f can be computed as follows (Ouyang et al. 1996):

$$G_f = \frac{K_{IC}^2}{E} \tag{5.4}$$

$$c_f = \frac{E\pi CTOD_c}{32G_f} - a_0 + \sqrt{a_0^2 + \left(\frac{E\pi CTOD_c}{32G_f}\right)^2} \tag{5.5}$$

where a_0 is the initial notch length.

Now, the size independent R-curve for the mortar can be determined using the following expressions proposed by Bažant and Kazemi (1990b):

$$R(c) = G_f \frac{g'(\alpha)}{g(\alpha_0)} \frac{c}{c_f} \tag{5.6}$$

and

$$\frac{c}{c_f} = \frac{g'(\alpha_0)}{g(\alpha_0)}\left(\frac{g(\alpha)}{g'(\alpha)} - \alpha + \alpha_0\right) \tag{5.7}$$

where $\alpha_0 = a_0/d$, $\alpha = a/d$, a = effective crack length, d is depth of the specimen, the prime symbol denotes derivative, $g(\alpha_0)$ and $g(\alpha)$ are functions that depend on the load configuration and the specimen geometry, which are defined below for specimen subjected to four-point bending having a span/depth ratio of 3 (Tada et al. 2000):

$$g(\alpha) = 9\pi\alpha\left(1.122 - 1.4\alpha + 7.33\alpha^2 - 13.08\alpha^3 + 14.0\alpha^4\right)^2 \tag{5.8}$$

By employing the relationship between the energy release rate, G, and the total energy released, W_p, one can derive an expression for the deflection due to fracture using Castigliano's second theorem as follows (Bažant et al. 1991):

$$u_c = \frac{\partial W_p}{\partial P} = \frac{2P}{Eb}\int_0^{\alpha} g(\alpha')d\alpha' \tag{5.9}$$

Also, by setting $G = R$, the expression for load, P, can be found as shown below:

$$P = b\sqrt{\frac{Ed}{g(\alpha)}R(c)} \tag{5.10}$$

The total deflection can now be computed by summing up the deflection due to fracture, u_c, and the deflection caused by bending, u_b, which can be determined as follows:

$$u_b = \frac{23PL^3}{108Ebd^3} \tag{5.11}$$

where L is the span of the specimen.

By selecting a set of α values, $R(c)$ was determined from the known value of G_f and c_f using Equation 5.6 and 5.7. Figure 5.23 shows the normalized crack growth resistance values against the effective crack extension. Finally, the load and the deflection of the mortar specimen were computed using Equations 5.9–5.11. The predicted response is shown along with three experimentally recorded data in Figure 5.24. It can be noticed that the predicted response agrees well with the experimental data. The apparent deviation in the descending portion of the load-deflection curve may be attributed to the errors associated with the data used to estimate G_f and c_f value. Note that due to the lack of experimental data, these values were computed from a single set of experimental data, thereby may not be capable of reproducing an accurate post-peak response. The accuracy of the load-deflection prediction can be improved by using the average results from several data sets when estimating the size independent fracture parameters.

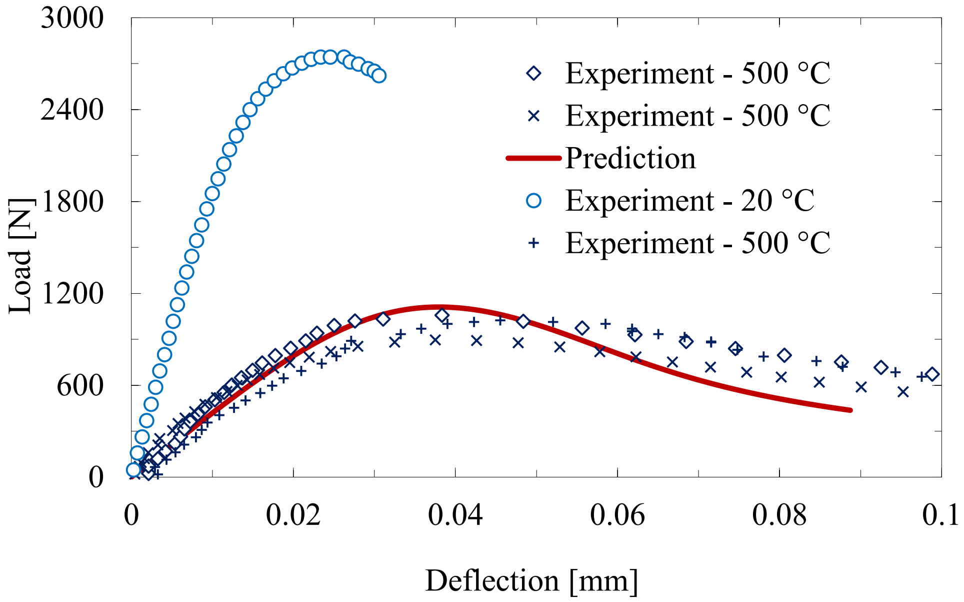

Figure 5.24 Predicted load-deflection response of the notched mortar beam under four-point bending—after an exposure to a temperature of 500 °C.

5.7 Conclusions

The experimentally evaluated mechanical properties of the mortar at sustained elevated temperatures are discussed—along with a structural response prediction model under pure bending—using fracture mechanical parameters. The work presented in this chapter can be summarized as follows:

- The residual uniaxial compressive strength generally decreases with the heating temperatures except a marginal increase around 200–300°C due to the hydration of the cement particle under steam pressure as well as reduction of disjoining pressure within C-S-H layers.

- The correlations between compressive strength, porosity, and mean pore radius were demonstrated.
- The modulus of elasticity of the mortar follows the same trend as the strength where the reduction is attributed to the extensive amount of microcracks in the interfacial region.
- The fracture energy of the mortar increases with the temperature, exhibiting a more ductile response as evidenced from higher value of the characteristic length.
- The crack growth resistance of the heated mortar drops with the increase in exposure temperature. In order to describe the unstable crack propagation using two parameter fracture criteria, the fracture toughness and the critical crack tip opening displacement were evaluated. In addition, two types of R-curve responses—based on the effective crack length and the crack tip opening displacement—were also presented to evaluate the crack growth resistance of the mortar.
- Using the size independent fracture parameters—limiting value of the fracture energy and the crack extension—one may predict the load-deflection response of the mortar under flexure from the peak load, the specimen geometry, and the material properties.

CHAPTER 6. DAMAGE ASSESSMENT USING ULTRASONIC PULSE VELOCITY AND X-RAY MICROTOMOGRAPHY

6.1 Introduction

Cement-based composites are known to be quasi-homogeneous in nature at macroscopic as well as microscopic scale. Fundamentally, these particulate composites may be treated as discontinuous filler particles embedded in a continuous matrix. Aggregates which have a relatively higher modulus of elasticity act as filler, whereas the matrix is composed of cement paste with lower elastic modulus. As with any typical composite materials, the response of concrete or mortar to applied load is significantly different than that of its constituent components. There are several factors that control the mechanical properties—volume fraction, and most importantly the interface between the phases. Due to the chemical reaction that occurs between the aggregates and cement particles during hydration, it is essential to account for the uniquely different properties of the interface while modelling the mechanical response. For instance, it is well established that the addition of a small fraction of aggregates to cement paste will result in a marginal decrease in strength because of the imperfections created in the composite through the filler-matrix interface. On the other hand, a larger amount of aggregates cause an increase in strength due to the crack arresting mechanism. Furthermore, the inherently porous nature of cement paste microstructure influences the load carrying capacity and the resistance to environmental effects, including exposure to high temperature.

The structure of the interface is significantly more porous than the rest of the bulk matrix due to the so called “wall effect” where the cement particles cannot pack around the aggregate efficiently. In addition, microcracks or other structural flaws exist in the interface even before subjecting the material to any external load or deleterious environment effects. Bleeding in fresh concrete causes accumulation of water around the aggregate interface which increases the local w/c ratio making it relatively weaker. Furthermore, the early age shrinkage and hydration process are responsible for volumetric change which causes microcracks at the interface due to the stiffness mismatch between the aggregate and the cement paste. These pre-existing cracks are the source of predominantly tensile mode of failure of cement-based materials. Even if the concrete is subjected to compressive load, the failure would still be controlled by tension or tension-shear failure. As the applied load increases, the cracks in the interface grow in number and length, and gradually enter the matrix phase in a stable manner. At about 70–80% of the ultimate load, crack propagation occurs in an unstable manner characterized by the continued growth of cracks at a constant load which ultimately leads to failure.

At sustained elevated temperature, a significant amount of microcracks develops at the interfacial region due to the differential thermal expansion between the aggregate and the cement paste. Depending on the severity of thermal exposure—characterized by the heating temperature, rate of heating, and duration of heating—cracks may appear in the cement paste as well. In addition, capillary and gel pore fraction increase due to the removal of adsorbed and chemically combined water from the hardened products.

6.2 Objectives

As explained above, the loss of strength carrying capacity is caused by the changes that occur under elevated temperatures. In order to evaluate the damage sustained by cement mortar at elevated temperature, the changes in stiffness was determined by employing the ultrasonic pulse velocity technique. Furthermore, the parameters of three dimensional pore structure were quantified through X-ray computed microtomography. Using these experimental techniques correlations were developed between UPV and damage parameters, and between microstructural observations and the damage parameters. The following sets of investigation form the overall objectives: (1) Determination of the changes in ultrasonic pulse velocity, (2) Evaluation of dynamic modulus of elasticity, (3) Determination of three dimensional pore space fractality, (4) Correlating the damage value with pore space fractality, (5) Evaluation of continuously connected fraction of porosity, (6) Quantification of pore tortuosity, and (7) correlating damage variable with specific pore surface area.

6.3 Background

As discussed earlier, cement-based materials contain interfacial microcracks before applying any external loads, due to their composite nature. In response to tensile loading, the interfacial cracks, which are largely oriented normal to the direction of applied load, grow while the ones aligned parallel to the loading direction tend to close. The opposite behaviour can be observed when the material is subjected to compression (Carpinteri and Ingraffea 2012). It is well established that the stress-strain response is controlled by the presence of microcracks especially those at the interface. At elevated temperatures, these pre-existing cracks grow due to thermal stress and pore pressure development as evident from the rapid loss of modulus of elasticity (Mehta et al. 2006). Furthermore, the reduction in the number of available load paths, due to the increased number of interconnected microcrack network, causes a decrease in the load carrying capacity.

Ultrasonic pulse velocity (UPV), a non-destructive test method, is a useful technique to evaluate the microstructural integrity of cement-based materials. When pressure wave travels through a solid, its velocity is dependent on the density and elastic properties of that material. Although the governing equation relating the elastic modulus and wave velocity is not exactly applicable to quasi-homogeneous materials such as concrete, UPV can still be a convenient method of quantifying relative damage values with a fair degree of accuracy. The non-destructive nature of this technique makes it particularly attractive.

X-ray computed microtomography is an image-based non-destructive method of investigating concrete microstructure in three dimension. In this method, high-energy X-ray source is used to acquire X-ray attenuation map of the specimen by rotating it at certain angular interval. These images were then reconstructed using suitable algorithms of mathematical tomography to generate the three dimensional microstructure. Since the brightness of the reconstructed images is related to the density of the material, the pore regions are identified as the voxels—volumetric picture element—having lower gray values. Using the readily available image processing algorithms, the pore structure parameters can easily be quantified.

Damage of a material under external load, either mechanical action or environmental effects, is the gradual deterioration of its microstructure, which ultimately leads to failure. A variable that can describe the damage sustained by the material may be defined in terms alteration of its mechanical properties or certain measure of imperfection (Lemaitre 1996). Several definitions of the damage variable can be found in the literature that are used to develop models capable of describing the physical process of degradation of the material. One such definition relates damage variable with the change in number of cracks within a representative volume, owing to the fact that the damage evolution is directly associated with the development and growth of microcracks. As Landis (2006) argued, this definition does not reflect the true nature of microstructural damage because at increased level of damage the number of cracks actually reduces due to the coalescence of cracks found in previous level. It has also been shown that variation in elastic properties, damaged area, crack surface area or volume, ultrasonic pulse velocity, density, micro-hardness, and electrical resistance are being used to describe microstructural damage of a continuum (Lemaitre 1996).

6.4 Experimental Details

In this study, the evolution of damage was examined using ultrasonic pulse velocity (UPV) technique and X-ray microtomography. The mortar specimens were first exposed to, upon reaching the target temperature at a heating rate of 5 °C/min, sustained temperature from 200–500 °C for two hours. At the end of the heat soaking period, the specimens were allowed to cool down to ambient temperature through natural cooling. At this stage, further preparation of the specimens is required for the damage assessment.

6.4.1 Materials

For the purpose of damage assessment using ultrasonic pulse velocity, plain and fibre reinforced mortar specimens were prepared using ordinary Portland cement and quartz sand. A w/c ratio of 0.5 was used along with an appropriate dosage of high range water reducing admixture to compensate for the loss of consistency due to the addition of polyester fibre. Cylindrical specimens with a diameter of 75 mm and a height of 150 mm were cast and cured at a relative humidity of 95% at 23 °C for 60 days. After thermal exposure as described above, the ultrasonic pulse velocity was determined. On the other hand, the specimens for X-ray microtomography scanning were extracted from prisms, having a dimension of 50 × 50 × 200 mm, after the thermal exposure using a coring instrument.

6.4.2 Ultrasonic Pulse Velocity

The ultrasonic pulse velocity of cement mortar specimens exposed to different elevated temperatures was determined using a portable UPV instrument. The instrument generates compressional wave having a frequency of 54 kHz. According to Popovics (1998), there is an optimum UPV frequency for a specific material that can provide meaningful information without missing critical microstructural features or creating electrical noise. The pulse generation frequency used in this study falls within the suggested range of 20–150 kHz, which was deemed to be appropriate for the velocity measurement of cylindrical mortar specimens with a lateral dimension of 75 mm and a length of travel 150 mm.

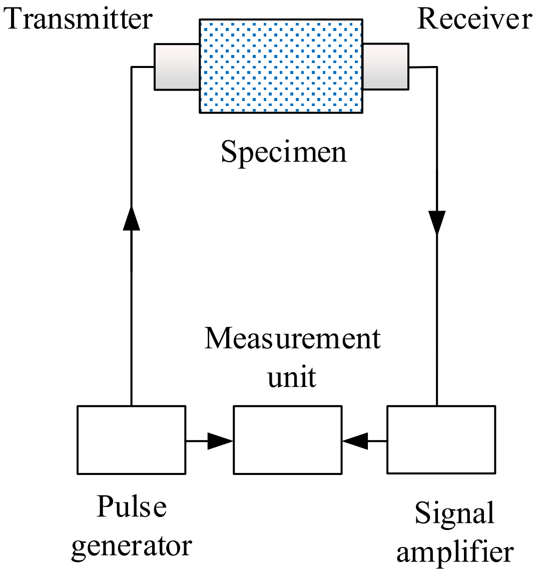

Figure 6.1 Ultrasonic pulse velocity technique used to determine the damage sustained by mortar specimens at elevated temperature.

The schematics of the experimental setup is shown in Figure 6.1. In order to ensure the effective transmission of ultrasonic waves, the specimen's ends were polished before exposing them to elevated temperature. Furthermore, to reduce the attenuation of pulse energy caused by imperfect contact between the transducers and the specimen, a viscous coupling paste was used. In addition, it has been shown (Naik et al. 2003) that the UPV increases with the increase in moisture content of the specimen. Therefore, to exclude the influence of moisture, the specimen were dried in an oven at a temperature of 103 °C for 24 hours prior to the UPV measurements.

6.4.3 X-ray Computed Microtomography

Three dimensional microstructure of the cement mortar specimens were rendered using X-ray computed microtomography. The scanning was performed using cylindrical cores having a diameter of 9 mm that were extracted from prisms exposed to different elevated temperatures. A schematic view of the overall scanning and reconstruction process is shown in Figure 6.2. Raw shadow images created by high-energy X-ray beam were captured using a cone-beam type scanner with a microfocus X-ray source. The X-ray source was set to an accelerating voltage of 100 kV and a tube current of 100 μA. The scanner was equipped with an image acquisition system consists of a scintillator and a 10 mega pixels camera capable of capturing high resolution projection images.

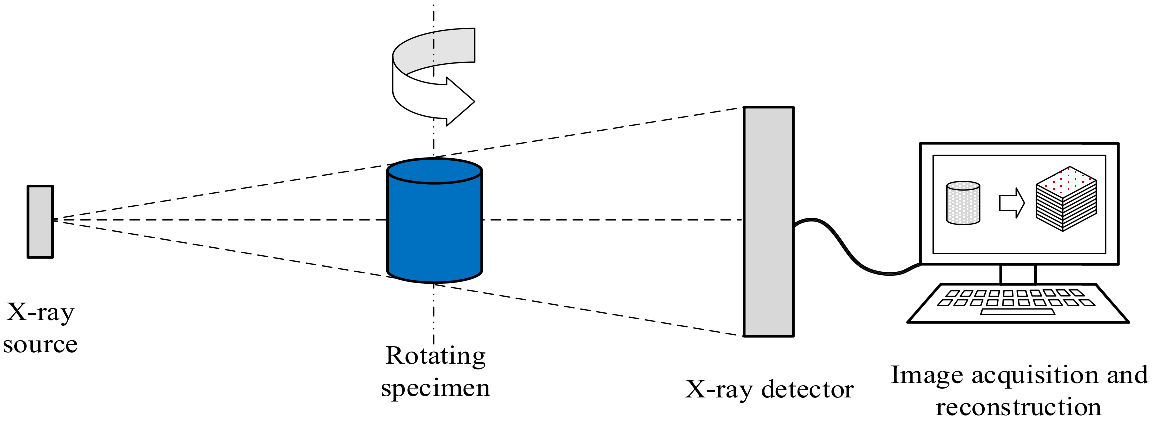

Figure 6.2 Schematics of cone-beam X-ray computed microtomography scanning process.

Note that when scanning the specimen, the presence of low energy X-rays in the beam causes a phenomenon known as beam hardening, which manifests as a relative higher density zone around the scanned image. There are several measures that can be implemented to minimize the beam hardening—by using metallic filters which can be placed between the specimen and X-ray source, by applying a beam hardening correction during reconstruction stage, and by using spherical or cylindrical specimen as opposed to irregularly shaped ones (Tarplee and Corps 2009). In this study, all three of the aforementioned techniques were employed to block the low energy X-rays—a 0.5 mm thick aluminum filter combined with a 0.04 mm thick copper filter, a beam hardening correction of 59%, and the use of cylindrical specimens. In order to maximize the contrast of the projection images, a flatbed correction was also applied. Furthermore, to improve the quality of the image, the scan was performed at an angular step of 0.3° for a total rotation of 360°, which also helps minimize the so called "ring artifact" in the reconstructed image. Finally, the projection images were mathematically reconstructed using the modified Feldkamp algorithm. When reconstructing the images, a ring artifact correction factor of 14 was found to be adequate to yield an optimum quality output. In the reconstructed image, a resolution of 4.34 µm/pixel was achieved, which enables a fairly reasonable estimation of microstructural parameters for the purpose of this study.

6.5 Results and Discussions

6.5.1 Ultrasonic Pulse Velocity

The ultrasonic pulse velocities of the plain and fibre reinforced cement mortar determined after thermal exposure, residual measurement, are shown in Figure 6.3. The maximum measured velocity is 3.7 km/s for unexposed specimens. It was found that the corresponding wave length of the transmitted compression waves was about 69 mm, based on the manufacturer provided frequency value of the transducers which is 54 kHz. If the calculated wave length is compared with the least dimension of the cylindrical specimens, which is 75 mm, one would find that the selection of the frequency for UPV measurement is satisfactory. It can be observed that the UPV values remain unchanged up to an exposure temperature of 200 °C, beyond which UPV gradually drops with the temperature. A reduction of 68% in UPV was observed at an exposure temperature of 600 °C. It can also be noticed that there is no significant variation between the plain and the polyester fibre reinforced series.

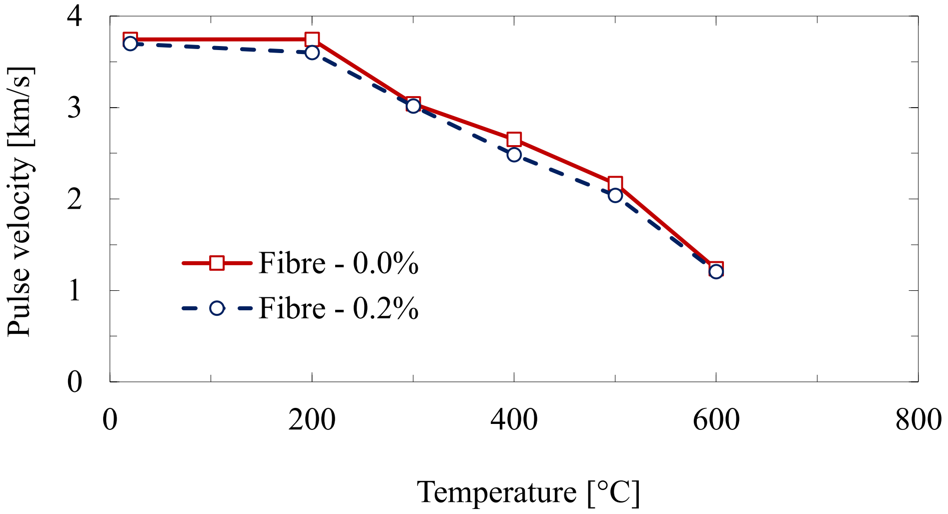

Figure 6.3 Ultrasonic pulse velocity at different exposure temperatures.

UPV is frequently used as a non-destructive method of evaluating the strength of cement-based composites (Bungey et al. 2006; Popovics 1998). Generally, a higher pulse velocity is recorded for concrete having a larger compressive strength. As discussed earlier, mortar exposed to increasingly high temperature shows an enhancement of the compressive strength as well as flexural strength at a temperature between 200–300 °C. One would naturally expect this variation to be reflected upon the measured UPV. However, the measured UPV values at the aforementioned temperature range do not produce the observed trend. This might be explained with the fact that theoretical dependence of UPV on the material properties is unable to capture the exact behaviour of quasi-heterogeneous material (Popovics 1998). Furthermore, the increased strength near 200 °C is largely caused by the reduction in disjoining pressure (Neville 2011) within C-S-H, which is not necessarily associated with significant alteration of microstructure to be reflected upon the measured transit time of ultrasonic wave. Nevertheless, the results of UPV tests are still useful for a comparative analysis of mortar microstructure.

Since UPV is related to the material properties—such as elastic modulus, Poisson's ratio, and density—it can be used to estimate the dynamic modulus of elasticity of the mortar. Although the value of dynamic Poisson's ratio is generally not known accurately, UPV can still be used to investigate the relative change in the dynamic modulus of thermally exposed mortar. The following simplified equation relates UPV with the abovementioned material properties:

$$E_d = \frac{\rho V^2}{K} \tag{6.1}$$

where E_d is the dynamic modulus of elasticity, ρ is the density of the mortar, V is the ultrasonic pulse velocity, and K is a function of the dynamic Poisson's ratio, ν, defined as:

$$K = \frac{(1-\nu)}{(1+\nu)(1-2\nu)} \tag{6.2}$$

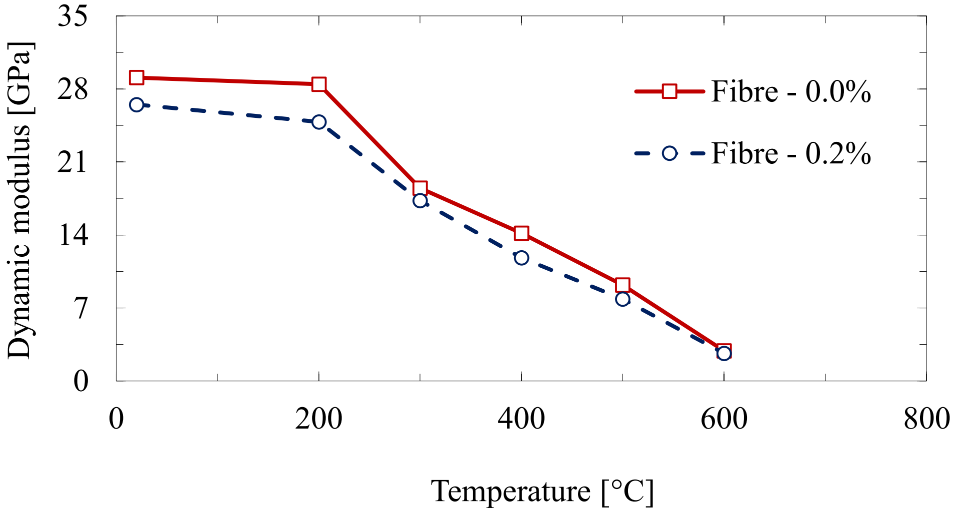

Figure 6.4 Dynamic modulus estimated from ultrasonic pulse velocity.

Generally, the value of ν is determined by vibrating a specimen at their natural frequency. For the usual range, 0.15–0.20, of ν values, the parameter K may be approximated as unity (Hernández-Olivares and Barluenga 2004). Dynamic modulus of elasticity, estimated using the Equation 6.1, yields a value similar to the one that can be computed from the initial tangent modulus of the stress-strain curve obtained through uniaxial compression test. As shown in Figure 6.4, the decreasing trend of dynamic modulus with increased temperature indicates a considerable degree of microcracking in the interfacial region of the mortar specimen.

At elevated temperature, pre-existing interfacial microcracks in the mortar grow along with an increase in the capillary and gel porosity. The response of such internally damaged composite to applied load is governed by the structure of the interface and relatively weaker cement paste matrix. Consequently, the stress-strain curves exhibit an increasingly non-linear response as the exposure temperature increases, which also indicates that the mortar has lower modulus of elasticity. In order to better describe this physical process of microstructural deterioration, a damage variable can be defined using the dynamic modulus estimated from UPV, as shown in the following Equation:

$$D_v = 1 - \frac{E}{E_0} \tag{6.3}$$

where D_v is the damage variable, E_0 and E are the dynamic moduli of undamaged and damaged mortar respectively.

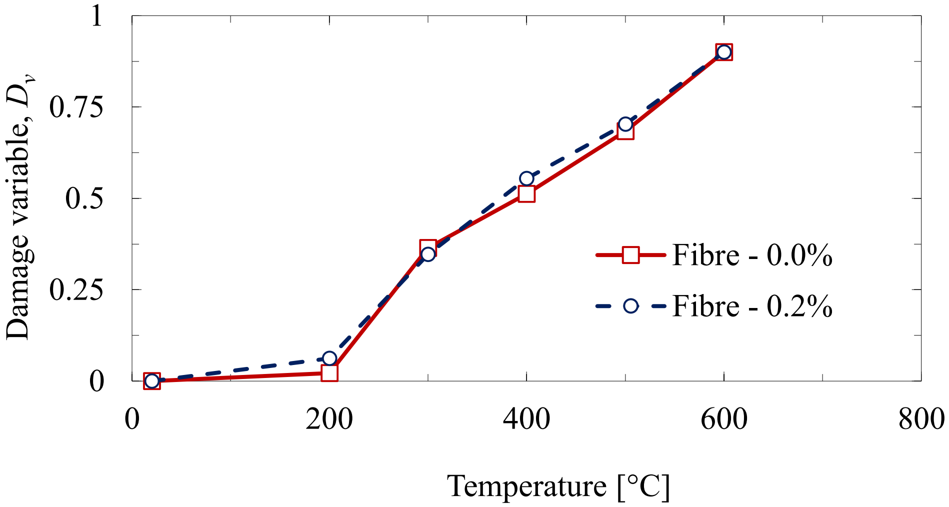

Figure 6.5 Damage variable at different exposure temperatures based on the estimated dynamic modulus of elasticity.

Figure 6.5 illustrates the calculated damage variable for the plain and fibre reinforced mortar against exposure temperatures. It can be observed that the mortar largely remains undamaged at 200 °C, which may be attributed to the hydration of unhydrated cement grains through a process known as internal autoclaving under steam generated pressure (Saad et al. 1996). As the temperature continues to increase the damage value increases steadily, characterized by the accumulation of interfacial microcracks.

6.5.2 Pore Space Fractality from X-ray Microtomography

X-ray computed microtomography (XCM) is a powerful imaging technique to explore the microstructure of an object in three dimension. With the advent of high resolution scanning technology, the pore structure geometry of cement-based composites can be visualized and modelled in considerable detail. In this study, XCM was used to evaluate the microstructural evolution of the mortar as a consequence of hygro-thermal process at sustained elevated temperature.

XCM captures a series of radiographic scans, known as shadow image or projection image, of the specimen at a specific angular interval, which is basically a map of X-ray attenuation coefficients. These image are then mathematically reconstructed, a process called back projection, as a series of two dimensional slices, which are then used to render a three dimensional model of the specimen. In order to determine the pore structure parameters, in this case the fractal dimension, the images require pre-processing—cropping, adjustment of brightness and contrast, filter, and binary conversion. In the cropping process any extraneous region around the image boundary is removed, whereas the brightness and contrast adjustment process improve the intensity of the gray value to yield a sharper image. Since high resolution XCM images tend to contain a fair amount noise, a suitable filter process was then used to minimize the impact of these noise. Note that to avoid the artifacts that may be introduced due to the excessive pre-processing, the processing parameters were kept at a consistent level. Finally, the conversion of 8-bit gray scale image into binary format was performed in order to be able to differentiate between the pores and solids in the mortar specimen. It can be accomplished either by a trial-and-error method, which is prone to bias, or a more systematic approach called critical overflow method (Promentilla et al. 2008; Wong et al. 2006). In this work, the latter technique was employed to select a threshold voxel intensity in order to segment the pore space from the solids. Figure 6.6 illustrates the details of threshold selection process. In Figure 6.7, a typical shadow image and a reconstructed image, along with a rendered models from XCM imaging are shown.

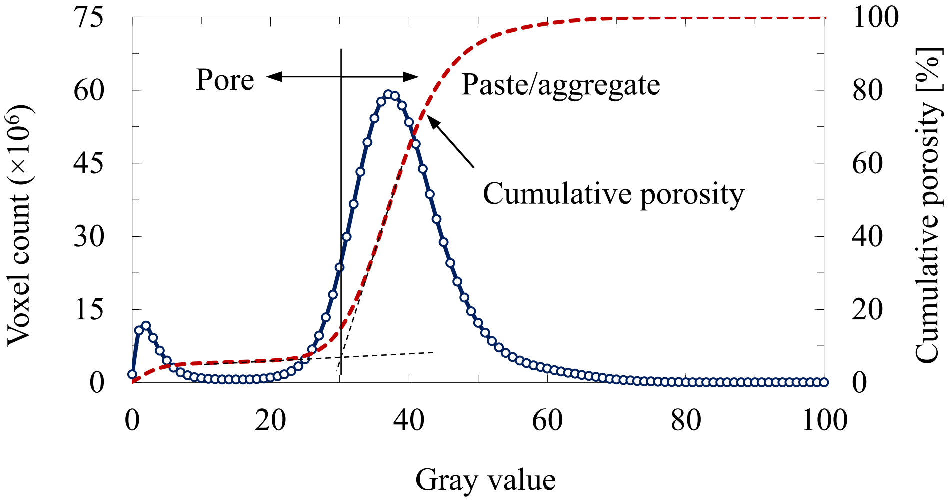

Figure 6.6 Threshold selection for the segmentation of images from X-ray microtomography.

The concept of fractal geometry is a convenient tool to describe the self-similar nature of the internal structure of a material. It is particularly useful in quantifying the level of complexity of microstructure in cement-based composites. Fractal geometry shows increasingly detail structure of an object as the scale of observation decreases. As discussed earlier in this thesis, this is true only for deterministic fractals, which are created mathematically. On the other hand, the real objects such as mortar or concrete specimen exhibit self-similarity only within a certain range scale of observation.

In this study, the fractal dimensions of the mortar specimens exposed to different temperatures were determined using the three dimensional XCM model geometry to describe the intricate nature of the pore or crack network that evolves over the course of high temperature exposure. Box-counting method is a simple technique that can be used to determine the fractal dimension. In this method, the three dimensional pore geometry is covered successively with smaller sized cubes and the required number of cubes that contain the feature of interest are counted. The size of the cubes started at 250 voxels, where 1 voxel is equal to 4.34 μm^3, which were gradually reduced to 7 voxels. A plot of the number of cubes against the size of the cubes is then employed to estimate the fractal dimension, as shown in Figure 6.8. The following Equation shows the computation of fractal dimension:

$$\log(N) = \log(C) + D_f \log(1/\varepsilon) \tag{6.4}$$

where N is the number cubes or boxes, C is the intercept of vertical axis, D_f is the fractal dimension, and ε is the size of cubes.

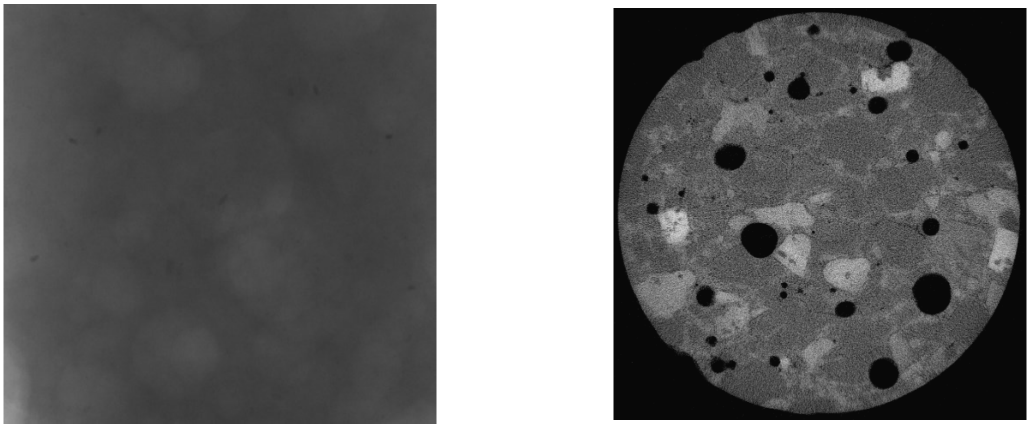

Projection image		Reconstructed image

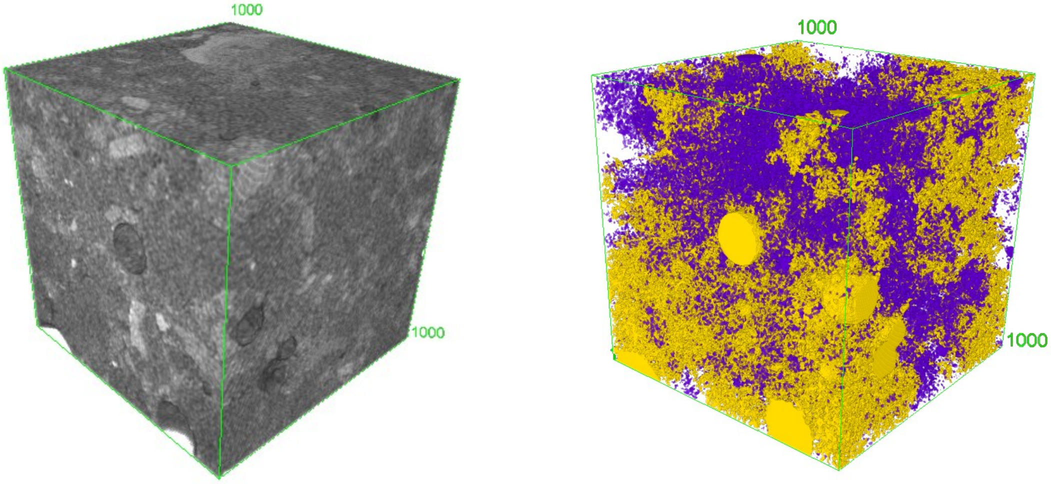

3D rendering of reconstructed image set		Segmented view—showing pores

Figure 6.7 Typical X-ray computed microtomographic images of mortar.

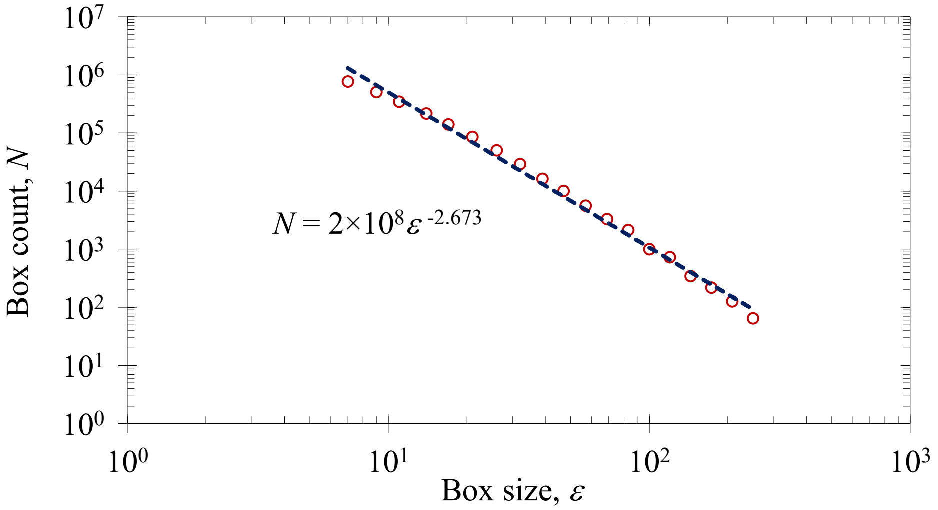

Figure 6.8 Typical estimated fractal dimension of 3D pore space using box-counting method.

The fractal dimensions (FD) of thermally damaged mortar are shown in Figure 6.9. Both the plain and fibre reinforced mixtures showed an increase in FD with increased temperature. The values are ranging from 2.45–2.80 indicating a space filling nature of the pore microstructures. As explained earlier in this work, the initial mortar microstructure gets transformed to a more complex one as the exposure temperature increases. There are several reasons that can be stated to explain such observation. First, the thermal decomposition of hydration products caused by the dehydration process results an increase in porosity. Second, the formation of microcracks network due to the thermally induced stress on the aggregate and cement paste matrix. Note that the increase in FD indicates the gradually increasing nature of the irregular and complex interconnected structure.

A correlation between the damage variable and fractal dimension is presented in Figure 6.10. It is to be noted that the damage variable in this illustration was computed using the chord modulus of elasticity from uniaxial stress-strain diagram. It can be noticed that the damage variables are negative at temperature up to 200 °C, due to the fact that mechanical behaviour of the mortar at this temperature enhances because of the reason explained in Section 6.5.1. The observed linear or bi-linear relationship suggests that the mechanical deterioration sustained by the mortar is dependent upon the complexity of the pore structure. In other words, the mortar tends to be more compliant as the FD increases due to the increasingly severe level of thermal degradation. As mentioned earlier, the increased thermal damage is associated with an increased amount of microcracking in the transition zone, which is reflected on the higher value of fractal dimension. The reduced elastic modulus, making the mortar more compliant, is also the outcome of severely deteriorated interfacial transition region, where a significant deformation in mortar can be observed in response to an imposed load. Landis (2005) also reported a similar relationship where the damages in the specimen were induced through external application of load at various stages. It is worth mentioning that the reproducibility of FD was relatively fair. Although the statistical variation was low, it is to be noted that the relatively small sampling volume could produce high variability. Since high resolution imaging requires considerably small specimen volume, the reproducibility of FD can be improved by increasing the number of observations.

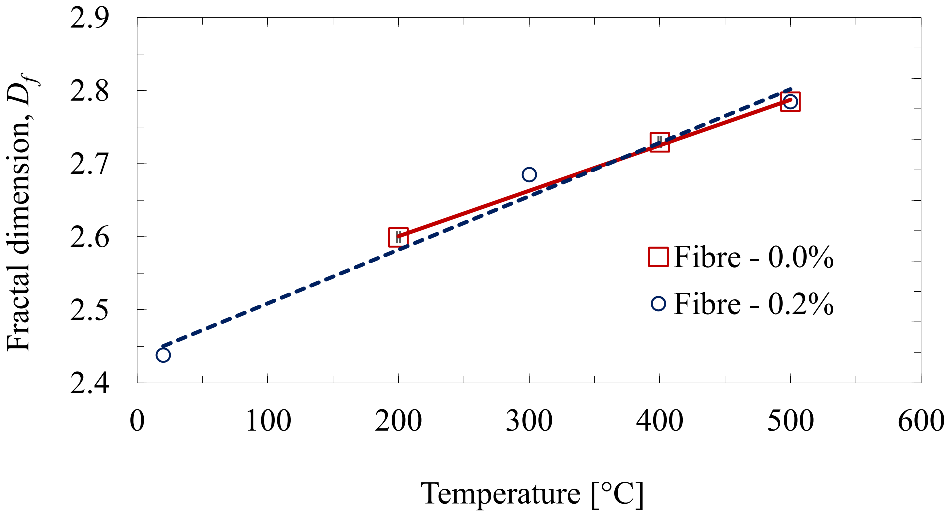

Figure 6.9 Pore space fractality of cement mortar at different temperatures.

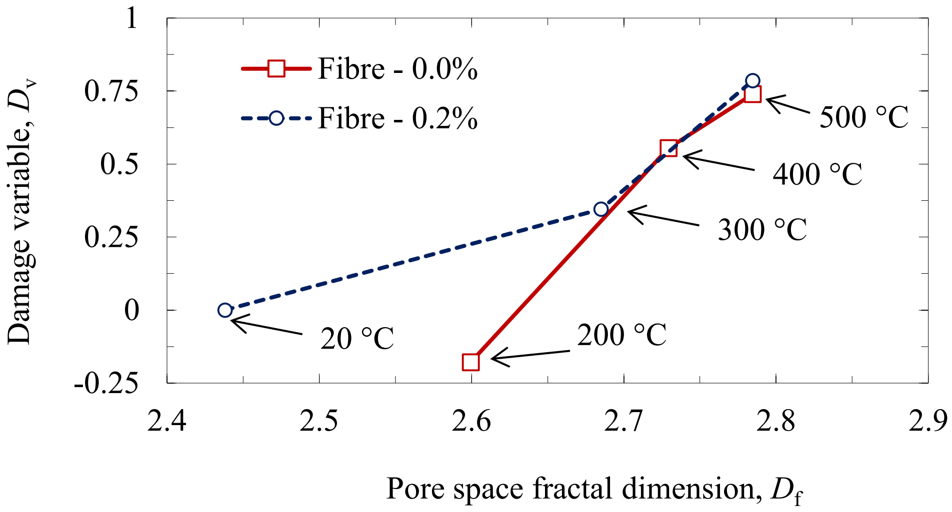

Figure 6.10 Correlation between the pore fractality and the damage variable computed from uniaxial compression test.

6.5.3 Connected Porosity

Quantification of continuously connected pore fraction can reveal useful information about the mortar microstructure while investigating the damage sustained due to high temperature. Note that the term "pore" is used in this section to include all forms of microstructural defects as well as capillary pore system that can be resolved by the resolution used to perform XCM scanning. In this study, XCM imaging technique was employed to measure the changes in connected fraction of pores due to thermal exposure.

In order to measure the connected porosity, XCM images were first preprocessed and converted to a set of binary images. Next, in order to identify the connectivity of pore voxels, each voxel was labelled according to their interface with the neighbouring voxels. A Mathematica®-based program developed by Nakashima and Kamiya (2007) was employed. The program implemented a fast cluster labelling algorithm originally developed by Hoshen and Kopelman (1976). When labelling the pore voxels, the algorithm determines the connectivity by examining whether the voxel shares at least one face with the neighbouring voxel. It eliminates those voxels that are only connected via a vertex or an edge. The algorithm scans the entire image set in a two-step process. In the first step, the voxels are assigned a set of provisional labels based on the interface with the neighbours and simultaneously records an errata sheet of potential labelling conflicts, where a voxel is mislabelled because of the way it performs the scanning. A second scan uses the errata information and assigns correct labels to the voxels. Once the image set is labelled according to their connectivity, a list of total voxel count in every cluster of connected pore voxels can be generated.

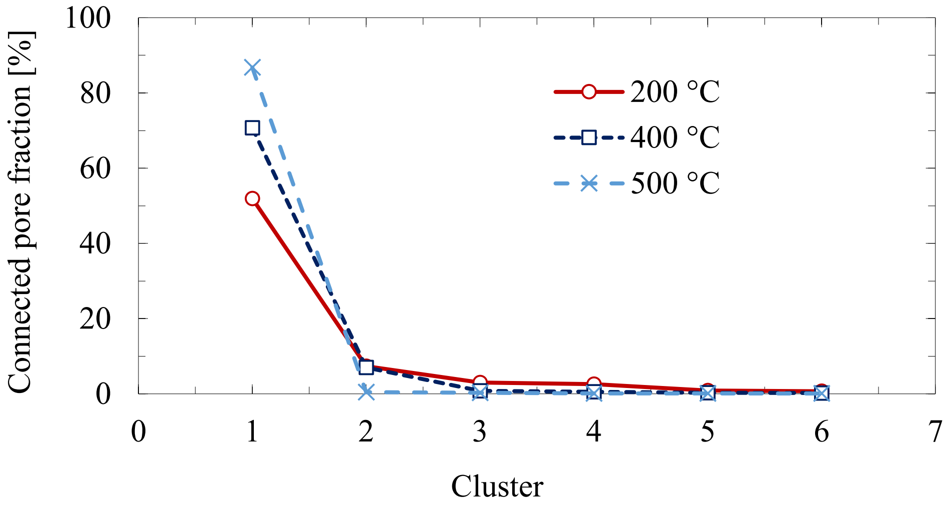

Figure 6.11 Pore connectivity at different temperature for the mixtures with 0.0% fibre.

The output of cluster labelling process is presented in Figure 6.11 and 6.12 for the plain and the fibre reinforced mortar respectively. The connected fraction of total porosity for all the clusters were sorted and the top six clusters are shown with first one being the largest of all. Fluid transport phenomena is usually studied based on the structure of the largest continuously connected pore cluster. It can be noticed that the largest cluster occupies a considerable portion of the overall porosity. As the temperature increases, the connected pore volume fraction of the largest cluster increases. It indicates the disappearance of the solid barriers that separated smaller clusters, as evident from the reduced voxel counts of the remaining smaller clusters. This enlargement of the connected pore fraction is the manifestation of the progressive hygro-thermal deterioration. The sources of the deterioration include the transformation of the gel pores into the capillary pores as well as the formation of interfacial and matrix microcracks. An implication of the increased volume of largest connected pore cluster would be the availability of favourable path for fluid transport through the mortar. The influence of fibre reinforcement can also be noticed, where at 20 °C the largest cluster occupies only 32% of the total porosity. Furthermore, the combined value of pore fraction occupied by the top six clusters is only about 65%, which implies the existence of a large number of smaller isolated clusters. However, the influence seems to be disappearing at higher temperatures.

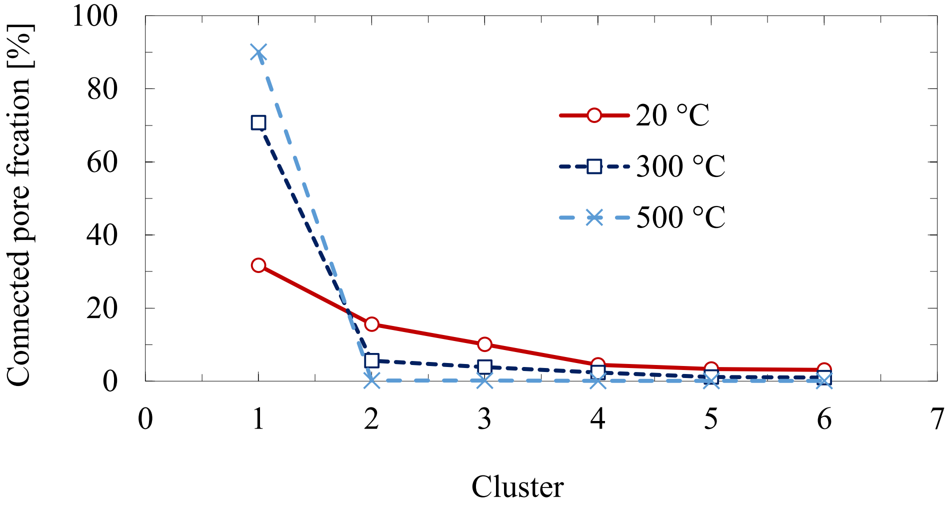

Figure 6.12 Pore connectivity at different temperature for the mixtures with 0.2% fibre.

Figure 6.13 presents the relationship between the connected porosity and the ultrasonic pulse velocity. It can be seen that the UPV values fall rapidly as the porosity of connected cluster increases. It is evident from the figure that the transit time required for a compression wave to pass through a thermally degraded mortar increases. It can be attributed to the scattering of transmitted pulse as it strikes an interface, which in this case is the region between the solid paste and the pore. Therefore, the microstructural damage in the mortar caused by an exposure to elevated temperature may be evaluated by UPV.

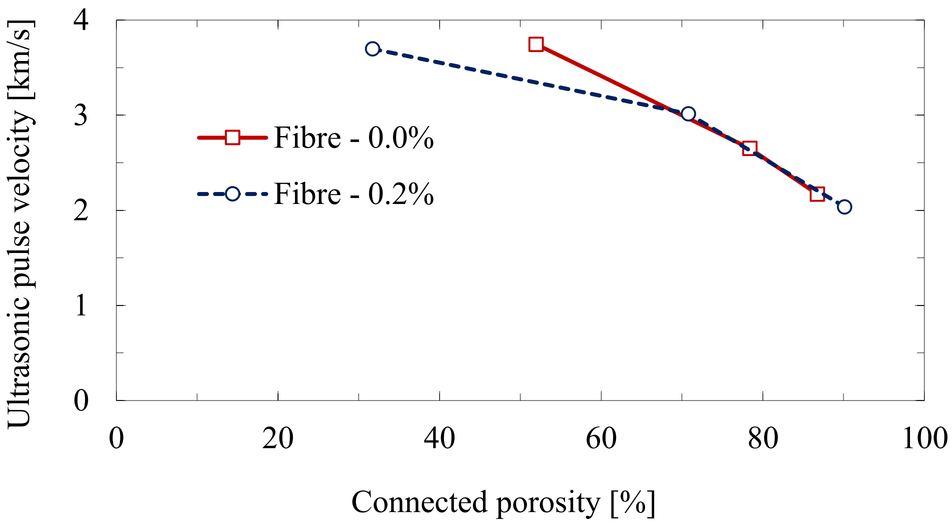

Figure 6.13 Relationship between the connected porosity and the ultrasonic pulse velocity.

6.5.4 Specific Surface Area

The pore-solid interface area was also determined through XCM imaging method. The specific surface area was then computed by normalizing the interface area with the bulk volume of the specimen. In Figure 6.14, the specific surface area is illustrated for different exposure temperatures. A marginal difference between the plain and fibre reinforced series was observed; but disappeared with increased temperature. The increased value of specific surface area with temperatures implies a reduction in the available load paths because of the presence of increasing number of microcracks. Therefore, it is likely that more microstructural cracks will have angular orientation in favour of externally applied load. The consequence of the crack development is manifested through a reduction in compressive strength as evidenced from the uniaxial compression tests, where the unstable crack growth is usually controlled by tension or tension-shear mode of failure.

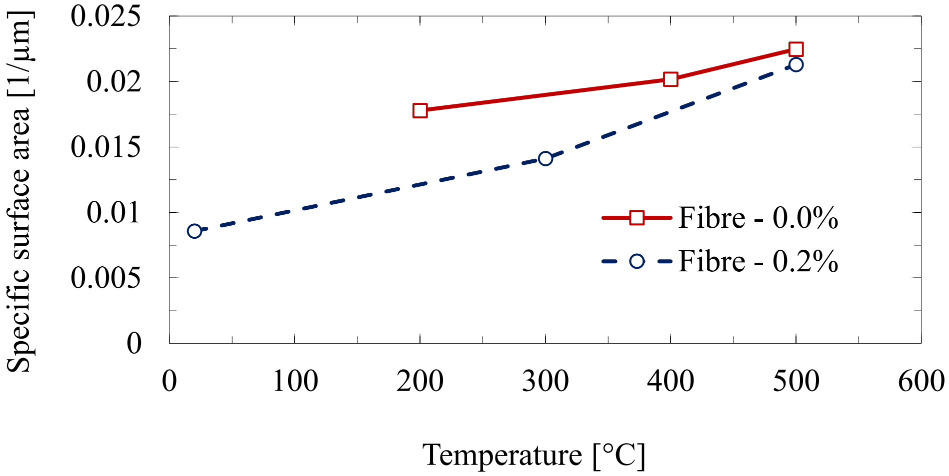

Figure 6.14 Specific surface area as determined from X-ray computed microtomography at different exposure temperature.

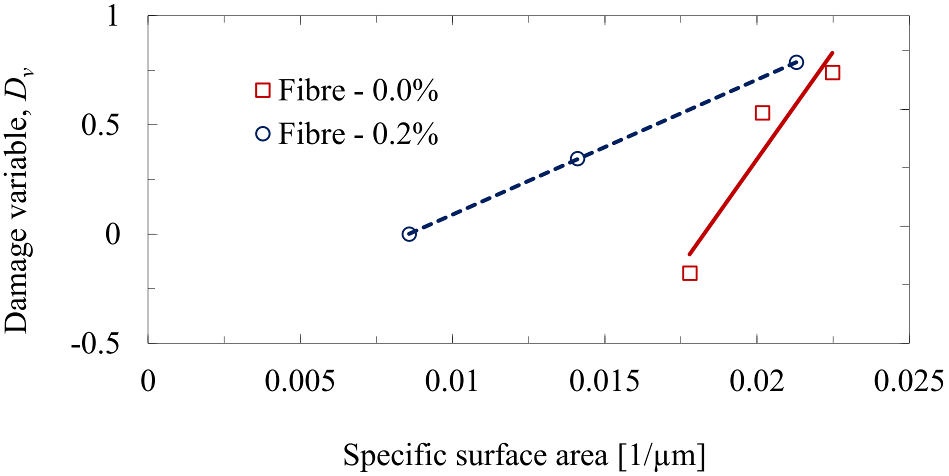

Figure 6.15 Correlation between the damage variable and the specific surface area. Note that the damage variable was computed based on uniaxial compression test.

A correlation between the damage variable and the specific surface area is shown in Figure 6.15. The linear relationship shows the effect of the increased amount microstructural flaws, which resulted from thermal degradation of the mortar, on the overall mechanical damage. It is well established (Mehta et al. 2006) that cracks in ITZ have considerable impact on the modulus of elasticity since they do not allow stress transfer across the aggregate-paste boundary. In order to transfer the imposed load, alternate load paths must be available. One other potential implication of the increased surface area, and hence the increased amount matrix and interfacial cracks, would be the higher probability of crack coalescence in response to the applied stress, which would reduce the load carrying capacity of the mortar.

6.5.5 Tortuosity

The measure of the deviation of a meandering path from a straight line connecting its two end points is termed as tortuosity. In the context of microstructure of cement-based composites, it refers to the intricate nature of the pathways composed to capillary pores, cracks in ITZ, and in the cement paste matrix. It has significant influence over the transport properties as well as the mechanical properties of a material. In this section, tortuosity is defined and its impact on the damage variable is discussed.

In this study, tortuosity was determined using the XCM image of the mortar scanned after high temperature exposure. Based on the concept of time-dependent diffusion coefficient of non-sorbing migrating agents, the diffusion tortuosity can be defined as the ratio of diffusion coefficient in free space to that in porous space (Nakashima et al. 2004; Nakashima and Kamiya 2007; Promentilla et al. 2008, 2016). It is can be expressed as follows:

$$\tau_d = \frac{D_0}{D} = \frac{d(r_{free}^2)/dt}{d(r^2)/dt} \tag{6.5}$$

where τ_d is the diffusion tortuosity, D_0 is the diffusion coefficient in free space, expressed as the time derivative of r_{free}^2, the mean square displacement in free space, D is the diffusion coefficient is porous space, expressed as the time derivative of r^2, the mean square displacement in porous space.

However, the classical geometric tortuosity, τ, of the porous path is not the same as τ_d and therefore, it can be computed from the diffusion tortuosity as follows (Promentilla et al. 2016):

$$\tau = \sqrt{\frac{D_0}{D}} \tag{6.6}$$

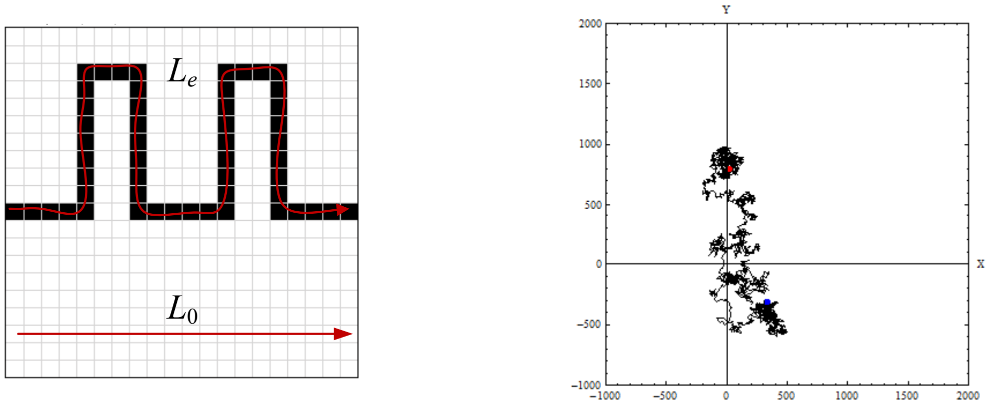

Definition of tortuosity

XY trajectory

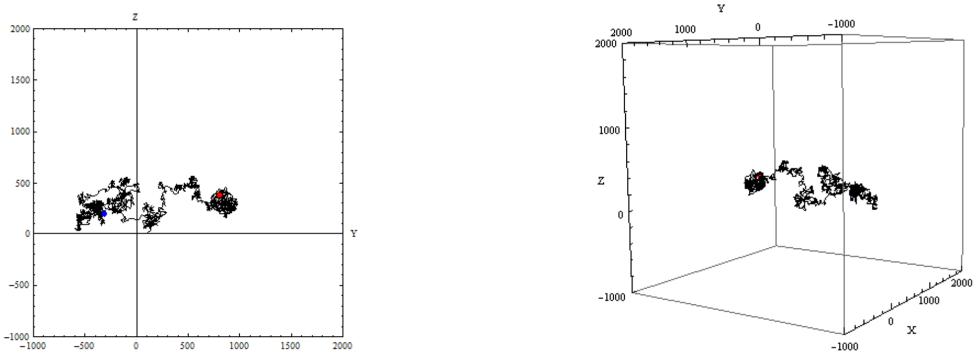

YZ trajectory

Three dimensional trajectory

Figure 6.16 Definition of tortuosity and typical trajectory of walkers from random-walk simulation—scales are in pixel, where 1 pixel = 4.34 µm.

According to classical definition, $\tau = L_e/L_0$, where L_e is the length of the tortuous path, L_0 is the length of the shortest path between the end points as shown in the illustration located on the top left corner of Figure 6.16. For instance, if the length of the tortuous path L_e is 52 pixels and the shortest path L_0 is 20 pixels, then the geometric tortuosity of this fictitious path is 52/20 = 2.6.

In this study, the geometric tortuosity from the diffusion tortuosity, as defined in Equation 6.5, was estimated using a random-walk simulation technique developed by Nakashima and Kamiya (2007). In this technique, the diffusion through the porous medium is simulated as the time-dependent displacements performed by a set of virtual "walkers". First, the walkers select a pore voxel at random as the starting position and then displace or jump to one of the six neighbouring voxels. If the randomly selected destination voxel is a solid one, then the jump is not performed. As the walkers jump or attempt to jump from voxel to voxel, a dimensionless time increment is recorded.

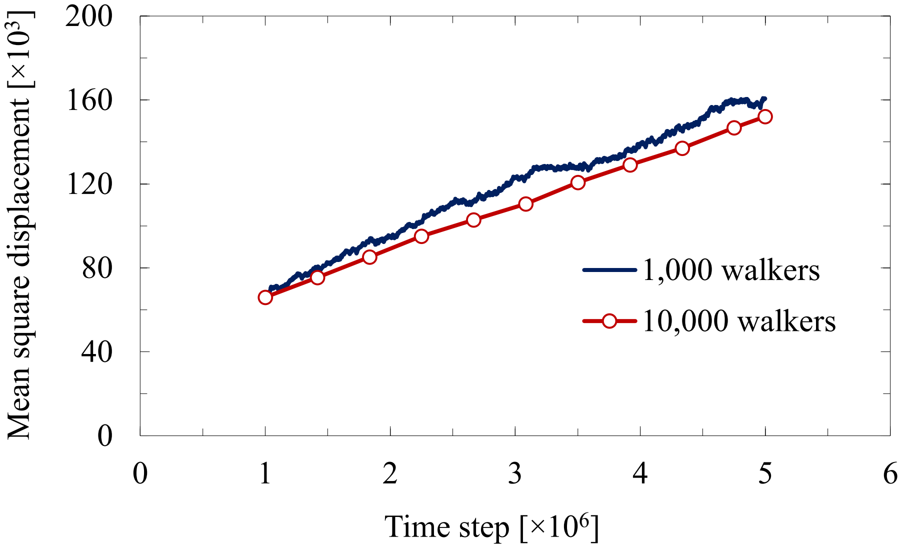

Figure 6.17 Typical mean square displacements plotted against the dimensionless time steps; showing the effect of the number of walkers on the accuracy of the random-walk simulation.

After a sufficiently long time interval, the walkers experience the tortuous nature of the pore space, which is manifested as the constant slope of the mean square displacement versus the dimensionless time plot, as shown in Figure 6.17. It is to be noted that the time derivative of the mean square displacement of walkers in free space tends to be unity. Thus, one may use Equation 6.5 and 6.6 to compute the diffusion tortuosity, and hence the geometric tortuosity. As shown in Figure 6.17, it is essential that one simulates the diffusion using a sufficiently large number of walkers to achieve the desired level of accuracy.

In order to perform the random-walk simulation in this work, XCM images were first pre-processed, binarized, and labelled to identify the largest connected pore cluster. A

Mathematica® based program by Nakashima and Kamiya (2007) was then used for the simulation. The program takes the labelled image as the input and performs some optimization steps including a mirroring process of the image set to achieve a periodic boundary condition, which allows the walkers to perform the simulation for a sufficiently long time to achieve a constant time derivative of the mean square displacement. A typical trajectory from the random-walk simulation is shown in Figure 6.16. The output of this program is presented in Figure 6.17, which illustrates the mean square displacement after a dimensionless time interval of one million. For the purpose of this study, it was found that a maximum time step of five million along with 10,000 walkers outputs a satisfactory results.

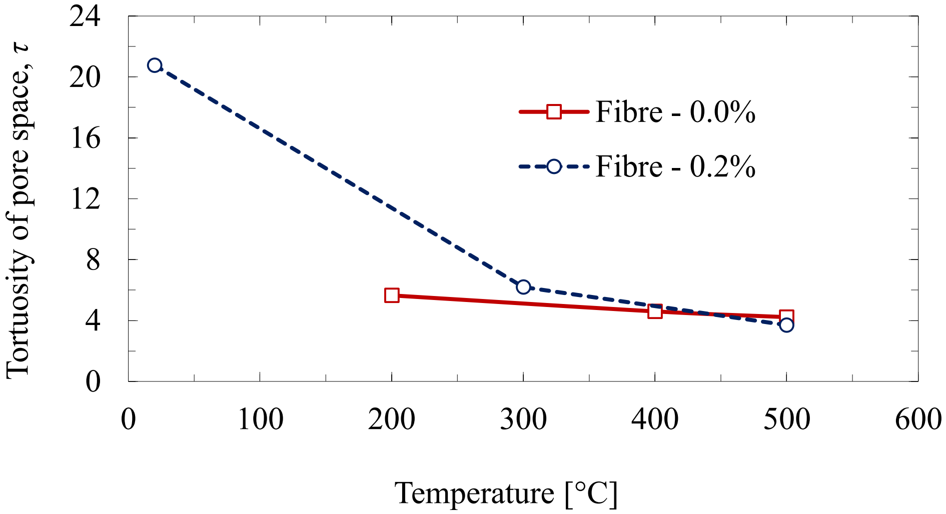

Figure 6.18 Geometric tortuosity of pore space estimated using random-walk simulation.

The tortuosity of the plain and fibre reinforced mortar exposed to different temperatures are presented in Figure 6.18. It is decreasing with the increase in exposure temperature for both types of mixture. As discussed earlier in this work, the porosity of the mortar increases due to thermal degradations. Consequently, the increased connectivity of the pore network causes a reduction in the tortuosity. From the fluid transport standpoint, it indicates a progressively higher value of fluid permeability. Mechanical properties such as fracture mechanical parameters can be correlated with the pore tortuosity along with the overall porosity (Rehder et al. 2014; Wagh et al. 1991). Therefore, it can be stated that the reduction in tortuosity implies increased mortar deterioration with the increase in the exposure temperatures, as shown in Figure 6.19.

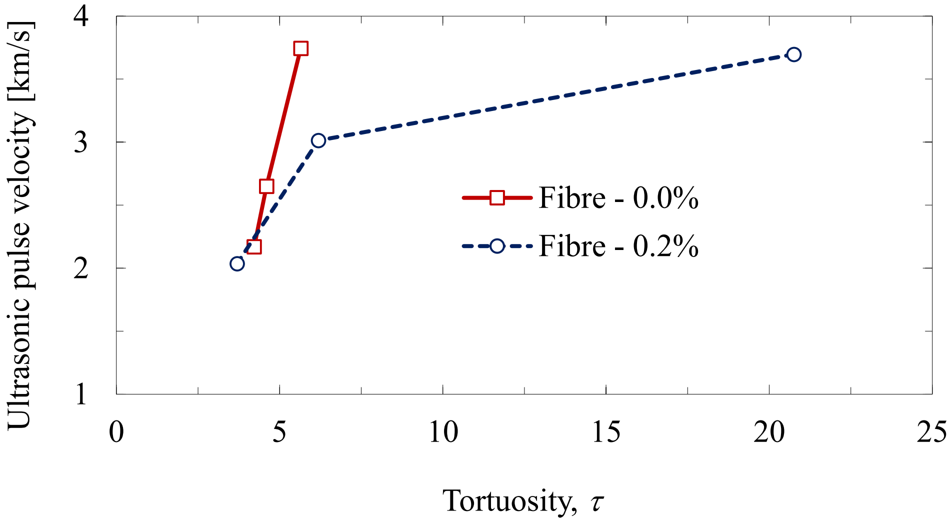

Figure 6.19 Relationship between the geometric tortuosity of pore space and the ultrasonic pulse velocity.

6.6 Conclusions

Based on the findings in this chapter, the following concluding remarks on the physical process of thermal degradation can be drawn:

- The ultrasonic pulse velocity of the mortar at elevated temperature, measured after cooling, gradually decreases for an exposure temperature beyond 200 °C due to the increased transit time caused by the presence of cracks in the internal structure of the mortar. The increase in corresponding damage value indicates a progressive deterioration, which is also evident from the reduction in elastic modulus.
- The pore fractal dimension, estimated from 3D XCM image, exhibits a space filling nature of the thermally degraded microstructure of the mortar. In addition, the change in the fractal dimension with the temperature indicates an increase in compliance.
- As the exposure temperature increases, the degree of pore connectivity increases which is evident from the shift in voxel count from the smaller clusters to the larger ones.

- The increased value of the specific surface area indicates a reduction in the available load paths due to the hygro-thermal damage sustained by the mortar.
- The pore space tortuosity of the mortar reduces with increased temperature, which has significant impact on the mechanical as well as the transport properties.

CHAPTER 7. CONCLUSIONS AND RECOMMENDATIONS

7.1 Summary of Conclusions

In the study presented in this thesis, fibre reinforced cement mortar was characterized at sustained elevated temperatures. The exposure temperature was limited to 600 °C because beyond this limit the cement-based system loses its structural integrity to a substantial degree. It is to be noted that the experimental investigations for in situ (i.e., ‘hot’) tests were conducted on oven-dried specimens. The microstructure of the mortar was studied at the micro and meso levels as it evolved with different exposure temperatures. Several state-of the-art digital image processing techniques were employed to examine the characteristics of thermally damaged microstructure. Subsequently, a fractal geometry-based modelling approach was used to predict the thermal conductivity. Finally, the fracture mechanical parameters and the damage sustained by the mortar were studied through computed X-ray microtomography. The principal outcome of this thesis can be summarized as follows:

- The microstructure of the thermally decomposed and dehydrated cement-based mortar under sustained elevated temperatures can be described using the concept of fractal geometry. Due to the conversion of gel pores into capillary pores and the formation (or evolution) of microcracks, the pore system can be characterized in terms of increasing fractal dimension of the system. This observation indicates the increasingly complex nature of the microstructure, at smaller scales of observation, under sustained elevated temperatures.
- The fracture mechanical investigations revealed the increasingly quasi-ductile nature of the mortar with an increase in the temperature of exposure. The crack-growth resistance of the mortar approaches a constant value at higher temperatures.
- The presence of polyester fibres increases the porosity at meso-level and thereby creates an interconnected pore network that provides an escape route for the water vapour generated at elevated temperatures, even before reaching the melting point of the fibre. This outcome confirms the hypothesis, regarding the role of fibres, whereby an alteration to the pore structure in the interfacial zone causes an increase in the pore connectivity.

- A fractal dimension-based model can be used to predict the thermal conductivity of cement-based systems at sustained elevated temperatures.
- The fracture energy, fracture toughness, and damage value, all correlate with fractal dimension evaluated from both two and three dimensional image processing techniques.

7.2 Concluding Remarks

A substantial part of the knowledge generated in this thesis was the outcome of extensive analysis of digital image. There are several factors, regarding the sampling process, that need to be considered to obtain statistically significant results. These include location of the specimen extraction, preparation of the specimen, and selection of the regions for microscopic examination. Furthermore, the resolution of the image limits the lowest dimension of microstructural feature that can be resolved with a fair degree of accuracy. It is worth mentioning that the image processing algorithm itself may affect the results. In order to avoid such artifacts, a consistent set of processing variables must be used, when preparing the raw images across all types of analyses. When reconstructing the computed microtomography images, it is essential to bear in mind that appropriate correction factors, for instance ring artifact and beam hardening, must be selected through a trial and error process for the best quality image output.

Fractal nature of the mortar microstructure indicates a statistical self-similarity which is characteristic of stochastic fractals. Besides, as observed, the increase in fractality with the temperature is valid over certain scales of observation. One may notice the trend describing the change in fractality with an increase in porosity of the mortar. It is essential to note that it is the very nature of the pore structure that renders fractality. For instance, the roughness of the pore perimeter, tortuous nature of the interfacial and matrix microcracks contribute to the observed statistical self-similarity.

Fracture mechanical approach was used in this study to predict the structural response of cement mortar subjected to flexural load. One may notice that the post peak response of the load-deflection curve deviates from the experimental observation slightly. It may be improved by estimating the size independent fracture parameters by analyzing the test results of several specimens and taking the average values. Further, this prediction relies on the assumption that the normalized crack growth resistance remains constant after reaching a value at peak flexural load.

7.3 Application of the Findings from This Study

Microstructural characterization of any composite helps understand the overall behaviour of the material when subjected to different external actions—mechanical load, thermal stress, and aggressive chemical actions. Response of a composite is largely governed by the interactions or transformations of its different constituent phases. For cement-based materials, the performance in resisting the imposed actions can be enhanced to a significant degree by investigating its microstructural features. To this end, the findings of this thesis is expected to have several applications in the development of cement-based materials having superior performance at sustained elevated temperature. A brief outline of the possible applications is presented below:

- The information presented in this thesis will be useful when predicting the fire resistance rating of structural components as required by the National Building Code of Canada. Estimating fire resistance of a material requires the evaluation of heat flow characteristics through a structural member which is governed by the thermal properties of the component material at elevated temperatures. This thesis provides a fractal-based model to predict these properties for cement-based systems.
- Properties of cement-based materials can be predicted from the experimental evaluations through modelling. Development of such prediction models can either be mathematically rigorous or may be based on simple rule-of-mixture depending the level of sophistication desired. In either case, prediction of physical properties from models allows a deeper understanding of the material’s response to external actions. It also provides a means to estimate the properties by avoiding time consuming experimental protocols. In addition, a well-developed model may provide an opportunity to perform

parametric study of certain properties that are otherwise impractical by following complicated experimental protocols.

- A potential area of application of the pore structure parameters is the simulation of the material. For instance, the porosity, pore size distribution, and the pore connectivity data may be utilized to generate a statistically equivalent microstructure. Furthermore, the evolution of these parameters with the increase in exposure temperature would allow one to predict their impact on the transport properties of the material.
- The discussion regarding the influence of fibre reinforcement on the meso-level pore structure may facilitate the mixture proportioning process of cement-based materials that are likely to be exposed to elevated temperatures.
- The concept of fractal geometry is a promising way of simulating microstructure of a material for the estimation of macrostructural properties. In fractal-based modelling, the structure of a material can be simulated using the pore space fractality by selecting an appropriate type of deterministic fractal. The most commonly employed mathematical fractal is the Sierpinski carpet for a two-dimensional idealization of porous surface of the material. Depending on the pore space fractal dimension, evaluated experimentally, the required number of iteration can be easily be determined. It is worth mentioning that the geometry of the selected deterministic fractal may require several iterations to achieve the desired level of porosity. Furthermore, the connectivity between the solid elements has considerable impact on the macro-level properties, which needs to be determined experimentally.
- Experimentally evaluated thermal properties such as thermal conductivity and thermal diffusivity can be used to model the heat flow phenomenon through cement-based materials. The outcome of the heat and mass transfer simulation can then be employed to predict the spalling of concrete under the prevailing moisture condition.
- With the aid of the theories from continuum mechanics and the experimentally evaluated thermal properties, hygrothermal damage sustained by cement-based materials can be estimated.
- Mechanical properties discussed in this thesis may be useful in estimating the residual performance of a structural member. Further, based on the post-fire assessment, a

number of realistic rehabilitation schemes may be developed with the aid of residual mechanical properties.

- Damage assessment and the related discussion help understand the impact of changes in pore structure caused by the exposure to elevated temperatures. Moreover, the X-ray microtomography investigation can be utilized to simulate three-dimensional structure of the material.

7.4 Recommendations for Further Studies

A number of studies can be found in the literature regarding the characterization of cement-based materials at elevated temperatures. This thesis made an effort to fill some of the knowledge gaps that were identified through a critical review of the existing literatures. Several aspects of material characterization regarding exposure to elevated temperature still remain to be investigated. An outline of these unresolved issues is presented below as recommended topics for further studies:

- Experimental protocol has significant influence on the reliability of the pore structure characterization. In this work, backscattered electron imaging was employed to study the microstructure. While it does not have the limitations imposed by conventionally used methods, such as mercury intrusion porosimetry, the resolution of the image, however, limits the detection of meso-level pores. Use of more sophisticated methods such as Woods metal intrusion may provide a more reliable description of the microstructure.
- Polymeric microfibre is known to have beneficial effects on the performance of cement-based materials at elevated temperature. This work attempted to describe the influence of these fibre on the connectivity of pore network at meso-level using nitrogen sorption technique. A more detailed examination of the influence of fibre may be conducted using the principles of cryoporometry.
- Effect of pre-existing stress on the thermal and mechanical properties has not been studied adequately. Further investigation is recommended to explore the influence of pre-loading on the evolution of microstructure at elevated temperatures.

- Fractal geometry-based three-dimensional modelling approach may provide a more accurate prediction of thermal properties. By using the three-dimensional pore space fractal dimension and an appropriate type mathematical fractal, one may simulate the behaviour of cement-based material in a more realistic manner.
- In this thesis, a fractal model to predict the thermal conductivity was employed by estimating the contact parameter—defining the contact resistance between solid elements—through a regression analysis. Further investigation may be carried out to relate this parameter using the characteristics of pore structure of the material.
- Very few studies have addressed the effect of specimen size on the fracture mechanical parameters at elevated temperature. An investigation of fracture energy through specimen size effect is recommended.
- Computed X-ray tomography is a convenient method to explore three-dimensional structure of a material non-destructively. Use of nano-tomography may allow simulation of the detailed structure of the material.
- Finite element based investigations have not been conducted in this study. High-resolution tomography data would allow one to generate finite element models for the simulation of heat flow phenomenon.

REFERENCES

Abell, A. B., Willis, K. L., and Lange, D. A. (1999). “Mercury Intrusion Porosimetry and Image Analysis of Cement-Based Materials.” *Journal of Colloid and Interface Science*, 211(1), 39–44.

Abrams, M. S. (1971). “Compressive Strength of Concrete at Temperatures to 1600F.” *ACI Special Publication*, 25, 33–58.

Agari, Y., and Uno, T. (1985). “Thermal conductivity of polymer filled with carbon materials: effect of conductive particle chains on thermal conductivity.” *Journal of Applied Polymer Science*, 30(5), 2225–2235.

Ali, F. (2002). “Is high strength concrete more susceptible to explosive spalling than normal strength concrete in fire?” *Fire and Materials*, 26(3), 127–130.

Aligizaki, K. K. (2005). *Pore Structure of Cement-Based Materials: Testing, Interpretation and Requirements*. Modern Concrete Technology, CRC Press.

Allen, T. (1990). *Particle size measurement*. Chapman and Hall, London.

Andiç-Çakır, Ö., and Hızal, S. (2012). “Influence of elevated temperatures on the mechanical properties and microstructure of self consolidating lightweight aggregate concrete.” *Construction and Building Materials*, 34, 575–583.

ASTM international. (2003). *ASTM C33 Standard Specification for Concrete Aggregates*. ASTM International, West Conshohocken, PA.

ASTM International. (2010). *ASTM C469 Standard Test Method for Static Modulus of Elasticity and Poisson’s Ratio of Concrete in Compression*. ASTM International, West Conshohocken, PA.

ASTM International. (2011). *ASTM C1363 Standard Test Method for Thermal Performance of Building Materials and Envelope Assemblies by Means of a Hot Box Apparatus*. ASTM International, West Conshohocken, PA.

ASTM International. (2013a). *ASTM C177 Standard Test Method for Steady-State Heat Flux Measurements and Thermal Transmission Properties by Means of the Guarded-Hot-Plate Apparatus*. ASTM International, West Conshohocken, PA.

ASTM International. (2013b). *ASTM C1437 Standard Test Method for Flow of Hydraulic Cement Mortar*. ASTM International, West Conshohocken, PA.

ASTM International. (2014). *ASTM D5334 Standard Test Method for Determination of Thermal Conductivity of Soil and Soft Rock by Thermal Needle Probe Procedure*. ASTM International, West Conshohocken, PA.

Baker, G. (1996). “The effect of exposure to elevated temperatures on the fracture energy of plain concrete.” *Materials and Structures*, 29(6), 383.

Balaguru, P., and Ramakrishnan, V. (1988). “Properties of Fiber Reinforced Concrete: Workability, Behavior under Long-Term Loading, and Air-Void Characteristics.” *ACI Materials Journal*, 85(3), 189–196.

Bangi, M. R., and Horiguchi, T. (2012). “Effect of fibre type and geometry on maximum pore pressures in fibre-reinforced high strength concrete at elevated temperatures.” *Cement and Concrete Research*, 42(2), 459–466.

Banthia, N., Sappakittipakorn, M., and Jiang, Z. (2012). "On permeable porosity in bio–inspired fibre reinforced cementitious composites." *International Journal of Sustainable Materials and Structural Systems*, 1(1), 29–41.

Banthia, N., and Sheng, J. (1996). "Fracture toughness of micro-fiber reinforced cement composites." *Cement and Concrete Composites*, Toughness of FRC Composites, 18(4), 251–269.

Barrett, E. P., Joyner, L. G., and Halenda, P. P. (1951). "The Determination of Pore Volume and Area Distributions in Porous Substances. I. Computations from Nitrogen Isotherms." *Journal of the American Chemical Society*, 73(1), 373–380.

Bazant, Z. P. (1997). "Analysis of pore pressure, thermal stress and fracture in rapidly heated concrete." 155–164.

Bažant, Z. P., Gettu, R., and Kazemi, M. T. (1991). "Identification of nonlinear fracture properties from size effect tests and structural analysis based on geometry-dependent R-curves." *International journal of rock mechanics and mining sciences & geomechanics abstracts*, 28(1), 43–51.

Bažant, Z. P., and Kaplan, M. F. (1996). *Concrete at High Temperatures: Material Properties and Mathematical Models*. Longman.

Bažant, Z. P., and Kazemi, M. T. (1990a). "Size Effect in Fracture of Ceramics and Its Use to Determine Fracture Energy and Effective Process Zone Length." *Journal of the American Ceramic Society*, 73(7), 1841–1853.

Bažant, Z. P., and Kazemi, M. T. (1990b). "Determination of fracture energy, process zone length and brittleness number from size effect, with application to rock and concrete." *International Journal of Fracture*, 44(2), 111–131.

Bazant, Z. P., and Pfeiffer, P. A. (1987). "Determination of Fracture Energy from Size Effect and Brittleness Number." *ACI Materials Journal*, 84(6), 463–480.

Bažant, Z. P., and Prat, P. C. (1988). "Effect of temperature and humidity on fracture energy of concrete." *ACI Materials Journal*, 85(4), 262–271.

Bažant, Z., and Planas, J. (1997). *Fracture and size effect in concrete and other quasi-brittle materials*. CRC press.

Behnood, A., and Ghandehari, M. (2009). "Comparison of compressive and splitting tensile strength of high-strength concrete with and without polypropylene fibers heated to high temperatures." *Fire Safety Journal*, 44(8), 1015–1022.

Bentur, A., and Mindess, S. (2006). *Fibre Reinforced Cementitious Composites, Second Edition*. CRC Press.

Bentz, D. P. (2000). "Fibers, percolation, and spalling of high-performance concrete." *ACI Materials Journal-American Concrete Institute*, 97(3), 351–359.

Bentz, D. P., and Garboczi, E. J. (1991). "Percolation of phases in a three-dimensional cement paste microstructural model." *Cement and Concrete Research*, 21(2–3), 325–344.

Bentz, D. P., Halleck, P. M., Clarke, M. N., Garboczi, E. J., and Grader, A. S. (2005). "Microstructure and Materials Science of Fire Resistive Materials." *Proceedings of the ASCE 2005 Structures Congress*.

Bentz, D. P., Peltz, M. A., Durán-Herrera, A., Valdez, P., and Juárez, C. A. (2011). "Thermal properties of high-volume fly ash mortars and concretes." *Journal of Building Physics*, 34(3), 263–275.

Berryman, J. G. (1985). "Measurement of spatial correlation functions using image processing techniques." *Journal of Applied Physics*, 57(7), 2374–2384.

Berryman, J. G., and Blair, S. C. (1986). “Use of digital image analysis to estimate fluid permeability of porous materials: Application of two-point correlation functions.” *Journal of applied Physics*, 60(6), 1930–1938.

Bilodeau, A., Kodur, V. K. R., and Hoff, G. C. (2004). “Optimization of the type and amount of polypropylene fibres for preventing the spalling of lightweight concrete subjected to hydrocarbon fire.” *Cement and Concrete Composites*, 26(2), 163–174.

Bindiganavile, V., and Banthia, N. (2005). “Generating dynamic crack growth resistance curves for fiber-reinforced concrete.” *Experimental Mechanics*, 45(2), 112–122.

Blair, S. C., Berge, P. A., and Berryman, J. G. (1996). “Using two-point correlation functions to characterize microgeometry and estimate permeabilities of sandstones and porous glass.” *Journal of Geophysical Research: Solid Earth*, 101(B9), 20359–20375.

Blundell, R., Dimond, C., and Browne, R. G. (1976). *The properties of concrete subjected to elevated temperatures*. CIRIA Underwater Engineering Group, London.

Bomberg, M., and Shirtliffe, C. J. (1978). “Influence of moisture and moisture gradients on heat transfer through porous building materials.” *Thermal transmission measurements of insulation*, STP660-EB, ASTM International, 211–233.

Bonnell, D. G. R., and Harper, F. C. (1950). “The thermal expansion of concrete.” *Journal of the Institution of Civil Engineers*, 33(4), 320–330.

Bouguerra, A. (1999). “Prediction of effective thermal conductivity of moist wood concrete.” *Journal of Physics D: Applied Physics*, 32(12), 1407.

Brandt, A. M. (2009). *Cement-Based Composites: Materials, Mechanical Properties and Performance, Second Edition*. CRC Press.

Browne, R. D. (1968). “Properties of concrete in reactor vessels.” *Prestressed concrete pressure vessels*, Thomas Telford Publishing, 131–151.

Bruggeman, D. (1935). “Dielectric constant and conductivity of mixtures of isotropic materials.” *Ann Phys (Leipzig)*, 24, 636–679.

Bu, Y., Spragg, R., and Weiss, W. J. (2014). “Comparison of the Pore Volume in Concrete as Determined Using ASTM C642 and Vacuum Saturation.” *Advances in Civil Engineering Materials*, 3(1), 308–315.

Bungey, J. H., Millard, S. G., and Grantham, M. (2006). *Testing of concrete in structures*. Taylor & Francis, London ; New York.

Campbell-Allen, D., and Thorne, C. P. (1963). “The thermal conductivity of concrete.” *Magazine of Concrete Research*, 15(43), 39–48.

Canadian Standards Association. (2013). *CSA A3001-13 Cementitious materials for use in concrete*. CSA Group, Mississauga, Ontario, Canada, 292.

Carpinteri, A., and Ingraffea, A. R. (2012). *Fracture mechanics of concrete: Material characterization and testing: Material Characterization and Testing*. Springer Science & Business Media.

Carslaw, H. S., and Jaeger, J. C. (1959). *Conduction of heat in solids*. Oxford University Press.

Castaño, V. M., Martinez, G., Alemán, J. L., and Jiménez, A. (1990). “Fractal structure of the pore surface of hydrated portland cement pastes.” *Journal of Materials Science Letters*, 9(9), 1115–1116.

Castellote, M., Alonso, C., Andrade, C., Turrillas, X., and Campo, J. (2004). “Composition and microstructural changes of cement pastes upon heating, as studied by neutron diffraction.” *Cement and Concrete Research*, 34(9), 1633–1644.

Çengel, Y. A., and Ghajar, A. J. (2015). *Heat and mass transfer: fundamentals & applications*. McGraw Hill Education, New York, NY.

Chan, S. Y. N., Luo, X., and Sun, W. (2000a). "Effect of high temperature and cooling regimes on the compressive strength and pore properties of high performance concrete." *Construction and Building Materials*, 14(5), 261–266.

Chan, S. Y. N., Peng, G.-F., and Anson, M. (1999). "Fire behavior of high-performance concrete made with silica fume at various moisture contents." *ACI Materials Journal*, 96(3).

Chan, Y. N., Luo, X., and Sun, W. (2000b). "Compressive strength and pore structure of high-performance concrete after exposure to high temperature up to 800 C." *Cement and Concrete Research*, 30(2), 247–251.

Chatterji, S. (2001). "A discussion of the paper 'Mercury porosimetry—an inappropriate method for the measurement of pore size distributions in cement-based materials' by S. Diamond." *Cement and Concrete Research*, 31(11), 1657–1658.

Cheng, S. C., and Vachon, R. I. (1969). "The prediction of the thermal conductivity of two and three phase solid heterogeneous mixtures." *International Journal of Heat and Mass Transfer*, 12(3), 249–264.

Chiaia, B., van Mier, J. G. M., and Vervuurt, A. (1998). "Crack Growth Mechanisms in Four Different Concretes: Microscopic Observations and Fractal Analysis." *Cement and Concrete Research*, 28(1), 103–114.

Choktaweekarn, P., Saengsoy, W., and Tangtermsirikul, S. (2009). "A model for predicting the specific heat capacity of fly-ash concrete." *ScienceAsia*, 35(2), 178–182.

Clauser, C., and Huenges, E. (1995). "Thermal Conductivity of Rocks and Minerals." *Rock Physics & Phase Relations*, T. J. Ahrens, ed., American Geophysical Union, 105–126.

Comite Euro-International Du Beton. (1993). *CEB-FIP Model Code 1990: Design Code*. Fédération internationale du béton.

Consolazio, G. R., McVay, M. C., and Rish III, J. W. (1998). "Measurement and prediction of pore pressures in saturated cement mortar subjected to radiant heating." *ACI Materials Journal*, 95(5).

Copier, W. J. (1983). "The Spalling of Normal Weight and Lightweight Concrete Exposed to Fire." *Special Publication*, 80, 219–236.

Cruz, C. R., and Gillen, M. (1980). "Thermal expansion of Portland cement paste, mortar and concrete at high temperatures." *Fire and materials*, 4(2), 66–70.

Demirboğa, R., and Gül, R. (2003). "The effects of expanded perlite aggregate, silica fume and fly ash on the thermal conductivity of lightweight concrete." *Cement and Concrete Research*, 33(5), 723–727.

Diamond, S. (1989). "Methodologies of PSD Measurements In HCP : Postulates, Peculiarities, And Problems." *MRS Online Proceedings Library Archive*, 137.

Diamond, S. (1999). "Aspects of concrete porosity revisited." *Cement and Concrete Research*, 29(8), 1181–1188.

Diamond, S. (2000). "Mercury porosimetry: An inappropriate method for the measurement of pore size distributions in cement-based materials." *Cement and Concrete Research*, 30(10), 1517–1525.

Diamond, S., and Huang, J. (2001). "The ITZ in concrete – a different view based on image analysis and SEM observations." *Cement and Concrete Composites*, Special Theme Issue on Image Analysis, 23(2–3), 179–188.

Dias, W. P. S., Khoury, G. A., and Sullivan, P. J. E. (1990). “Mechanical Properties of Hardened Cement Paste Exposed to Temperatures up to 700 C (1292 F).” *ACI Materials Journal*, 87(2), 160–166.

Diederichs, U., and Schneider, U. (1981). “Bond strength at high temperatures.” *Magazine of Concrete Research*, 33(115), 75–84.

Dugdale, D. S. (1960). “Yielding of steel sheets containing slits.” *Journal of the Mechanics and Physics of Solids*, 8(2), 100–104.

Eins, S. (1995). “An improved dilation method for the measurement of fractal dimension.” *Acta Stereologica*, 14(2), 169–178.

Fares, H., Noumowe, A., and Remond, S. (2009). “Self-consolidating concrete subjected to high temperature.” *Cement and Concrete Research*, 39(12), 1230–1238.

Fares, H., Remond, S., Noumowe, A., and Cousture, A. (2010). “High temperature behaviour of self-consolidating concrete. Microstructure and physicochemical properties.” *Cement and Concrete Research*, 40(3), 488–496.

Feng, Y., Yu, B., Zou, M., and Zhang, D. (2004). “A generalized model for the effective thermal conductivity of porous media based on self-similarity.” *Journal of Physics D: Applied Physics*, 37(21), 3030–3040.

Fricke, H. (1924). “A Mathematical Treatment of the Electric Conductivity and Capacity of Disperse Systems I. The Electric Conductivity of a Suspension of Homogeneous Spheroids.” *Physical Review*, 24(5), 575–587.

Garboczi, E. J., Snyder, K. A., Douglas, J. F., and Thorpe, M. F. (1995). “Geometrical percolation threshold of overlapping ellipsoids.” *Physical review E*, 52(1), 819.

Gefen, Y., Aharony, A., and Mandelbrot, B. B. (1984). “Phase transitions on fractals: III. Infinitely ramified lattices.” *Journal of Physics A: Mathematical and General*, 17, 1277–1289.

Gefen, Y., Mandelbrot, B. B., and Aharony, A. (1980). “Critical Phenomena on Fractal Lattices.” *Physical Review Letters*, 45(11), 855–858.

Goldman, A., and Bentur, A. (1992). “Effects of pozzolanic and non-reactive microfillers on the transition zone in high strength concretes.” *Interfaces in cementitious composites*, RILEM Proceedings 18, J. C. Maso, ed., E & FN Spon.

Gonzalez, R. C. (2009). *Digital Image Processing*. Pearson Education.

Gustafsson, S. E. (1991). “Transient plane source techniques for thermal conductivity and thermal diffusivity measurements of solid materials.” *Review of Scientific Instruments*, 62(3), 797–804.

Haddad, R. H., Al-Saleh, R. J., and Al-Akhras, N. M. (2008). “Effect of elevated temperature on bond between steel reinforcement and fiber reinforced concrete.” *Fire Safety Journal*, 43(5), 334–343.

Haddad, R. H., and Shannis, L. G. (2004). “Post-fire behavior of bond between high strength pozzolanic concrete and reinforcing steel.” *Construction and Building Materials*, 18(6), 425–435.

Hafner, B. (2007). *Scanning electron microscopy primer*. Characterization Facility, University of Minnesota-Twin Cities.

Hager, I. (2013). “Behaviour of cement concrete at high temperature.” *Bulletin of the Polish Academy of Sciences: Technical Sciences*, 61(1), 145–154.

Hamilton, R. L., and Crosser, O. K. (1962). "Thermal Conductivity of Heterogeneous Two-Component Systems." *Industrial & Engineering Chemistry Fundamentals*, 1(3), 187–191.

Hansen, T. C. (1986). "Physical structure of hardened cement paste. A classical approach." *Materials and Structures*, 19(6), 423–436.

Harada, T., Takeda, J., Yamane, S., and Furumura, F. (1972). "Strength, Elasticity and Thermal Properties of Concrete Subjected to Elevated Temperatures." *Special Publication*, 34, 377–406.

Harmathy, T. (1964). "Variable-State Methods of Measuring the Thermal Properties of Solids." *Journal of Applied Physics*, 35(4), 1190–1200.

Harmathy, T., and Allen, L. (1973). "Thermal properties of selected masonry unit concretes." *ACI Journal Proceedings*, 70(2), 132–142.

Harmathy, T. Z. (1965). "Effect of moisture on the fire endurance of building elements." *ASTM special technical publication 385*, 74–95.

Harmathy, T. Z. (1970). "Thermal properties of concrete at elevated temperatures." *Journal of Materials*, 5(1), 47–74.

Hashin, Z., and Shtrikman, S. (1962). "A variational approach to the theory of the effective magnetic permeability of multiphase materials." *Journal of applied Physics*, 33(10), 3125–3131.

Hasselman, D. P. H., and Johnson, L. F. (1987). "Effective Thermal Conductivity of Composites with Interfacial Thermal Barrier Resistance." *Journal of Composite Materials*, 21(6), 508–515.

He, Y. (2005). "Rapid thermal conductivity measurement with a hot disk sensor: Part 1. Theoretical considerations." *Thermochimica Acta*, 436(1–2), 122–129.

He, Y., and Ng, G. S. (2002). "Hot Disk: A Transient Plane Source Technique for Rapid Thermal Conductivity Measurement." *International symposium for testing and failure analysis*, ASM International; 1998, 513–522.

Helfen, L., Dehn, F., Mikulík, P., and Baumbach, T. (2005). "Three-dimensional imaging of cement microstructure evolution during hydration." *Advances in Cement Research*, 17(3), 103–111.

Heo, Y.-S., Sanjayan, J. G., Han, C.-G., and Han, M.-C. (2010). "Synergistic effect of combined fibers for spalling protection of concrete in fire." *Cement and Concrete Research*, 40(10), 1547–1554.

Hernández-Olivares, F., and Barluenga, G. (2004). "Fire performance of recycled rubber-filled high-strength concrete." *Cement and Concrete Research*, 34(1), 109–117.

Hertz, K. (1982). "The anchorage capacity of reinforcing bars at normal and high temperatures." *Magazine of Concrete Research*, 34(121), 213–220.

Hertz, K. D. (1992). "Danish Investigations on Silica Fume Concretes at Elevated Temperatures." *ACI Materials Journal*, 89(4), 345–347.

Hertz, K. D., and Sørensen, L. S. (2005). "Test method for spalling of fire exposed concrete." *Fire Safety Journal*, 40(5), 466–476.

Hillerborg, A., Modéer, M., and Petersson, P.-E. (1976). "Analysis of crack formation and crack growth in concrete by means of fracture mechanics and finite elements." *Cement and Concrete Research*, 6(6), 773–781.

Hoshen, J., and Kopelman, R. (1976). “Percolation and cluster distribution. I. Cluster multiple labeling technique and critical concentration algorithm.” *Physical Review B*, 14(8), 3438–3445.

Hossain, K. (2006). “Macro-and microstructural investigations on strength and durability of pumice concrete at high temperature.” *Journal of materials in civil engineering*, 18(4), 527–536.

Hu, J. (2004). “Porosity of concrete-morphological study of model concrete.” Master’s Thesis, Delft University of Technology.

Hung-Wan, C., and Kwok, S. L. (1985). “Assessing fire damage of concrete by the ultrasonic pulse technique.” *Cement, concrete and aggregates*, 7(2), 84–88.

Irwin, G. R. (1958). *Handbuch der Physik, Vol VI*. Springer, Berlin.

Jambor, J. (1973). “Influence of phase composition of hardened binder pastes on its pore structure and strength.” *Proceedings of Symposium on Pore structure and properties of materials*, Prague, D75–D96.

Jansson, R. (2004). *Measurement of thermal properties at elevated temperatures*. SP Report 46, Swedish National Testing and Research Institute, Borås, Sweden.

Jenq, Y., and Shah, S. P. (1985). “Two parameter fracture model for concrete.” *Journal of engineering mechanics*, 111(10), 1227–1241.

Ji, X., Chan, S. Y. N., and Feng, N. (1997). “Fractal model for simulating the space-filling process of cement hydrates and fractal dimensions of pore structure of cement-based materials.” *Cement and Concrete Research*, 27(11), 1691–1699.

Johnston, C. D. (2010). *Fiber-Reinforced Cements and Concretes*. CRC Press.

Kadoya, K., Matsunaga, N., and Nagashima, A. (1985). “Viscosity and thermal conductivity of dry air in the gaseous phase.” *Journal of physical and chemical reference data*, 14(4), 947–970.

Kalifa, P., Chene, G., and Galle, C. (2001). “High-temperature behaviour of HPC with polypropylene fibres: From spalling to microstructure.” *Cement and concrete research*, 31(10), 1487–1499.

Kalifa, P., Menneteau, F.-D., and Quenard, D. (2000). “Spalling and pore pressure in HPC at high temperatures.” *Cement and concrete research*, 30(12), 1915–1927.

Katz, A., and Thompson, A. H. (1985). “Fractal sandstone pores: implications for conductivity and pore formation.” *Physical Review Letters*, 54(12), 1325.

Kaye, B. H. (1989). *A Random Walk through Fractal Dimensions*. VCH Publishers, New York, NY, USA.

Khaliq, W., and Kodur, V. (2011). “Thermal and mechanical properties of fiber reinforced high performance self-consolidating concrete at elevated temperatures.” *Cement and Concrete Research*, 41(11), 1112–1122.

Khoury, G. (1992). “Compressive strength of concrete at high temperatures: a reassessment.” *Magazine of concrete Research*, 44(161), 291–309.

Khoury, G. A. (2008). “Polypropylene fibres in heated concrete. Part 2: Pressure relief mechanisms and modelling criteria.” *Magazine of Concrete Research*, 60(3), 189–204.

Khoury, G. A., and Anderberg, Y. (2000). *Concrete spalling review*. Swedish National Road Administration.

Khoury, G. A., Majorana, C. E., Pesavento, F., and Schrefler, B. A. (2002). “Modelling of heated concrete.” *Magazine of Concrete Research*, 54(2), 77–101.

Khoury, G. A., Majorana, C. E., and Salomoni, V. A. (2008). “Polypropylene fibres and explosive spalling in tunnel constructions.”

Khoury, G. A., and Willoughby, B. (2008). “Polypropylene fibres in heated concrete. Part 1: Molecular structure and materials behaviour.” *Magazine of Concrete Research*, 60(2), 125–136.

Kim, K.-H., Jeon, S.-E., Kim, J.-K., and Yang, S. (2003). “An experimental study on thermal conductivity of concrete.” *Cement and Concrete Research*, 33(3), 363–371.

Kodur, V. (2014). “Properties of Concrete at Elevated Temperatures.” *International Scholarly Research Notices*, 2014, e468510.

Kodur, V. K. R. (2000). “Spalling in high strength concrete exposed to fire—concerns, causes, critical parameters and cures.” 1–8.

Kodur, V., and Khaliq, W. (2011). “Effect of Temperature on Thermal Properties of Different Types of High-Strength Concrete.” *Journal of Materials in Civil Engineering*, 23(6), 793–801.

Komonen, J., and Penttala, V. (2003). “Effects of High Temperature on the Pore Structure and Strength of Plain and Polypropylene Fiber Reinforced Cement Pastes.” *Fire Technology*, 39(1), 23–34.

Krischer, O., and Kroll, K. (1956). *Die wissenschaftlichen Grundlagen der Trocknungstechnik*. Springer, Berlin.

Lamond, J. F., and Pielert, J. H. (2006). *Significance of tests and properties of concrete and concrete making materials*. ASTM International.

Landis, E. (2006). “Toward a Physical Damage Variable for Concrete.” *Journal of Engineering Mechanics*, 132(7), 771–774.

Landis, E. N. (2005). “Damage variables based on three-dimensional measurements of crack geometry.” *Strength, Fracture and Complexity*, 3(2), 163–173.

Landis, E. N., and Keane, D. T. (2010). “X-ray microtomography.” *Materials Characterization*, 61(12), 1305–1316.

Landis, E. N., Zhang, T., Nagy, E. N., Nagy, G., and Franklin, W. R. (2007). “Cracking, damage and fracture in four dimensions.” *Materials and Structures*, 40(4), 357–364.

Lange, D. A., Jennings, H. M., and Shah, S. P. (1994). “Image analysis techniques for characterization of pore structure of cement-based materials.” *Cement and Concrete Research*, 24(5), 841–853.

Lankard, D. R. (1970). “The Dimensional Instability of Heated Portland Cement Concrete.” Ph.D. Thesis, Ohio State University.

Lee, G., Han, D., Han, M.-C., Han, C.-G., and Son, H.-J. (2012). “Combining polypropylene and nylon fibers to optimize fiber addition for spalling protection of high-strength concrete.” *Construction and Building Materials*, 34, 313–320.

Lemaitre, J. (1996). *A Course on Damage Mechanics*. Springer Berlin Heidelberg.

Li, L. Y., Purkiss, J. A., and Tenchev, R. T. (2002). “An engineering model for coupled heat and mass transfer analysis in heated concrete.” *Proceedings of the Institution of Mechanical Engineers, Part C: Journal of Mechanical Engineering Science*, 216(2), 213–222.

Lie, T. T., and Kodur, V. K. R. (1996). “Thermal and mechanical properties of steel-fibre-reinforced concrete at elevated temperatures.” *Canadian Journal of Civil Engineering*, 23(2), 511–517.

Lin, W.-M., Lin, T. D., and Powers-Couche, L. J. (1996). “Microstructures of fire-damaged concrete.” *ACI Materials Journal*, 93(3).

Log, T., and Gustafsson, S. E. (1995). “Transient plane source (TPS) technique for measuring thermal transport properties of building materials.” *Fire and Materials*, 19(1), 43–49.

Lu, S., Landis, E. N., and Keane, D. T. (2006). “X-ray microtomographic studies of pore structure and permeability in Portland cement concrete.” *Materials and Structures*, 39(6), 611–620.

Luo, X., Sun, W., and Chan, Y. N. (2000). “Residual compressive strength and microstructure of high performance concrete after exposure to high temperature.” *Materials and Structures*, 33(5), 294–298.

Ma, Y., Yu, B., Zhang, D., and Zou, M. (2003). “A self-similarity model for effective thermal conductivity of porous media.” *Journal of Physics D: Applied Physics*, 36(17), 2157–2164.

Maierhofer, C., Reinhardt, H.-W., and Dobmann, G. (2010). *Non-Destructive Evaluation of Reinforced Concrete Structures, Volume 2 - Non-Destructive Testing Methods*. Woodhead publishing in materials.

Majorana, C. E., Khoury, G. A., and Salomoni, V. A. (2013). “Effects of polypropylene fibres in concrete under fire conditions.”

Majorana, C. E., Salomoni, V. A., Mazzucco, G., and Khoury, G. A. (2010). “An approach for modelling concrete spalling in finite strains.” *Mathematics and Computers in Simulation*, 80(8), 1694–1712.

Malhotra, H. L. (1956). “The effect of temperature on the compressive strength of concrete.” *Magazine of Concrete Research*, 8(23), 85–94.

Marechal, J. C. (1972). “Creep of Concrete as a Function of Temperature.” *ACI Special Publication*, 34, 547–564.

Mehta, P. K., Mehta, P. K., and Monteiro, P. J. M. (2006). *Concrete: microstructure, properties, and materials*. McGraw-Hill.

Mehta, P. K., and Monteiro, P. J. M. (2013). *Concrete: Microstructure, Properties, and Materials*. McGraw-Hill Education, New York.

Mindess, S., Young, J. F., and Darwin, D. (2003). *Concrete*. Prentice Hall.

Mitchell, L. J. (1953). “Thermal Expansion Tests on Aggregates, Neat Cements, and Concretes.” *Proceedings of American Society for Testing and Materials*, ASTM International, 963–977.

Mohamedbhai, G. T. G. (1986). “Effect of exposure time and rates of heating and cooling on residual strength of heated concrete.” *Magazine of Concrete Research*, 38(136), 151–158.

Morley, P. D., and Royles, R. (1980). “The influence of high temperature on the bond in reinforced concrete.” *Fire Safety Journal*, 2(4), 243–255.

Morley, P. D., and Royles, R. (1983). “Response of the Bond in Reinforced Concrete to High Temperatures.” *Magazine of Concrete Research*, 35(123), 67–74.

Naik, T. R., Malhotra, V. M., and Popovics, J. S. (2003). “The Ultrasonic Pulse Velocity Method.” *Handbook on Nondestructive Testing of Concrete Second Edition*, CRC Press, 8-1-8–19.

Nakashima, Y., and Kamiya, S. (2007). “Mathematica Programs for the Analysis of Three-Dimensional Pore Connectivity and Anisotropic Tortuosity of Porous Rocks using X-ray Computed Tomography Image Data." *Journal of Nuclear Science and Technology*, 44(9), 1233–1247.

Nakashima, Y., Nakano, T., Nakamura, K., Uesugi, K., Tsuchiyama, A., and Ikeda, S. (2004). "Three-dimensional diffusion of non-sorbing species in porous sandstone: computer simulation based on X-ray microtomography using synchrotron radiation." *Journal of Contaminant Hydrology*, 74(1–4), 253–264.

Naus, D. J. (2010). *A Compilation of Elevated Temperature Concrete Material Property Data and Information for Use in Assessments of Nuclear Power Plant Reinforced Concrete Structures*. United States Nuclear Regulatory Commission.

Neville, A. M. (2011). *Properties of concrete*. Pearson, Harlow, England; New York.

Ochiai, S. (1993). *Mechanical Properties of Metallic Composites*. CRC Press.

Ohama, Y. (1995). *Handbook of Polymer-Modified Concrete and Mortars: Properties and Process Technology*. William Andrew.

Ollivier, J. P., Maso, J. C., and Bourdette, B. (1995). "Interfacial transition zone in concrete." *Advanced Cement Based Materials*, 2(1), 30–38.

Ouyang, C., Tang, T., and Shah, S. P. (1996). "Relationship between fracture parameters from two parameter fracture model and from size effect model." *Materials and Structures*, 29(2), 79.

Peng, G.-F., Bian, S.-H., Guo, Z.-Q., Zhao, J., Peng, X.-L., and Jiang, Y.-C. (2008). "Effect of thermal shock due to rapid cooling on residual mechanical properties of fiber concrete exposed to high temperatures." *Construction and Building Materials*, 22(5), 948–955.

Peng, G.-F., and Huang, Z.-S. (2008). "Change in microstructure of hardened cement paste subjected to elevated temperatures." *Construction and Building Materials*, 22(4), 593–599.

Penner, E. (1970). "Thermal conductivity of frozen soils." *Canadian Journal of Earth Sciences*, 7(3), 982–987.

Pereira de Oliveira, L. A., and Castro-Gomes, J. P. (2011). "Physical and mechanical behaviour of recycled PET fibre reinforced mortar." *Construction and Building Materials*, 25(4), 1712–1717.

Phan, L. T. (2008). "Pore pressure and explosive spalling in concrete." *Materials and Structures*, 41(10), 1623–1632.

Pietrak, K., and Wisniewski, T. S. (2015). "A review of models for effective thermal conductivity of composite materials." *Journal of Power Technologies*, 95(1), 14.

Pliya, P., Beaucour, A.-L., and Noumowé, A. (2011). "Contribution of cocktail of polypropylene and steel fibres in improving the behaviour of high strength concrete subjected to high temperature." *Construction and Building Materials*, 25(4), 1926–1934.

Poinard, C., Piotrowska, E., Malecot, Y., Daudeville, L., and Landis, E. N. (2012). "Compression triaxial behavior of concrete: the role of the mesostructure by analysis of X-ray tomographic images." *European Journal of Environmental and Civil Engineering*, 16(sup1), s115–s136.

Poon, C.-S., Azhar, S., Anson, M., and Wong, Y.-L. (2003). "Performance of metakaolin concrete at elevated temperatures." *Cement and Concrete Composites*, 25(1), 83–89.

Popovics, S. (1998). *Strength and Related Properties of Concrete: A Quantitative Approach*. John Wiley & Sons.

Pourchez, J., Valdivieso, F., Grosseau, P., Guyonnet, R., and Guilhot, B. (2006). "Kinetic modelling of the thermal decomposition of ettringite into metaettringite." *Cement and Concrete Research*, 36(11), 2054–2060.

Progelhof, R. C., Throne, J. L., and Ruetsch, R. R. (1976). "Methods for predicting the thermal conductivity of composite systems: A review." *Polymer Engineering & Science*, 16(9), 615–625.

Promentilla, M. A. B., Cortez, S. M., Papel, R. A. D., Tablada, B. M., and Sugiyama, T. (2016). "Evaluation of microstructure and transport properties of deteriorated cementitious materials from their X-ray computed tomography (CT) images." *Materials*, 9(5), 388.

Promentilla, M. A. B., and Sugiyama, T. (2007). "Studies on 3D micro-geometry and diffusion tortuosity of cement-based materials using X-ray microtomography." 389–396.

Promentilla, M. A. B., Sugiyama, T., Hitomi, T., and Takeda, N. (2008). "Characterizing the 3D Pore Structure of Hardened Cement Paste with Synchrotron Microtomography." *Journal of Advanced Concrete Technology*, 6(2), 273–286.

Rehder, B., Banh, K., and Neithalath, N. (2014). "Fracture behavior of pervious concretes: The effects of pore structure and fibers." *Engineering Fracture Mechanics*, 118, 1–16.

Rostásy, F. S., Weiβ, R., and Wiedemann, G. (1980a). "Changes of pore structure of cement mortars due to temperature." *Cement and Concrete Research*, 10(2), 157–164.

Rostásy, F. S., Weiβ, R., and Wiedemann, G. (1980b). "Changes of pore structure of cement mortars due to temperature." *Cement and Concrete Research*, 10(2), 157–164.

Russ, J. C. (1992). *Fractal Surfaces*. Plenum Press, New York.

Russ, J. C., and Dehoff, R. T. (2012). *Practical Stereology*. Springer Science & Business Media.

Russ, J. C., and Neal, F. B. (2016). *The Image Processing Handbook, Seventh Edition*. CRC Press.

Russell, H. W. (1935). "Principles of heat flow in porous insulators." *Journal of the American Ceramic Society*, 18(1–12), 1–5.

Saad, M., Abo-El-Enein, S. A., Hanna, G. B., and Kotkata, M. F. (1996). "Effect of temperature on physical and mechanical properties of concrete containing silica fume." *Cement and Concrete Research*, 26(5), 669–675.

Saito, H. (1966). "Explosive Spalling of Prestressed Concrete in Fire." *Bulletin of Japan Association for Fire Science and Engineering*, 15(2), 23–30.

Schneider, U. (1988). "Concrete at high temperatures—A general review." *Fire Safety Journal*, 13(1), 55–68.

Schneider, U., Diederichs, U., and Ehm, C. (1982). "Effect of temperature on steel and concrete for PCRV's." *Nuclear Engineering and Design*, 67(2), 245–258.

Schneider, U., and Herbst, H. J. (1989). *Permeabilitaet und Porositaet von Beton bei hohen Temperaturen*. Deutscher Ausschuss fuer Stahlbeton, 23–52.

Scrivener, K. L. (1989). "The Use of Backscattered Electron Microscopy and Image Analysis to Study the Porosity of Cement Paste." *Proceedings of Symposium on Pore Structure and Permeability of Cementitious Materials*, MRS Online Proceedings Library Archive, 129–140.

Scrivener, K. L. (2004). "Backscattered electron imaging of cementitious microstructures: understanding and quantification." *Cement and Concrete Composites*, 26(8), 935–945.

Scrivener, K. L., and Nemati, K. M. (1996). "The percolation of pore space in the cement paste/aggregate interfacial zone of concrete." *Cement and Concrete Research*, 26(1), 35–40.

Scrivener, K., Snellings, R., and Lothenbach, B. (2015). *A Practical Guide to Microstructural Analysis of Cementitious Materials*. CRC Press.

Sellevold, E. J., and Bjøntegaard, Ø. (2006). "Coefficient of thermal expansion of cement paste and concrete: Mechanisms of moisture interaction." *Materials and Structures*, 39(9), 809–815.

Shah, S. P., Swartz, S. E., and Ouyang, C. (1995). *Fracture Mechanics of Concrete: Applications of Fracture Mechanics to Concrete, Rock and Other Quasi-Brittle Materials*. John Wiley & Sons.

Shah, S. P., and Winter, G. (1968). "Inelastic Behavior and Fracture of Concrete." *Special Publication*, 20, 5–28.

Shimada, Y., and Young, J. F. (2001). "Structural changes during thermal dehydration of ettringite." *Advances in Cement Research*, 13(2), 77–81.

Shin, K.-Y., Kim, S.-B., Kim, J.-H., Chung, M., and Jung, P.-S. (2002). "Thermo-physical properties and transient heat transfer of concrete at elevated temperatures." *Nuclear Engineering and Design*, 212(1–3), 233–241.

Sideris, K. K., and Manita, P. (2013). "Residual mechanical characteristics and spalling resistance of fiber reinforced self-compacting concretes exposed to elevated temperatures." *Construction and Building Materials*, 41, 296–302.

Skorokhod, V. V. (1995). "Theory of the physical properties of porous and composite materials and the principles for control of their microstructure in manufacturing processes." *Powder Metallurgy and Metal Ceramics*, 34(1), 48–63.

Stuckes, A. D., and Simpson, A. (1985). "The effect of moisture on the thermal conductivity of aerated concrete." *Building Services Engineering Research and Technology*, 6(2), 49–53.

Suhaendi, S. L., Watanabe, K., Shimura, K., and Horiguchi, T. (2007). "Fracture energy of hybrid fiber reinforced high strength concrete under high temperature condition." *Japan Concrete Institute Proceedings*, 29(1), 387–392.

Sullivan, P. J. E. (2004). "A probabilistic method of testing for the assessment of deterioration and explosive spalling of high strength concrete beams in flexure at high temperature." *Cement and Concrete Composites*, 26(2), 155–162.

Sullivan, P. J., and Poucher, M. P. (1971). "The Influence of Temperature on the Physical Properties of Concrete and Mortar in the Range 20 C to 400 C." *ACI Special Publication*, 25, 103–136.

Tada, H., Paris, P. C., and Irwin, G. R. (2000). *The Stress Analysis of Cracks Handbook, Third Edition*. ASME, Three Park Avenue New York, NY 10016-5990.

Taoukil, D., El bouardi, A., Sick, F., Mimet, A., Ezbakhe, H., and Ajzoul, T. (2013). "Moisture content influence on the thermal conductivity and diffusivity of wood–concrete composite." *Construction and Building Materials*, 48, 104–115.

Tarplee, M. F., and Corps, N. (2009). *Acquiring optimal quality X-ray µCT scans*. Queen Mary University of London.

Thelandersson, S. (1972). *Effect of High Temperatures on Tensile Strength of Concrete*. Lund Institute of Technology.

Thompson, N. E. (1968). “A note on the difficulties of measuring the thermal conductivity of concrete.” *Magazine of Concrete Research*, 20(62), 45–49.

Torquato, S. (2000). “Modeling of physical properties of composite materials.” *International Journal of Solids and Structures*, 37(1), 411–422.

Torquato, S. (2002). *Random Heterogeneous Materials: Microstructure and Macroscopic Properties*. Springer, New York, NY.

Tsimbrovska, M., Kalifa, P., Quenard, D., and Daian, J. F. (1997). “High performance concretes at elevated temperature: permeability and microstructure.” Lyon, France, 475–482.

Underwood, E. (1968). “Particle size distribution.” *Quantitative microscopy*, R. T. DeHoff and F. N. Rhines, eds., McGraw-Hill.

Vodák, F., Trtík, K., Kapičková, O., Hošková, Š., and Demo, P. (2004). “The effect of temperature on strength – porosity relationship for concrete.” *Construction and Building Materials*, 18(7), 529–534.

Vydra, V., Vodák, F., Kapičková, O., and Hošková, Š. (2001). “Effect of temperature on porosity of concrete for nuclear-safety structures.” *Cement and Concrete Research*, 31(7), 1023–1026.

Wagh, A. S., Poeppel, R. B., and Singh, J. P. (1991). “Open pore description of mechanical properties of ceramics.” *Journal of Materials Science*, 26(14), 3862–3868.

Wang, C. H. (1971). “Creep of Concrete at Elevated Temperatures.” *Special Publication*, 27, 387–400.

Wang, M., and Pan, N. (2008). “Predictions of effective physical properties of complex multiphase materials.” *Materials Science and Engineering: R: Reports*, 63(1), 1–30.

Wang, Y. (1995). “Microstructural study of hardened cement paste by backscatter scanning electron microscopy and image analysis.” Ph.D. Thesis, Purdue University.

Weigler, H., and Fischer, R. (1972). “Influence of High Temperatures on Strength and Deformation of Concrete.” *ACI Special Publication*, 34, 481–494.

Westermarck, S. (2000). “Use of mercury porosimetry and nitrogen adsorption in characterisation of the pore structure of mannitol and microcrystalline cellulose powders, granules and tablets.” Academic Dissertation, University of Helsinki.

Willis, K. L., Abell, A. B., and Lange, D. A. (1998). “Image-based characterization of cement pore structure using wood’s metal intrusion.” *Cement and Concrete Research*, 28(12), 1695–1705.

Winslow, D. N. (1985). “The fractal nature of the surface of cement paste.” *Cement and Concrete Research*, 15(5), 817–824.

Wong, H. S., Head, M. K., and Buenfeld, N. R. (2006). “Pore segmentation of cement-based materials from backscattered electron images.” *Cement and Concrete Research*, 36(6), 1083–1090.

Woodson, R. D. (2009). *Concrete Structures: Protection, Repair and Rehabilitation*. Butterworth-Heinemann.

Xu, Y., Wong, Y. L., Poon, C. S., and Anson, M. (2001). “Impact of high temperature on PFA concrete.” *Cement and Concrete Research*, 31(7), 1065–1073.

Yang, H., Lin, Y., Hsiao, C., and Liu, J.-Y. (2009). “Evaluating residual compressive strength of concrete at elevated temperatures using ultrasonic pulse velocity.” *Fire Safety Journal*, 44(1), 121–130.

Ye, G., Liu, X., De Schutter, G., Taerwe, L., and Vandevelde, P. (2007). “Phase distribution and microstructural changes of self-compacting cement paste at elevated temperature.” *Cement and Concrete Research*, 37(6), 978–987.

Yu, B., and Cheng, P. (2002). “Fractal Models for the Effective Thermal Conductivity of Bidispersed Porous Media.” *Journal of Thermophysics and Heat Transfer*, 16(1), 22–29.

Yu, B., Lee, L. J., and Cao, H. (2001). “Fractal characters of pore microstructures of textile fabrics.” *Fractals*, 09(02), 155–163.

Yu, B., and Li, J. (2001). “Some fractal characters of porous media.” *Fractals*, 09(03), 365–372.

Yu, B.-M., and Yao, K.-L. (1988). “Critical percolation probabilities for site problems on Sierpinski Carpets.” *Zeitschrift für Physik B Condensed Matter*, 70(2), 209–212.

Yu, J., Yu, K., and Lu, Z. (2012). “Residual fracture properties of concrete subjected to elevated temperatures.” *Materials and Structures*, 45(8), 1155–1165.

Zeiml, M., Leithner, D., Lackner, R., and Mang, H. A. (2006). “How do polypropylene fibers improve the spalling behavior of in-situ concrete?” *Cement and Concrete Research*, 36(5), 929–942.

Zelić, J., Rušić, D., and Krstulović, R. (2002). “Kinetic Analysis of Thermal Decomposition of Ca(OH)2 Formed During Hydration of Commercial Portland Cement by DSC.” *Journal of Thermal Analysis and Calorimetry*, 67(3), 613–622.

Zhang, G., Xia, Y., Wang, H., Tao, Y., Tao, G., Tu, S., and Wu, H. (2010). “A Percolation Model of Thermal Conductivity for Filled Polymer Composites.” *Journal of Composite Materials*, 44(8), 963–970.

Zhang, H. Y., Kodur, V., Wu, B., Cao, L., and Wang, F. (2016). “Thermal behavior and mechanical properties of geopolymer mortar after exposure to elevated temperatures.” *Construction and Building Materials*, 109, 17–24.

Zhang, Q., and Ye, G. (2012). “Microstructural modeling of heated portland cement paste.” *Proceedings of 2nd International conference on Microstructural-related Durability of Cementitious Composites*, G. Ye, K. V. Breugel, W. Sun, and C. Miao, eds., RILEM Publications SARL, 848–856.

Zhang, W., Min, H., Gu, X., Xi, Y., and Xing, Y. (2015). “Mesoscale model for thermal conductivity of concrete.” *Construction and Building Materials*, 98, 8–16.

Zhao, H., and Darwin, D. (1990). *Quantitative Backscattered Electron Analysis Techniques for Cement-Based Materials*. University of Kansas Center for Research, Inc.

Zhao, H., and Darwin, D. (1992). “Quantitative backscattered electron analysis of cement paste.” *Cement and concrete research*, 22(4), 695–706.

Zhao, J. (2012). “Fire-Induced Spalling Modeling of High-Performance Concrete.” Ph.D. Thesis, Delft University of Technology.

Zheng, Z., and Feldman, D. (1995). “Synthetic fibre-reinforced concrete.” *Progress in Polymer Science*, 20(2), 185–210.

Zhou, Q., and Glasser, F. P. (2001). “Thermal stability and decomposition mechanisms of ettringite at < 120 °C.” *Cement and Concrete Research*, 31(9), 1333–1339.

Zhukov, V. V. (1975). *Explosive failure of concrete during a fire (in Russian)*. Joint Fire Research Organisation, Borehamwood.

Zoldners, N. G. (1971). “Thermal Properties of Concrete under Sustained Elevated Temperatures.” *Special Publication*, 25, 1–32.

APPENDIX A

A1 Supplementary Data

Table A1 Chemical composition of CSA A3001 Type GU cement

Oxide	Mass %
SiO_2	20.53
Al_2O_3	4.63
Fe_2O_3	2.77
CaO	62.7
MgO	2.48
Na_2O	0.21
K_2O	0.71
SO_3	3.23

Table A2 Chemical compounds in CSA A3001 Type GU cement; calculated using Bogue Equation

Compound	Mass %
C_3S	54.95
C_2S	17.41
C_3A	7.58
C_4AF	8.43

Table A3 Porosity of mortar (PT-0) at different exposure temperatures

	SEM		ASTM C642	
Temperature	Porosity	Standard deviation	Porosity	Standard deviation
[°C]	[%]	[%]	[%]	[%]
20	21.07	6.06	15.43	3.08
200	23.08	3.92	15.83	2.58
300	26.07	1.04	16.67	2.50
400	26.98	6.47	17.50	1.93
500	29.57	4.57	21.90	1.50

* PT-0 = 0% polyester fibre; PT-1 = 1% polyester fibre; PT-2 = 2% polyester fibre; PT-3 = 3% polyester fibre.

Table A4 Specific surface area and characteristic pore radius (PT-0)

	Specific surface area		Characteristic pore radius	
Temperature	Average	Standard deviation	Average	Standard deviation
[°C]	[1/μm]	[1/μm]	[μm]	[μm]
20	0.159	0.020	2.308	0.121
200	0.182	0.013	2.554	0.196
300	0.235	0.015	2.510	0.103
400	0.218	0.019	2.774	0.071
500	0.218	0.021	3.339	0.259

Table A5 Specific surface area and characteristic pore radius (PT-1)

	Specific surface area		Characteristic pore radius	
Temperature	Average	Standard deviation	Average	Standard deviation
[°C]	[1/μm]	[1/μm]	[μm]	[μm]
20	0.155	0.026	2.24	0.173
200	0.177	0.018	2.32	0.127
300	0.183	0.035	2.79	0.182
400	0.174	0.011	3.22	0.549
500	0.193	0.011	3.58	0.308

Table A6 Specific surface area and characteristic pore radius (PT-2)

Temperature	Specific surface area Average	Specific surface area Standard deviation	Characteristic pore radius Average	Characteristic pore radius Standard deviation
[°C]	[1/μm]	[1/μm]	[μm]	[μm]
20	0.16	0.034	2.30	0.240
200	0.17	0.017	2.68	0.263
300	0.18	0.014	3.15	0.356
400	0.17	0.002	3.66	0.385
500	0.18	0.025	3.75	0.166

Table A7 Fractal dimension using box-counting method

Temperature (°C)	**Mixture**	**Fractal dimension**	**Standard deviation**
20	PT-0	1.495	0.037
200		1.571	0.029
300		1.615	0.028
400		1.618	0.033
500		1.692	0.032
20	PT-1	1.470	0.035
200		1.522	0.032
300		1.558	0.034
400		1.580	0.030
500		1.659	0.032
20	PT-2	1.424	0.029
200		1.465	0.027
300		1.518	0.032
400		1.532	0.031
500		1.563	0.030
20	PT-3	1.475	0.031
200		1.515	0.032
300		1.544	0.030
400		1.572	0.034
500		1.613	0.029

Table A8 Effect of moisture on thermal properties at 20 °C.

Mixture	**T**	**TC**	**S.D.**	**TD**	**S.D.**	**Sp. heat**	**S.D.**	**Moisture**
	°C	W/(m·K)	W/(m·K)	mm^2/s	mm^2/s	MJ/m^3K	MJ/m^3K	by mass [%]
PT-0	20	2.300	0.063	0.910	0.047	2.531	0.111	7.58
	20	2.085	0.091	1.076	0.063	1.947	0.183	3.92
	20	1.750	0.062	0.966	0.049	1.814	0.071	0.01
PT-1	20	2.084	0.069	0.798	0.084	2.633	0.262	8.05
	20	1.908	0.072	1.030	0.101	1.863	0.149	3.88
	20	1.576	0.063	0.943	0.061	1.677	0.134	0.01
PT-2	20	2.097	0.091	0.869	0.051	2.419	0.166	7.74
	20	2.001	0.134	1.031	0.077	1.953	0.223	4.26
	20	1.616	0.074	0.978	0.038	1.653	0.090	0.01
PT-3	20	1.957	0.083	0.816	0.044	2.401	0.076	7.52
	20	1.542	0.060	0.925	0.075	1.675	0.130	4.24
	20	1.772	0.116	0.994	0.158	1.820	0.317	0.01

Note: TC = Thermal conductivity, TD = Thermal diffusivity, S.D. = Standard deviation

Table A9 Residual thermal properties of cement mortar at elevated temperature

Mixture	**T**	**TC**	**S.D.**	**TD**	**S.D.**	**Sp. heat**	**S.D.**
	°C	W/(m·K)	W/(m·K)	mm^2/s	mm^2/s	MJ/m^3K	MJ/m^3K
PT-0	20	1.756	0.067	0.971	0.052	1.810	0.079
	100	1.838	0.055	0.952	0.039	1.833	0.060
	200	1.773	0.067	1.007	0.031	1.762	0.105
	300	1.584	0.092	1.079	0.070	1.476	0.174
	400	1.516	0.094	0.996	0.056	1.521	0.030
	500	1.140	0.049	0.752	0.033	1.518	0.070
	600	1.091	0.068	0.781	0.027	1.397	0.039
PT-1	20	1.587	0.064	0.942	0.068	1.692	0.144
	100	1.601	0.088	0.936	0.036	1.712	0.089
	200	1.593	0.028	1.068	0.088	1.497	0.100
	300	1.512	0.035	0.919	0.041	1.646	0.066
	400	1.368	0.011	0.842	0.086	1.636	0.165
	500	1.010	0.043	0.600	0.034	1.689	0.153
	600	0.938	0.023	0.728	0.012	1.288	0.021
PT-2	20	1.632	0.069	0.971	0.038	1.682	0.064
	100	1.606	0.032	0.962	0.077	1.675	0.106
	200	1.642	0.101	0.966	0.049	1.701	0.113
	300	1.437	0.116	0.908	0.030	1.583	0.123
	400	1.371	0.043	0.850	0.024	1.615	0.093
	500	1.070	0.047	0.662	0.049	1.623	0.191
	600	0.983	0.073	0.700	0.034	1.404	0.084
PT-3	20	1.535	0.064	0.936	0.078	1.646	0.122
	100	1.558	0.046	0.998	0.050	1.565	0.127
	200	1.459	0.112	0.949	0.063	1.537	0.064
	300	1.449	0.051	0.918	0.028	1.580	0.092
	400	1.380	0.089	0.893	0.037	1.545	0.072
	500	1.012	0.064	0.745	0.060	1.362	0.113
	600	1.021	0.063	0.690	0.013	1.478	0.088

Note: TC = Thermal conductivity, TD = Thermal diffusivity, S.D. = Standard deviation

Table A10 Modelling of thermal conductivity using fractal approach

Mixture	**T**	**TC**	**S.D.**	**TD**	**S.D.**	**Sp. heat**	**S.D.**
	°C	W/(m·K)	W/(m·K)	mm^2/s	mm^2/s	MJ/m^3K	MJ/m^3K
PT-0	20	1.755776	0.067304	0.971099	0.052272	1.810466	0.078544
	100	1.718049	0.010291	0.927912	0.010652	1.851723	0.028089
	200	1.601733	0.080014	0.788345	0.1211	2.06343	0.239484
	300	1.338358	0.056823	0.579396	0.074299	2.331802	0.202121
	400	1.076875	0.013697	0.528362	0.011127	2.039048	0.061379
	500	1.239373	0.105208	0.592784	0.120789	2.135687	0.270871
PT-1	20	1.586677	0.064368	0.941865	0.068026	0.941865	0.143979
	100	1.565414	0.029098	0.77625	0.079785	0.77625	0.156994
	200	1.50466	0.086768	0.727251	0.161466	0.727251	0.337552
	300	1.354085	0.062035	0.670205	0.113404	0.670205	0.294457
	400	1.041357	0.095657	0.562399	0.139241	0.562399	0.377992
	500	1.170229	0.009961	0.47024	0.018794	0.47024	0.090468
PT-2	20	1.632417	0.06877	0.970981	0.037804	1.681971	0.063879
	100	1.573833	0.000794	0.909309	0.007655	1.73088	0.014098
	200	1.471548	0.042817	0.731627	0.064814	2.019424	0.122528
	300	1.343322	0.031236	0.644398	0.055017	2.095737	0.159348
	400	1.100098	0.128162	0.645682	0.091282	1.712409	0.123597
	500	1.270525	0.119021	0.653455	0.113546	1.970161	0.203589
PT-3	20	1.53474	0.064131	0.936451	0.078217	1.646105	0.122111
	100	1.631612	0.016803	0.773188	0.01552	2.110522	0.021829
	200	1.47106	0.091636	0.700897	0.134425	2.149449	0.319826
	300	1.392754	0.098606	0.746888	0.114972	1.882003	0.169584
	400	1.065473	0.104287	0.558376	0.122151	1.953266	0.310894
	500	1.212455	0.074027	0.606626	0.141275	2.064705	0.357773

Note: TC = Thermal conductivity, TD = Thermal diffusivity, S.D. = Standard deviation

Table A11 Model parameters for thermal conductivity using fractal approach

Temperature	Fractal parameters		Porosity		Fractal dimension	
[°C]	C	L	Measured	Simulated	Measured	Simulated
20	8	10	0.15	0.12	1.50	1.56
200	7	9	0.16	0.14	1.57	1.58
300	6	8	0.17	0.17	1.61	1.60
400	8	11	0.18	0.20	1.62	1.69
500	9	13	0.22	0.25	1.69	1.75

Table A12 Compressive strength, elastic modulus, and Poisson’s ratio for PT-0

	Mean	S.D.	Mean	S.D.	Mean	S.D.
Temperature	Max. stress		Mod. elasticity		Poisson's ratio	
[°C]	[MPa]	[MPa]	[MPa]	[MPa]		
20	44	4	23565	631	0.178	0.013
200	53	5	27789	1657	0.199	0.013
300	44	0	16003	746	0.166	0.009
400	39	1	10497	1174	0.269	0.059
500	29	2	6150	430	0.206	0.013
600	17	1	1582	381	0.120	0.016

Table A13 Compressive strength, elastic modulus, and Poisson’s ratio for PT-1

	Mean	S.D.	Mean	S.D.	Mean	S.D.
Temperature	Max. stress		Mod. elasticity		Poisson's ratio	
[°C]	[MPa]	[MPa]	[MPa]	[MPa]		
20	59	5	25939	5476	0.212	0.034
200	62	5	29147	2366	0.202	0.003
300	55	5	17910	2059	0.167	0.010
400	44	5	10936	1061	0.230	0.014
500	34	2	6226	102	0.192	0.004
600	23	0	1743	306	0.142	0.013

Table A14 Compressive strength, elastic modulus, and Poisson’s ratio for PT-2

	Mean	S.D.	Mean	S.D.	Mean	S.D.
Temperature	Max. stress		Mod. elasticity		Poisson's ratio	
[°C]	[MPa]	[MPa]	[MPa]	[MPa]		
20	40	5	24403	4681	0.229	0.044
200	45	2	25526	918	0.190	0.005
300	41	4	15985	816	0.167	0.009
400	35	2	9335	1550	0.214	0.009
500	27	1	5230	295	0.191	0.012
600	14	1	1117	86	0.162	0.026

Table A15 Compressive strength, elastic modulus, and Poisson’s ratio for PT-3

	Mean	S.D.	Mean	S.D.	Mean	S.D.
Temperature	Max. stress		Mod. elasticity		Poisson's ratio	
[°C]	[MPa]	[MPa]	[MPa]	[MPa]		
20	39	3	23081	603	0.198	0.007
200	40	5	24062	1548	0.206	0.018
300	39	3	15329	223	0.178	0.016
400	31	2	8704	160	0.237	0.010
500	24	1	5114	547	0.199	0.011
600	14	1	1562	199	0.193	0.005

Table A16 Modulus of rupture, fracture toughness, fracture energy, and characteristic length for PT-0

	Mean	S.D.	Mean	S.D.	Mean	S.D.	Mean	S.D.
T	MOR	MOR	K_{IC}	K_{IC}	G_F	G_F	l_{ch}	l_{ch}
[°C]	[MPa]	[MPa]	[MPa·√m]	[MPa·√m]	[N/m]	[N/m]	mm	mm
20	4.95	0.08	0.78	0.04	36.07	12.26	111.84	38.40
200	5.66	0.16	0.93	0.04	22.23	9.48	46.48	13.80
300	3.84	0.53	0.66	0.08	35.79	21.03	74.67	25.34
400	2.90	0.35	0.50	0.05	76.99	2.46	449.49	32.32
500	2.98	0.12	0.49	0.02	98.61	20.98	194.50	17.17

Table A17 Modulus of rupture, fracture toughness, fracture energy, and characteristic length for PT-1

	Mean	S.D.	Mean	S.D.	Mean	S.D.	Mean	S.D.
T	MOR	MOR	K_{IC}	K_{IC}	G_F	G_F	l_{ch}	l_{ch}
[°C]	[MPa]	[MPa]	[MPa·√m]	[MPa·√m]	[N/m]	[N/m]	mm	mm
20	4.74	0.18	0.75	0.04	35.80	4.28	134.51	25.48
200	5.15	0.11	0.80	0.02	27.45	3.98	94.84	13.56
300	3.74	0.14	0.60	0.02	33.08	0.74	118.77	23.65
400	2.72	0.34	0.44	0.08	90.63	8.15	490.75	113.80
500	2.25	0.13	0.36	0.02	89.03	19.45	320.23	0.71

Table A18 Modulus of rupture, fracture toughness, fracture energy, and characteristic length for PT-2

	Mean	S.D.	Mean	S.D.	Mean	S.D.	Mean	S.D.
T	MOR	MOR	K_{IC}	K_{IC}	G_F	G_F	l_{ch}	l_{ch}
[°C]	[MPa]	[MPa]	[MPa·√m]	[MPa·√m]	[N/m]	[N/m]	mm	mm
20	4.95	0.37	0.73	0.04	27.87	3.18	89.60	6.02
200	4.66	0.17	0.79	0.06	20.13	0.65	78.63	9.27
300	3.17	0.24	0.53	0.01	74.93	0.63	419.32	20.21
400	2.29	0.03	0.39	0.02	100.05	5.12	574.63	46.21
500	2.18	0.34	0.34	0.06	104.60	15.30	422.47	45.37

Table A19 Modulus of rupture, fracture toughness, fracture energy, and characteristic length for PT-3

	Mean	S.D.	Mean	S.D.	Mean	S.D.	Mean	S.D.
T	MOR	MOR	K_{IC}	K_{IC}	G_F	G_F	l_{ch}	l_{ch}
[°C]	[MPa]	[MPa]	[MPa·√m]	[MPa·√m]	[N/m]	[N/m]	mm	mm
20	4.70	0.28	0.76	0.06	34.72	2.72	140.05	32.36
200	5.35	0.59	0.85	0.13	30.85	6.67	106.36	28.07
300	3.51	0.23	0.60	0.05	24.90	4.87	106.53	14.01
400	2.27	0.03	0.38	0.01	105.38	14.92	574.88	74.07
500	2.12	0.30	0.32	0.05	109.09	15.53	407.50	64.12

Table A20 Fractal dimension of three dimensional pore space based on X-ray computed microtomography

Mixture ID	T	Fractal dimension	
	[°C]	Mean	S.D.
PT-0	200	2.599	0.066
PT-0	400	2.729	0.017
PT-0	500	2.785	0.030
PT-2	20	2.438	0.057
PT-2	300	2.685	0.048
PT-2	500	2.785	0.023

Table A21 Ultrasonic pulse velocity, estimated dynamic modulus, and damage variable based on dynamic modulus.

	Velocity				
Temperature [°C]	Mean [km/s]	S.D. [km/s]	Density [g/cm^3]	Dynamic modulus [GPa]	Damage variable
		Fibre -0.0%			
20	3.745	0.043	2.07	29	0.00
200	3.746	0.099	2.03	28	0.02
300	3.039	0.039	2.00	18	0.36
400	2.651	0.032	2.02	14	0.51
500	2.170	0.005	1.95	9	0.68
600	1.235	0.117	1.90	3	0.90
		Fibre -0.1%			
20	3.888	0.058	1.91	29	0.00
200	3.806	0.040	1.98	29	0.01
300	3.220	0.078	1.94	20	0.30
400	2.588	0.101	1.91	13	0.56
500	2.130	0.038	1.89	9	0.70
600	1.320	0.091	1.83	3	0.89
		Fibre -0.2%			
20	3.697	0.064	1.94	27	0.00
200	3.600	0.039	1.92	25	0.06
300	3.015	0.044	1.90	17	0.35
400	2.482	0.019	1.92	12	0.55
500	2.037	0.045	1.90	8	0.70
600	1.205	0.073	1.83	3	0.90
		Fibre -0.3%			
20	3.565	0.032	1.91	24	0.00
200	3.488	0.080	1.88	23	0.05
300	3.026	0.037	1.92	18	0.28
400	2.461	0.026	1.92	12	0.52
500	2.010	0.027	1.88	8	0.69
600	1.283	0.102	1.86	3	0.87

Table A22 Connected porosity at different temperature

		Mean connected pore fraction			S.D.
Mixture ID	T [°C]	Cluster # 1 [%]	Cluster # 2 [%]	Cluster # 3 [%]	Largest cluster (# 1) [%]
PT-0	20	51.94	7.37	3.04	3
PT-0	400	78.40	7.04	0.80	13
PT-0	500	86.76	9.60	3.42	3
PT-2	20	31.69	15.60	10.10	14
PT-2	300	70.79	5.58	3.83	11
PT-2	500	90.12	0.16	0.15	1

Table A23 Geometric tortuosity estimated using random -walk simulation

		Tortuosity	
Mixture ID	T [°C]	Mean	S.D.
		Fibre - 0.0%	
PT-0	200	5.65	0.88
PT-0	400	4.60	0.95
PT-0	500	4.22	0.44
		Fibre - 0.2%	
PT-2	20	20.76	4.42
PT-2	300	6.19	1.59
PT-2	500	3.70	0.20

Table A24 Specific surface area measured from X-ray computed microtomography

Mixture ID	T	Surface area		Specific surface area
		Mean	S.D.	
	[°C]	[μm^2]	[μm^2]	[1/μm]
PT-0-2	200	1453826144	231904495	0.01778
PT-0-4	400	1649346509	186494350	0.02018
PT-0-5	500	1836956375	202891296	0.02247
PT-2-1	20	700803788	91335310	0.00857
PT-2-3	300	1153013098	158431928	0.01410
PT-2-5	500	1740015110	141291958	0.02129

A2 Additional Figures

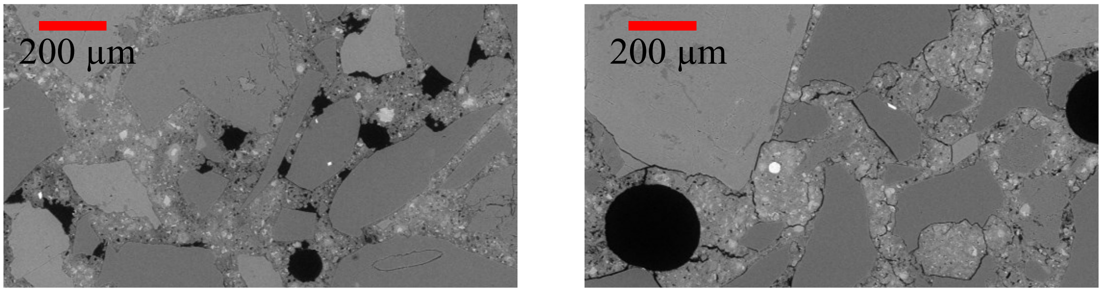

20 °C

500 °C

Figure A1 Scanning electron microscopy images of mortar at ambient temperature and at 500 °C.

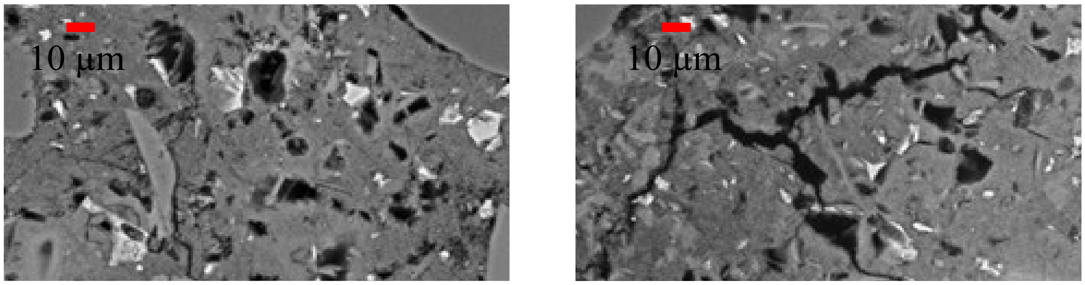

20 °C

500 °C

Figure A2 Enlarged scanning electron microscopy images of mortar at ambient temperature and at 500 °C.

APPENDIX B

B1 Determination of Fracture Toughness Using Compliance Calibration

The crack mouth opening displacement, *CMOD*, may theoretically be evaluated by:

$$CMOD = \frac{4\sigma a}{E} V_1(\alpha)$$

where σ is the flexural stress from four-point bending test equals to PL/bd^2, with P is the applied load; L, b, and d are the span, width, and depth of the beam respectively; $\alpha = (a + t)/(d + t)$, with a is the crack length and t is the thickness of the CMOD gauge attachment; E is modulus of elasticity, and $V_1(\alpha)$ is defined, for $L/d = 3$, as (Tada et al. 2000):

$$V_1(\alpha) = 0.8 - 1.7\alpha + 2.4\alpha^2 + 0.66/(1-\alpha)^2$$

Using the two equations above, a theoretical expression for E can be written as:

$$E = \frac{4P}{CMOD} \frac{aL}{bd^2} V_1(\alpha)$$

Using the above equation of E for the bend over point, A, as shown in Figure B1, and for any other point, for instance A', the following relationship can be derived:

$$E = \frac{4}{c(a_0)} \frac{a_0 L}{bd^2} V_1\left(\alpha_0\right)\bigg|_{\text{at point } A} = \frac{4}{c(a_{eff})} \frac{a_{eff} L}{bd^2} V_1\left(\alpha_{eff}\right)\bigg|_{\text{at any point } A'}$$

where $\alpha_0 = (a_0 + t)/(d + t)$, $\alpha_{\text{eff}} = (a_{\text{eff}} + t)/(d + t)$ with a_0 is the initial notch length and a_{eff} is effective crack length, and $c(a_0)$ and $c(a_{\text{eff}})$ is the compliance as a function of a_0 and a_{eff} defined by *CMOD*/*P*.

By rearranging the terms of the preceding equation, the effective crack length can be evaluated as follows:

$$a_{eff} = \frac{c(a_{eff})}{c(a_0)} a_0 \frac{V_1(\alpha_0)}{V_1(\alpha_{eff})}$$

Once the value of effective crack length is determined, the stress intensity factor can be computed as follows (Tada et al. 2000):

$$K_I(a_{eff}) = \sigma\sqrt{\pi a_{eff}}\, F_1(a_{eff})$$

where K_I is the stress intensity factor, and $F_1(a_{\mathrm{eff}})$ for $L/d = 3$ can be found from the following:

$$F_1(a_{eff}) = 1.122 - 1.4a_{eff} + 7.66a_{eff}^2 - 13.08a_{eff}^3 + 14.0a_{eff}^4$$

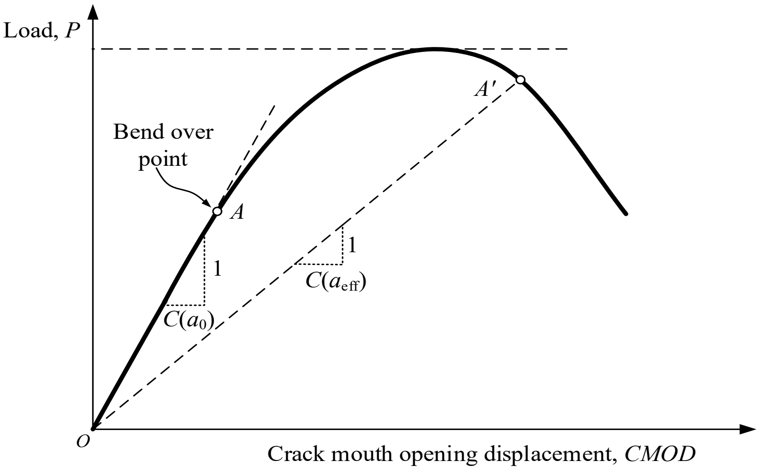

Figure B1 Determination of effective crack length using compliance calibration.

Crack tip opening displacement, *CTOD*, is evaluated using the following expression (Banthia and Sheng 1996):

$$CTOD = CMOD \cdot Z(\alpha, \beta)$$

where $Z(\alpha, \beta)$ is function dependent on the specimen geometry, which is defined as follows:

$$Z(\alpha,\beta) = \left[(1-\beta)^2 + (1.081 - 1.149\alpha)(\beta - \beta^2)\right]^{1/2}$$

where $\alpha = (a + t)/(d + t)$ and $\beta = (a_0 + t)/(a + t)$.